HAL
open science

Search for dark matter using XENONnT electron recoil data

Sid El Moctar Ahmed Maouloud

To cite this version:

Sid El Moctar Ahmed Maouloud. Search for dark matter using XENONnT electron recoil data. Astrophysics [astro-ph]. Sorbonne Université, 2022. English. NNT : 2022SORUS408 . tel-03978219

HAL Id: tel-03978219

https://theses.hal.science/tel-03978219v1

Submitted on 8 Feb 2023

HAL is a multi-disciplinary open access archive for the deposit and dissemination of scientific research documents, whether they are published or not. The documents may come from teaching and research institutions in France or abroad, or from public or private research centers.

L'archive ouverte pluridisciplinaire **HAL**, est destinée au dépôt et à la diffusion de documents scientifiques de niveau recherche, publiés ou non, émanant des établissements d'enseignement et de recherche français ou étrangers, des laboratoires publics ou privés.

Sorbonne Université

Ecole doctorale des Sciences de la Terre et de l'Environnement et Physique de l'Univers

UMR 7585 - LPNHE - Laboratoire de physique nucléaire et de hautes énergies

Thèse présentée pour obtenir le grade universitaire de Docteur

Discipline : Physique
Spécialité : Physique de l'Univers

Sid El Moctar AHMED MAOULOUD

Recherche de matière noire en utilisant les données de recul électronique de XENONnT

Search for dark matter using XENONnT electron recoil data

Sous la direction de Luca SCOTTO LAVINA

Soutenance le 06/10/2022 devant le jury composé de :

Bertrand LAFORGE	Président
Mariangela SETTIMO	Rapportrice
Björn HERRMANN	Rapporteur
Sara DIGLIO	Examinatrice
Davide FRANCO	Examinateur
Claudia NONES	Examinatrice
Fabrice HUBAUT	Examinateur
Luca SCOTTO LAVINA	Directeur de thèse

Résumé

Depuis plus d'un siècle, les astronomes ont procédé à un inventaire minutieux de la matière dans l'Univers. La comparaison de la masse visible avec la matière déduite des calculs dynamiques (faites à l'aide des courbes de vitesse de rotation des étoiles dans les galaxies, les mouvements des paires de galaxies et le comportement des galaxies dans les amas et super-amas) révèle que la nature d'au moins les trois quarts de la matière de l'Univers nous est totalement inconnue. Cette composante énigmatique de la matière dans l'Univers à pris le nom de **matière noire**.
Dans ce contexte d'incertitude et de questionnements, plusieurs arguments théoriques complémentaires aux modèles standards ont vu le jours enfin de résoudre le mystère de la matière noire. Ces derniers se divisent en deux catégories, ceux qui prédisent que la matière noire est sous forme de matière ordinaire et ceux qui prédisent qu'elle est sous forme de particules non baryoniques créées dès le Big Bang. Neamoins, le consensus général étant que les deux formes sont présentes dans l'Univers.
Malgré le grand nombre de questions sans réponses au sujet de la matière noire, certaines de ces propriétés ont été cernées. Nous savons, par exemple, que cette composante de la matière est très sombre (au sens optique du terme) et domine la cinématique interne, les propriétés de regroupement et les mouvements des systèmes galactiques. Elle joue également un rôle crucial dans la formation et l'évolution des grandes structures de l'Univers, et il est peu probable que des galaxies se soient formées sans sa présence.
La détermination de la nature de la matière noire est reconnue comme l'un des problèmes non résolus les plus fondamentaux de la cosmologie moderne. révéler la nature de la matière noire, en plus de corriger les théories fondamentales de la physique, permettrait de reconstruire l'histoire de l'Univers et de prédire son destin.

Bien qu'à ce jour, aucune particule non baryonique exotique et stable n'ait été détectée, selon le modèle standard, les abondances d'éléments déterminées à partir de l'ère de la nucléosynthèse suggèrent que la matière noire ne peut pas être entièrement baryonique. Ainsi, la matière noire pourrait être constituée d'une ou plusieurs nouvelles particules, censées être électriquement neutres, non colorées, à faible interaction et stables. Étant donné que le modèle standard de la physique de particules ne parvient pas à fournir un candidat de matière noire, il est nécessaire d'envisager des scénarios au-delà du modèle standard, qui peuvent également avoir une large phénoménologie lié à d'autres problèmes en physique des particules. Les nouveaux scénarios de physique reposent généralement sur de nouvelles symétries brisées aux hautes énergies ou aux dimensions supplémentaires. A ce titre, ils peuvent impacter les propriétés de l'Univers primordial, soit par la présence de nouvelles particules dans le bain thermal primordial, soit via des transitions de phase.

Les expériences de détection directe de la matière noire visent à détecter les particules de matière noire directement en laboratoire. Des preuves positives

prouveraient que la matière noire est composée de particules et permettraient d'étudier leurs propriétés en détail. De telles études détaillées sont essentielles pour la physique des particules élémentaires car elles stimuleront l'émergence d'un nouveau domaine au-delà du modèle standard de la physique des particules. Les expériences de détection directe de la matière noire s'attendent à ce que les particules de matière noire interagissent avec la matière ordinaire, comme les nucléons. C'est une hypothèse raisonnable supposant le fait que les particules de matière noire ont été produites thermiquement dans l'Univers primitif, que leur densité a diminué par annihilation en matière ordinaire, leur densité est alors figée après que l'Univers a atteint un volume qui ne permet plus aux particule de matière noire de se rencontrer (facilement). Étant donné que l'interaction devrait être faible, ces particules sont appelées **WIMPs** (acronyme anglais pour Weakly Interacting Massive Particles, pouvant se traduire par *particules massives interagissant faiblement*). Enfin, ils doivent être massifs car toute particule sans masse ne peut pas se comporter comme de la matière.

La recherche de particules de matière noire avec des masses inférieures au GeV représente une nouvelle frontière expérimentale importante et qui fait l'objet d'une attention accrue ces dernières années. Contrairement aux modèles de recherches traditionnelles par détection directe, qui recherchent des particules de matière noire se diffusant élastiquement avec des noyaux, la recherche de matière noire inférieure au GeV se base sur la mesure d'un ou de quelques électrons ionisés à la suite d'interaction de particules de matière noire avec les électrons dans le détecteur.

XENON est un projet de recherche directe de matière noire situé dans le laboratoire souterrain italien, LNGS. La génération précédente du détecteur XENON, XENON1T, a atteint une exposition de 1 ton×an, fixant les limites les plus strictes sur la section efficace de diffusion indépendante du spin des particules WIMP sur les nucléons pour presque toute la gamme de masses de WIMP supérieures à 120 MeV. Le détecteur multitonne XENONnT est la prochaine étape dans l'évolution du projet XENON. Le détecteur consiste en une chambre à projection temporelle (TPC) à deux phases située à une profondeur moyenne de 3600 m équivalent eau. La région active du TPC contient 5,9 tonnes de Xénon liquide (LXe). Une particule entrant dans le TPC peut diffuser sur un noyau de Xénon ou un électron, générant respectivement une interaction de recul nucléaire ou de recul électronique. Ces interactions créent des photons de scintillation par désexcitation des dimères Xe_2 et des électrons libres à la suite de l'ionisation des atomes de Xe. Le signal de scintillation, appelé S1, est détecté par deux réseaux de tubes photomultiplicateurs (PMT) situés en haut et en bas du TPC. Un champ électrique est ensuite utilisé pour faire dériver les électrons libres du lieu d'interaction vers l'interface liquide-gaz. Enfin, un deuxième champ plus fort extrait les électrons dans la phase gazeuse de xénon (GXe), qui produit alors un signal de scintillation secondaire, appelé S2, qui est amplifié proportionnellement au nombre d'électrons extraits. La position tridimensionnelle de l'emplacement de l'interaction est déduite du modèle d'impact de la lumière S2 sur le réseau PMT supérieur (position x-y) et de la différence de temps entre S1 et S2 due au temps de dérive des électrons d'ionisation permets d'avoir la profondeur à laque-

lle l'interaction a eu lieu (position z). Et le rapport S2/S1 peut être utilisé pour discrimineer entre reculs nucléaires et reculs électroniques.

Les interactions des particules avec des masses inférieures au GeV dans le détecteur XEENONnT ne produisent que quelques signaux de photons de scintillation. Ainsi, les signaux S1 observés peuvent tomber en dessous du seuil de détection. Cependant, en raison du gain de scintillation proportionnel dans le volume GXe, les signaux S2 produits par des particules plus légères peuvent toujours être observés. Ainsi, pour abaisser le seuil d'énergie et pouvoir rechercher ces candidats matiere noire de masse plus légère, l'exigence d'avoir détecté un signal S1 est supprimée. Cette analyse est dite *S2-seulement* ou *S2-only*.

Cette thèse vise à rechercher la détection directe de la matière noire sub-GeV via la diffusion des électrons de l'atome de Xénon au sein du détecteur XENONnT. Les modèles considérés correspondent à la diffusion matière noire-électron, dans laquelle un fermion ou un boson scalaire candidat à la matière noire diffuse sur un électron lié dans un atome de Xénon, ou un pseudo-scalaire, comme les particules de type axion, ou photons noirs, par absorption par des atomes de Xénon. Une telle étude phénoménologique contribue à résoudre le problème de basse énergie des détecteurs tels que XENON, LUX, PANDA-X ou DarkSide. En permettant l'accès à un nouvel espace paramétrique encore inaccessible pour ce genre de détecteur, qui sont contraints de sonder la matière noire dans des régions de masses élevées où la composante de matière noire semble être sous-dominante.

Abstract

For more than a century, astronomers have carried out a meticulous inventory of matter in the Universe. The comparison of the visible mass with the matter deduced from dynamic calculations, made using rotation curves of stars in the galaxies, the movements of pairs of galaxies, and the behavior of galaxies in clusters and super-clusters, reveals that the nature of at least three-quarters of the matter in the Universe is entirely unknown to us. This enigmatic matter component of the Universe has taken the name of **dark matter**.
In this context of uncertainty and questioning, several theoretical arguments complementary to standard models have emerged intending to solve the mystery of dark matter. They can be divided into two categories, those which predict that dark matter is in the form of ordinary matter and those which predict that it is in the form of non-baryonic particles created by the Big Bang. Nevertheless, the consensus is that both forms are present in the Universe.
Despite many unanswered questions about dark matter, some of these properties have been identified. For example, we know that this matter component is very dark (in the optical sense of the term) and dominates the internal kinematics, clustering properties, and motions of galactic systems. It also plays a crucial role in the formation and evolution of large structures in the Universe. In particular, galaxies are unlikely to have formed without its presence.
Determining the nature of dark matter is recognized as one of the most fundamental unsolved problems of modern cosmology. Revealing the nature of dark matter, in addition to correcting fundamental theories of physics, would make it possible to reconstruct the history of the Universe and predict its fate.

Although no exotic and stable non-baryonic particles have been detected to date, according to the Standard Model, element abundances determined from the era of nucleosynthesis suggest that dark matter cannot be fully baryonic. Thus, dark matter could consist of one or more new particles, believed to be electrically neutral, uncolored, weakly interacting, and stable. Since the Standard Model of particle physics fails to provide a dark matter candidate, it is necessary to consider scenarios beyond the Standard Model, which may also have broad phenomenology related to other problems in particle physics. New physics scenarios usually rely on new broken symmetries at high energies or extra dimensions. As such, they can impact the properties of the primordial Universe, either by the presence of new particles in the primordial thermal bath or via phase transitions.

Direct dark matter experiments aim to detect dark matter particles directly in the laboratory. Positive evidence would prove that dark matter is composed of particles and allow their properties to be studied in detail. Such detailed studies are essential for elementary particle physics since they will stimulate the emergence of a new field beyond the standard model of particle physics.
Direct dark matter detection experiments expect dark matter particles to interact with ordinary matter, such as nucleons. This is a reasonable hypothesis assuming that dark matter particles were produced thermally in the early Universe and

that their density decreased by annihilation in ordinary matter. Their density is then fixed after the Universe reaches a volume that no longer allows dark matter particles to meet (easily). Since the interaction should be weak, these particles are called **WIMPs** (an acronym for Weakly Interacting Massive Particles). Finally, they must be massive because a massless particle cannot behave like matter.

The search for dark matter particles with sub-GeV masses represents an essential new experimental frontier recently receiving increased attention. Unlike traditional direct detection search models, which search for elastically scattering dark matter particles with nuclei, the search for sub-GeV dark matter is based on the measurement of one or a few ionized electrons as a result of the interaction of dark matter particles with electrons in the detector.

XENON is a direct search project for dark matter. The previous generation of the XENON detector, XENON1T, achieved an exposure of 1 ton×year, setting the most stringent limits on the spin-independent scattering cross-section of WIMP particles over nucleons for nearly the entire mass range of WIMP greater than 120 MeV.
The XENONnT multi-ton detector is the next step in the evolution of the XENON project. The detector consists of a two-phase time projection chamber (TPC) located in the Italian underground laboratory, LNGS, at an average depth of 3600 m water equivalent. The active region of the TPC contains 5.9 tonnes of Liquid Xenon (LXe). A particle entering the TPC can scatter onto a Xenon nucleus or an electron, generating a nuclear recoil or electronic recoil interaction, respectively. These interactions create scintillation photons by de-excitation of Xe_2 dimers and free electrons following ionization of Xe atoms. The scintillation signal, called S1, is detected by two photomultiplier tube (PMT) arrays at the top and bottom of the TPC. An electric field is then used to divert the free electrons from the interaction place toward the liquid-gas interface. Finally, a second stronger field extracts the electrons in the gas phase of xenon (GXe), producing a secondary scintillation signal called S2, which is amplified in proportion to the number of electrons extracted. The three-dimensional position of the interaction location is inferred from the S2 light pattern on the upper PMT (x-y position), and the time difference between S1 and S2, due to the electron drift time, allows having the depth at which the interaction took place (position z). Moreover, the ratio S2/S1 can be used to discriminate between nuclear recoils and electronic recoils.

Particle interactions with sub-GeV masses in the XEENONnT detector produce only a few scintillation photon signals. Thus, the observed S1 signals may fall below the detection threshold. However, due to the proportional scintillation gain in the GXe volume, S2 signals produced by lighter particles can still be observed. Thus, to lower the energy threshold and be able to search for these dark matter candidates of lighter mass, the requirement of detecting a signal S1 is removed. This type of analysis is called *S2-only*.

This thesis aims to search for direct detection of sub-GeV dark matter via diffusion of electrons from the Xenon atom within the XENONnT detector. The models considered correspond to the DM-electron scattering, in which a fermion

or scalar boson dark matter candidate scatters off an electron bound in a Xenon atom, and the pseudo-scalar dark matter, such as axion-like particles, or dark photons, through absorption by Xenon atoms. Such a phenomenological study contributes to solving the low-energy problem of detectors such as XENON, LUX, PANDA-X, or DarkSide. By allowing access to a new parametric space still inaccessible for this kind of detector, which is forced to probe dark matter in regions of high masses where the dark matter component seems to be subdominant.

Remerciements

La réalisation de cette thèse n'aurait pas été possible sans le soutien et les encouragements de plusieurs personnes. Par conséquent, je voudrais profiter de cette occasion pour montrer ma gratitude à ceux qui m'ont aidé de multiples façons.

Je tiens à remercier toutes les personnes qui ont contribué aux travaux décrits dans cette thèse. Tout d'abord, je remercie mon directeur de thèse, Luca Scotto Lavina, de m'avoir accepté dans son groupe. Au cours de ma période de thèse, il a contribué à une expérience d'études et de travail enrichissante et agréable, en me donnant une une grande liberté intellectuelle dans mon travail, en soutenant ma participation à diverses conférences, en m'engageant dans de nouveaux domaines et en exigeant un travail de haute qualité. De plus, je tiens à remercier les membres du groupe XENON au LPNHE, Bernard Andrieu, Romain Gaior, Erwann Masson, ainsi que Jean-Philippe Zopounidis pour leur aide, leur accueil, et l'ambiance de travail agréable qu'ils contribuent à faire régner.

Enfin, je remercie ma famille à qui je dois énormément. À mon défunt père, Ismaël, merci de m'avoir encouragé et soutenut contre vents et marée. À mon frère Ahmed, merci pour ton soutien. Merci également à ma sœur Mariem. Et enfin, la seule personne qui a rendu tout cela possible est ma mère Fatimetou. Elle a été une source constante de soutien et d'encouragement et a fait un nombre incalculable de sacrifices pour moi, en particulier pour que je puisse poursuivre mes études à l'étranger. Mes parents sont une grande source d'inspiration pour moi. Par conséquent, une grande appréciation et un énorme merci leur sont dus, car, sans leur compréhension et leur soutien, cette thèse n'aurait jamais eu lieu. Je vous remercie tous.

A la mémoire de mon père

Contents

1 Introduction **1**
1.1 Preamble and early history . . . 1
1.2 The era of the first precision measurements . . . 4
1.3 Gravitation or particles? . . . 7
1.3.1 Modified Newtonian Dynamics . . . 7
1.3.2 Dark matter as particles . . . 11
1.4 The search for dark matter . . . 19
1.4.1 Direct search of dark matter . . . 19
1.4.2 Indirect search of dark matter . . . 21
1.4.3 Dark matter production by high-energy colliders . . . 22
1.5 Direct detection of Dark Matter . . . 24
1.5.1 Distribution and local flux of dark matter . . . 26
1.5.2 Supersymmetric WIMPs . . . 27
1.5.3 Axions and axion-like particles . . . 39
1.5.4 Light dark matter of the Hidden Sector . . . 43

2 XENON dark matter research project **45**
2.1 Detection principle . . . 47
2.1.1 The choice of the target . . . 47
2.1.2 The Dual-phase Xenon TPC . . . 49
2.1.3 Energy reconstruction . . . 51
2.2 XENONnT . . . 55
2.2.1 The muon veto . . . 55
2.2.2 The neutron veto . . . 57
2.2.3 Photomultiplier tubes . . . 59
2.2.4 Electric field configuration . . . 61
2.2.5 Cryogenics and purification systems . . . 63
2.2.6 Slow control . . . 65
2.2.7 Data acquisition . . . 66
2.2.8 Data transfer . . . 67
2.2.9 Data processing . . . 67
2.2.10 Calibrations . . . 72
2.3 Simulations and backgrounds . . . 79
2.3.1 Simulation framework . . . 79
2.3.2 Backgrounds . . . 80
2.4 Projected XENONnT sensitivity . . . 83

2.4.1 Statistical model 83
2.5 Summary 86
2.6 Summary of my contributions to XENONnT 87

3 Analysis of single electron signals with XENONnT 90
3.1 Introduction 90
3.2 Phenomenology of single electrons 91
3.2.1 Single electrons from photoionization 91
3.2.2 The waveform properties of single electrons 91
3.2.3 Single electrons rate 93
3.3 Modelization of the single electrons spectrum 96
3.3.1 Comparison with a fit with a sum of Gaussians 98
3.4 Single electrons as a calibration tool 100
3.4.1 The electrodes sagging 100
3.4.2 Secondary scintillation gain as a function of the XY position 102
3.4.3 Time evolution of the secondary scintillation gain 103
3.5 Modelization of the secondary scintillation gain 105
3.5.1 Comparison between the model and the measured value of the secondary scintillation gain 106
3.6 Systematic studies of single electrons 109
3.7 Data selection and cuts 111
3.7.1 The transverse wires problem 113
3.7.2 Fiducial volume 114
3.7.3 Single electron selection 116
3.7.4 Area fraction top cut 118
3.7.5 Classification and selection of primary S2 signals 121
3.7.6 Primary live-time cut 126
3.7.7 Cut on overlapping S2s 128
3.7.8 Position correlation cut 130

4 Search for sub-GeV dark matter using SR0 XENONnT electronic recoils data 135
4.1 Introduction 135
4.2 Direct detection rates 138
4.2.1 Excitation rates 139
4.2.2 Ionization form factor 142
4.2.3 Events rate 145
4.3 Detector response 147
4.3.1 Ionization electrons 148
4.3.2 Detected electrons 149
4.3.3 Generation of the S2 signal 151
4.3.4 Systematic uncertainties 153
4.4 Backgrounds for sub-GeV DM search in XENONnT 153
4.4.1 Coherent neutrino-nucleus scattering 154
4.4.2 Residual ER background 155
4.4.3 Comparison between background sources 155
4.5 Search for bosonic dark matter 156

4.5.1 Dark photon 156
4.5.2 Axion-like particles 157
4.5.3 In-medium correction 158
4.6 Limits setting on the neutrino magnetic moment 159
4.6.1 Solar neutrinos ν-e scattering 161
4.6.2 Neutrino magnetic moment 161
4.6.3 Limit setting procedure 163
4.7 Limits on dark photons from solar emission 164
4.7.1 Dark photons production in the Sun 164
4.8 Dark photon absorption in LXe 166
4.9 Conclusion 167

5 Conclusion **168**

List of Figures

1.1 William Thomson, 1st Baron Kelvin. 1

1.2 Fritz Zwicky. 3

1.3 Example of a rotation curve of a spiral galaxy. The yellow dots correspond to the average circular speed of the stars, and the blue dots correspond to the average circular speed of the gas using the Hydrogen 21 cm line measured by the Doppler effect [10]. 4

1.4 Observed rotation curve of galaxy ESO138-G014 (data points) and MOND prediction (red curve) $a_0 = 1.35 \cdot 10^{-8}$ cm s^{-2} [26]. 9

1.5 Bullet Cluster's false-color image, where the pink regions indicate the mass distribution as measured directly and the blue regions represent the mass as measured by gravitational lensing (X-ray: NASA/CXC/CfA/[28]; Optical: NASA/STScI,[27]; lensing map: NASA/STScI ESO WFI,[27]) 10

1.6 Temperature variations in the cosmic microwave background (fluctuations of the order of 10^{-6}). (ESA and the Planck Collaboration [43]). 12

1.7 Sensitivity of the acoustic temperature spectrum to four fundamental cosmological parameters (a) the curvature as quantified by Ω_{tot} (b) the dark energy as quantified by the cosmological constant Ω_Λ ($w_\Lambda = -1$) (c) the physical baryon density $\Omega_b h^2$ (d) the physical matter density $\Omega_m h^2$, all varied around a fiducial model of $\Omega_{tot} = 1$, $\Omega_\Lambda = 0.65$, $\Omega_b h^2 = 0.02$, $\Omega_m h^2 = 0.147$, $n = 1$, $z_{\mathrm{ri}} = 0$, $E_i = 0$. (Figures from Xenon [45]) 15

1.8 Power spectrum of the CMB radiation temperature anisotropies as a function of the angular scale. (ESA and the Planck Collaboration [20]). 16

1.9 Illustration of freeze-out and freeze-in scenarios in the evolution of thermal dark matter abundance for $m_\chi = 100$ GeV as a function of $x = m_\chi/T$ for different annihilation rates. The horizontal band gives the observed relic density from Planck data [20]. Figure from [46]. 17

1.10 Schematic showing the possible dark matter detection channels. . . 19

1.11 Sensitivity projections (90% upper limits) for spin-independent WIMP-nucleon scattering. (APPEC Committee Report [53]). 20

1.12 Illustration of the three indirect dark matter detection channels. . . 21

1.13 95% upper limits on the thermally-averaged cross-section for dark matter particles annihilating into $b\bar{b}$ (upper-left), W^+W^- (upper-right), $\tau^+\tau^-$ (bottom-left) and $\mu^+\mu^-$ (bottom-right) pairs. Thick solid lines show the limits obtained by combining Fermi-LAT observations of 15 dwarf spheroidal galaxies (dSphs) with MAGIC observations of Segue 1. Dashed lines show the observed individual MAGIC (short dashes) and Fermi-LAT (long dashes) limits. The thin dotted line, green and yellow bands show, respectively, the median and the symmetrical, two-sided 68% and 95% containment bands for the distribution of limits under the null hypothesis. The red-dashed-dotted line shows the thermal relic cross-section. (MAGIC collaboration [59]). 23

1.14 90% upper limits (solid lines) and expected sensitivity (dotted) on the spin-dependent cross-section as a function of WIMP mass obtained by 7 years of IceCube DeepCore data. The dark and light-shaded bands show the central 68% and 95% expected limits, respectively. Also shown are limits from the Super-K, PICO-60, and ANTARES experiments. (IceCube [60]). 24

1.15 Exclusion limit and sensitivity for main exciting and planned dark matter production experiments. Figure from [61]. 25

1.16 The Milky Way can be divided into three structural components: the galactic bulge, the galactic disk, and the dark matter halo, respectively, in blue, green, and red. 26

1.17 Illustration of the expected *dark matter wind*, which is due to the movement of the Sun relative to the dark matter halo of the Milky Way. It is also possible to see the origin of the modulation of this wind during the year. Figure from [64] 26

1.18 Feynman diagrams of WIMP-nucleus interaction 30

1.19 The differential interaction rate as a function of the recoil energy for different targets, for $M_\chi = 60$ GeV. 36

1.20 The evolution of the detection cross-section of a direct dark matter detector as a function of the mass of the WIMPs, the threshold energy, and the mass number of the target nucleus. Continuous curve $A = 40$ (Argon), dotted curve $A = 132$ (Xenon) with E_s (keV) = $\{1;10;30\}$. 37

1.21 Form factor as a function of recoil energy E_R for different mass numbers. In dotted lines are represented the one corresponding to Xenon. 39

1.22 Limits on the axions-like particles mass established by cosmology and astrophysics. Light grey regions are model dependent. The green regions indicate the planned reach of future upgrades. The cold dark matter exclusion range is particularly uncertain; ranges for pre-inflation and post-inflation Peccei-Quinn transitions are shown (see [80] for more details). Figure from [80]. 41

1.23 Energy spectra of solar axions produced due to the axion–photon (Primakoff effect) and axion–electron couplings (atomic de-exitation/recomb., Bremsstrahlung, Compton). Figure from [87]. 42

1.24 Illustration contrasting the Standard Model with the Hidden Sector. The particles of the Standard Model and the Hidden Sector could interact through "portals," which are particular coupling mechanisms such as the dark photon-photon coupling. Figure from [90]. 44

2.1 Fits to the data under various hypotheses. For the tritium (a), solar axion (b), and neutrino magnetic moment (c) searches, the null hypothesis is the background model B_0, and the alternative hypothesis is B_0 plus the respective signal. The null and alternative hypotheses in each scenario are denoted by gray (solid) and red (solid) lines, respectively. Dashed lines illustrate contributions from selected components in each alternative hypothesis. Panel (d) shows the best fits for an additional statistical test on the solar axion hypothesis, where an unconstrained tritium component is included in both null and alternative hypotheses. This tritium component contributes significantly to the null hypothesis, but its best-fit rate is negligible in the alternative hypothesis, which is illustrated by the orange dashed line in the same panel. (Figures from [99]) 47

2.2 Illustration of the chain reaction following excitation or ionization of a Xenon atom in the volume target of the detector. 50

2.3 The process leading to the primary signal S1 (excitation) in the liquid part of the detector and to the signal S2 (ionization) in the gaseous part. 51

2.4 Calculation of g_1 and g_2 in XENONnT. This was performed using multiple mono-energetic lines with known energies to extract the best fit for the value of the gains (g_1,g_2) by making a “Doke plot”, a plot in charge yield and light yield space. Different energy or different eclectic field are expected to have different charge yield and light yield, but these points will only move along the line as the total quanta number is fixed. 54

2.5 Illustration of the XENONnT cryostat and TPC 56

2.6 The location of the XENON experiment within the LNGS. 57

2.7 Geant4 rendering of the three nested detectors, including muon and neutron veto. The water tank walls, which support the muon veto PMTs, the neutron veto support structure, and other components (e.g. calibration systems) are omitted for clarity. Reflector panels, which optically separate the neutron and muon vetos, are shown as transparent turquoise surfaces. 58

2.8 Detection principle of radiogenic neutrons captured in XENONnT neutrons veto. 59

2.9 (Left) SPE gain of XENONnT as a function of the calibration number. (Right) Single PE gain distribution for 5 random PMTs. The solid line shows the mean, and dashed lines show the +/- 1%. 60
2.10 SPE resolution defined as σ_{1PE}/μ_{1PE} for the two PMT arrays (top and bottom) + total. The mean and the standard deviation come from the fitting of the SPE spectrum, with very low illumination LED data calibration. The solid black line shows the average SPE resolution. 61
2.11 Afterpulse spectrum of PMT 296, which has the largest Xenon afterpulse rate of all XENONnT PMTs of about 2.5%. The vertical lines indicate the calculated (theoretical) ion delay time and mass-to-charge ratio. 62
2.12 Illustration of the TPC, with LXe/GXe piping included. Includes zoom into the top and bottom grid regions. 62
2.13 Photo showing me treating pieces of shaping rings with a nitric acid bath. 64
2.14 (Left) Electron lifetime improvement after the start of cryogenic LXe purification with the high-efficiency O_2 filter. (Right) Electron lifetime improvement after switching to cryogenic LXe purification with the low-Rn O_2 filter. 64
2.15 Slow Control block diagram. 65
2.16 XENONnT DAQ diagram. 66
2.17 S1 and S2 waveform as well as S2 hit pattern of a krypton calibration event. 68
2.18 A Naive Bayes Bayesian Network Graph. 68
2.19 A plot of ^{83m}Kr calibration data in corrected S2 area (ionization signal size) vs. corrected S1 area (scintillation signal size). Main S2 area with the color dimension illustrating the S1 of each scatter point's likelihood of being an S2 using the Bayes method. A left-most color scale value indicates that the S1 looks highly canonical or statistically most like the training (simulation) S1. The median color bar values indicate that the S1 looks neither like a canonical S1 or S2, and the rightmost color bar values (where very few points exist) would indicate that the S1 looks most like a canonical S2. . 69
2.20 Hit pattern and event position reconstruction with a neural network. 70
2.21 ER (left) and NR (right) bands comparisons between XENONnT first science run (SR0) and the NEST model. 71
2.22 (Left) ^{83m}Kr S1 spectra before and after S1 (x,y,z) correction under 18 V/cm drift field. The S1 resolution is much better after correction. Inset plot: The time difference between ^{83m}Kr double scatters. The fitted 157 ± 1 ns half-life is close to the literature value of 156 ns. (Right) Distributions of S2, electron lifetime corrected S2 and cS2 under 18.3 V/cm drifting field. 72
2.23 (Left) Computer-aided design render of the inner part of the detector with calibration systems highlighted. (Right) Photos with labels of the XENONnT calibration systems. 73

2.24 Computer-aided design render of the entire detector. The viewpoint is designed to reflect what a viewer would see if they stood outside the water tank, looking up toward the top of the water tank. 75

2.25 The production of the isomeric state ^{83m}Kr by electron capture decay of ^{83}Rb. The isomeric $1/2^-$ state, with its half-life of 1.83 h, is populated in about 78% of all ^{83}Rb decay processes and de-excites by two highly converted γ-transitions. Figure from [130]. . 76

2.26 cS1 and cS2 distributions of ^{83m}Kr population under 18.3 V/cm drifting field. The plot on the top is the cS1 spectrum, and the one on the right is cS2. Although the two-step decay is visible in cS1 space, due to the large width (~ 4000 ns, strongly dependent on drift time) of ^{83m}Kr cS2 compared with the half-life of the decay (~ 150 ns), most of the cS2 are merged and indistinguishable. While the 32.1 keV and 41.5 keV bulges are true populations, the 9.4 keV bulge shares the same cS2 as the 32.1 keV bulge, as they are from the same double S1 single S2 population. 77

2.27 The decay chain of ^{220}Rn, following its emanation from a ^{228}Th source. (Figure from [131]). 78

2.28 The results on the charge yield for the ^{37}Ar L peak and K peak energies (green dots) obtained from XENON1T data are compared with other measurements of the charge yield at different energies. The cyan line is the prediction from BBF, and the violet line is the prediction from NEST. The dotted vertical bar represents the value of 11.5 eV, which is the work function value of the Xenon used. . 79

2.29 3D plot showing the distribution of events during AmBe calibration and for two separate positions of the source. Also shown are the top and bottom u-tubes. The AmBe source position is indicated in the red dot. 80

2.30 XENONnT background energy spectrum using 4.2-day background data. The spectrum presents two blinded regions, as shown in the figure. 81

2.31 (Left) Main ER background source by isotope. (Right) Main ER background source by material component. 82

2.32 Main NR background source by material component. 83

2.33 The XENONnT sensitivity and discovery power projections in the search for spin-independent WIMP-nucleon couplings. (Left) Median 90% CL exclusion limit (black solid line) for a 20 t.y exposure, with the 1σ (green) and 2σ (yellow) bands. The current strongest exclusion limit obtained with XENON1T [96], is shown in blue. The gray dashed-dotted line represents the discovery limit of an idealized LXe-based experiment with CEνNS as unique background source and a 1000 t.y exposure [137]. The atmospheric neutrino background would significantly slow down the improvement of the discovery potential with increasing exposure below that line. (Right) Sensitivity as a function of exposure, for searching for a 50 GeV/c^2 WIMP in the assumed 4 tons fiducial mass. The dashed (dotted) black lines in both panels indicate the smallest cross-sections at which the experiment would have a 50% chance of observing an excess with significance greater than 3σ (5σ). A two-sided profile construction is used to compute the confidence intervals. (Figure from [100]). 87

2.34 (Left) ER background rate in the (3, 100) PE cS1 observable ROI as a function of the ^{222}Rn concentration in LXe. The orange dashed line represents the ^{222}Rn fractional contribution to the total ER background. The dotted grey lines indicate the XENONnT goal of 1 µBq/kg and the 4.5 µBq/kg ^{222}Rn concentration achieved in XENON1T [138]. (Right) Projection of the XENONnT sensitivity to spin-independent couplings of a 50 GeV/c^2 WIMP as a function of the ^{222}Rn concentration in LXe. (Figure from [100]). 88

2.35 Evolution of the radon rate in XENONnT during initial distillation. The distillation is in an intermediate gas-only mode, pending cleaning of the column to be compatible with the high electron lifetime achieved. An additional rate reduction by a factor of ~ 2 is predicted for the final column mode based on previous data from distillation commissioning. 89

3.1 A schematic representation of the primary single electron production mechanism. (this illustration is from XENON100, hence the "62 kg"). 92

3.2 Waveform of a ^{83m}Kr calibration event showing the primary S1, S2 as well as the alternate S1, S2 (see Section 2.2.10) in addition to the S2 signal tail, which corresponds to single electrons.) 93

3.3 Raw spectrum of low energy S2 peaks (single electrons). 93

3.4 The rate of delayed single electron emission as a function of time following an energy deposition in the detector. Also shown the rate observed by XENON1T. The dotted vertical line at 750 µs and 2.2 ms indicates the maximum drift time in XENON1T and XENONnT, respectively. A high rate of delayed SE is observed for several times the maximum drift time. This is due to scintillation light produced from the extraction of photoionization electrons into the GXe region, producing additional photoionization electrons. . . 94
3.5 The number of delayed electrons observed from 0.1 ms to 1 s after the S2 primary as a function of the size of the S2 primary in photoelectrons. A general trend towards more delayed electrons after larger S2 primaries is observed. This trend seems to follow a power law, as shown by the fit. 95
3.6 Rate of first 4 multi-electron signals as a function of the delay after larger S2s (> 150 PE). The vertical dotted line shows the value of the maximum drift time (2.2 ms). 95
3.7 The fit plot of the SE spectrum with model (3.4), choosing $N = 5$. In this figure, it is possible to see the value given by the fit for the secondary scintillation gain μ, its standard deviation σ, and the contribution of each electron population to the spectrum. The value `ln_prob_s1` < -100 indicates the probability limit chosen to cut the S1 (see Section 2.2.9). 97
3.8 Fit of the SE spectrum obtained with different limits on `ln_prob_s1`. 98
3.9 Comparison between the distributions given by a fit of 5 Gaussians (orange) and that given by model (3.4) with $N = 5$ (blue). The detection efficiency of S2 is also shown (red). 99
3.10 (Left) The distribution of selected events in width vs. energy parameter space shows the selected region within the horizontal gray lines. (Right) Comparison between the fit of the two distributions with isolated low-energy S2 events. 100
3.11 Photo of the gate where it is possible to see the two additional transverse wires. 101
3.12 Width signal as a function of S2 of single electrons population containing 1 electron. Data extracted from XENONnT SR0 background data set. 102
3.13 The width of single electron signals (1 e^-) as a function of their reconstructed position. 103
3.14 (Left) Map obtained with the fit function used. (Right) The difference between the data and the result of the fit function for each bin. The fact that the fit is not centered in (x, y) suggests that the TPC is not perfectly vertical, and this translation of the center is therefore related to gravitational effects. 103
3.15 Map of the spatial dependence of secondary scintillation gain of single electrons (projected on the XY plane). 104
3.16 The secondary scintillation gain for each run in SR0. In blue are the krypton calibration periods. 105

3.17 Time evolution of the secondary scintillation gain, calculated with the fit of the SE spectrum. Krypton calibration data (pre-SR0, January 2021). 107
3.18 The values of the anode potential, the pressure, and the width of the gas gap corresponding to the time at which the selected data were taken (pre-SR0). 108
3.19 Time evolution of the secondary scintillation gain, calculated with the empirical model (3.6). 109
3.20 Plans for the future XeLab detector. 110
3.21 Summary of the different data taking and calibration periods during the XENONnT SR0 run. The "dark matter" data are in dark green ("Blinded Background SR0"). 111
3.22 (Top) Secondary scintillation gain for each run present in the SR0 background dataset calculated with pure Gaussian model, the horizontal black line indicates the average value and the bands indicate the region of one and two standard deviations, respectively, in green and yellow. (Bottom) The standard deviation of the first Gaussian of the single electron spectrum calculated for the same dataset as the gain. The large gap between August and October corresponds to dark matter data with some irregularities, such as the presence of a hot spot or if the anode was powered up less than three days before; therefore, this can affect the SE gain or during DAQ firmware tests, etc. 112
3.23 Map of SE emissions as a function of XY (using multilayer perceptron algorithm for position reconstruction). For clarity, the figure on the left is left intact. The figure on the right shows the location of the 2 transverse wires of the gate ('–') and the 4 of the anode ('-.'). 113
3.24 Map of SE emissions as a function of XY (using convolutional neural network algorithm for position reconstruction). For clarity, the figure on the left is left intact. The figure on the right shows the location of the 2 transverse wires of the gate ('–') and the 4 of the anode ('-.'). 114
3.25 Map of SE emissions as a function of XY, showing the near transverse wires cut. 115
3.26 Distribution of SE as a function of the square of the radius. Also shown in orange is the Gaussian fit of the distribution region that is expected to be originating from edge emissions. 115
3.27 The sensitivity (as explained above) as a function of R^2. 116
3.28 S2 signal temporal width at 50% area of the peak (left) and number of event (right) as function of the S2 energy. 117
3.29 Fit the SE spectrum using Equation 3.7. The red, blue, and green bands respectively indicate the limits for the selection of populations with one electron, two electrons, and 3 to 5 electrons. 118
3.30 AFT distribution of single electrons. The red lines delimit the selection of the retained events; those between the two fits. 119
3.31 Acceptance of S2AFT cut on single electrons. 120

3.32 Distribution of primary S2 signals as a function of the AFT and the width at 50%. Also, shown in red is the cut in each parameter. 121
3.33 Width at 50% distribution of S1-like events 122
3.34 AFT value as a function of S2. The blue dashed line indicates the threshold of the gas event. 123
3.35 Width at 50% distribution of track events. 123
3.36 Cut box selection of alpha events. 124
3.37 Distribution of the number of S2 signals in an event as a function of the energy of the main S2. 125
3.38 Distribution of the signal width at 50% for specific secondary S2 peaks. 126
3.39 Distribution of the number of S2 signals surviving the liquid event cut in an event as a function of the energy of the main S2. 127
3.40 Primary S2 live-time distribution. In red the fit of the distribution with a power law. 128
3.41 Diagram illustrating the overlap between the SE trains following primary S2 signals. 129
3.42 SE rate following an S2 primary. The dotted vertical line marks the maximum drift time. In black, the curve fit of rate after the maximum drift time. 131
3.43 Position correlation of SE signals to the preceding primary 132
3.44 (Top) The difference in x-y between SE and the previous primary S2. (Bottom) Comparison between the observed and expected difference on the x-axis. The orange line shows the expected difference if no position correlation exists. The dashed green line represents the best fit of a Cauchy-Lorentz distribution to the correlated population. The combined model is shown in cyan. The red (blue) lines indicate the position correlated (uncorrelated $<$ 5 cm) selection. . 134

4.1 Current status of searches for spin-independent elastic WIMP-nucleus scattering assuming the standard parameters for an isothermal WIMP halo: ρ_0 = 0.3 GeV/cm^3, v_0 = 220 km/s, v_{esc} = 544 km/s. Results labeled "M" were obtained assuming the Migdal effect [158]. Results labeled "Surf" are from experiments not operated underground. The ν-floor shown here for a Ge target is a discovery limit defined as the cross section σ_d at which a given experiment has a 90% probability of detecting a WIMP with a scattering cross section $\sigma > \sigma_d$ at $\geq$ 3 sigmas. It is computed using the assumptions and the methodology described in [159, 160]. However, it has been extended to a very low dark matter mass range by assuming an unrealistic 1 meV threshold below 0.8 GeV/c^2. (Figure from [53]). 136
4.2 The maximum electronic recoil energy as a function of dark matter velocity. The cyan curve gives the velocity distribution of the standard halo model. 140

4.3 The scattering of a dark matter particle with a bound electron. The DM transfers momentum $\vec{q}$ to the Xe atom, exciting it from the ground state X to an excited state X^*, which can be either a higher-energy bound state or an ionized state. (Figure taken from [170]) 141
4.4 Distribution of the ionization form factor calculated from Equation (4.26), considering the Hartree-Fock calculation of the unbound states. The dashed white line shows $q = \sqrt{2m_e(E_b + E_R)}$, with E_b the binding energy and E_R the recoil energy. This region is approximately where the form factor is strongest. Red contours show the kinematically allowed region (that is, where the minimum required DM velocity is less than the maximum DM velocity under the standard halo model) for: $m_\chi = 10$ MeV$/c^2$ (solid), $m_\chi = 100$ MeV$/c^2$ (dashed) and $m_\chi = 1000$ MeV$/c^2$ (dotted). 146
4.5 Event rate as a function of recoil energy, calculated from Equation (4.28). Also presented the individual contributions to the total rate of each atomic orbital of the outer and adjacent shells. 147
4.6 Event rates for $F_{DM} = 1/q^2$. Also presented the individual contributions to the total rate of each atomic orbital of the outer and adjacent shells. 148
4.7 Electron lifetime evolution for the background datasets used in the analysis. 150
4.8 Comparison between the expected event rate as a function of electron lifetime. The values chosen correspond to the values of XENON1T and the value taken here for XENONnT. The rate was calculated for $F_{DM} = 1$ (top) and $F_{DM} = 1/q^2$ (bottom). 151
4.9 Rate of observed electrons coming from each atomic orbital. The rate was calculated for $F_{DM} = 1$ (top) and $F_{DM} = 1/q^2$ (bottom). . . 152
4.10 Electron-DM interaction event rates compared to CEνNS and flat ER background in the SE region. 156
4.11 Dark photon differential events rate. 157
4.12 Refraction index plot of the XENON10 analysis. (Figure from [100]).160
4.13 In-medium correction effect on the dark photons absorption rate. . 160
4.14 Solar neutrino spectrum 162
4.15 (Left) Electroweak one-loop contributions to the magnetic neutrino moment. (Right) General vertex function to the elastic neutrino scattering off an electron. 163
4.16 Differential events rate of the scattering through a magnetic neutrino moment. 163
4.17 Derived parameters from the solar model. 165
4.18 Dark photon flux at earth from resonant solar production. 166

List of Tables

1.1 Values of the atomic number Z, the total nuclear spin J, and the expectation values of the proton and neutron spins within the nucleus $\langle S_{p,n} \rangle$ for various nuclei with odd numbers of protons or neutrons, leading to the relative sensitivities to spin-dependent interactions Table from [65]. 34

2.1 List of natural Xenon isotopes. Data from the *Encyclopedia of Geochemistry* [106] 48
2.2 Main nuisance parameters in the detector response model of XENON1T. Lower and upper errors of the posterior are calculated as the difference between the median and the 15.4% and 84.6% percentiles of the posterior. (Values from [117]). 53
2.3 Estimated background event rates in the 4 t fiducial volume of XENONnT, based on the energy of the recoil event. The energy region of interest in which the event rates are integrated is $(1, 13)$ keV for ERs, and $(4, 50)$ keV for NRs. Assuming an activity concentration of 1 μBq/kg of ^{222}Rn and 0.1 ppt (mol/mol) ^{nat}Kr/Xe. The background contributions from Xe isotopes are determined assuming the 8.9% and 0.095% natural abundances of ^{136}Xe and ^{124}Xe, respectively. (Table from [100]). 82

3.1 List of cuts to select the one-electron population of the SE spectrum. 99
3.2 List of parameters and the chi-square extracted from each distribution. 100
3.3 Extracted mean, purity, and efficiency for each electron population. 119

4.1 Systematic uncertainties related to the detector response 154

Abbreviations list

M/L . . . . . Mass-to-light ratio
DM . . . . . Dark Matter
RC . . . . . Rotation Curve
CMB . . . . . Cosmic Microwave Background
ESA . . . . . European Space Agency
SM . . . . . Standard Model
MoND . . . . . Modified Newtonian Dynamics
HDM . . . . . Hot Dark Matter
CDM . . . . . Cold Dark Matter
WIMP . . . . . Weakly Interacting Massive Particle
WDM . . . . . Warm Dark Matter
dSph . . . . . dwarf Spheroidal galaxy
LHC . . . . . Large Hadron Collider
SUSY . . . . . SUperSYmmetry
SD . . . . . Spin-Dependent
SI . . . . . Spin-Independent
QCD . . . . . Quantum ChromoDynamics
ALP . . . . . Axion-Like Particle
BSM . . . . . Beyond the Standard Modeling
TPC . . . . . Time Projection Chamber
LNGS . . . . . Laboratori Nazionali del Gran Sasso
nVeto . . . . . neutron Veto
LXe . . . . . Liquid Xenon
PMTs . . . . . PhotoMulTiplier tubes
ER . . . . . Electronic Recoils
NR . . . . . Nuclear Recoils
TI . . . . . Thomas-Imel
NEST . . . . . Noble Element Simulation Technique
PE . . . . . PhotoElectron
LCE . . . . . Light Collection Efficiency
SE . . . . . Single Electron
PTFE . . . . . PolyTetraFluoroEthylene (Teflon)
ePTFE . . . . . expanded PTFE

SPE . . . . . Single PhotoElectron
GE . . . . . General Electric
PAC . . . . . Programmable Automation Controller
SCADA . . . . . Supervisory Control And Data Acquisition
OPC . . . . . Open Platform Communication
DAQ . . . . . Data AcQuisition
TPF . . . . . Top Pattern Fit
NN . . . . . Neural Network
SR0 . . . . . Science Run 0
BBF . . . . . Bayesian Band fitting Framework
MC . . . . . Monte Carlo
DSN . . . . . Diffuse SuperNova
CEνNS . . . . . Coherent Elastic neutrino-Nucleus Scattering
MLE . . . . . Maximum Likelihood Estimator
PDF . . . . . Probability Density Function
RHF . . . . . Roothaan-Hartree-Fock

Chapter 1

Introduction

This chapter begins with an introduction and a history of the problem of the Universe's missing mass. This introduction is followed by a discussion of the different theories that could explain the observations, mainly if the missing mass is due to flaws in the theory or to fundamental particles not detected directly to date. Finally, the chapter ends with a detailed study of the direct detection of the particles supposedly composing this missing mass.

1.1 Preamble and early history

For centuries, our knowledge of the Universe came from observations that astronomers could make of it. The closest celestial objects are the planets of our solar system, some of which are visible to the naked eye. Our solar system is part of a galaxy of some 100 billion stars called the Milky Way. It takes its name from its appearance, like a vast whitish veil crossing the night sky, visible mainly from the Earth's southern hemisphere. Through increasingly powerful instruments, we discovered that our Universe is populated by many galaxies of all shapes and sizes, some grouped in clusters containing up to thousands. Thus, until the end of the 19th century, our Universe was considered entirely made up of stars surrounded by emptiness through observation

This idyllic vision of our universe changes radically soon after. Without knowing it, at the beginning of the 20th century, Thomson (Lord Kelvin) wrote the first page of what, in many ways, resembles a long and fascinating scientific investigation [1].

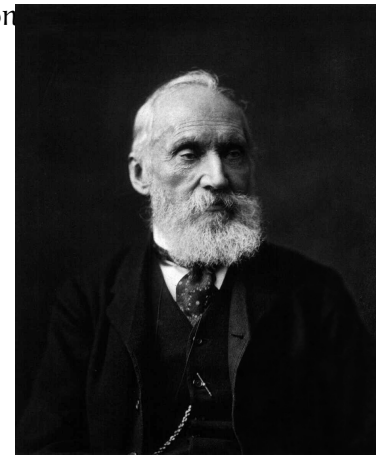

Figure 1.1: William Thomson, 1st Baron Kelvin.

Kelvin became the pioneer in research on the dynamics of stellar systems in the Milky Way by applying arguments from the kinetic theory of gases. His hypotheses were simple but powerful: if on a large scale of distances, we can assimilate the stars and star clusters of the Milky Way into a gas of particles acting under the influence of gravity, then we can establish a relationship between the mass M_{Tot} of the system of radius

R_{Tot} and the dispersion of the velocities $\langle v^2 \rangle$ within it.

Kelvin had to resort to this method because as soon as more than two bodies are in gravitational interaction, the calculation of the individual trajectories quickly becomes complex. The solutions strongly depend on the initial conditions (position, velocity) imposed on the objects, and the calculations had to be, most often, carried out numerically. This problem is known as the *N-body problem*.

Even if the determination of the individual trajectories of the particles in a system with N bodies remains delicate, the global properties (one would say *macroscopic* in statistical physics) of the system are nevertheless accessible. In particular, the *statistical* determination of its temperature, momentum, and mechanical energy.

In 1870, Clausius demonstrated a general theorem concerning the temporal mean of various mechanical quantities associated with a confined punctual masses system [2]. This relation with the name of *virial theorem* is as follows:

For any system at *equilibrium*, with kinetic energy $E_{C,Tot}$, submitted only to forces derived from a *homogeneous potential* energy U of degree α, we have the relationship:

$$2E_{C,Tot} = \alpha U. \tag{1.1}$$

Knowing that the kinetic energy of a star, of mass m and velocity v is $E_C = \frac{1}{2}mv^2$, then the total kinetic energy of a system of N stars is $E_{C,Tot} = \frac{1}{2}N\langle m \rangle \langle v^2 \rangle = \frac{1}{2}M_{Tot}\langle v^2 \rangle$. In the case of *spherical symmetry* and according to the Gauss theorem, we have the potential energy $E_p = -\frac{3}{5}\frac{GM_{Tot}^2}{R_{Tot}}$. Consequently, the virial theorem gives, for a situation at dynamic equilibrium:

$$\frac{1}{2}M_{Tot}\langle v^2 \rangle = \frac{3}{10}G\frac{M_{Tot}^2}{R_{Tot}} \implies M_{Tot} = \frac{5R_{Tot}\langle v^2 \rangle}{3G}, \tag{1.2}$$

with G the gravitational constant.

Elliptical galaxies can also tell us about the amount of mass they contain. Unlike spirals, they contain a small proportion of gas, and few new stars can form in them [3]. Moreover, these stars' movement is not circular as with spirals but random. Elliptical galaxies find their equilibrium through the compensation of gravitational forces with dynamic pressure forces. The gravitational potential energy of an elliptical galaxy with N stars of mass m and a radial position r is, therefore

$$U = -\frac{1}{2}\sum_{\substack{i,j \\ i \neq j}}^{N} \frac{Gm_i m_j}{|\vec{r_i} - \vec{r_j}|}, \tag{1.3}$$

which becomes, by averaging the mass distribution and defining the characteristic size of the system R_{Tot},

$$U = -\frac{1}{2}\sum_{\substack{i,j \\ i \neq j}}^{N} \frac{G\langle m \rangle^2}{R_{Tot}} \simeq -\frac{1}{2}\frac{GM_{Tot}^2}{R_{Tot}}. \tag{1.4}$$

Finally, the virial theorem makes it possible to relate the mass M_{Tot} to the dispersion of velocities $\langle v^2 \rangle$ via

$$\frac{1}{2} M_{Tot} \langle v^2 \rangle = \frac{1}{4} G \frac{M_{Tot}^2}{R_{Tot}} \implies M_{Tot} = \frac{2 R_{Tot} \langle v^2 \rangle}{G}. \tag{1.5}$$

Therefore, it is sufficient for astronomers to measure star velocities' dispersion in galaxies to estimate their gravitational mass. Spectroscopic analyzes allow us also to estimate the mass-to-light ratio (M/L) [4]. As a result, M/L ratios serve as tools to measure the luminous mass, unlike the dynamic mass obtained through the virial theorem.

Based on Lord Kelvin's estimate [1], it is possible to conclude, given the velocity at which the visible stars rotate around the center of the Galaxy and their velocity dispersion, that the mass of the Galaxy must be greater than the total mass of visible stars. That means that many stars in the Milky Way should be bodies of very low luminosity or even not emitting light in the visible spectrum. Henri Poincaré, in 1906, just after the results obtained by Lord Kelvin, was the first to suggest the name of *dark matter* (DM) for these faint light bodies [5].

Later, in the 1930s, the first clues appeared. As soon as the Swiss astronomer Zwicky tried to make the energy balance of the Coma Cluster (Abell 1656), he realized the problem: the galaxies' kinetic energy was several orders of magnitude greater than their potential energy. We would need at least 400 times more mass to hold them together than that visible in galaxies [6]. In 1939, Horace W. Babcock published the rotation curve (RC) of the Andromeda galaxy, giving the first robust indications that this galaxy's mass-to-light ratio is greater than unity. He also suggested that the M/L ratio increases radially. However, Babcock attributed this phenomenon either to light absorption in the galaxy or to dynamic change in Andromeda's outer parts, but not to invisible matter [7].

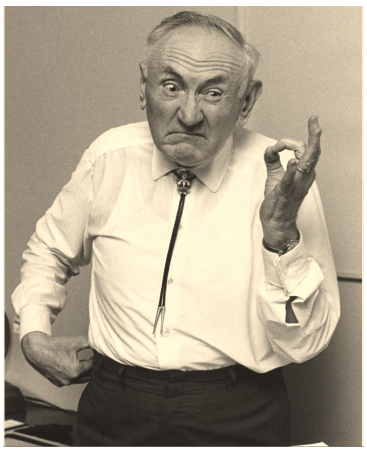

Figure 1.2: Fritz Zwicky.

Gradually, more and more systems of galaxies were found in which mass discrepancy appeared. Astronomers started to talk about missing matter across the Universe. Prompted by these developments, the Soviet-Armenian astrophysicist Ambartsumian proposed a new explanation for these bizarre observations, which was different from Zwicky's hypothesis of unknown dark matter. Ambartsumian argued that the observed discrepancies were due to the absence of *dynamical equilibrium* in these groups and clusters: their galaxies were rapidly flying apart, which was to produce the discrepancy.

Ambartsumian's controversial idea quickly became an influential hypothesis in the analysis of clusters. In the summer of 1961, a conference was held in Santa Barbara, California, dedicated to critically examining Ambartsumian's instability hypothesis. During the conference, the idea of cluster instability, as well

as that of unseen mass, was discussed, together with other less popular alternatives. Both the hypotheses of instability and additional matter were problematic. If groups and clusters of galaxies were indeed unstable, then they would not last more than 10 to 1000 million years, which was argued to be very short compared to the time scale of the universe. Most clusters should already have been dissolved in such a scenario, in conflict with the observations. The alternative (additional matter), however, was equally rejected, according to the conference organizers: this would imply that in the field of astronomy, "theories are based on observations of less than 1% of the matter that is there!" [8].

In the 1960s, many solutions to the cluster discrepancies were proposed: Brown Dwarfs, Black Holes, Gas, or Neutron star. Then in the 1970s, particle physicists got involved and proposed neutralino, gravitino, or others from supersymmetry theories to account for the missing mass [9].

Poincaré's expression *dark matter* was made famous by the results of Kelvin, Zwicky, and Babcock to refer to this invisible form of matter associated with the missing mass in galaxies and clusters of galaxies.

1.2 The era of the first precision measurements

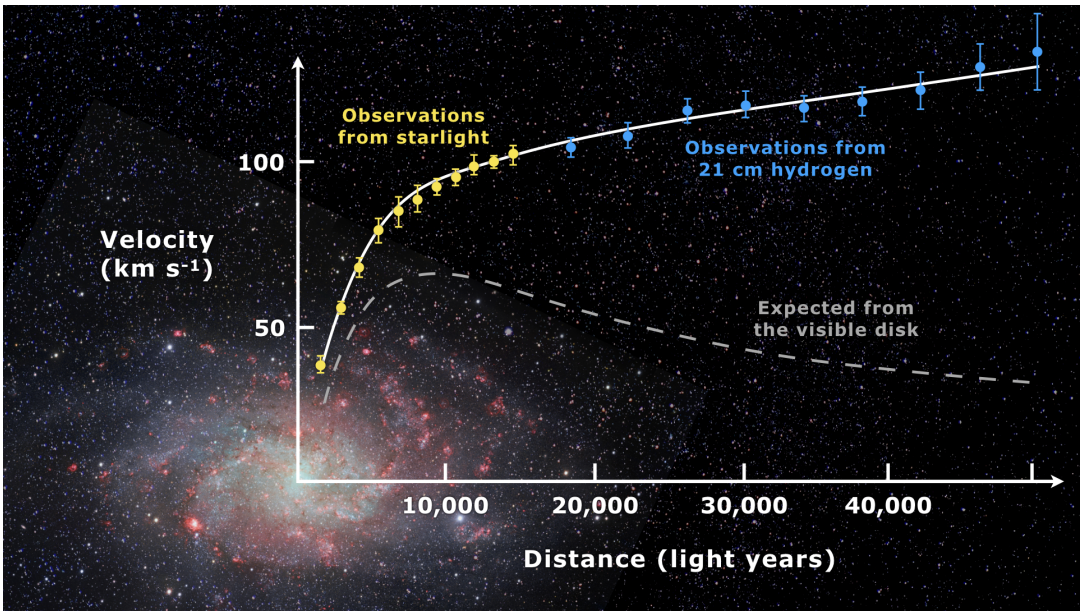

Figure 1.3: Example of a rotation curve of a spiral galaxy. The yellow dots correspond to the average circular speed of the stars, and the blue dots correspond to the average circular speed of the gas using the Hydrogen 21 cm line measured by the Doppler effect [10].

Observations show that the velocity with which stars and gas orbit the center of their galaxy is independent of their distance from the center, so the orbital speed is constant or increases slightly with distance rather than decreasing, as expected. To account for this, the galaxy's mass distribution in the orbit of stars must increase linearly with the distance from the center, as shown in Figure 1.3.

Since observations were difficult and left some uncertainty, astronomers did not find it problematic and hypothesized that the discoveries of non-luminous objects would solve the problem. However, the rapid development of photometric techniques and their applications in astrophysics enabled Vera Rubin, W. Kent Ford, and Albert Bosma during the 1960s and 1970s to measure for the first time, with a high degree of precision, the rotation curve of many galaxies. They provided substantial evidence of either an invisible form of matter or contradictions in Newtonian dynamics. Their results were based on the precise measurement of the circular velocity of stars and gases in spiral galaxies. Rubin's work led to the conclusion that most galaxies must contain about six times more dark matter than their visible matter [11, 12].

Until 1980, for most astronomers, dark matter must have been composed of ordinary matter, therefore of baryons[1]. However, in 1984 it was definitively established that most dark matter could not be a baryonic matter for two reasons. First, the abundance of deuterium and helium formed in primordial nucleosynthesis is only compatible with observations if the baryon fraction represents only 5% of the critical density[2] [13]. Second, expansion prolongs the formation of structures in the Universe under the effect of gravity, and ordinary matter, ionized and highly coupled to photons, takes time to collapse under gravity. If we wait for the expansion's temperature to drop below 3000°K, for hydrogen to recombine, and for the gas to collapse, there is not enough time to form the galaxies. Therefore, it is necessary to have an exotic matter without interactions with light, which can collapse soon after the Big Bang, even before the ordinary matter can do so [14].

Our universe, therefore, seems to be filled with dark matter, and the investigation continues, with efforts now focusing on advances in cosmology and particle physics. However, as the measures become precise, the situation only gets worse!

The Standard Model of cosmology[3] predicts that the density of ordinary matter (baryonic matter) present in the universe is larger than that measured by astronomers by observing in various wavelengths [9]. In conclusion, there is, therefore, ordinary matter not yet detected, which we call ***baryonic dark matter***. Astronomers race to identify a whole collection of stars of varying sizes or other candidates that might contribute to the missing mass. These could be gas or intergalactic planets. They could also be low-mass stars (typically less than half the mass of the Sun) bearing the poetic names of brown or red dwarfs, too light to initiate the nuclear reactions that would allow them to shine. Or stars at the end of their lives having consumed all their fuel, such as white dwarfs, neutron stars, or black holes.

However, the observed difference between visible matter and dark matter density is of the order of 10 to 100, much greater than the difference predicted by

[1]The word baryons are used here in its general sense to designate subatomic particles such as protons, neutrons, and electrons.

[2]The value of the average matter density of the Universe, below which its expansion will continue indefinitely and above which the expansion will stop and be followed by a contraction.

[3]Also called the *Concordance Cosmological Model* or the ΛCDM *model*.

the Standard Model of cosmology [15]. We must, therefore, also invoke another constituent of dark matter, which cannot be composed of neutrons and protons without violating the Standard Model of cosmology confirmed many times elsewhere: it is called ***exotic dark matter***. The first candidates are neutrinos, which were discovered to have a mass. Nevertheless, hope is only short-lived: although neutrinos are among the most represented particles in the universe (around 330 per cubic centimeter, all species combined [16]), their mass is not enough to explain all dark matter.

The dark matter dossier takes the form of a reasonably practical tote in which there is an inevitable confusion fueled by rantings from the wildest of the most inventive theorists. Most candidates are hypothetical particles never observed before, either in the laboratory or in experiments dedicated to their detection.

Around the 1990s, the 60-year-old mystery hardly changed in the right direction. The known fraction of the universe has shrunk to a few percent, with ordinary matter (and dark matter) constituting less than a quarter of the missing mass, while most of it is entirely unknown [17].

The Standard Model of cosmology imposes an extraordinarily dense and warm beginning on our universe, followed by an expansion slowed down over time by the gravitational pull of the objects that constitute it. Einstein had introduced into his equations a ***cosmological constant*** which counteracted the effect of gravity and allowed a static universe. However, from the first observations confirming the universe expansion, he retracted, declaring that he had committed there *the biggest blunder of his life* [18]. New observations, however, challenged everything once again.

In 1998, studies on explosions of stars (supernovae) showed that these objects are further away than expected or that the photons from the explosion propagated longer in the Universe than expected according to the classic expansion scheme [19]. Therefore, requiring a slower pace of expansion in the past and a recent acceleration phase: the opposite of the expected slowdown. It is the return of the famous cosmological constant, otherwise known as ***dark energy*** since it is unidentified energy and does not meet known criteria since it presents the appearance of repulsive gravity. It is a shock to physicists, who see their understanding of the Universe reduced once again. Therefore, the very matter constitutes only a third of the Universe [17], all the rest being in a new form misunderstood to date.

In conclusion, the apparent need for dark matter is a significant yet unsolved problem in observational astronomy and cosmology. At the end of the 20th century, a stream of new observations, not only by the rotation curves of galaxies but also by gravitational lenses, the distribution of the temperature of hot gas in galaxies and clusters, and finally by the cosmic microwave background (CMB), all indicate the presence of dark matter in the Universe. Thus, according to the most recent estimates, this hypothetical and invisible form of matter seems to prevail over all ordinary matter by a ratio of almost five to one, which suggests that we barely know our Universe [20]. The scientific community's main consensus is that dark matter is mainly composed of an unknown type of subatomic particles of non-baryonic nature, constituting today one of the biggest challenges of the

Standard Model (SM) of particle physics and the ΛCDM model in cosmology.

In search of the truth about the constitution of our Universe, we are adding new pieces to the scaffolding year after year, which has become very wobbly. One may ask: would we not be reproducing on the scale of the Universe the perception of Ptolemy, who, to describe the movement of the planets by a set of concentric spheres centered on the supposedly fixed Earth, was forced to introduce up to twenty epicycles[4] in order to correct trajectories? Is the truth so confusing?

1.3 Gravitation or particles?

All observations can equally be well explained by either adding unknown components, remaining within the framework of general relativity as the theory of gravitation or by a fundamental modification of this theory. Would it not be easier to do the latter? In the 19th century, the French astronomer Le Verrier discovered an abnormal rotation (known as precession) of the orbit of Mercury [21]. It could be explained either by "dark matter," in this case, a new planet inside the orbit of Mercury (called Vulcan by Le Verrier), or by a modification of Newton's laws. This second option proved correct when Newtonian gravitation was replaced by Einstein's, and a relativistic effect explained Mercury's excess precession.

1.3.1 Modified Newtonian Dynamics

Although no experiment has, to date, definitively inverted Einstein's theory of relativistic gravitation, General Relativity, a growing number of anomalies observed at the astrophysical or cosmological levels, can be attributed to a failure of this theory to account for all gravitational phenomena. At the forefront of these anomalies are the galaxies and clusters' abnormal dynamics and the recent acceleration of the Universe's expansion. These two problems, called *dark matter* and *dark energy*, signal the inadequacy of the forms of matter known to date to explain the kinematics and dynamics of some astrophysical objects on the one hand and the Universe as a whole on the other hand.

In this revived and particularly promising context, the general study of alternative gravitational theories, which could solve in a new way the problems of dark matter or dark energy (i.e., without necessarily being limited to the introduction of an unknown matter component), becomes very attractive.

The modifications of gravity on scales greater than that of the Solar System are alternatives to explain the rotation curve of galaxies and the phenomenon of the missing mass in the Universe more generally. One of the most successful models in that respect is Modified Newtonian Dynamics (MoND) [22].

Since general relativity and its Newtonian limit work well across the Solar System, following the demonstration here [23], one can postulate that below

[4]Small additional circles whose centers themselves were in a circular motion.

a length scale r_0 (in kpc[5]), rotation curves can be suitably described by the Newtonian velocity of stars and gas. Beyond this scale, we know that Newtonian speed behaves like $v_N^2(r) \sim r^{-1}$; therefore, to reproduce a flat rotation curve, the behaviour of this velocity should be changed. The simplest way to do so is to multiply $v_N^2(r)$ by the distance r. These two conditions, in terms of acceleration, can be written:

$$\frac{v^2(r)}{r} = \begin{cases} \dfrac{v_N^2(r)}{r}, & r \ll r_0, \\[2ex] \dfrac{v_N^2(r)}{r}\dfrac{r}{r_0}, & r \gg r_0. \end{cases} \tag{1.6}$$

The above relation tries to explain the rotation curve without resorting to a surplus of matter; it is only based on the modifications of the Newtonian dynamics applied to the luminous matter moving at the circular speed $v_N^2(r)$. It should be noted that this is a purely kinematic relation and that it could be transformed into a dynamic relation by introducing a characteristic acceleration scale a_0, linked to r_0 by a dimensional analysis argument $r_0 a_0 = v_0^2$, where v_0 is the constant speed where the Newtonian regime begins to fail.

The main question now is: how to connect the two regimes through a continuous process? The change from one regime to another should be gradual and continuous, with a sufficiently good transient function that is called in the literature *interpolation function*. If we write $a(r) = v^2(r)/r$ and $a_N(r) = v_N^2(r)/r$, and recalling that $a(r) = v_0^2/r$ in the $r \gg r_0$ regime, then the Equation (1.6) can be rewritten:

$$a(r) = \begin{cases} a_N(r), & r \ll v_0^2/a_0, \\[2ex] \sqrt{a_N(r)\, a_0}, & r \gg v_0^2/a_0. \end{cases}, \quad \text{or,} \quad a_N(r) = \begin{cases} a(r), & r \ll v_0^2/a_0, \\[2ex] a(r)\,\dfrac{a(r)}{a_0}, & r \gg v_0^2/a_0. \end{cases}$$

The connection between the two regimes is now easier to find by writing $a_N(r) = a(r)\mu(a(r)/a_0)$, where $\mu(x)$ is the interpolation function mentioned above which must satisfy:

$$\mu(x) = \begin{cases} 1, & x \ll 1, \\ x, & x \gg 1. \end{cases}$$

The $x \gg 1$ regime is usually called the MONDian regime to distinguish it from the Newtonian regime ($x \ll 1$).

In the literature, many interpolation functions are proposed by different rotation curve studies of galaxies, of which the two most known are:

$$\mu_I(x) = \frac{x}{\sqrt{1+x^2}}, \tag{1.7}$$

$$\mu_{II}(x) = \frac{x}{1+x}, \tag{1.8}$$

[5]The parsec (pc) is defined as the distance at which an *astronomical unit* subtends an angle of one second of arc —knowing that an astronomical unit corresponds to the distance Earth-Sun. 1 pc is equivalent to 3.26 light-year, 206,265 astronomical units, or about 30,900 billion km.

where $\mu_I(x)$ and $\mu_{II}(x)$ are called respectively *Standard Interpolation Function* and *Simple Interpolation Function*, and the corresponding modified velocities are [23]:

$$v_I^2(r) = \frac{v_N^2(r)}{\sqrt{2}} \sqrt{1 + \sqrt{1 + \left(\frac{2a_0 r}{v_N^2(r)}\right)^2}}, \tag{1.9}$$

$$v_{II}^2(r) = \frac{v_N^2(r)}{2} \left(1 + \sqrt{1 + \frac{4a_0 r}{v_N^2(r)}}\right). \tag{1.10}$$

For a rough estimate of a_0, we can take the typical galactic length scale $r_0 \sim 1$ kpc and the velocity in the periphery of the galaxy, which is about 100 km/s [23], so $a_0 = v_0^2/r_0 \sim 10^{-8}$ cm s^{-2}. A more realistic estimate should come from real experimental data such as rotation curves. For example, in [24], Begeman *et al.*. found, with Equation (1.9) $a_0 = 1.2 \cdot 10^{-8}$ cm s^{-2}; while in [25], Famaey *et al.* got with the Equation (1.10) a value of $a_0 = 1.35 \cdot 10^{-8}$ cm s^{-2} [26].

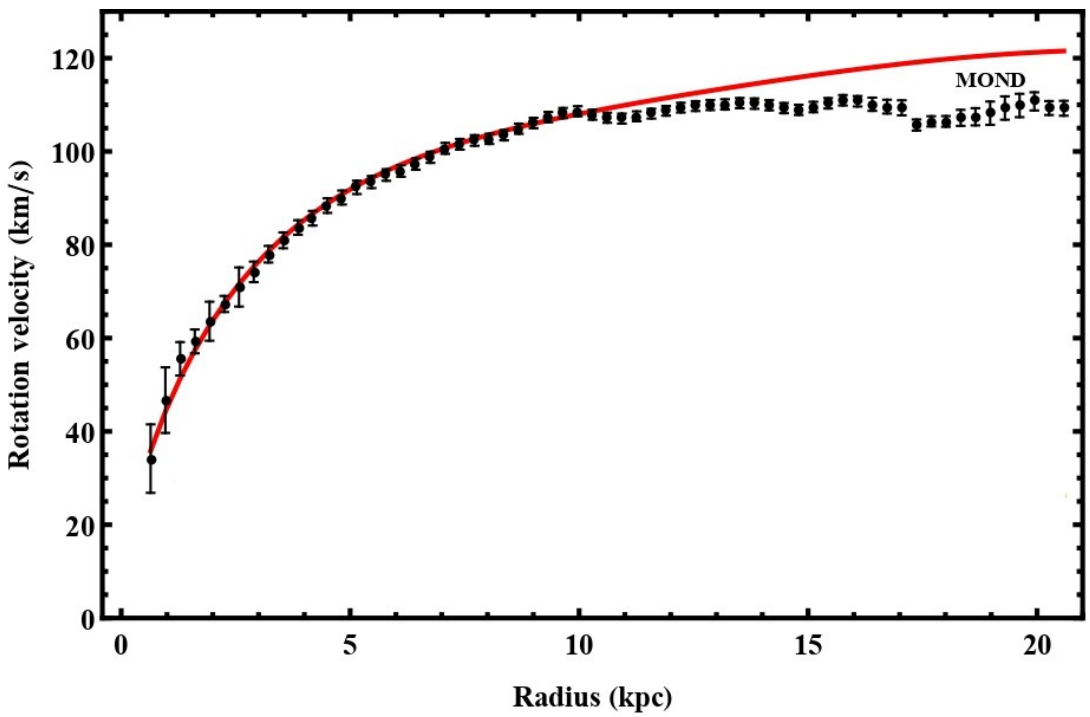

Figure 1.4: Observed rotation curve of galaxy ESO138-G014 (data points) and MOND prediction (red curve) $a_0 = 1.35 \cdot 10^{-8}$ cm s^{-2} [26].

The MoND theory (and its generalizations) faces a severe problem, which results from the 2006 observations [27] of a pair of clusters of colliding galaxies, known as the Bullet Cluster. These observations pose a significant challenge for MoND and any modified gravity theory proposing a solution to the problem of missing mass in the Universe. General relativity predicts that the image on Earth of an astronomical object is distorted when light rays pass through an intense gravitational field. Also, Einstein field equations allow us to go back to its mass and spatial distribution by analyzing these deformations. The interest

of this method lies in the fact that it gives us access to the gravitational potential regardless of the nature of the objects that induce it.

Figure 1.5 shows the Bullet Cluster in false colors: the pink regions indicate the mass distribution as measured directly (by X-rays), while the blue regions represent the mass as measured by gravitational lensing. These distributions are not in agreement at all. Indeed in MoND, one would expect the mass to be entirely visible. However, the gravitational lensing observations clearly show that the mass in this system does not follow the distribution of the visible, baryonic matter. Therefore, another source of gravitational potential, such as that provided by dark matter, should instead dominate the system's mass.

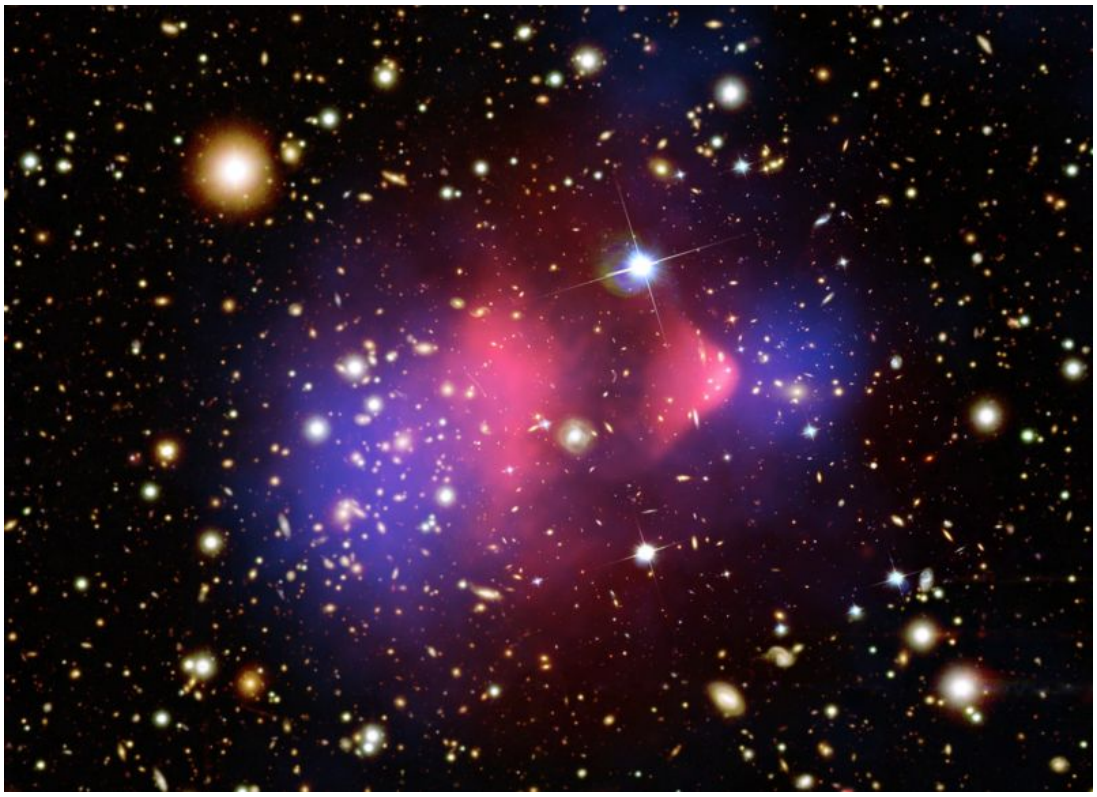

Figure 1.5: Bullet Cluster's false-color image, where the pink regions indicate the mass distribution as measured directly and the blue regions represent the mass as measured by gravitational lensing (X-ray: NASA/CXC/CfA/[28]; Optical: NASA/STScI,[27]; lensing map: NASA/STScI ESO WFI,[27])

Collisions of galaxy clusters are generally observed in the visible and X domains. Therefore, it is possible to compare the distribution of the ionized gas that makes up most of the visible mass with the cluster's total mass distribution. Over 70 galaxy collisions have been analyzed, and the general conclusion is that the two distributions do not coincide [29]. Nevertheless, it has been postulated [30] that Standard Model neutrinos (at $m_\nu = 2$eV; knowing that the experimental upper limit is $m_\nu = 2.2$eV [31]) can provide the missing dark mass of clusters. Nevertheless, more recent studies [32, 33, 34] have shown that even under very favorable circumstances, considering the absolute upper limit of a possible neu-

trino density[6], a second species of dark matter would be needed to explain the dynamics of galaxy clusters and groups, which more or less rules out Standard Model neutrinos as good candidates.

This new fact leaves two alternatives: either an invisible source of non-baryonic mass must exist in galaxy clusters, which is detrimental to the elegance of MoND, or we must take into account another kind of neutrinos[7], which could explain the observations and conserve the success of the theory at galactic scales [33, 30]. This last idea appeared promising as sterile neutrinos with MoND could solve the Bullet Cluster problem and correctly reproduce the power spectrum of the CMB [34, 35]. On the other hand, more recent MoND cosmological simulations with sterile neutrinos have shown that too many galaxy clusters are forming and that they are too massive [36].

1.3.2 Dark matter as particles

Even though modified gravity theories are a perfectly reasonable explanation for rotation curves in galaxies, they still fail to explain the anomalies associated with larger and more complex objects, such as galaxy clusters. To alleviate this problem, astrophysicists propose the second point of view that involves other particles, the nature of which is uncertain but plays a vital role in the structural formation of the Universe.

The general idea of dark matter is that there is a kind of matter in the Universe that neither emits nor absorbs light. While modern ideas about dark matter are somehow exotic, the initial thought was very prosaic. Thus, shortly after the discovery of dark matter abnormality, astronomers considered candidates for dark matter made of ordinary or baryonic matter since the mass of ordinary matter lies in the baryons (protons and neutrons) at the center of atoms, for example, hot gas, brown dwarfs or neutron stars [37].

Nevertheless, there is strong evidence that baryonic dark matter represents only a small fraction of the missing mass [38]. Indeed, recent measurements have already eliminated several plausible candidates for baryonic dark matter. X-ray observations of galaxies imply that only a small fraction of the mass of a typical galaxy is in the form of hot gas [39]. Even in rich galaxy clusters, hot gas accounts for less than 20% of the total mass of the system [40]. Moreover, the often-proposed hypothesis that dark matter is made up of low-mass stars has been rejected by Hubble Space Telescope observations, which show that these stars contribute less than 6% of the invisible matter in the galactic halo [41]. One of the remaining possibilities is that dark matter is not baryonic, as, for example, relic neutrinos from the first moments of the Universe.

The dark matter non-baryonic particles scenario seems more appealing from the point of view of particle physics because of the need to postulate new physics beyond the Standard Model, which is also necessary to explain other phenom-

[6]The Pauli exclusion principle limits the number of fermions in a given phase space. Therefore, it provides an upper limit on the neutrino density, known as *Tremaine-Gunn bound*.

[7]More precisely, *sterile neutrinos*, whose hypothetical mass is subject to debate since even the origin of the mass of the Standard Model neutrinos remains unexplained.

ena (gravity, dark energy, neutrino masses, and matter-antimatter asymmetry). Therefore, theoretical and experimental efforts must be carried out to solve this confusing problem, including astrophysical and accelerator experiments.

Large-scale studies of cosmic structures suggest that these hypothetical particles must be electrically neutral and not contain quarks and gluons. If they were charged, they would be heated by starlight and galaxies and would be observable. If they contained quarks and gluons, then cosmic rays would interact with them, and they could be detected.

Cosmic microwave background and dark matter

The cosmic microwave background (often abbreviated CMB) is a globally homogeneous and isotropic black-body radiation (in the form of photons) decoupled from matter approximately 380,000 years after the Big Bang [20]. Since then, with the Universe expansion, it has cooled down to its current temperature of 2.7K [42]. This radiation was observed for the first time in microwaves[8], hence its name. It originated in the hot state of the Universe and was released when the density of protons and electrons became sufficiently low with cooling so that photons have little interaction with matter and travel freely. This transition is called *decoupling* and occurred at a redshift[9] $z = 1100$ approximately [17].

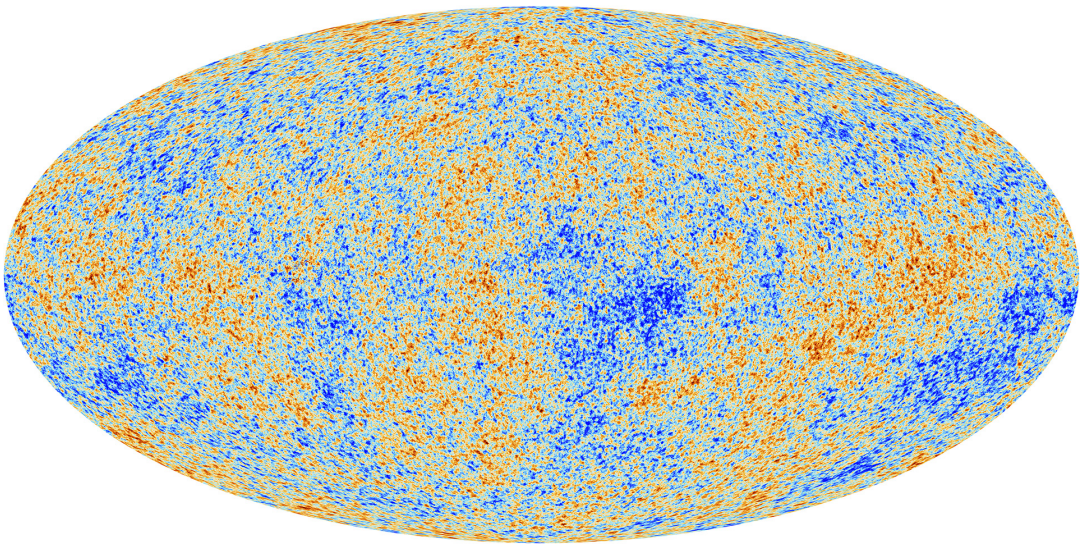

Figure 1.6: Temperature variations in the cosmic microwave background (fluctuations of the order of 10^{-6}). (ESA and the Planck Collaboration [43]).

As shown by Figure 1.6, the cosmic microwave background is not perfectly homogeneous. The map of its projection on the sky contains certain anisotropies. Their measurement can tell us about many cosmological parameters (including

[8]Microwaves have approximately wavelengths in the range of 30 cm (1 GHz) to 1 mm (300 GHz). The term *microwave comes from the fact that these waves have a "shorter" wavelength than the* radio waves *used prior to microwave technology.*

[9]The redshift in astronomy is a dimensionless quantity called z, characterized by the relative difference between an object's observed and emitted wavelengths (or frequency). $z = \frac{\lambda_{\text{obsv}} - \lambda_{\text{emit}}}{\lambda_{\text{emit}}}$

the content of the Universe and the Hubble constant) and primordial density fluctuations. These initial deviations from homogeneity gave rise to the large structures of the Universe.

Consider the evolution of small perturbations that can be treated using linear perturbation theory. These fluctuations are represented by first-order perturbation δ in the matter density ρ, the local velocity $\vec{v}$, the potential ϕ:

$$\begin{cases} \rho(t,\vec{x}) &= \bar{\rho}(t) + \delta\rho(t,\vec{x}) \\ \vec{v}(t,\vec{x}) &= \bar{\vec{v}}(t,\vec{x}) + \delta\vec{v}(t,\vec{x}) \\ \phi(t,\vec{x}) &= \bar{\phi}(\vec{x}) + \delta\phi(t,\vec{x}), \end{cases} \tag{1.11}$$

where $\bar{\rho}$, $\bar{\vec{v}}$, and $\bar{\phi}$ are the average of ρ, $\vec{v}$, and ϕ respectively, $\vec{x}$ is the moving coordinates. We can deduce a first-order perturbative solution by injecting these terms into the equations which govern fluid mechanics, namely Euler and Poisson equations:

$$\begin{cases} \dot{\rho} + \nabla\cdot(\rho\vec{v}) &= 0 \text{ (continuity equation)} \\ \dot{\vec{v}} + (\vec{v}\cdot\nabla)\vec{v} &= -\nabla(\phi + \dfrac{P}{\rho}) \text{ (Newton's second law)} \\ \nabla^2\phi &= 4\pi G\rho \text{ (Poisson's equation)}, \end{cases} \tag{1.12}$$

with P the pressure and G the gravitational constant.

By applying Equation (1.12) on the perturbed terms and by carrying out the appropriate eliminations[10] we obtain:

$$\begin{cases} \dot{\delta}(t,\vec{x}) &= -\nabla\cdot\delta(t,\vec{x})v(t,\vec{x}) \\ \delta\dot{\vec{v}}(t,\vec{x}) + (\delta\vec{v}(t,\vec{x})\cdot\nabla)\bar{\vec{v}}(t,\vec{x}) &= -\frac{1}{\bar{\rho}(t)}\nabla\delta P - \nabla\delta\phi \\ \nabla^2\delta\phi(t,\vec{x}) &= 4\pi G\delta\rho(t,\vec{x}). \end{cases} \tag{1.13}$$

At this point, and as the space is expanding, it would be more convenient to change to comoving coordinates $\vec{r}$. These coordinates are defined for a spherical system such as $\vec{x} \equiv a(t)\vec{r}$, where the function $a(t)$ is the scale factor, which describes the expansion of space as a function of time. It is with this scale factor that the *Hubble parameter* is defined; $H(t) \equiv \frac{\dot{a}(t)}{a(t)}$.

It then appears that the solution in the frequency domain (after the spatial Fourier transform $\vec{x} \to \vec{k}$ of $\delta\rho$) is:

$$\ddot{\delta\rho}(\vec{k}) + 2H\dot{\delta\rho}(\vec{k}) + \left(\frac{v_s^2\vec{k}^2}{a^2} - 4\pi G\bar{\rho}\right)\delta\rho(\vec{k}) = 0, \tag{1.14}$$

where $k \equiv 2\pi/\lambda$ denotes the wave number of the perturbation, $v_s \equiv \frac{\partial p}{\partial \rho}$ denotes the adiabatic sound speed, and $a(t)$ denotes the scale factor.

There are two types of solutions:

- If $k < a\sqrt{4\pi G\bar{\rho}}/v_s$, then the solutions are an endless growth of perturbation.

[10]The terms corresponding to the temporal or spatial derivative of average variables and the perturbation terms of second-order or higher.

- Otherwise, the solutions are damped oscillations with a time constant $\tau = 1/H$.

For a matter-dominated Universe, the scale factor takes the form of $a(t) \propto t^{2/3}$ [44]. the observed fluctuations of the CMB are of the order of 10^{-6} [20], if these perturbations grow as $\delta \propto t^{2/3}$, then by the time to reach redshift zero, they will have grown by almost a factor of ~ 1000, and becoming of the order of 10^{-3}. Therefore, these disturbances alone cannot explain the highly inhomogeneous density distribution that we observe. Dark matter provides a solution to this problem. Perturbations in the dark matter are coupled to the radiation field only by their gravitational influence and can therefore be much larger than disturbances in the ordinary matter, and this without disturbing the CMB. It would then be possible to reach the $\delta \sim 1$ regime much earlier, which makes it possible to form the observed structures.

To statistically exploit the anisotropies of the CMB, we use the power spectrum, and since we observe the CMB on the sky, which is a sphere, we have to use spherical harmonics Y_{lm} instead of plane waves to do a *Fourier analysis*. Therefore, the power spectrum came from the decomposition of the temperature map into spherical harmonics:

$$a_{lm} = \int \Theta(\theta, \phi) Y^*_{lm}(\theta, \phi) d^2\Omega. \tag{1.15}$$

Here, Θ is the fluctuation from the average temperature in a given direction:

$$\Theta(\theta, \phi) = \frac{T(\theta, \phi) - \bar{T}}{\bar{T}}, \tag{1.16}$$

from which we draw the power spectrum:

$$C_l = \sum_{-l \leq m \leq l} \frac{|a_{lm}|^2}{2l + 1}. \tag{1.17}$$

The multipole l represents an angular scale π/l, so the coefficients at low l indicate the correlation between large portions of the sky. When l is small, the sum is made on a small number of terms because few independent *m-modes* are available. This implies a statistical error of the order of $\sqrt{2/(2l+1)}$ on C_l, unsurpassable by experiment, called the *cosmic variance*.

The measurement of the power spectrum of the cosmic microwave background's anisotropies makes it possible to deduce the values of the Standard Cosmological model parameters. Figure 1.7 shows how these parameters affect the shape of the spectrum, while Figure 1.8 shows the temperature fluctuations in the cosmic microwave background detected by the Planck space observatory at different angular scales on the sky [20].

Freeze-out and freeze-in mechanisms

The freeze-out mechanism explains the amount of dark matter in the Universe now. At the Universe's earliest moments, thermal equilibrium is assumed where

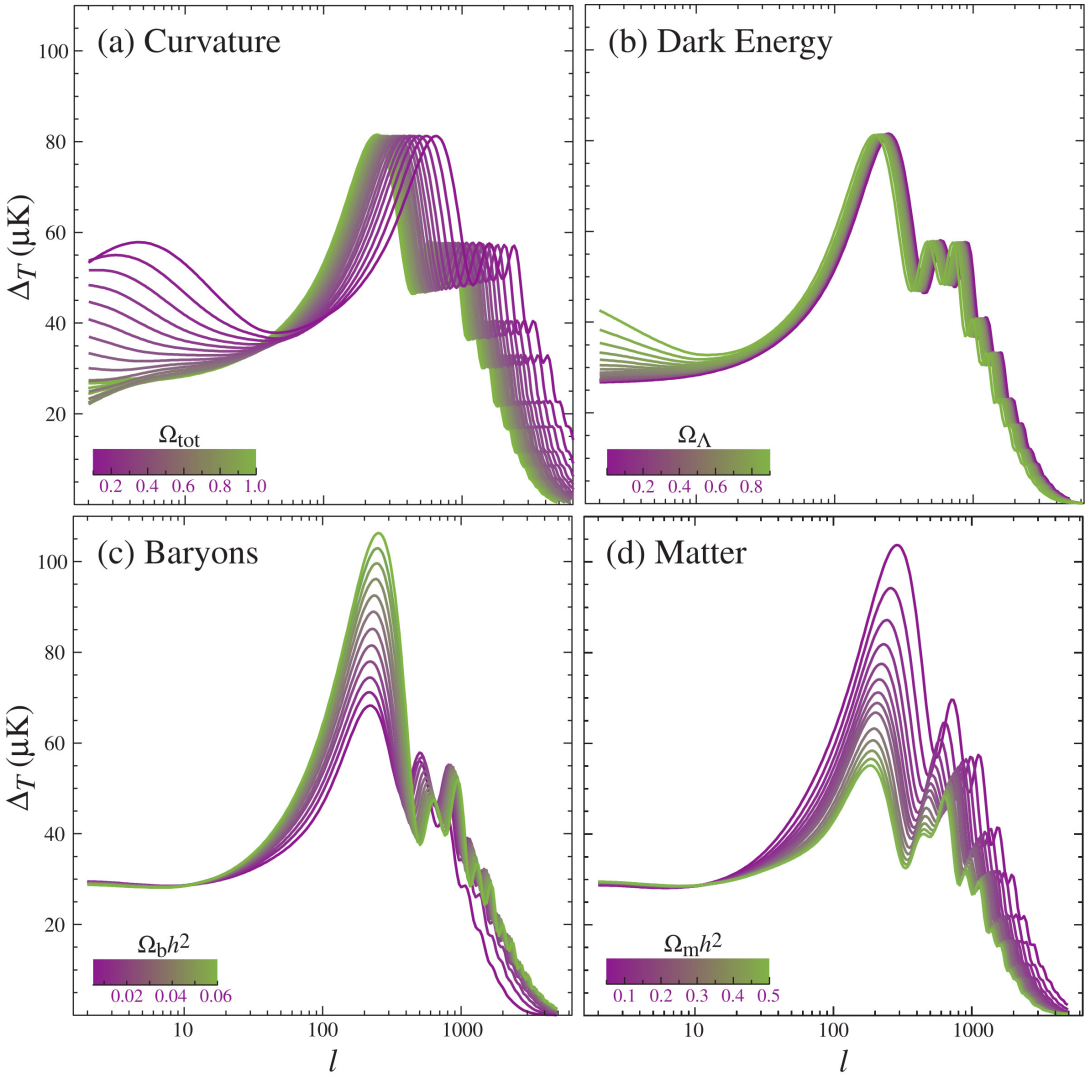

Figure 1.7: Sensitivity of the acoustic temperature spectrum to four fundamental cosmological parameters (a) the curvature as quantified by Ω_{tot} (b) the dark energy as quantified by the cosmological constant Ω_Λ ($w_\Lambda = -1$) (c) the physical baryon density $\Omega_b h^2$ (d) the physical matter density $\Omega_m h^2$, all varied around a fiducial model of $\Omega_{tot} = 1$, $\Omega_\Lambda = 0.65$, $\Omega_b h^2 = 0.02$, $\Omega_m h^2 = 0.147$, $n = 1$, $z_{\rm ri} = 0$, $E_i = 0$. (Figures from Xenon [45])

the density of any particle (dark matter included) equals the density of photons. Equilibrium comes from the fact that two reactions balance each other exactly: First, pairs of dark matter particles are created during the scattering of very energetic lighter particles, which is possible given the very high temperature of the Universe at this time. Second, pairs of dark matter particles can annihilate into lighter particles. The density of dark matter is, therefore, constant since the losses of dark matter are compensated by the creation of dark matter.

However, during the evolution of the Universe, it cools and expands. Therefore, there is a time when lighter particles will no longer be energetic enough to create dark (heavier) matter. From this moment, only dark matter annihilation

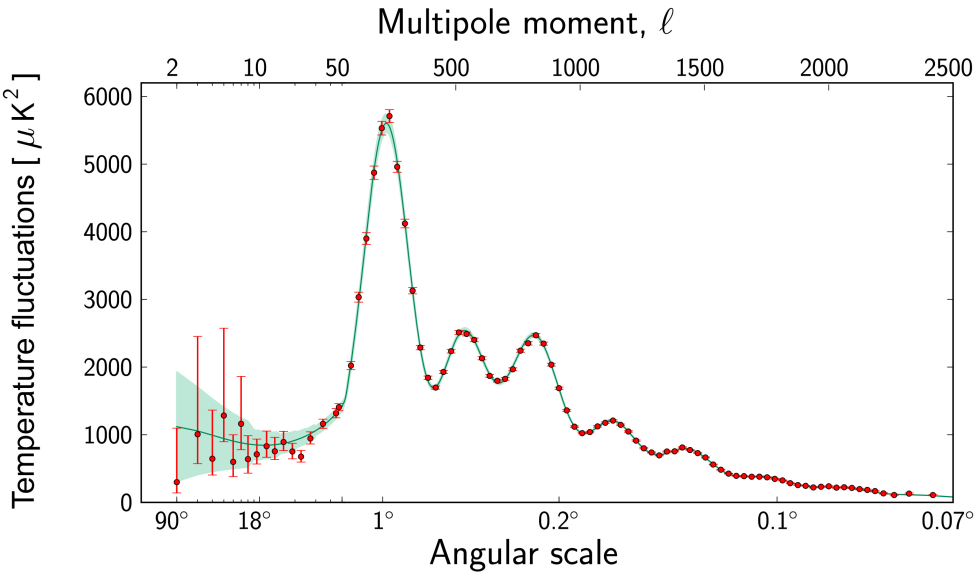

Figure 1.8: Power spectrum of the CMB radiation temperature anisotropies as a function of the angular scale. (ESA and the Planck Collaboration [20]).

occurs, and the density of dark matter decreases. As the Universe expands, there is a time when the dark matter will be too diluted to annihilate. The density of dark matter then becomes constant. Both of the reactions have ceased (see Figure 1.9).

The freeze-in mechanism postulates that dark matter particles are very weakly coupled to the primordial plasma and, therefore, cannot reach thermal equilibrium with the plasma before decoupling. However, weak interactions with SM particles (either directly or through a portal[11]) could produce dark matter until the interaction rate falls below the expansion rate. At this stage, the abundance of dark matter freezes.
In this case, the final abundance is directly proportional to the coupling strength; the more significant the interaction cross-section, the more dark matter particles are produced. In this sense, the freeze-in can be seen as the opposite process of the freeze-out [46].

Constraints on candidates: the primordial kinematics

With the existence of dark matter strongly supported, it remains to be seen what constitutes it. The candidate particle must satisfy the following properties:

- stability,
- charge neutrality,
- non-relativistic character.

[11] See Section 1.5.4

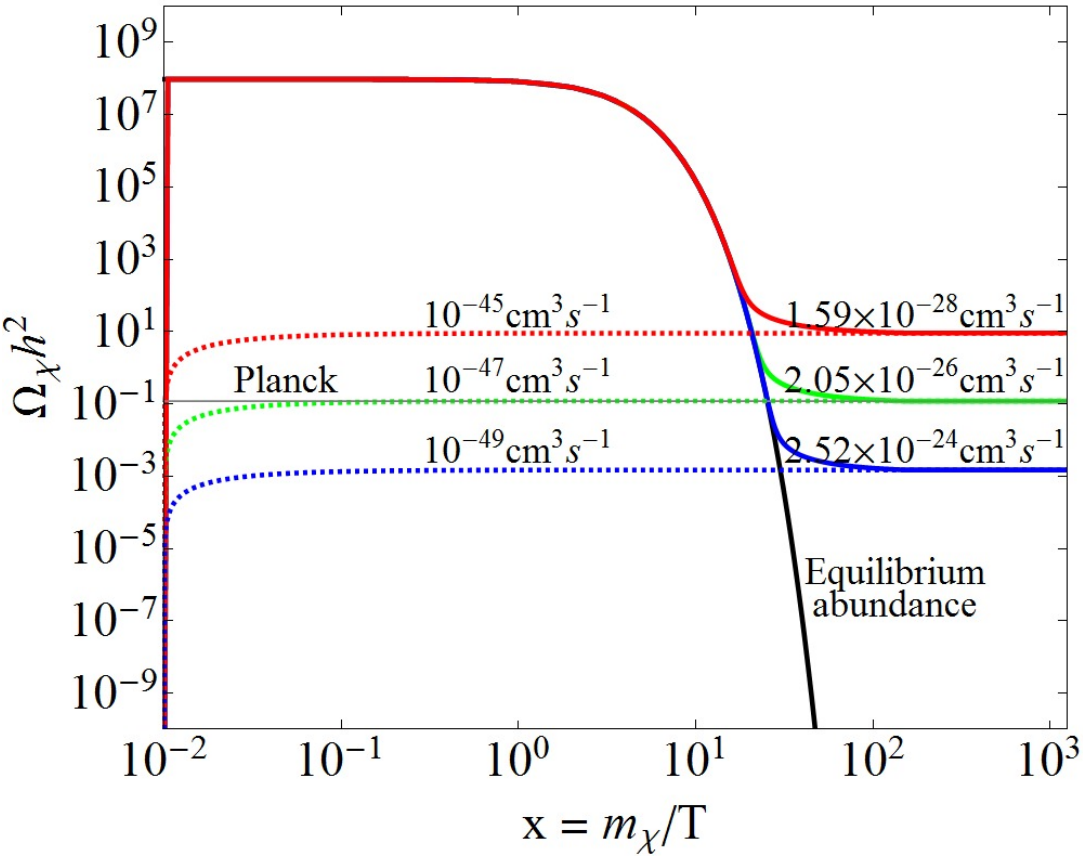

Figure 1.9: Illustration of freeze-out and freeze-in scenarios in the evolution of thermal dark matter abundance for $m_\chi = 100$ GeV as a function of $x = m_\chi/T$ for different annihilation rates. The horizontal band gives the observed relic density from Planck data [20]. Figure from [46].

The characteristics of dark matter make it possible to consider many candidates. Depending on its velocity at the time of decoupling, dark matter can be divided into three kinematic categories hot, cold and warm.

Hot dark matter (HDM) is composed of particles moving at a velocity very close to that of light, and the best candidates for HDM are light neutrinos of the Standard Model [47]. Since the mass of neutrinos is 1 eV or less, then, when they circulate freely, they are in the ultra-relativistic regime at the moment of decoupling and remain in this state when the process of galaxy formation starts. However, highly relativistic particles prevent the formation of galaxies by destroying the small-scale structures of the Universe, which is in contradiction with the cosmological observations of large-scale structures, which disadvantage this hypothesis. Therefore, although it certainly exists in the Universe in the form of neutrinos, HDM can only represent a small part of the total amount of matter.

Cold dark matter (CDM) is the extreme opposite of the HDM. It would be non-relativistic at the time of decoupling with a mass usually considered to be of the order of GeV or beyond. The most popular candidates for CDM include Weakly Interacting Massive Particles (WIMPs) and axions[12].
Those non-relativistic particles exert very little pressure and allow the formation of small-scale structures; this corresponds to the hierarchical scenario, where large structures are formed by merging smaller ones.

Warm dark matter (WDM) behaves as a compromise between HDM and CDM hypotheses and is formed by particles in the mass range at least around keV. It would be relativistic at the moment of decoupling but becomes non-relativistic during the matter-radiation transition. Possible candidates for WDM include sterile neutrino and light gravitino [49].

The hypothesis, according to which the dark matter is formed of cold dark matter particles, is for the moment, the one that is considered to be the strongest [17]. CDM particles are generically called WIMPs. The concept of a WIMP as used in the literature is somewhat ambiguous. In general, it encompasses a broad category of hypothetical candidates from specific theoretical scenarios or their classes. In general, it includes any non-baryonic massive particle (even with a very small mass) that interacts with any weak or sub-weak (e.g., axionic, gravitational) interaction.
In a more commonly used sense, WIMP refers to a particle whose mass is in the GeV-TeV range [50]. They interact with the primordial plasma, and their density decreases exponentially as the Universe cools down. When their density becomes low enough, the equilibrium with the plasma is upset, and the density no longer changes (apart from the dilution factor caused by the Universe's expansion). The relic density observed today is sufficient to explain all the dark matter if the self-annihilation cross-section of WIMP is approximately $3 \times 10^{-26}\text{cm}^3\ \text{s}^{-1}$ [51], and remarkably, this cross-section coincides with that expected for a WIMP in the 100 GeV mass range. This coincidence is sometimes called the *WIMP miracle*. This finding has led many researchers to consider models having such a particle as a candidate for dark matter.

However, the fact that experiments still have not detected them causes the idea of a WIMP miracle to lose its importance. A canonical approach to account for these observations is based on relaxing the constraints on the dark matter parameter space and considering an alternative framework where direct DM-hadron interactions do not occur and where the dark matter couples exclusively to standard model leptons [52]. This approach leads to the dark matter as being *leptophilic*.

In conclusion, the WIMP (in its general definition) solution to the dark matter problem is attractive for several reasons:

[12] Axions were introduced to solve the problem of CP symmetry in chromodynamics. These particles can be created non-thermally and contribute to the total density of dark matter while having a very low mass (10^{-5} to 10^{-3} eV) [48].

1. WIMPs can easily be accommodated in a large number of theoretical models.
2. For reasonable mass and annihilation cross-section ranges of WIMPs, the relic abundance of dark matter can be achieved by the robust mechanism of thermal freezing.
3. Thermal WIMPs represent a promising target for detection experiments. The typical interaction rate is within the range of current or planned detectors, making their existence testable.

1.4 The search for dark matter

The detection of dark matter can be separated along three axes, as shown in Figure 1.10: direct and indirect search, in addition to production by high-energy colliders.

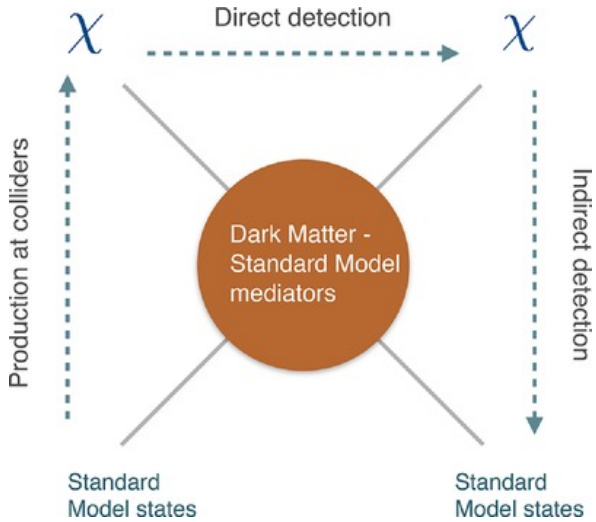

Figure 1.10: Schematic showing the possible dark matter detection channels.

Direct detection experiments search for a scattering signal between a dark matter particle and a SM particle with the lowest possible background noise. Therefore, this type of experiment is installed underground. Indirect detection experiments aim to observe known particles, such as neutrinos, gamma rays, or antiprotons produced when dark matter particles interact with ordinary matter. Finally, collider experiments look for the emergence of new dark matter particles in high-energy collisions.

1.4.1 Direct search of dark matter

Since the end of the '80s, after the paradigm shift that made dark matter an exotic and non-baryonic matter, efforts have been undertaken to search for candidate particles, through their interaction, even very weak, with ordinary matter.

Most direct detection experiments seek to measure the recoil energy deposited when a dark matter particle interacts with a nucleus in the detector, also known

as recoil energy (E_R). The recoiling nucleus will then transfer this energy to the electrons or other nuclei, causing in the first case an ionization or scintillation and, in the second case, production of heat [53]. From the number of events observed, their distribution in recoil energy, and even the angle (directional detection), it is possible to strongly constrain the cross-section of the interaction of dark matter particles as a function of their mass. The difficulty of this approach comes from the significant background noise, which requires methods of discrimination of these events to be sensitive to the expected rate of dark matter particle events.

The limit of the detection methods with nuclear recoil consists of the fact that the dark matter particles must have a minimum mass to produce a signal. Instead, lighter dark matter particles could be detected efficiently through their scattering with electrons.

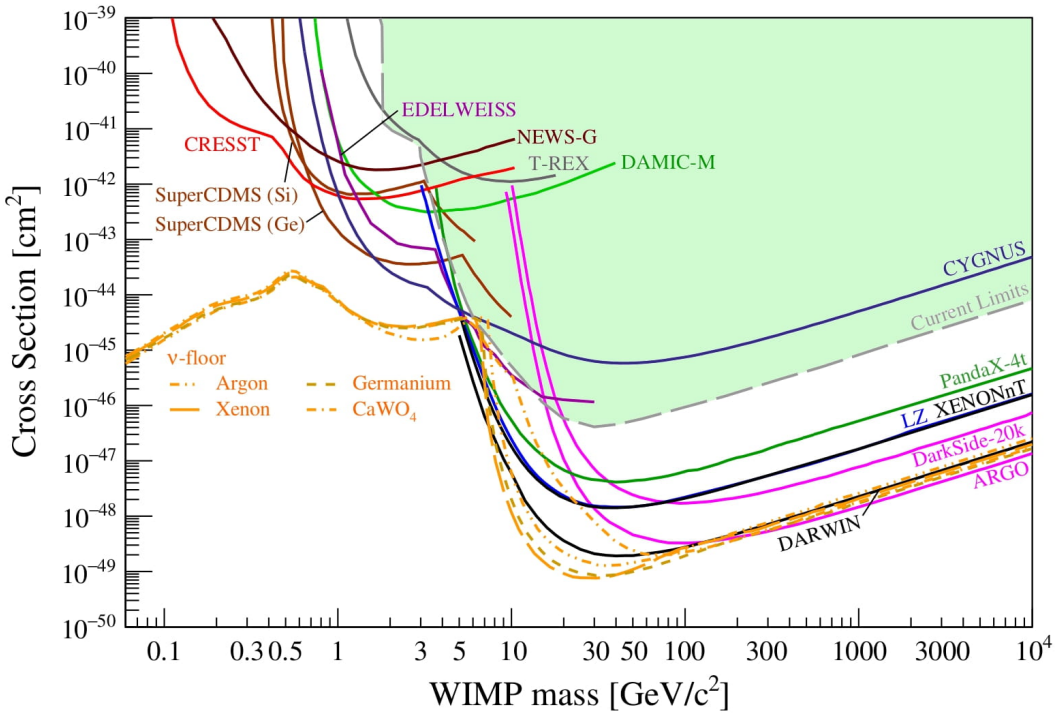

Figure 1.11: Sensitivity projections (90% upper limits) for spin-independent WIMP-nucleon scattering. (APPEC Committee Report [53]).

Figure 1.11 shows the current status as well as the sensitivity projection for spin-independent WIMP-nucleon scattering. Considering the expected sensitivities for future experiments, the neutrino fog[13] will be reached soon, and therefore it will be very challenging for the direct search of WIMPs to discriminate between neutrinos interactions and WIMP interaction.

More detail on direct dark matter detection will be presented in Section 1.5.

[13]The neutrino fog represents the regime of the parameter space where the expected events due to the dark matter signals become saturated by the number of neutrino events or when this excess of events is lower than the statistical fluctuations of the background.

1.4.2 Indirect search of dark matter

Most models of dark matter particles predict that they can annihilate in pairs or decay [54]. Although annihilation/decay rates should be low today and no longer affect the cosmological abundance of dark matter, nevertheless, it is still enough to be detected, especially in some regions of overdensity. These processes generate Standard Model particles, including high-energy photons and charged particles, which can propagate to Earth and be measured. The indirect dark matter detection focuses on three channels: cosmic rays, γ-rays, and neutrinos as illustrated in Figure 1.12.

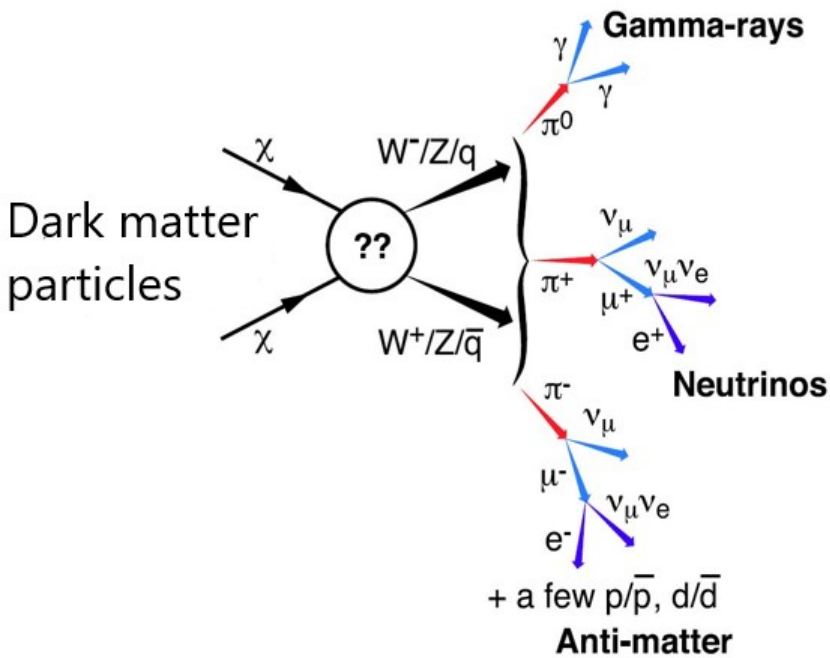

Figure 1.12: Illustration of the three indirect dark matter detection channels.

The annihilation of dark matter produces (among others) antimatter particles. Given the small number of known astrophysical mechanisms capable of creating antimatter, the background associated with the flux of antimatter cosmic rays is relatively low. This is why searching for dark matter through antiparticles is a promising strategy. Nevertheless, the fact that charged cosmic rays are subject to interactions due to the magnetic field of the galaxies makes it challenging to trace the position of their source.

According to the models in which the dark matter interacts with the weak force, the dark matter particles can produce also gamma-ray signals by pair annihilation [54]. This signal can either be a monochromatic line if the dark matter annihilates directly into photons or a continuous spectrum if it annihilates into a pair of intermediate particles that would secondarily produce gamma rays. The gamma photons produced by the annihilation of dark matter are sought in various astrophysical systems, starting with our Galaxy center, as the flux of gamma photons increases with the density of dark matter. Towards the center of the Galaxy, the spectra of the gamma rays emitted have been studied in

detail [55], but have always been explained by an astrophysical source, and no indirect detection of dark matter has been reported convincingly. Nevertheless, in 2019, an excess relative to the astrophysical background was observed by the Fermi-LAT satellite in the direction of the outer halo of Andromeda Galaxy [56]. This can be interpreted by the presence of dark matter particles whose mass is ~46–73 GeV annihilating to bottom quarks with the cross-section ranging from $\sim 8\times10^{-27} - 4\times10^{-24}$ cm^3 s^{-1} [57]. However, it is very possible that these photon flux anomalies can also be explained by standard astrophysical mechanisms or observational biases.
The satellite galaxies of the Milky Way, and in particular the dwarf spheroid galaxies, constitute privileged systems for the observation of incident photons resulting from the annihilation of dark matter. These galaxies are among the objects most dominated by dark matter, with mass-to-luminosity ratios of 10 to 1000 [58]. Therefore, baryonic matter only counts for 0.1 to 10% of their total mass. These satellites can be close (Segue 1 is, for example about 23 kpc away) and have the advantage of not emitting γ radiation of astrophysical origin (interaction of cosmic rays with the interstellar medium of Segue 1 is very weak). As result, the absence of background noise provides robust constraints on the properties of dark matter. Nevertheless, no signature of the presence of dark matter in these systems has been reported to date, and strong constraints on the dark matter annihilation cross-section have been derived from combined statistical analyzes of several of these objects (see Figure 1.13) [59]. These constraints strongly depend on the astrophysical assumptions and, in particular, on the estimation of the J-factor[14].

The annihilation reaction of dark matter can also produce neutrinos that can propagate over long distances due to their weak interaction with the environment and make it possible to identify their source. An up-and-coming method highlights the presence of dark matter in the core of the Sun; If the interaction cross-section of dark matter with baryonic matter is high enough, dark matter can be gravitationally bound, lose energy, and accumulate in the center of the Sun. From there, it can annihilate and produce neutrinos observable from Earth (see Figure 1.14). Experiments like KM3NeT or IceCube track cosmic neutrinos, but no signal distinguishable from the astrophysical background and compatible with the dark matter has been detected to date.

1.4.3 Dark matter production by high-energy colliders

The efforts to produce dark matter are mainly concentrated at the Large Hadron Collider (LHC) at CERN, involving the ATLAS and CMS experiments. The search for dark matter particles is done indirectly by detecting abnormal missing energy in the final state of the reaction studied. Figure 1.15 shows the state-of-the-art limit on the production of dark matter in particle accelerators.

For many years, the leading candidate for cold dark matter has been the

[14]The J-factor describes the amount of dark matter particle annihilation in an astrophysical environment with a distribution of dark matter at a given distance from the observer. It is defined as $J = \int\int \rho^2_{DM}(l,\Omega) dl d\Omega.$, with ρ_{DM} the dark matter density.

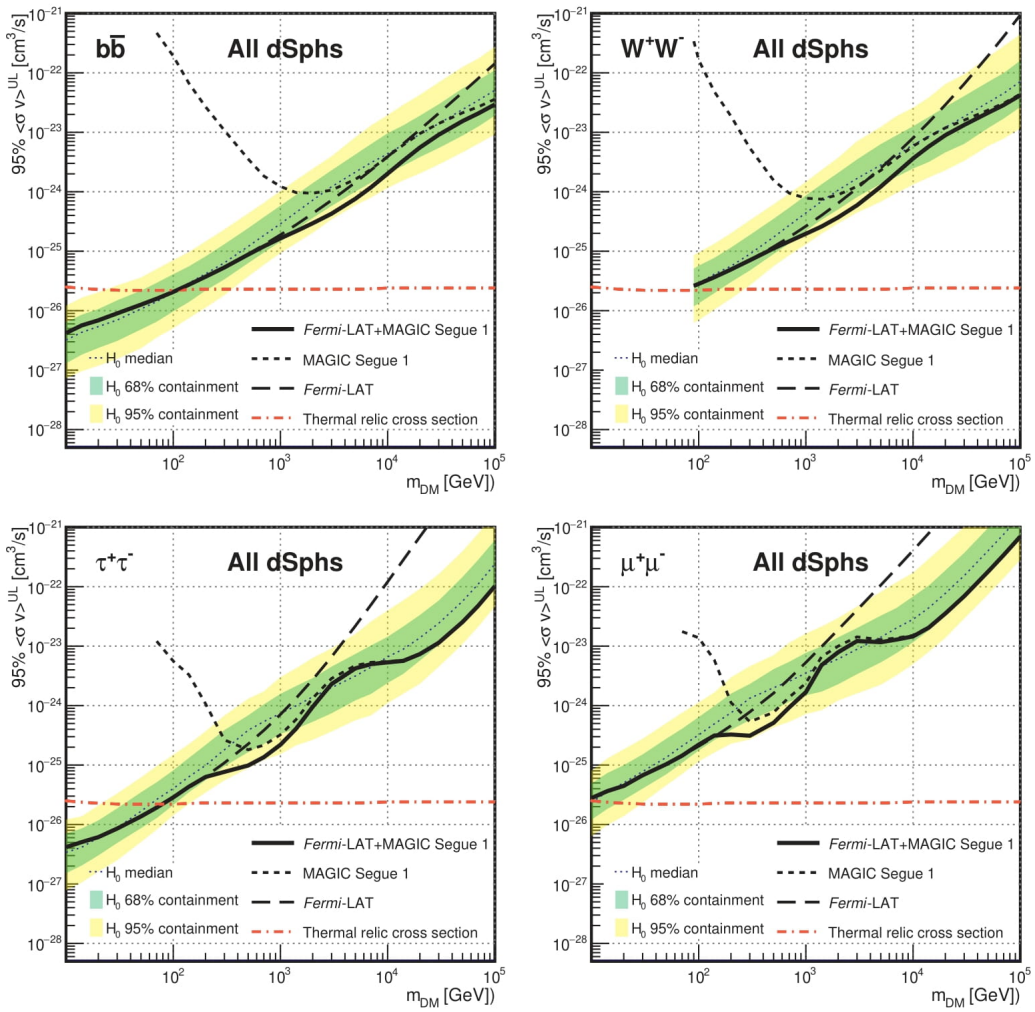

Figure 1.13: 95% upper limits on the thermally-averaged cross-section for dark matter particles annihilating into $b\bar{b}$ (upper-left), W^+W^- (upper-right), $\tau^+\tau^-$ (bottom-left) and $\mu^+\mu^-$ (bottom-right) pairs. Thick solid lines show the limits obtained by combining Fermi-LAT observations of 15 dwarf spheroidal galaxies (dSphs) with MAGIC observations of Segue 1. Dashed lines show the observed individual MAGIC (short dashes) and Fermi-LAT (long dashes) limits. The thin dotted line, green and yellow bands show, respectively, the median and the symmetrical, two-sided 68% and 95% containment bands for the distribution of limits under the null hypothesis. The red-dashed-dotted line shows the thermal relic cross-section. (MAGIC collaboration [59]).

neutralino. A hypothetical particle part of the extension beyond the Standard Model of elementary particles, allowed by supersymmetry theory [53]. Each known particle would have a supersymmetric partner particle, more massive and of complementary spin (i.e., a fermion for a boson, and vice versa). The neutralino is the most stable particle of this set, into which the other supersymmetric particles decay. The neutralino is a linear combination of three particles: the zino, the photino, and the Higgsino, superpartners of bosons (Z, photon, and

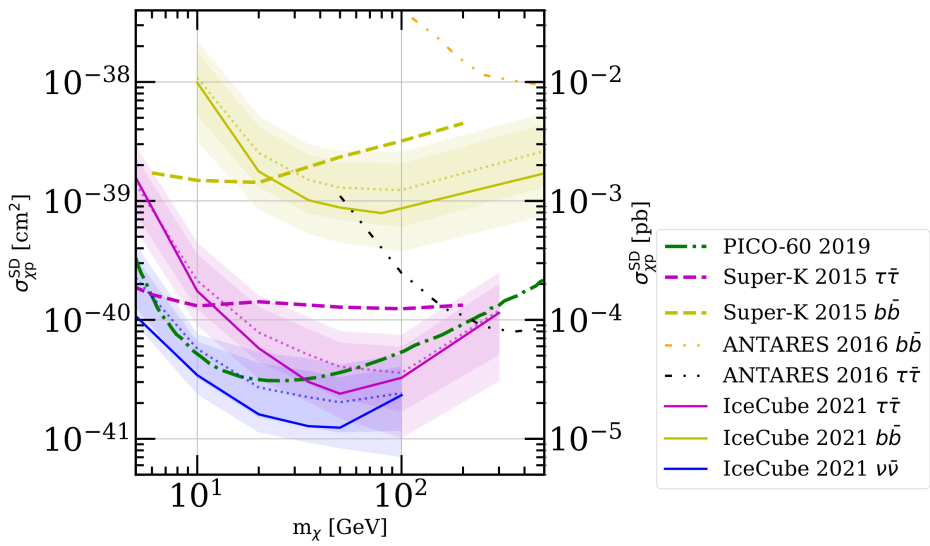

Figure 1.14: 90% upper limits (solid lines) and expected sensitivity (dotted) on the spin-dependent cross-section as a function of WIMP mass obtained by 7 years of IceCube DeepCore data. The dark and light-shaded bands show the central 68% and 95% expected limits, respectively. Also shown are limits from the Super-K, PICO-60, and ANTARES experiments. (IceCube [60]).

Higgs). Four types of stable neutralinos can be formed depending on the factors of this combination. Although the LHC has not revealed these particles, the hope remains to discover them at higher energies [62]. If the LHC detects such particles, to confirm it as dark matter, this particle (with the same energy) should be detected in non-accelerator experiments to demonstrate its presence in the Galaxy. Similarly, suppose a non-accelerator experiment detects a candidate for dark matter; in that case, it should be produced and its existence confirmed by the LHC if it happens to be in the energy range accessible. Therefore, the two types of experiences are complementary.

1.5 Direct detection of Dark Matter

WIMP particles can interact with both electrons and nucleons. Depending on their mass M_χ, large-mass WIMPs tend to interact with the nucleus, while small-mass WIMPs (or other dark matter candidates) interact with electrons.

When preparing a direct dark matter detection experiment, as in any other particle physics experiment, it is necessary to estimate how many events the detector will observe after an exposure time T. This number is given by:

$$N = M_t T R, \tag{1.18}$$

where M_t is the total mass of the target material and R is the interaction rate, which is the first (and most important) estimate to be made. It is given per

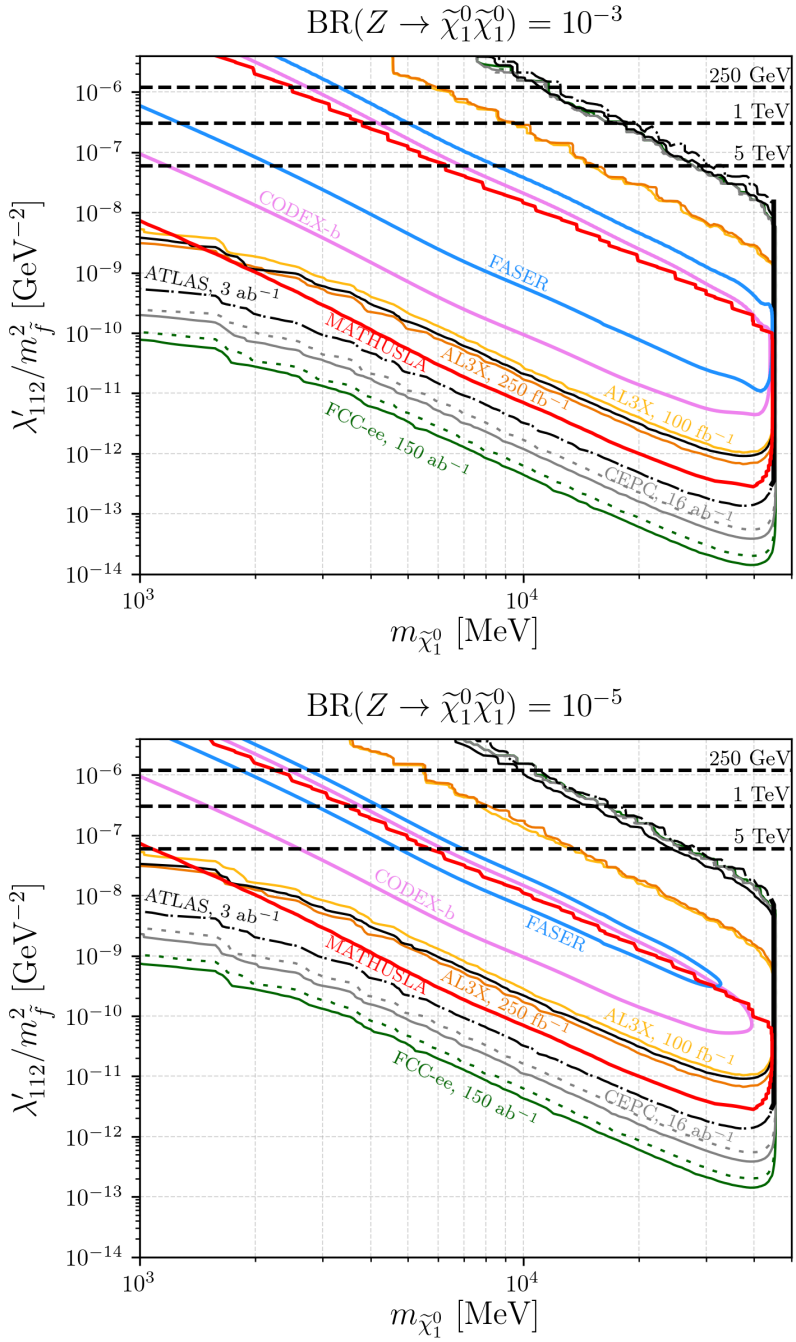

Figure 1.15: Exclusion limit and sensitivity for main exciting and planned dark matter production experiments. Figure from [61].

kilogram of target mass, integrated over all recoil energies, by the relationship:

$$R \simeq \frac{\rho_{DM}}{M_\chi} \frac{\bar{v}_{DM}\sigma}{A}, \tag{1.19}$$

where ρ_{DM} and $\bar{v}$ are, respectively, the mass of the dark matter particles and

their velocity relative to the target. A is the mass number of the target nucleus. And σ is the cross-section for a dark matter nucleus or electron interaction.

1.5.1 Distribution and local flux of dark matter

According to cosmological models, the galaxies' luminous matter is gravitationally bound to a more massive and extensive dark matter halo. As a result, our solar system and the Earth would pass through a flux of dark matter particles, which constitute the dark halo of the Milky Way. The distribution of dark matter in the Galaxy can be estimated from the rotation curves of stars in the Milky Way and extrapolated by numerical simulations. These simulations differ in the choice of the model of the galactic halo. Nevertheless, the standard hypothesis leads to a density value of $\rho_\chi = 0.3$ GeVc^{-2}cm^{-3} [63].

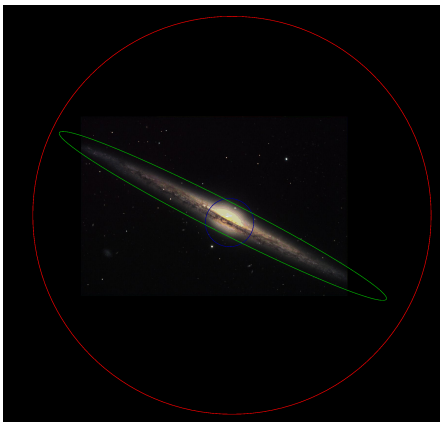

Figure 1.16: The Milky Way can be divided into three structural components: the galactic bulge, the galactic disk, and the dark matter halo, respectively, in blue, green, and red.

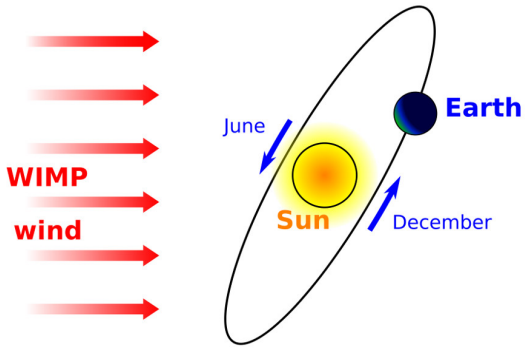

Figure 1.17: Illustration of the expected *dark matter wind*, which is due to the movement of the Sun relative to the dark matter halo of the Milky Way. It is also possible to see the origin of the modulation of this wind during the year. Figure from [64]

The dark matter flux depends on the local dark matter density ρ_χ, on the average dark matter velocity $\bar{v}$ (which is typically around 230 km/s for the Solar System [65]) and on the mass of the dark matter m_χ:

$$\Phi = \frac{\rho_\chi}{m_\chi}\bar{v} \tag{1.20}$$

While an order of magnitude estimation of the event rate can often be obtained by simply using the average velocity of a dark matter particle, for quantitative measurement of dark matter properties, knowledge of its velocity distribution is necessary. A canonical framework has emerged in this field, in which the dark matter halo is considered to be an isothermal, Maxwellian distribution with a cutoff corresponding to the escape velocity [66]. In the galactic reference frame, it is given by the distribution (1.21), characterized by the dispersion of the

quadratic mean of the velocities σ_v and the mean velocity of the galactic halo given by $v_0 = \sqrt{3/2\sigma_v^2}$:

$$f_{gal}(\mathbf{v}) = \begin{cases} k(\frac{3}{2\pi\sigma_v^2})^{3/2} e^{\frac{-3v^2}{2\sigma_v^2}} & v \leq v_e, \\ 0 & v > v_e, \end{cases} \tag{1.21}$$

with v_e *the release or escape velocity* and k is a normalization factor defined as:

$$\frac{1}{k} = \mathrm{erf}(z) - \frac{2ze^{-z^2}}{\sqrt{\pi}}, \tag{1.22}$$

where $z = v_e/v_0$.

To find the actual velocity distribution of dark matter in the Earth frame, one must consider the fact that the motion of the Earth inside the dark matter distribution is the combination of the motion of the Sun in the Galaxy and the orbital Earth motion. Thus, the Earth's orbital speed is added to Sun's speed during the summer and subtracted from it during the winter. This results in a modulation of up to 10% [63]. Thus, the velocity distribution of dark matter in the Earth rest frame $f_E(\mathbf{v}, t)$ is obtained from the distribution in the Galactic rest frame $f_{gal}(\mathbf{v})$ by:

$$f_E(\mathbf{v}, t) = f_{gal}(\mathbf{v} + \mathbf{v}_S + \mathbf{v}_E(t)). \tag{1.23}$$

In the coordinate system where x points towards the Galactic center, y towards the Galactic rotation direction, and z towards the Galactic north pole, we obtain for the speed of the Sun $\mathbf{v}_S = (0; 230; 0) + (10; 13; 7)$ km/s (including the local Keplerian speed of 230 km/s as well as the particular speed of the Sun). To describe the movement of the Earth around the Sun, we use the parametrization: $\mathbf{v}_E(t) = \overline{v_E}(\boldsymbol{e}_1 sin\lambda - \boldsymbol{e}_2 cos\lambda)$, with $\overline{v_E} = 2\pi$ au/year = 29.8 km/s, $\boldsymbol{e}_1 = (-0.0670\,; 0.4927\,; -0.8676)$, $\boldsymbol{e}_2 = (-0.9931\,; -0.11070\,; 0.01032)$ and $\lambda(t) = 2\pi(t - 0.218)$.

By adding the different contributions, we get:

$$f_E(\mathbf{v}, t) = \frac{vk}{\sqrt{\pi} v_E v_0} \begin{cases} e^{-\frac{(v-v_E)^2}{v_0^2}} - e^{-\frac{(v+v_E)^2}{v_0^2}} & v \leq v_e - v_E \\ e^{-\frac{(v-v_E)^2}{v_0^2}} - e^{-\frac{v_e^2}{v_0^2}} & v_e - v_E < v \leq v_e + v_E \\ 0 & v > v_e + v_E \end{cases} \tag{1.24}$$

Thus, Equation (1.24) corresponds to the local flux of dark matter expected on Earth.

1.5.2 Supersymmetric WIMPs

The Standard Model of particle physics is a gauge theory[15] that describes the properties and interactions of all particles known to date. This model describes

[15]Field theory in which it is possible to modify the phase of the matter fields at each space-time point while simultaneously performing a transformation (known as a gauge transformation) on a vector field in such a way that the measurable quantities are unchanged.

with great precision the electroweak and strong interactions. One of the great successes of this model is the discovery of its predicted Higgs particle in 2012 by ATLAS [67], and CMS [68] experiments at the LHC.
Despite its many successes, the Standard Model has several limitations, it leaves several phenomena unexplained. It thus does not provide any theoretical justification for gravitation, as described by general relativity, nor does it account for the acceleration of the expansion of the Universe (which could be explained by dark energy). This model also does not contain particles that could compose dark matter, possessing all the properties required by cosmological observations. It also does not correctly describe the oscillation of neutrinos or their mass.
Developing new theories *beyond the standard model* is therefore necessary.

Supersymmetry (SUSY) [69, 70] is a boson-fermion symmetry, which would be a new symmetry of space-time and established in the process of unifying the fundamental forces of nature (electroweak, strong, and gravitational). This is allowed by the addition to the generators of Poincaré group (space-time translations and rotations) of N new generators (N can go up to 8). Unlike gauge symmetries, these generators change the spin of particles by half-integer values, creating a supermultiplet of bosons and fermions. Therefore, supersymmetry requires the existence of a new state for each state/degree of freedom of the Standard Model. These supersymmetric partners differ by half a spin unit, e.g., the sleptons (partners of leptons) and squarks (quarks partners) have a spin of 0, gauginos (partners of gauge bosons) and higgsino (partner of the Higgs boson) have a spin of 1/2. The main argument favoring supersymmetry is that this theory solves one of the principal problems of the Standard Model in a "very elegant way" [71].

Hierarchy problem, this problem concerns the energy scale at which the weak interaction and the quantum electrodynamics unify, around 10^2 GeV. The only other known relative scale, the Planck mass, is around 10^{19} GeV. Thus, the difference between the two is several orders of magnitude.
More technically, in the Standard Model, the mass of the Higgs boson receives quantum corrections from fermionic loop diagrams. The total mass of the Higgs boson is therefore written:

$$m_H^2 = m_{H_0}^2 + C, \tag{1.25}$$

where m_{H_0} is *inherent* or *bare* mass of the Higgs boson and C represents the corrections. These corrections can be written as:

$$C \propto \lambda \Lambda_{\mathrm{UV}} \tag{1.26}$$

where λ is the coupling constant and Λ_{UV} is called the ultraviolet cutoff and is the scale up to which the Standard Model is valid. If Λ_{UV} is of the order of the Planck scale, then the mass of the Higgs boson becomes of the order of the Planck scale. This is not possible, since the mass of the Higgs boson has been determined to be (125.10 ± 0.14) GeV by the ATLAS and CMS experiments [17].
Supersymmetry introduces into the calculation of the radiative corrections to the mass of the Higgs boson a sfermionic contribution (superpartner of the fermions). The fermionic and sfermionic radiative corrections will then compensate each

other:

$$C = \lambda(\Lambda_{\mathrm{UV}}^2 + m_b^2) - \lambda(\Lambda_{\mathrm{UV}}^2 + m_f^2) \tag{1.27}$$
$$= \lambda(m_b^2 - m_f^2). \tag{1.28}$$

Assuming that $|m_b^2 - m_f^2| < 1\,\mathrm{TeV}$, the quadratically diverging corrections disappear naturally.

WIMP-nucleus interaction

The direct detection of dark matter particles by observing nuclear recoils produced by the elastic interaction of these particles with the baryonic matter was first proposed by Goodman and Witten in the mid-1980s [72]. The WIMP being neutral, only the nuclear recoil can be detected in these collisions. The probability of having inelastic scattering or interaction with an electron is lower if the dark matter is not leptophilic.
In the highly non-relativistic approximation (the relative average velocity of a WIMP in the halo is of the order of the velocity of the sun in the galaxy, 230 km/s) and taking into account that the WIMP is its own antiparticle, only two types of interactions remain.
The first coupling is axial or spin-dependent (SD) since it couples the WIMP to the spin of the nucleus. The second is scalar or spin-independent (SI) as it only depends on the number of nucleons present in the nucleus. Depending on the nature of the WIMP, the relative importance of the two types of interaction, SI or SD, varies. The total interaction cross-section of a neutralino will be the sum of the cross-section of these two types of couplings. The intermediate particle may be a squark in the SI and SD cases. Another reaction is possible by exchanging a Higgs boson for the SI case and a Z boson for the SD case. The energy transferred during such a collision is very low and, in most scenarios, the WIMP and the nucleus remain intact.

Calculation of the interaction cross-section: Using an effective approach and assuming that the WIMP consists of a candidate or a bound state of candidates proposed by the supersymmetric theory. The candidates proposed by supersymmetry are super-partners of Standard Model bosons, and since supersymmetry changes bosons into fermions, these candidates are then Dirac fermions of spin 1/2. Therefore, considering a WIMP which interacts with a quark via a vector boson ϕ of mass m_ϕ. This interaction is described by the Lagrangian density:

$$\mathcal{L} = g(q^2, m_\phi)\ \bar{\chi}\ \Gamma_\chi\ \chi \bar{Q}\ \Gamma_Q\ Q,$$

where Q represents the quark field, $\Gamma_{\chi,Q} = \{I, \gamma^5, \gamma^\mu, \gamma^\mu\gamma^5, \sigma^{\ muv}, \sigma^{\mu\nu}\gamma^5\}$ and $g(q^2, m_\phi)$ is an effective coupling factor proportional to $\frac{1}{m_\phi^2 + q^2}$ with q the exchanged momentum.

In the case of a spin-independent interaction, the calculation is relatively straightforward. Also considering that the interaction takes place such that $q^2 \ll m_\phi^2$ with an effective Lagrangian density:

$$\mathcal{L} = g_\phi \bar{\chi}\chi\bar{Q}Q. \tag{1.29}$$

To obtain the interaction between a WIMP and a nucleon, the Lagrangian can be rewritten:

$$\mathcal{L} = f_p \bar{\chi}\chi\bar{p}p + f_n\bar{\chi}\chi\bar{n}n, \tag{1.30}$$

where the $f_{p,n}$ are the coupling coefficients between a WIMP and a proton or a neutron, this factor is derived from a quantum chromodynamics (QCD) calculation. According to [73], for one proton, it is equal to

$$f_p = \sum_{q=u,d,s} m_p \frac{g_\phi}{m_q} f^p_{T_q} + \frac{2}{27} f^p_{T_G} \sum_{q=c,b,t} m_p \frac{g_\phi}{m_q}, \tag{1.31}$$

with $m_p f^p_{T_q}$ the fraction of the proton mass represented by each quark flavor, defined by:

$$m_p f^p_{T_q} = \left\langle p \middle| m_q \bar{Q}Q \middle| p \right\rangle \qquad \text{and} \qquad f^p_{T_G} = 1 - \sum_{q=u,d,s} f^p_{T_q}.$$

A similar relation applies to WIMP-neutron coupling. The fraction $f^p_{T_q}$ is determined experimentally, while $f_{p,n}$ are constants from theory once g_ϕ is defined.

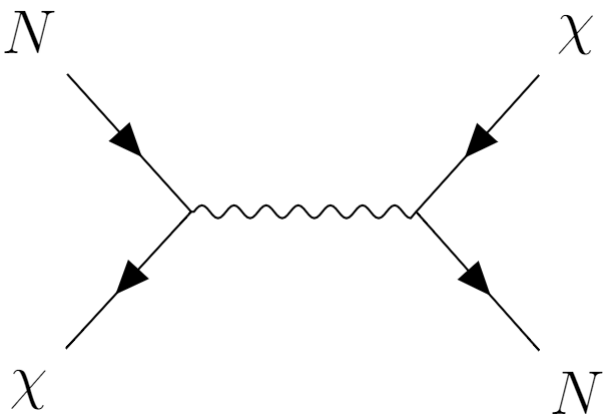

Figure 1.18: Feynman diagrams of WIMP-nucleus interaction

.

From the Feynman diagram 1.18, we can write the scattering amplitude as a function of WIMP interactions with protons and neutrons as:

$$\mathcal{M} = f_p \bar{\chi}\chi\bar{p}p + f_n\bar{\chi}\chi\bar{n}n. \tag{1.32}$$

Since $\bar{p}p$ and $\bar{n}n$ respectively give the number of protons and neutrons in the nucleus, we can deduce that:

$$\mathcal{M} = [Zf_p + (A - Z)f_n]F(q), \tag{1.33}$$

with $F(q)$ the form factor. It is usually taken equal to [63] (see Section 1.5.2):

$$F(q) = 3\, e^{-q^2 s^2/2} \frac{\sin(qr_n) - qr_n \cos(qr_n)}{(qr_n)^3},$$

where the effective nucleus radius is given by $r_n^2 = c^2 + \frac{7}{3}\pi^2 a^2 - 5s^2$, with $a \simeq 0.52$ fm , $s \simeq 0.9$ fm and $c = 1.23A^{1/3} - 0.6$ fm.

In the spin-independent case, we have, according to Fermi's golden rule:

$$\frac{d\sigma^{SI}}{dq^2} = \frac{1}{\pi v^2}|\mathcal{M}|^2 = \frac{1}{\pi v^2}\Big[Zf_p + (A-Z)f_n\Big]^2 F^2(q)\frac{d\sigma^{SI}}{dq^2} \tag{1.34}$$

$$= \frac{\sigma_0^{SI}F^2(q)}{4\mu^2 v^2}. \tag{1.35}$$

The factor $(\pi v^2)^{-1}$ comes from the final state density and the standard golden rule factor, $2\pi/\hbar$. First of all, taking into consideration the differential cross-section as a function of the momentum transferred q^2:

$$\sigma_0^{SI} = \int \frac{d\sigma_0^{SI}}{dq^2}dq^2. \tag{1.36}$$

The goal is to prove that for an isotropic cross-section (no dependence on the scattering angle θ) the differential cross-section can be written as follows:

$$\frac{d\sigma_0^{SI}}{dq^2} = \frac{\sigma_0^{SI}}{4\mu^2 v^2}. \tag{1.37}$$

The proof is immediate if bearing in mind that:

$$q^2 = 2\mu^2 v^2(1-\cos\theta) \Rightarrow \quad \left|\frac{dq^2}{d\cos\theta}\right| = 2\mu^2 v^2. \tag{1.38}$$

Finally, the result is obtained explicitly by performing the change of variable:

$$\int \frac{d\sigma_0^{SI}}{dq^2}dq^2 = \int_{-1}^{1}\frac{\sigma_0^{SI}}{4\mu^2 v^2}2\mu_N^2 v^2 d\cos\theta = \sigma_0^{SI} \tag{1.39}$$

$$\Rightarrow \sigma_0^{SI} = \frac{4\mu^2}{\pi}\Big[Zf_p + (A-Z)f_n\Big]^2 \tag{1.40}$$

The spin-dependent case is more complex. Nevertheless, the typical example of spin-dependent interactions according to [73] is defined by:

$$\mathcal{L}_{eff} \propto \bar{\chi}\gamma_\mu\gamma^5\chi\bar{Q}\gamma^\mu\gamma^5 Q. \tag{1.41}$$

And following [74] it is customary to write the differential cross-section as:

$$\frac{d\sigma^{SD}}{dq^2} = \frac{8}{\pi v^2}G_F^2\Lambda^2 J(J+1)F_{SD}^2(q) \tag{1.42}$$

$$= \frac{1}{\pi v^2}\left(\frac{g^2}{4M_W^2}\right)^2 4\Lambda^2 J(J+1)F_{SD}^2(q),$$

where G_F is the Fermi coupling constant and v is the WIMP-nucleus relative velocity. The prefactor $1/\pi v^2$ comes from the phase space and kinematics, as in the case of the spin-independent cross-section. The 4 results from the spin

factor since, in the case of an exchange of a ϕ boson, the virtual ϕ can have two polarization states. Λ is a coefficient which depends both on particle physics and on the particular hypothesis of the distribution of the nuclear spin J among the nucleons. If the interaction is by exchange of Z, the part relating to particle physics of Λ is 1 while the nuclear spin part is non-trivial. If the interaction occurs by exchanging a different particle, such as a squark, Λ may additionally contain correction factors due to the different couplings and propagators. Finally, $F^2_{SD}(q)$ is the form factor.

The nuclear shell model[16] is the simplest model to calculate Λ. All nucleons are assumed to be spin-paired singlets, except for an unpaired proton and an unpaired neutron. We assume that the nucleus's total spin $\vec{J}$ is given by the angular momentum and the spin of these unpaired nucleons. The coupling is assumed to be via the exchange of Z, so Λ only contains spin factors. The WIMP-quark coupling is proportional to $\vec{s_\chi} \cdot \vec{s_q}$ and therefore, the WIMP-nucleon coupling is given by $\vec{s_\chi} \cdot \vec{S_N}$.

Consider the case of a single unpaired nucleon so that only the $\vec{S}$ and $\vec{L}$ of the nucleon determine the $\vec{J}$ of the nucleus. The nuclear Hamiltonian depends on the square of the total angular momentum, $J^2 = (\vec{L} + \vec{S})^2$. In such a system, the angular momentum operators that commute are J^2, L^2, S^2, and J_z, as given by quantum mechanics, the nuclear spin $\vec{J}$ determines the quantization axis. The projection of the nucleon spin operator along the WIMP spin axis, $\vec{s_\chi} \cdot \vec{S}$, is not necessarily part of the Hamiltonian. However, the projection of $\vec{S}$ according to $\vec{J}$, given by $\vec{S}\vec{J}$, satisfied:

$$\vec{S} \cdot \vec{J} = \frac{1}{2}(J^2 - L^2 + S^2), \tag{1.43}$$

and so commutes with the Hamiltonian, i.e., the average value $\left\langle \vec{S}\vec{J} \right\rangle$ is nonzero, while the average values of the other projections of $\vec{S}$ cancel each other. It is, therefore, this projection to which the spin of WIMP can be coupled. Thus, Λ is given by:

$$\Lambda^2 = \left[\frac{\vec{S} \cdot \vec{J}}{J^2} \right]^2 . \tag{1.44}$$

The above formula can be generalized to:

$$\Lambda = \frac{1}{J}[a_p \langle S\, p \rangle + a_n \langle S\, n \rangle], \tag{1.45}$$

where a_p and a_n satisfy:

$$a_p = \sum_{q=u,d,s} \frac{d_q}{g^2/4M_W} \Delta_q^{(p)} \qquad \text{et} \qquad a_n = \sum_{q=u,d,s} \frac{d_q}{g^2/4M_W} \Delta_q^{(n)}.$$

The $\Delta_q^{(p,n)}$ are the contributions to the spin of the quark q within the nucleon. d_q is the term's coefficient in the effective Lagrangian at the origin of the interaction.

[16]The nuclear shell model is based on the fact that nucleons are quantum objects, therefore in quantized states, that they are fermions, at spin 1/2, which follow the Pauli exclusion principle (like electrons), and that they bathe in a simple attractive potential $V(r)$.

The $\langle S_{p,n} \rangle$ are the average values of the proton and neutron spin in the ground state.

In the end, the formula obtained in the equation of the spin-dependent cross-section is obtained with:

$$\frac{d\sigma^{SD}}{dq^2} = \frac{8}{\pi v^2} G_F^2 \Lambda^2 J(J+1) F_{SD}^2(q) \tag{1.46}$$

$$= \frac{\sigma_0^{SD} F^2(q)}{4\mu^2 v^2}, \tag{1.47}$$

and similarly to the spin-independent cross-section, we have:

$$\frac{d\sigma_0^{SD}}{dq^2} = \frac{\sigma_0^{SD}}{4\mu^2 v^2}. \tag{1.48}$$

Thereby:

$$\sigma_0^{SD} = 8G_F^2 \frac{J+1}{J} \Big(a_p \langle S_p \rangle + a_n \langle S_n \rangle \Big)^2,$$

from which we deduce the differential WIMP-nucleon cross-section comprising a term σ_0 independent of the momentum transferred q and a form factor term $F(q)$ containing the energy dependence:

$$\boxed{\sigma_0 = \frac{4\mu^2}{\pi} \left(\Big[Z f_p + (A-Z) f_n \Big]^2 + 8G_F^2 \frac{J+1}{J} (a_p \langle S_p \rangle + a_n \langle S_n \rangle)^2 \right)} \tag{1.49}$$

The cross-section σ_0, can be written in terms of spin-independent (mostly scalar) and spin-dependent (mostly axial vector) [65]:

$$\sigma_0 = \frac{4\mu^2}{\pi} \left(\Big[Z f_p + (A-Z) f_n \Big]^2 + 8G_F^2 \frac{J+1}{J} (a_p \langle S_p \rangle + a_n \langle S_n \rangle)^2 \right), \tag{1.50}$$

where $\mu = M_\chi M_t / (M_\chi + M_t)$ is the reduced mass of the nucleus-WIMP system, Z is the atomic number of the target nucleus, $f_{p,n}$ and $a_{p,n}$ are respectively the spin-independent and spin-dependent couplings of WIMPs to nucleons, G_F is the Fermi coupling constant, J the total angular momentum of the nucleus and $\langle S_{p,n} \rangle$ are the mean spin values of the nucleons in the nucleus.

The spin-dependent contributions of protons and neutrons often compensate each other [65]. So nuclei with an even number of nucleons have almost no sensitivity to spin-dependent interactions. In particular, nuclei with an even number of protons and neutrons, such as argon, are insensitive to spin-dependent interactions.

For many models, $f_p \approx f_n$ [65], which yields a spin-independent WIMP-nuclei cross-section of the form:

$$\sigma_0^{SI} \approx \frac{4\mu^2}{\pi} f_n^2 A^2. \tag{1.51}$$

This gives, using the cross-section per nucleon σ_N^{SI} given by $4\mu_N^2 f_n^2/\pi$, and the reduced mass per nucleon μ_N,

$$\sigma_0^{SI} = \sigma_N^{SI} \frac{\mu^2}{\mu_N^2} A^2. \tag{1.52}$$

Table 1.1: Values of the atomic number Z, the total nuclear spin J, and the expectation values of the proton and neutron spins within the nucleus $\langle S_{p,n}\rangle$ for various nuclei with odd numbers of protons or neutrons, leading to the relative sensitivities to spin-dependent interactions Table from [65].

Nucleus	Z	Odd Nuc.	J	$\langle S_p\rangle$	$\langle S_n\rangle$	$\frac{4\langle S_p\rangle^2(J+1)}{3J}$	$\frac{4\langle S_n\rangle^2(J+1)}{3J}$
^{19}F	9	p	1/2	0.477	-0.004	9.1×10^{-1}	6.4×10^{-5}
^{23}Na	11	p	3/2	0.248	0.020	1.3×10^{-1}	8.9×10^{-4}
^{27}Al	13	p	5/2	-0.343	0.030	2.2×10^{-1}	1.7×10^{-3}
^{29}Si	14	n	1/2	-0.002	0.130	1.6×10^{-5}	6.8×10^{-2}
^{35}Cl	17	p	3/2	-0.083	0.004	1.5×10^{-2}	3.6×10^{-5}
^{39}K	19	p	3/2	-0.180	0.050	7.2×10^{-2}	5.6×10^{-3}
^{73}Ge	32	n	9/2	0.030	0.378	1.5×10^{-3}	2.3×10^{-1}
^{93}Nb	41	p	9/2	0.460	0.080	3.4×10^{-1}	1.0×10^{-2}
^{125}Te	52	n	1/2	0.001	0.287	4.0×10^{-6}	3.3×10^{-1}
^{127}I	53	p	5/2	0.309	0.075	1.8×10^{-1}	1.0×10^{-2}
^{129}Xe	54	n	1/2	0.028	0.359	3.1×10^{-3}	5.2×10^{-1}
^{131}Xe	54	n	3/2	-0.009	-0.227	1.8×10^{-4}	1.2×10^{-1}

Thus, the interaction cross-section depends on the mass number of the target nuclei; therefore, the choice of target nuclei is one of the crucial parameters in direct dark matter detection experiments.

Recoil energy spectrum

Knowledge of the WIMP-nucleus cross-section and the velocity distribution allows for calculating the interaction rate and the recoil spectrum. Thus, the event rate per unit mass on a target of atomic mass A, with cross-section per nucleus σ_0 is:

$$dR = \frac{\mathcal{N}_A}{A}\sigma_0 dn, \tag{1.53}$$

where $\mathcal{N}_A$ is Avogadro number and dn is the differential number density of WIMP defined by $dn = \frac{\rho_\chi}{M_\chi k} f(v, v_e)\,\mathrm{d}^3v$, with $f(v, v_e) = e^{-(v+v_E)^2/v_0^2}$ [65].

In order to simplify the calculation, we define R_0 as the rate of events per unit mass for $v_E = 0$ and $v_e \to \infty$, i.e.:

$$R_0 = \frac{\mathcal{N}_A}{A}\sigma_0 \int v \frac{\rho_\chi}{M_\chi k} e^{-v^2/v_0^2}\,\mathrm{d}^3v \tag{1.54}$$

For $v_e v\infty$, $k = (\pi v_0^2)^{3/2}$, then,

$$R_0 = \frac{\mathcal{N}_A}{A}\sigma_0 \int v \frac{\rho_\chi}{M_\chi(\pi v_0^2)^{3/2}} e^{-v^2/v_0^2}\,\mathrm{d}^3v \tag{1.55}$$

$$= \frac{1}{(\pi v_0^2)^{3/2}} \frac{\mathcal{N}_A}{A} \frac{\rho_\chi}{M_\chi}\sigma_0 4\pi \frac{v_0^4}{2} \tag{1.56}$$

Using the expression of σ_0^{SI} in Equation (1.52), this last equation can be written to have R_0 in a number of events per kg of the mass of the target per day of exposure in the following way:

$$R_0 = \frac{2}{\pi^{1/2}} \frac{\mathcal{N}_A}{A} \sigma_N^{SI} \frac{\mu^2}{\mu_N^2} A^2 \frac{\rho_\chi}{M_\chi} v_0 \tag{1.57}$$

$$= \frac{6.25.10^{-13}}{M_\chi} \frac{\mu^2}{\mu_N^2} A \left(\frac{\sigma_N^{SI}}{10^{-46}\ \mathrm{cm}^2}\right)\left(\frac{\rho_\chi}{0.3\ \mathrm{GeV}c^{-2}\mathrm{cm}^{-3}}\right)\left(\frac{v_0}{230\ \mathrm{km\ s}^{-1}}\right) \quad \mathrm{kg}^{-1}\mathrm{s}^{-1} \tag{1.58}$$

$$= \frac{1.97.10^{-2}}{M_\chi\ (\mathrm{GeV}/c^2)} \frac{\mu^2}{\mu_N^2} A \left(\frac{\sigma_N^{SI}}{10^{-46}\ \mathrm{cm}^2}\right)\left(\frac{\rho_\chi}{0.3\ \mathrm{GeV}c^{-2}\mathrm{cm}^{-3}}\right)\left(\frac{v_0}{230\ \mathrm{km\ s}^{-1}}\right) \quad \mathrm{ton}^{-1}\mathrm{year}^{-1} \tag{1.59}$$

Thus, for a WIMP mass of 50 GeV/c^2 and with a WIMP-nucleon cross-section of 10^{-46} cm^2, one would expect an interaction rate of about 58 collisions per year and per ton of target material.

In a detector, if the initial kinetic energy of WIMP is $E_i = M_\chi v^2/2$, the recoil energy transferred to the nucleus by a WIMP is:

$$E_R = E_i r \frac{(1 - cos\theta)}{2} \tag{1.60}$$

where r is a dimensionless parameter, with 1 as the maximum value, related to the masses of WIMP and target nucleus by:

$$r = \frac{4\mu^2}{M_t M_\chi} = \frac{4M_t M_\chi}{(M_t + M_\chi)^2} \tag{1.61}$$

In the case of elastic scattering, the differential nuclear recoil spectrum dR/dE_R can be derived from the Equation (1.19) by integrating over the energy of WIMP, or equivalently over the velocity of WIMP. The minimum velocity for which an interaction can occur is given by $v_{min} = \sqrt{2E_{min}/M_\chi} = \sqrt{2E_R/(rM_\chi)}$ (for scattering with $\theta = \pi$), while the maximum velocity is the escape velocity. In the simple case of a detector in a reference frame at rest, with an infinite escape velocity, the differential spectrum is:

$$\frac{dR}{dE_R}(E_R) = \int_{E_{min}}^{E_{max}} \frac{dR(E_i)}{E_i r} \tag{1.62}$$

$$= \int_{E_R/r}^{\infty} \frac{1}{(M_\chi v^2/2)r} \frac{R_0}{2\pi v_0^2} v e^{-v^2/v_0^2} (4\pi v^2 dv) \tag{1.63}$$

$$= \frac{R_0}{(M_\chi v_0^2/2)r} \int_{v_{min}}^{\infty} \frac{2}{v_0^2} e^{-v^2/v_0^2} v dv = \frac{R_0}{E_0 r} e^{-E_R/E_0 r} \tag{1.64}$$

where $E_0 = M_\chi v_0^2/2$ is the most probable incident energy of WIMP. As the energy spectrum drops exponentially (Figure 1.20), it is essential to have a very low energy threshold in this kind of experiment.

In the end, the recoil energy spectrum takes the form (see also FIGURE 1.19:

$$\frac{dR}{dE_R} = \frac{R_0}{E_0 r} e^{-E_R/E_0 r} \tag{1.65}$$

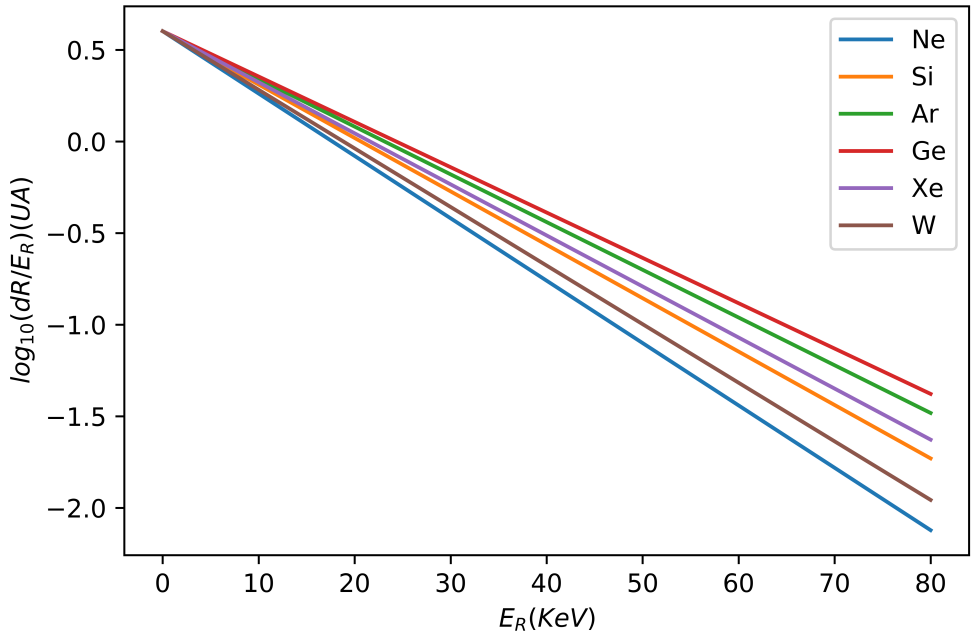

Figure 1.19: The differential interaction rate as a function of the recoil energy for different targets, for $M_\chi = 60$ GeV.

By integrating from E_s, which represents the detection threshold energy up to infinity, we obtain:

$$R = R_0\ e^{-E_s/E_0 r} \quad \Longleftrightarrow \quad \frac{R}{r} = \frac{R_0}{r}\ e^{-E_s/E_0 r} \tag{1.66}$$

$$\Longrightarrow \quad \frac{R_0}{r} = \frac{R}{r}\ e^{E_s/E_0 r} \tag{1.67}$$

where R is taken as a constant.
On the other hand, $M_t \approx 0.932A$ GeV/c^2, where A is the mass number of the target nucleus, with that we get:

$$r = \frac{4M_\chi 0.932A}{(M_\chi + 0.932A)^2} \tag{1.68}$$

Therefore:

$$\frac{R_0}{r} = f(M_\chi, E_s, A) = \frac{R(M_\chi + 0.932A)^2}{4M_\chi 0.932A}\ e^{E_s(M_\chi+0.932A)^2/E_0 4M_\chi 0.932A} \tag{1.69}$$

And by plotting the function f we get the FIGURE 1.20.

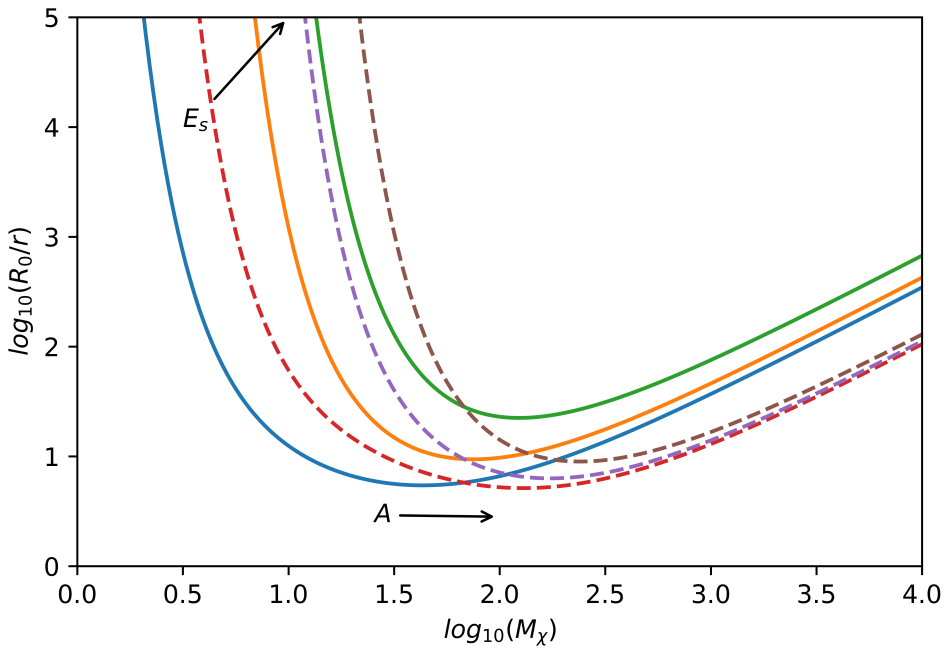

Figure 1.20: The evolution of the detection cross-section of a direct dark matter detector as a function of the mass of the WIMPs, the threshold energy, and the mass number of the target nucleus. Continuous curve $A = 40$ (Argon), dotted curve $A = 132$ (Xenon) with E_s (keV) = {1; 10;30}.

The complete calculation of the energy spectrum for WIMP-nucleus elastic scattering, including the effects of both escape velocity and Earth velocity, Ref. [63, 65] gives the energies of recoil such that $v_{min}(E_R) < v_e - v_E$:

$$\frac{dR}{dE_R} = \frac{R_0}{E_0 r}\left\{\frac{v_0\sqrt{\pi}}{4v_E}\left[\mathrm{erf}\left(\frac{v_{min}+v_E}{v_0}\right) - \mathrm{erf}\left(\frac{v_{min}-v_E}{v_0}\right)\right] - e^{-v_e^2/v_0^2}\right\}, \tag{1.70}$$

whereas if $v_e - v_E < v_{min}(E_R) < v_e + v_E$,

$$\frac{dR}{dE_R} = \frac{R_0}{E_0 r}\left\{\frac{v_0\sqrt{\pi}}{4v_E}\left[\mathrm{erf}\left(\frac{v_{min}}{v_0}\right) - \mathrm{erf}\left(\frac{v_{min}-v_E}{v_0}\right)\right] - \frac{v_e+v_E-v_{min}}{2v_E}e^{-v_e^2/v_0^2}\right\}. \tag{1.71}$$

Form factor

The analysis of direct detection experiments requires knowledge of nuclear structure factors. For a given coupling between WIMPs and nucleons, these encode aspects of nuclear structure relevant to WIMP-nucleus diffusion. In other words, the form factor parameterizes the loss of coherence for the WIMP-nucleus interaction as the energy of WIMP increases.

The form factor represents a contribution from nuclear physics. It depends on the type of WIMP interaction since the elastic scattering cross-section has two distinct interaction channels: a scalar or spin-dependent channel and an axial or spin-independent channel. Therefore, depending on the spin properties

of the target nuclei, the appropriate form factor should be used. To consider this, we must include a nuclear form factor F, which corrects the fact that we assumed a fixed σ_0 in the Equation (1.50), instead of a decreasing cross-section with recoil energy, as the rules of quantum mechanics predict.

For **spin-independent interaction**, F can be represented by a simple function [63] $F(qr_n/\hbar)$ where $q = (2M_tE_R)^{1/2}$ is the momentum transferred to the target nucleus and r_n the effective nuclear radius that can be modeled by the equation:

$$r_n = a_nA^{1/3} + b_n. \tag{1.72}$$

Using Born's first approximation[17] and the target density distribution proposed by Helm [75] and using units in which $\hbar = 1$, one can obtain the following expression for the form factor:

$$F(qr_n) = \frac{3j_1(q\,r_n)}{q\,r_n}e^{-(q\,s)^2/2} = 3\,e^{-q^2s^2/2}\frac{\sin(q\,r_n) - q\,r_n\cos(q\,r_n)}{(q\,r_n)^3}, \tag{1.73}$$

where j_1 is the first-order Bessel function, and s is a measure of nuclear skin thickness. Using $\hbar = 197.3$ MeV fm [17], we can express the form factor argument as a dimensionless quantity:

$$q\,r_n = 6.92.10^{-3}A^{1/2}E_R^{1/2}(a_nA^{1/3} + b_n), \tag{1.74}$$

The **spin-dependent interaction** case is more complex because there is no simple analytical expression for the form factor. In order to take into account the contribution of all the nucleons, it must have three terms: one due to neutrons, one due to protons as well as an interference term [63]:

$$F^2(qr_n) = \frac{S(q)}{S(0)}, \tag{1.75}$$

where,

$$S(q) = a_0^2S_{00}(q) + a_1^2S_{11}(q) + a_0a_1S_{01}(q); \tag{1.76}$$

The S_{ij} factors can be calculated using the nuclear shell model for the specific nucleus. The isoscalar (a_0) and isovector (a_1) coefficients are linked to the WIMP-nucleon coupling factors a_p, a_n such as:

$$S(q) = (a_p + a_n)^2S_{00}(q) + (a_p - a_n)^2S_{11}(q) + (a_p^2 + a_n^2)S_{01}(q) \tag{1.77}$$

In general, for a spin-dependent interaction, $F(q) < 1$ when the de Broglie wavelength $\lambda < r_n$, in this case, the WIMP ceases to interact coherently with the entire nucleus. Since the nuclear radius $r_n \approx A^{1/3}$ fm, this can be translated with

$$\lambda = \frac{\hbar}{q} = \frac{\hbar c}{\sqrt{2M_Ac^2E_{\mathrm{R}}}} = \frac{197\ \mathrm{MeV\ fm}}{\sqrt{2AE_{\mathrm{R}}(\mathrm{keV})}} < A^{1/3}. \tag{1.78}$$

[17]The principle of the Born approximation is based on the fact that the Coulomb interaction potential between a projectile and the different constituents of the target is weak compared to the total energy of the target and incident projectile. Therefore, the scattering potential can be treated as a perturbation. Born's first approximation then consists in retaining only the first-order terms.

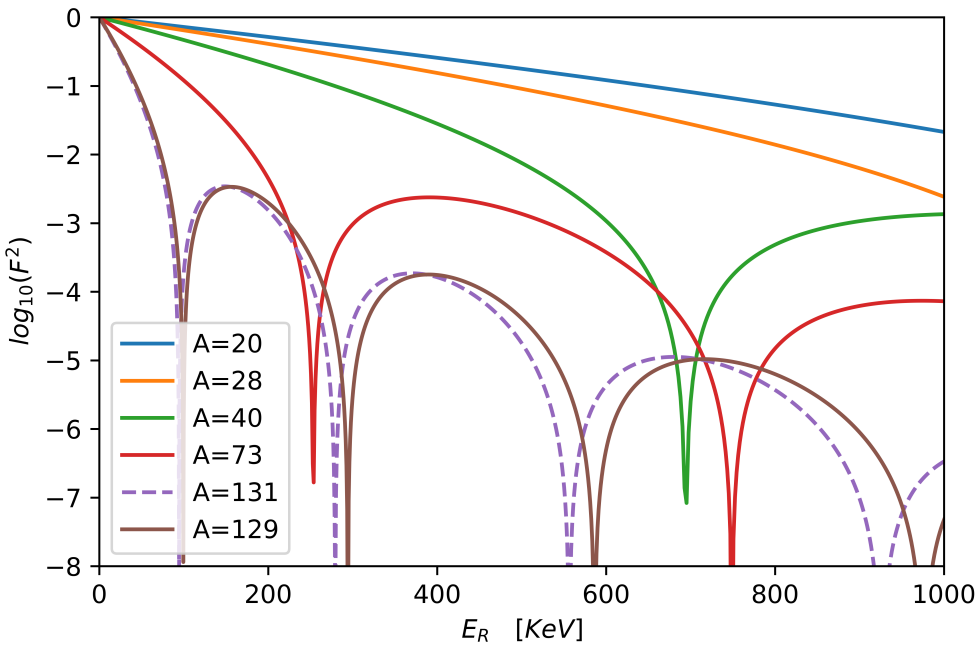

Figure 1.21: Form factor as a function of recoil energy E_R for different mass numbers. In dotted lines are represented the one corresponding to Xenon.

Therefore, coherence is lost when

$$E_{\mathrm{R}} > \frac{2 \times 10^4}{A^{5/3}} \text{ keV} \sim 100 \text{ keV}. \tag{1.79}$$

The strong dependence on A indicates that coherence is lost much earlier for targets with high A, as shown in Figure 1.21. This loss of coherence considerably reduces the advantage of using particularly heavy target materials; in practice, using materials heavier than Ge results in only modest increases in the overall rate, well below the A^2 increase that would occur without the loss of coherence. Since the loss of coherence makes these high A targets inherently insensitive to high-energy deposition, it is especially critical that experiments with high A materials reach low energy thresholds.

1.5.3 Axions and axion-like particles

The axion is a boson proposed in the 1970s to explain why strong interactions conserve P (parity) and CP (charge-parity) symmetries. The QCD Lagrangian contains a term allowing the violation of CP, which is expressed in the form

$$\mathcal{L}_\theta = \theta_0 \frac{g^2}{32\pi^2} G_{\mu\nu} \tilde{G}^{\mu\nu} \tag{1.80}$$

where θ_0 is the so-called QCD vacuum angle, a free parameter of the theory, g is the QCD gauge coupling constant, and G is the dual field strength tensor.

Measurements of the neutron's electric dipole moment show that the value of θ_0 is smaller than 10^{-10} [76], implying that the strong interactions do not violate C and CP. The reason why this value is so small is unknown, and this is what constitutes the *strong CP violation problem*.

Peccei and Quinn provided an answer by introducing additional $U(1)$ chiral symmetry (now called $U(1)_{PQ}$) [77]. This symmetry breaks spontaneously, giving rise to a Goldstone boson[18] a, called the axion. The θ_0 parameter is then replaced by a/f_a in the $\mathcal{L}_\theta$ Lagrangian, where f_a is the expected value in the vacuum of the Peccei-Quinn field.
In the primordial universe, f_a vanishes, and the $U(1)_{PQ}$ symmetry is respected. The universe cools, and when its temperature T is of the order of f_a, the axions come into play through the Higgs mechanism. The axion field acquires a small mass $m_a \sim \Lambda^2_{\mathrm{QCD}}/f_a$ at temperatures T of the order of the QCD confinement scale Λ_{QCD}. The axions' mass came from their interactions with gluons that induce transitions to $q\bar{q}$ states and thus to neutral pions. As a result a and π^0 mix with each other ($m_a f_a \approx m_\pi f_\pi$), therefore m_a can be estimated and it is given by:

$$m_a = 5.7\,\mu\mathrm{eV}\left(\frac{10^{12}\,GeV}{f_a}\right), \tag{1.81}$$

If boson particles (like axion) have very light mass and hence high density (to explain the whole dark matter mass), they tend to go into a single quantum state called Bose-Einstein condensate. In the Bose-Einstein condensate state, all particles have the same wave function and hence the same velocity. Almost no velocity dispersion. This very low-velocity dispersion of axions and their extremely weak couplings implies that these particles behave as cold dark matter. The axions contribution to the critical density is given by:

$$\Omega_a h^2 \approx \frac{f_a}{10^{12}\mathrm{GeV}} \tag{1.82}$$

The mass of the QCD axions can be constrained by imposing that Ω_a does not exceed Ω_{DM}. The result is that the mass $m_a \gtrsim 1\ \mu$eV. Moreover, too heavy QCD axions could alter the explosion mechanisms of supernovae and cool the neutrinos emanating from them, hence the limit $m_a \lesssim 10^{-2}$ eV [79].

Figure 1.22 gives some of the most recent constraints on axions-like particles mass.

Axion-ordinary matter interaction

The details of the low-energy couplings between the axion and the Standard Model particles (photon, electron, nuclei) depend on the theory under consideration. Nevertheless, two explicit models serve as references, the KSVZ model [81] called hadronic, in which Goldstone pseudoscalar is coupled to the QCD via additional heavy quarks, and the DFSZ model [82, 83], for which all the fermions are coupled to axions via a second Higgs doublet.

[18] According to Goldstone's theorem, for each spontaneously broken continuous symmetry, there are scalar and massless particles which we call Goldstone bosons [78]

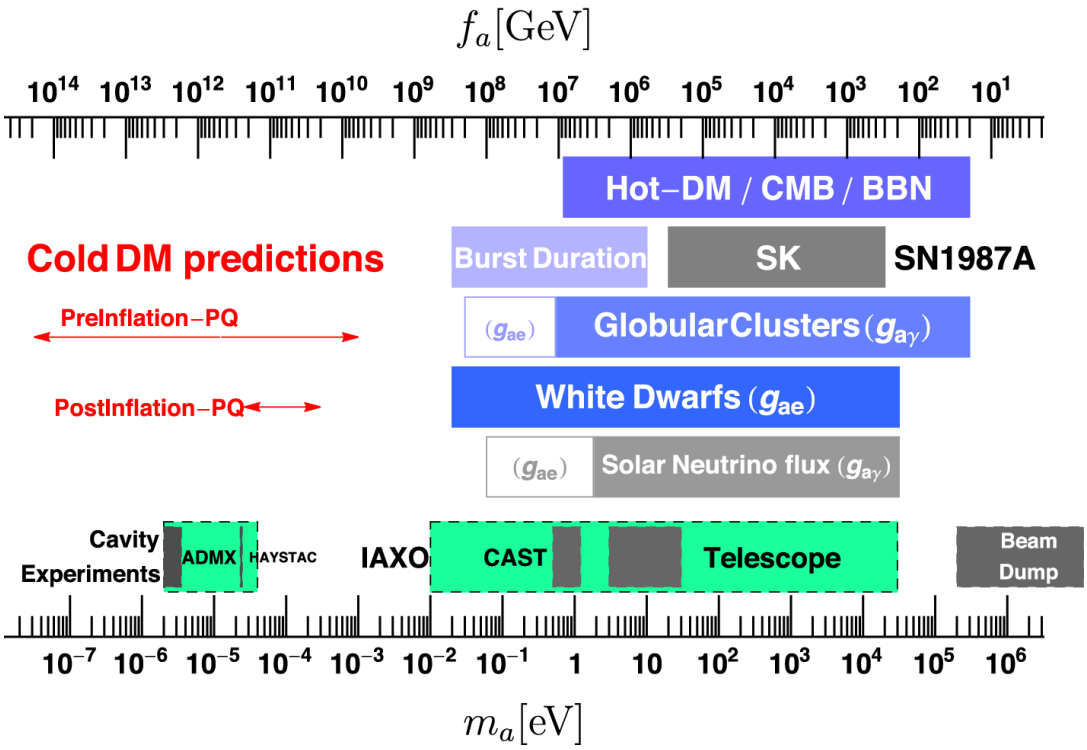

Figure 1.22: Limits on the axions-like particles mass established by cosmology and astrophysics. Light grey regions are model dependent. The green regions indicate the planned reach of future upgrades. The cold dark matter exclusion range is particularly uncertain; ranges for pre-inflation and post-inflation Peccei-Quinn transitions are shown (see [80] for more details). Figure from [80].

In addition to QCD axions, axion-like particles (ALPs) are pseudoscalars that do not necessarily solve the strong CP problem but have been introduced by many models beyond the Standard Model. The most general effective Lagrangian up to dimension 5 is given by (see Ref. [84] for a detailed discussion)

$$\begin{aligned}\mathcal{L}_{\text{eff}}^{D\leq 5} = & \frac{1}{2}\left(\partial_\mu a\right)(\partial^\mu a) - \frac{m_{a,0}^2}{2}a^2 + \frac{\partial^\mu a}{f}\sum_F \bar{\psi}_F \boldsymbol{c}_F \gamma_\mu \psi_F \\ & + c_{GG}\frac{\alpha_s}{4\pi}\frac{a}{f}G^a_{\mu\nu}\tilde{G}^{\mu\nu,a} + c_{WW}\frac{\alpha_2}{4\pi}\frac{a}{f}W^A_{\mu\nu}\tilde{W}^{\mu\nu,A} + c_{BB}\frac{\alpha_1}{4\pi}\frac{a}{f}B_{\mu\nu}\tilde{B}^{\mu\nu}.\end{aligned} \tag{1.83}$$

Where $G^a_{\mu\nu}$, $W^A_{\mu\nu}$ and $B_{\mu\nu}$ are the field-strength tensors of $SU(3)_c$, $SU(2)_L$ and $U(1)_Y$, and $\alpha_s = g_s^2/(4\pi)$, $\alpha_2 = g^2/(4\pi)$ and $\alpha_1 = g'^2/(4\pi)$ denote the corresponding coupling parameters. $\tilde{B}^{\mu\nu} = \frac{1}{2}\epsilon^{\mu\nu\alpha\beta}B_{\alpha\beta}$ etc. (with $\epsilon^{0123} = 1$) are the dual field-strength tensors.

Axions and ALPs can give rise to observable signatures in detectors via their coupling to photons ($g_{a\gamma}$), electrons (g_{ae}), or nuclei (g_{aN}). For example, the coupling to electrons can be tested via electron emission of a target under the effect of the axio-electric mechanism [85]. This process is analogous to the photoelectric effect with the absorption of an axion instead of a photon. The

axio-electric cross section is given, both for QCD axions and ALPs, by [86]

$$\sigma_{ae} = \sigma_{pe}(E_A)\frac{{g_{ae}}^2}{\beta_a}\frac{3{E_a}^2}{16\pi\,\alpha_{em}\,{m_e}^2}\left(1-\frac{\beta_a^{2/3}}{3}\right), \tag{1.84}$$

where, σ_{pe} is the photoelectric cross section, E_A is the axion energy, α_{em} is the fine structure constant, m_e is the electron mass, and β_A is the axion velocity over the speed of light, c.

Solar axion flux

The Sun would constitute an intense source of ALPs (referred to as solar axions), where they can be produced via Bremsstrahlung, Compton scattering, axio-recombination, and axio-desexitation [86], and one could thus possibly detect a flux of solar axions coming directly from the core of the Sun, similar to solar neutrinos. The dominant production mechanism depends on the relative importance of the different couplings involved. Figure 1.23 illustrates the energy distributions of solar axion fluxes associated with various generation modes.

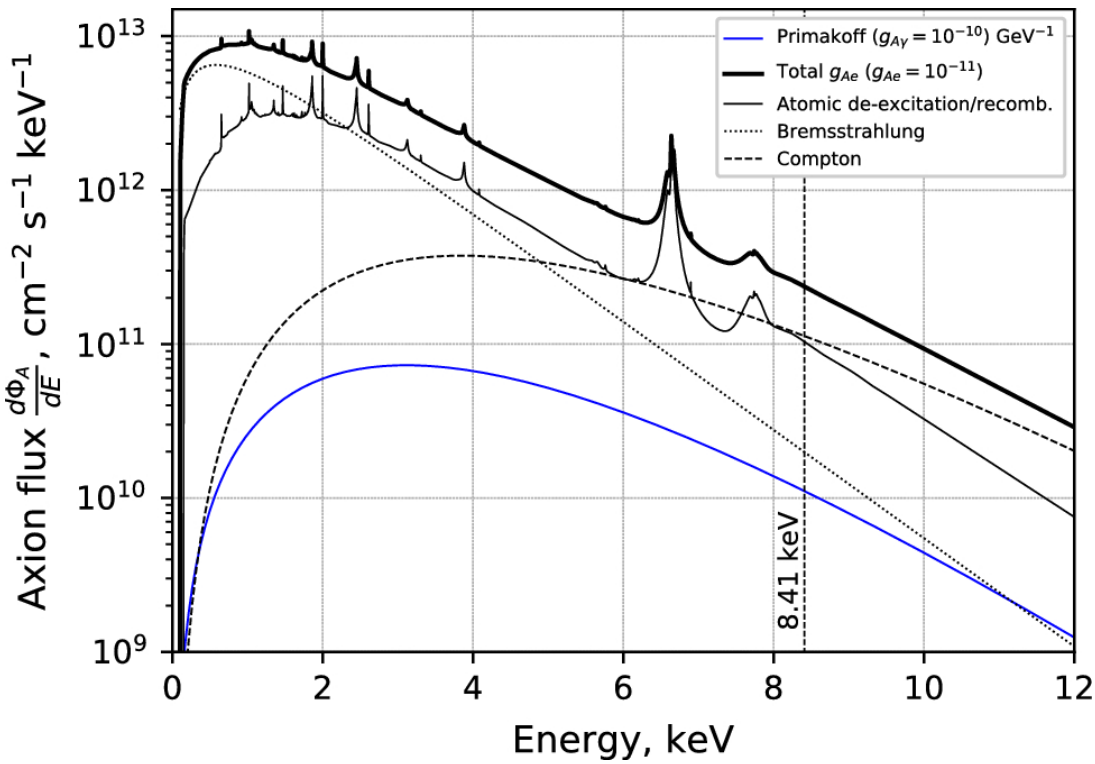

Figure 1.23: Energy spectra of solar axions produced due to the axion–photon (Primakoff effect) and axion–electron couplings (atomic de-exitation/recomb., Bremsstrahlung, Compton). Figure from [87].

The Primakoff flux ($\gamma + Ze \rightarrow Ze + a$) is due to axion-photon interactions resulting from the conversion of thermal photons in the electromagnetic field of the solar plasma. The Primakoff flux is given by [88]

$$\frac{d\Phi_a^{\text{Prim}}}{dE_a} = 6\times10^{10}\text{cm}^{-2}\text{s}^{-1}\text{keV}^{-1}\times\left(\frac{g_{a\gamma}}{10^{-10}\text{GeV}}\right)^2\left(\frac{E_a}{\text{keV}}\right)^{2.481} e^{-E_a/(1.205\text{keV})}.$$

where, $g_{a\gamma}$ is the axion-photon coupling constant. for **Compton** and **Bremsstrahlung**, similar parametrizations as for the Primakoff flux can also be used [88].

1.5.4 Light dark matter of the Hidden Sector

The WIMP hypothesis is accredited mainly because it is the simplest, but it has unfortunately not yet found a positive result. As a result, we should start to look at other candidates. Particles are, for example, considered in a *Hidden Sector*: they would thus have no interaction with the SM particles. More precisely, a Hidden Sector in these generalizations is a group of particle fields that couple weakly to other Standard Model fields, there is no "direct" coupling with Standard Model gauge bosons. Figure 1.24 explains how it would still be possible to detect particles in the hidden sector through the concept of a "portal."
Since we know nothing about the nature or even the origin of these possible particles, the potential candidates are numerous and sometimes very speculative. Nevertheless, in a relatively canonical way, the dark sector offers a set of particles that could be constituents of dark matter. Particles such as the **axion**, the **dark photon**, or the **sterile neutrino** would only interact with those of the Standard Model through the weak interaction. And new bosons, called dark bosons, would be the vectors of this interaction and responsible for the interactions between dark matter particles through a force derived from ordinary electromagnetism and called "dark electromagnetism" [89].

In the same way, as in the Standard Model, dark electromagnetism is a gauge quantum field based on the gauge group $U(1)$[19]. The dark photon carries this new force, denoted A', which interacts directly with dark matter and indirectly with Standard Model particles [89]. Therefore, unlike the classical photon, the dark photon is an extremely unstable boson due to its non-zero mass. This instability leads to its rapid decay either into undetectable dark matter particles, photons or SM leptons [91].

In chapter 4, a more detailed discussion is presented regarding the detection of light dark matter from the Hidden Sector.

[19]The group $U(1)$ corresponds to the unit circle (T), composed of all the complex numbers having as an absolute value (or modulus) 1: $\mathbb{T} = \{z \in \mathbb{C} : |z| = 1\}$. The group $U(1)$ integrates the gauge symmetry and allows building the electromagnetic interaction.

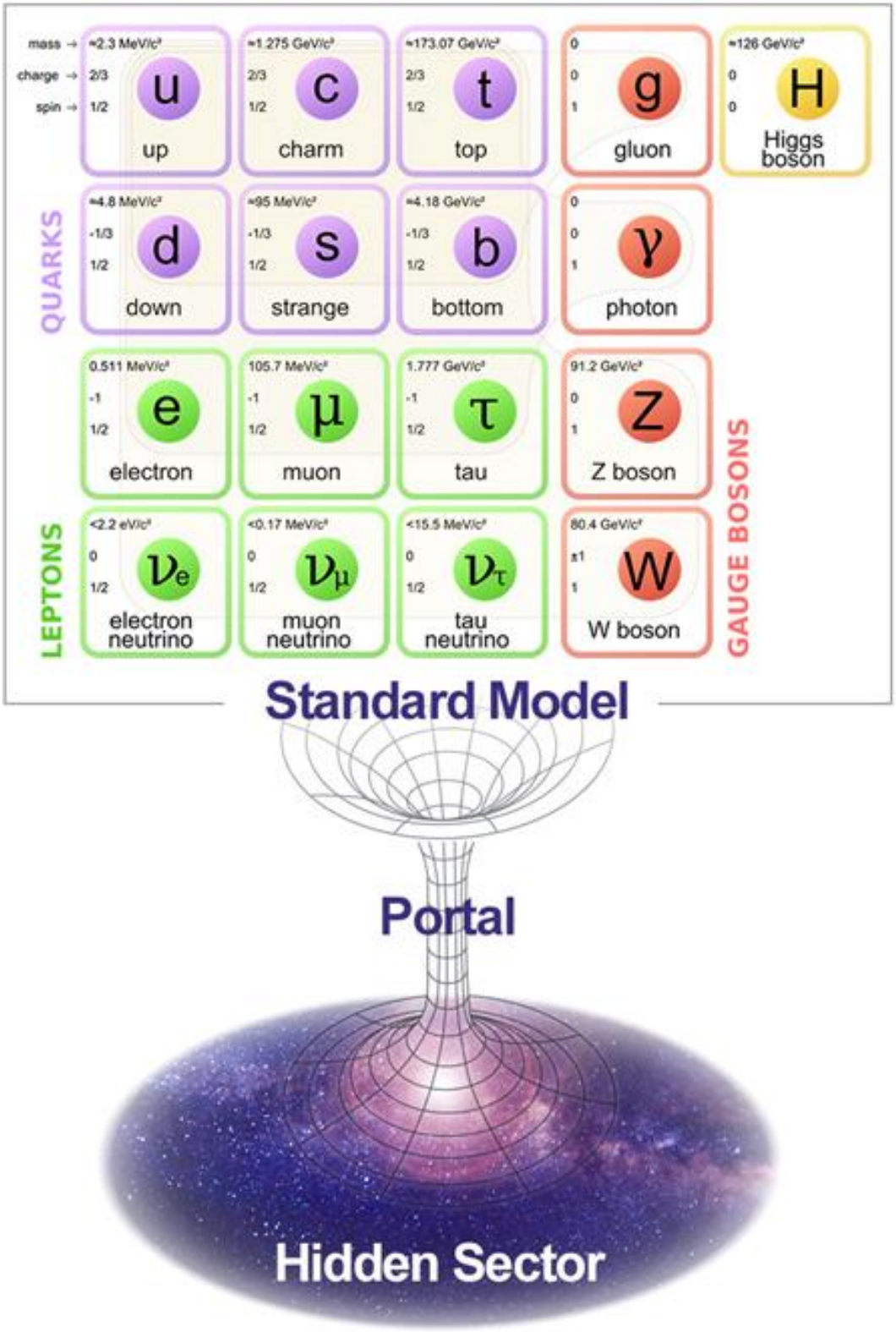

Figure 1.24: Illustration contrasting the Standard Model with the Hidden Sector. The particles of the Standard Model and the Hidden Sector could interact through "portals," which are particular coupling mechanisms such as the dark photon-photon coupling. Figure from [90].

Chapter 2

The XENON dark matter research project

This chapter presents the XENON experience in general while focusing on the current detector (XENONnT). The chapter begins with an introduction to the XENON dual-phase detectors and their operating principle, followed by a general description of the XENONnT detector. Finally, the chapter discusses the backgrounds expected for XENONnT and the projected sensitivity at the end of its lifetime.

The XENON dark matter research project, operated at the Laboratori Nazionali del Gran Sasso (LNGS) in Italy, is an underground research project that operates experiments to detect dark matter particles. To achieve this, the collaboration measures a signal from rare interactions in the form of nuclear or electronic recoils in a target volume constituted of liquid Xenon. The experiment detects the scintillation and ionization produced when particles interact in the target volume, intending to demonstrate an excess of events, which would provide the first experimental evidence of direct detection of a dark matter particle. The XENON project is currently one of the most promising experiments for the direct detection of dark matter.

The project's prototype was XENON10, a time projection chamber[1] (TPC) with 15 kg of liquid Xenon inside a passive shield[2]. It was designed to test the feasibility, the background noise rejection power, and the sensitivity of such Xenon-based experiments [92].

The research and development phase, which ended with the XENON10 TPC, involved several smaller detectors dedicated to studying many properties and characteristics of a two-phase TPC in the energy regime relevant to the direct detection of dark matter particles interacting Xenon nuclei.

The XENON10 detector was deployed underground in the Spring of 2006 and mounted in its shield in the Summer of 2006. The experiment has been operating continuously for five months, with high stability and good performance.

Using a fiducial mass of 5.4 kg, XENON10 managed to exclude previously un-

[1] See Section 2.1.2.

[2] As opposed to an active shield, which allows events to be tagged in such a way to reduce or eliminate a particular component of the background, a passive shield reduces all types of background without distinction.

explored parameter space, setting a new 90% confidence level upper limit for the WIMP-nucleon spin-independent cross-section of $8.8 \cdot 10^{-44}$ cm^2 for a WIMP mass of 100 GeV/c^2, and $4.5 \cdot 10^{-44}$cm^2 for a WIMP mass of 30 GeV/c^2 [93].
The XENON10 results and the exceptionally fast timescale in which they were obtained validated the scientific scope of a position-sensitive, homogeneous, and self-triggered liquid Xenon TPC to direct dark matter detection. New and improved liquid Xenon dark matter detectors, with a target mass on the scale of 100 kg (XENON100), were thus able to emerge afterward. Moreover, they made it possible to advance the field with a significant improvement in sensitivity over the following years.

The second detector phase, XENON100 started the first science run at the LNGS in 2009, with 165 kg of liquid Xenon, 62 kg in the target region. XENON100 exhibited a 10-fold increase in mass and a 100-fold reduction in radioactive background noise, with 50 times better sensitivity compared to XENON10 [94]. Furthermore, XENON100 was the dark matter detector with the lowest background noise in the world.
Considering the very encouraging results of XENON100, the XENON project decided to increase the target mass of Xenon by a factor of 10 to bring it up to the order of a ton.

The third detector phase, XENON1T, contained 3.2 tons of ultra-pure liquid Xenon with a fiducial volume of approximately 1.3 tons [95]. Using 278.8 days of data collection equivalent to 1 ton×year exposure, XENON1T set the most stringent limits on the spin-independent scattering cross-section of WIMPs on nucleons for nearly the complete range of dark matter particle masses above 120 MeV [96, 97, 98].
XENON1T also detected an excess of low-energy electronic recoil events above the expected background. While this excess may have come from the β decay of tritium, which was not previously included in the background model, other beyond the standard model possibilities, including solar axions and a magnetic moment of the neutrinos, have been mentioned [99]. With a trace of tritium $(6.2 \pm 2.0) \cdot 10^{-20}$ mol/mol added to the background model, the anomaly is explained with a significance of 3.2 σ, while the significances of the solar axion and neutrino magnetic moment hypotheses are decreased to 2.0 σ and 0.9 σ, respectively if an unconstrained tritium component is included in the fitting (see Figure 2.1).

The multi-tonne XENONnT detector is the next step in the evolution of the XENON project. The detector utilizes 5.9 tons of instrumented (inside the TPC) liquid Xenon [100]. The expected overall background in the detector is based on dedicated screening results of all detector materials. In contrast, improvements in mitigating intrinsic backgrounds from electronic recoil sources allow XENONnT to reduce this background compared to its predecessor. Adding a neutron veto (nVeto) around the XENONnT cryostat also allows for a significant rejection of the neutron background. XENONnT aims at achieving a 20 ton×year exposure over its lifetime.
The signal excess in Figure 2.1 can be further explored with XENONnT, allowing to study the excess in much more detail if it persists. Preliminary studies suggest

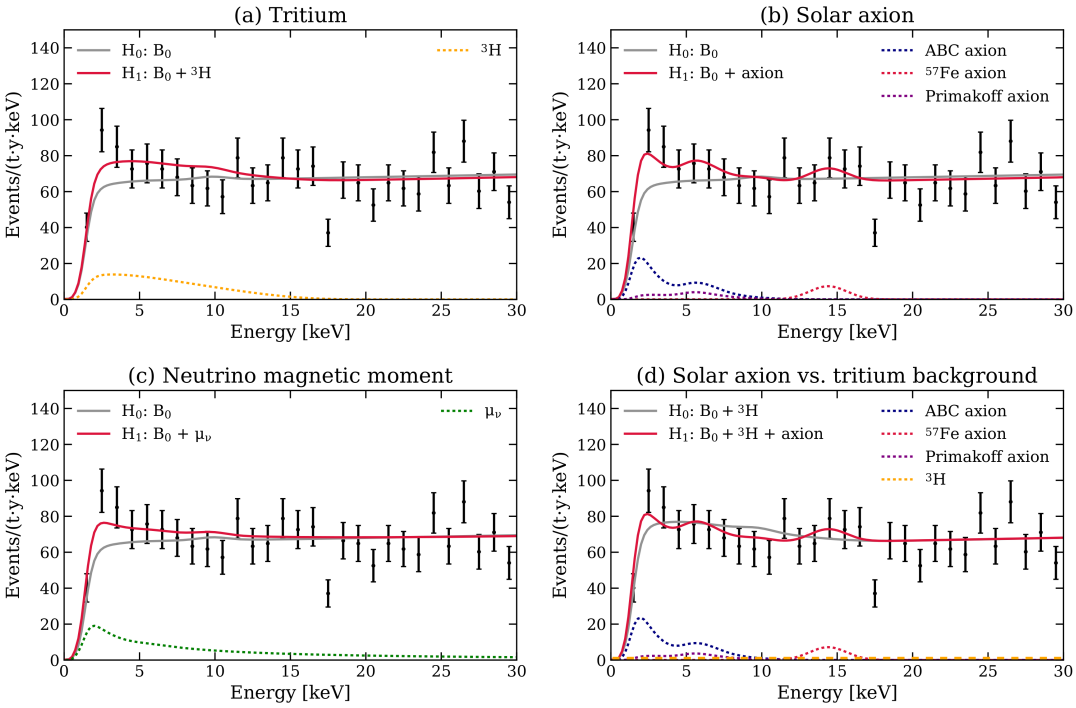

Figure 2.1: Fits to the data under various hypotheses. For the tritium (a), solar axion (b), and neutrino magnetic moment (c) searches, the null hypothesis is the background model B_0, and the alternative hypothesis is B_0 plus the respective signal. The null and alternative hypotheses in each scenario are denoted by gray (solid) and red (solid) lines, respectively. Dashed lines illustrate contributions from selected components in each alternative hypothesis. Panel (d) shows the best fits for an additional statistical test on the solar axion hypothesis, where an unconstrained tritium component is included in both null and alternative hypotheses. This tritium component contributes significantly to the null hypothesis, but its best-fit rate is negligible in the alternative hypothesis, which is illustrated by the orange dashed line in the same panel. (Figures from [99])

.

that a solar axion signal could be differentiated from a tritium background at 5 σ level after only a few months of XENONnT taking data.

The first XENONnT data excluded this excess observed by XENON1T [101].

2.1 Detection principle

2.1.1 The choice of the target

There are a variety of materials used for dark matter detection. The most common materials are semiconductors like germanium (Ge) or silicon (Si) and noble gases like Xenon (Xe) or argon (Ar). While semiconductors are very sensitive to low-mass dark matter, it is more challenging for them to reveal information about dark matter above 10 GeV. This is explained by a much smaller energy

threshold (a few eV); therefore, "the cost of the electron" is minimal. As a result, heavy dark matter particles will produce signals of several ionization electrons identical to those produced by other mechanisms considered background noise. The noble elements are excellent supports for building large, homogeneous, and self-shielded detectors in their liquid phase. Of all the noble gases, only argon and Xenon are currently used as targets for dark matter detection. Neon has been suggested to detect low-energy neutrinos and could potentially be used in the search for WIMP [102]. Liquid Xenon (LXe) and liquid argon are excellent scintillators, and good ionizers in response to the passage of radiation [103].

The idea of using liquid Xenon as a particle detection medium was first mooted in 1968 by Nobel Prize winner Luis Walter Alvarez [104] and realized by building a proportional counter[3] filled with liquid Xenon at Berkeley in 1971 [105].

Experiments aimed at detecting rare events seek to increase the probability of detecting the desired signal while reducing the background noise. In this context, liquid Xenon is more attractive as a target material for several reasons. It is a heavy medium ($A = 131$), dense ($\rho \sim 3$ g/cm^3), and a good scintillator. The high mass number provides excellent detection capabilities for spin-independent WIMP-nucleon scattering ($\sigma \propto A^2$, see Section 1.5.2 and particularly Equation (1.52)). The abundance of odd isotopes (about 50%) allows the detection of spin-dependent interactions ($\sigma \propto J(J+1)$). Moreover, the high density combined with a large Z provides self-shielding against external radiation.

Table 2.1: List of natural Xenon isotopes. Data from the *Encyclopedia of Geochemistry* [106]

Nuclide	N	Half-life [y]	Decay mode	Daughter	Natural abundance [%]
^{124}Xe	70	1.8×10^{22}	Double EC	^{124}Te	0.095
^{126}Xe	72	Stable*	None	None	0.089
^{128}Xe	74	Stable	None	None	1.910
^{129}Xe	75	Stable	None	None	26.4
^{130}Xe	76	Stable	None	None	4.017
^{131}Xe	77	Stable	None	None	21.23
^{132}Xe	78	Stable	None	None	26.91
^{134}Xe	80	Stable*	None	None	10.44
^{136}Xe	82	2.2×10^{21}	$\beta^-\beta^-$	^{136}Ba	8.86

* ^{126}Xe and ^{134}Xe are thought to be able to undergo double beta decay, but this has not yet been observed [107, 108].

Table 2.1 lists all known natural Xenon isotopes. As one can see, Xenon has virtually no long-lived, naturally abundant radioactive isotopes, except for

[3] A *proportional counter* is a particle detector that reveals particle interactions by measuring the charge produced by the ionization of molecules of a gas caused by the particle's passage. This charge is *proportional* to the energy emitted by the particle.

the two-neutrino double-beta decay[4] of ^{136}Xe and to a lesser extent the double electron capture[5] of ^{124}Xe.

2.1.2 The Dual-phase Xenon TPC

Initially, single-phase gas-filled projection chambers were developed for high-energy physics by David R. Nygren in 1974 [109]. The design was modified and applied to a single-phase liquid argon TPC by Carlo Rubbia in 1977 [110]. Over time, due to their excellent particle detection capabilities, single-phase and two-phase noble gas TPCs have been deployed throughout the direct dark matter experimental field using Xenon (ZEPLIN, LUX, XENON, PandaX) and Argon (WARP, DarkSide, MiniCLEAN, ArDM, DEAP) [53].

The XENON collaboration currently operates a two-phase time projection chamber named XENONnT, which uses a mostly liquid Xenon target with a small gaseous portion above, as shown in Figures 2.3. Two arrays of photomultiplier tubes (PMTs), one at the top of the gas phase and another at the bottom of the liquid, detect scintillation and electroluminescence light produced when particles interact in the detector. An electric field is applied vertically across the detector; a second electric field in the gas phase must be large enough to pull electrons out of the liquid phase.

When a particle interacts with Xenon, the energy deposition results in excitation (Xe^*) and ionization (Xe^+) of the Xenon atoms. Excited Xe^* atoms combine with ground-state Xe atoms to form excited dimers:

$$Xe^* + Xe \longrightarrow Xe_2^*. \tag{2.1}$$

Ionized Xe^+ atoms combine with ground-state Xe atoms to form ionized dimers:

$$Xe^+ + Xe \longrightarrow Xe_2^+. \tag{2.2}$$

The two processes occur within picoseconds [111].
Excimer desexcite by emitting a $175-178$ nm photon, within 24 ns for the singlet state and 3.1 ns for the triplet state [112]:

$$Xe_2^* \longrightarrow 2Xe + h\nu. \tag{2.3}$$

In the absence of an electric field, the ionized dimers form excited Xe atoms by capturing nearby free electrons. Then, excited atoms desexcite by releasing heat:

$$Xe_2^+ + e^- \longrightarrow Xe + Xe^{**} \tag{2.4}$$

$$Xe^{**} \longrightarrow Xe^* + \text{heat}. \tag{2.5}$$

[4]The double beta decay process ($\beta\beta2\nu$) is a mode of radioactive decay allowed by the SM. This process simultaneously transforms two neutrons into two protons by emitting anti-neutrinos. Many experiments try to highlight the double beta decay without neutrino ($\beta\beta0\nu$), which the SM prohibits; this can occur if neutrinos are Majorana particles, i.e., identical to their antiparticles, thus, there would be a non-zero probability that the two neutrinos produced would annihilate.

[5]The double electron capture is a type of radioactivity of specific isotopes. In this type of decay, two orbital electrons are captured by two protons from the nucleus to form two neutrons, with the emission of two neutrinos. Since two protons turn into two neutrons, atomic mass A remains unchanged, but the disappearance of two protons means that the atomic number Z is reduced by two, so the double electron capture has transformed the nuclide into another element.

Applying an electric field in the medium can eliminate this recombination process or at least significantly reduce it. FIGURE 2.2 illustrate the whole chain reaction.

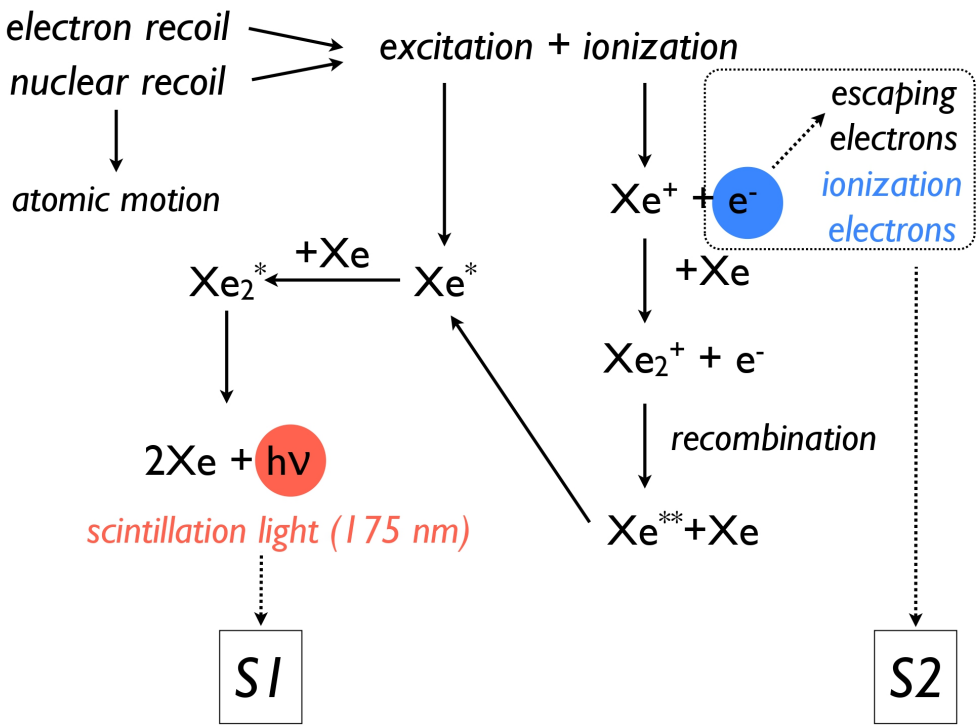

Figure 2.2: Illustration of the chain reaction following excitation or ionization of a Xenon atom in the volume target of the detector.

Particle interactions in the liquid Xenon target produce scintillation and ionization. The scintillation light signal is detected within 100 ns by the PMTs and is called *S1 signal*. The applied electric field prevents the recombination of the majority of electrons produced from the particle interaction in the TPC. These electrons are carried upwards from the liquid phase by the electric field. The electrons are then pulled out of the liquid phase by the stronger electric field applied at the liquid-gas interface. The electric field then accelerates the electrons to the point that they create a secondary proportional scintillation signal, also known as electroluminescence, as they travel through the thin layer of Xenon gas. This second signal is called the *S2 signal* [113]. The detection working principle is illustrated in FIGURE 2.3.

The detector allows a complete determination of the 3D position of the interaction. Electrons in LXe have a uniform drift velocity. This makes it possible to determine the depth at which the interaction event took place by measuring the time difference between the signals S1 and S2, noted Δt. The event's position in the XY plane can be determined by looking at the light pattern on the PMT arrays. The full 3D position allows fiducialization of the detector, in which a low background region is defined in the internal volume of the TPC. This fiducial volume has a significantly reduced background event rate compared to the

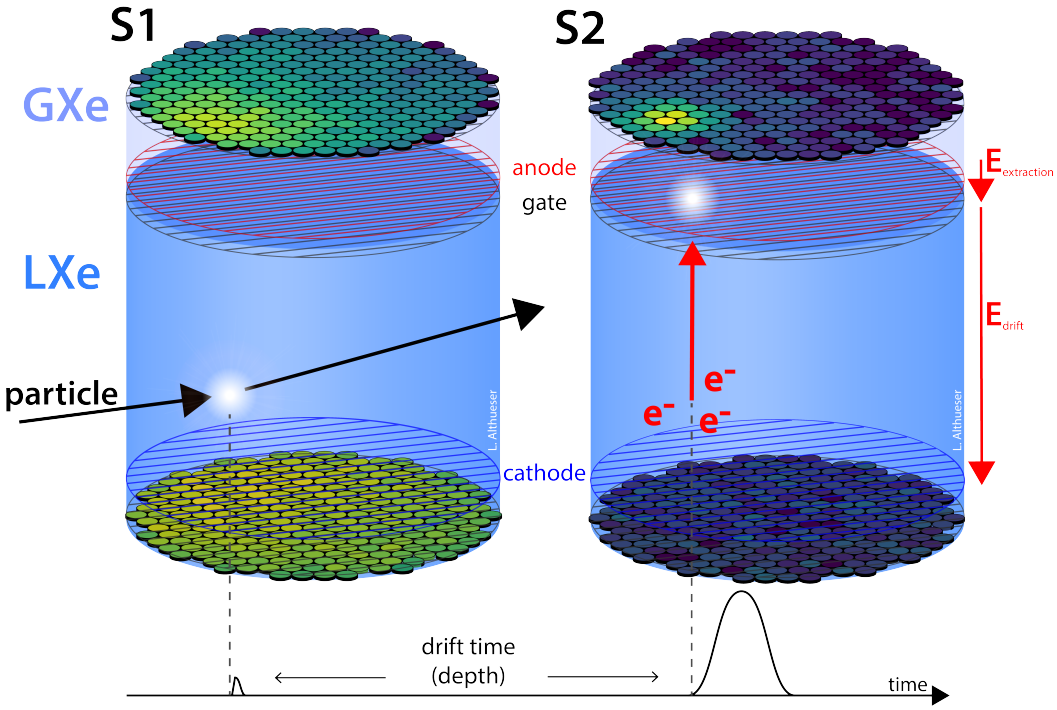

Figure 2.3: The process leading to the primary signal S1 (excitation) in the liquid part of the detector and to the signal S2 (ionization) in the gaseous part.

detector regions at the edge of the TPC due to the self-shielding properties of liquid Xenon. This allows much higher sensitivity when looking for very rare events.

Particles passing through the detector are expected to interact with the electrons of the Xenon atoms. Two types of interaction are expected; electronic recoils (ER), mostly from γ and β, but would also be expected from leptophilic or light dark matter particles, and nuclear recoils (NR), mostly from neutrons background (α, n), but also are predicted from WIMP or high mass dark matter particles. For a given amount of energy deposited by a particle in the detector, the ratio of S2/S1 can be used as a discrimination parameter to distinguish between electronic and nuclear recoil events. This ratio should be higher for electronic recoils than nuclear ones. In this way, signals from electronic recoils can be distinguished by more than 99% while retaining 50% of nuclear recoil events [113].

2.1.3 Energy reconstruction

The energy ϵ deposited by a particle is given by:

$$\epsilon = LW(N_i + N_{ex}), \tag{2.6}$$

where the quenching factor L represents the fraction of the energy lost as heat and $W = 11.5$ eV [114] (This is the most recent value and is different from the 13.8 eV [115] often considered) is the Xenon work function. These two factors

are multiplied by the total number of quanta produced (N_q), which is the sum of N_i (number ion-electron pairs) and N_{ex} (number of excitons). For electronic recoils, the fraction of energy dissipated by heat is constant with energy, in this case, $L_{ER} = 1$ [116] and W includes the heat loss. For nuclear recoils, secondary recoils emerge below the excitation threshold W, this results in an NR signal being smaller than an ER signal of the same energy.

The exciton-to-ion ratio N_{ex}/N_i is related to the excitation and ionization cross-sections of particles scattering off Xenon atoms. For ERs, it is assumed to be constant and is given a uniform prior ranging from 0.06 to 0.20 [117].

$$N_{ex}/N_i = \alpha F^{-\zeta}\left(1 - e^{-\beta\varepsilon}\right), \tag{2.7}$$

where ϵ is the reconstructed energy. α, β and ζ are tuned parameters of the model [117]. The binomial fluctuations of N_{ex} and N_i can be written as

$$\begin{aligned} N_i &\sim \mathrm{Binom}\left(N_q, \tfrac{1}{1+\langle N_{\mathrm{ex}}/N_i\rangle}\right), \\ N_{\mathrm{ex}} &= N_q - N_i. \end{aligned} \tag{2.8}$$

Ionization electrons have a probability $1 - r$ to escape the cloud of ion-electron pairs, where r is referred to as the recombination fraction,

$$\begin{aligned} N_e &\sim \mathrm{Binom}\left(N_i, 1 - r\right), \\ N_\gamma &= N_i - N_e + N_{\mathrm{ex}}, \end{aligned} \tag{2.9}$$

where N_γ and N_e are the number of photons generated by de-excitation of the initial excitons and ion-electron recombination, and of the escaping electrons, respectively. Due to detector effects, such as field non-uniformity, and intrinsic fluctuations, the recombination fraction r fluctuates, and is modeled as a Gaussian distribution,

$$r \sim \mathrm{Gauss}\left(\langle r\rangle, \Delta r\right). \tag{2.10}$$

The mean recombination fraction $\langle r\rangle$ depends on the deposited energy and the electric field, and is described by the Thomas-Imel (TI) box model [118, 119],

$$\langle r\rangle = 1 - \frac{\ln\left(1 + N_i\varsigma/4\right)}{N_i\varsigma/4}, \tag{2.11}$$

where ς is the field-dependent TI model parameter. Δr is the recombination fluctuation, parameterized as

$$\Delta r = q_2(1 - e^{-\varepsilon/q_3}), \tag{2.12}$$

where q_2 and q_3 are free parameters. The parameterization is empirically chosen to take into account both the fact that a constant recombination fluctuation is observed with deposit energy larger than 2 keV and the assumption that the recombination fluctuation diminishes as deposit energy goes to zero.

For low-energy ERs (below 10 keV), measurements indicate that the TI box model cannot fully describe the recombination process. Therefore, XENON uses a modified TI box model for the ER recombination fraction $\langle r\rangle_{\mathrm{er}}$,

$$\langle r \rangle_{er} = \left(1 - \frac{\ln(1 + N_i \varsigma_{\mathrm{er}}/4)}{(N_i \varsigma_{\mathrm{er}}/4)}\right) \Big/ \left(1 + e^{-(\varepsilon - q_0)/q_1}\right), \tag{2.13}$$

$$\varsigma_{\mathrm{er}} = \gamma_{\mathrm{er}} e^{-\varepsilon/\omega_{\mathrm{er}}} F^{-\delta_{\mathrm{er}}}, \tag{2.14}$$

where the Fermi-Dirac term in Equation (2.13) and the exponential term in Equation (2.14) were empirically added to the TI box model to account for the deviation of measurements in the < 3 keV and > 10 keV energy ranges, respectively [117]. The field dependence of the ER TI box parameter ς_{er} follows a power law as introduced in NEST (Noble Element Simulation Technique) model [120]. The free parameters q_0, q_1, γ_{er}, ω_{er}, and δ_{er} are obtained by matching the detector response model to XENON1T data (see table 2.2), without any additional constraints. The mean photon $\langle N_\gamma \rangle/\varepsilon$ and charge yields $\langle N_e \rangle/\varepsilon$ are defined as

$$\langle N_\gamma \rangle/\varepsilon = \frac{1}{W} \frac{\langle r \rangle + \langle N_{\mathrm{ex}}/N_i \rangle}{1 + \langle N_{\mathrm{ex}}/N_i \rangle}, \tag{2.15}$$

$$\langle N_e \rangle/\varepsilon = \frac{1}{W} \frac{1 - \langle r \rangle}{1 + \langle N_{\mathrm{ex}}/N_i \rangle}. \tag{2.16}$$

Table 2.2: Main nuisance parameters in the detector response model of XENON1T. Lower and upper errors of the posterior are calculated as the difference between the median and the 15.4% and 84.6% percentiles of the posterior. (Values from [117]).

Parameter	Prior	Posterior
$\langle N_{\mathrm{ex}}/N_i \rangle$	0.06 - 0.20	$0.15^{+0.04}_{-0.06}$
α	1.240±0.079	1.280±0.063
β	239±28	273^{+24}_{-20}
ζ	0.047±0.009	$0.045^{+0.009}_{-0.008}$
q_0 [keV]	free	$1.13^{+0.24}_{-0.32}$
q_1 [keV]	free	$0.47^{+0.18}_{-0.15}$
q_2	free	0.034±0.003
q_3 [keV]	free	$1.7^{+1.3}_{-1.1}$
γ_{er}	free	0.124±0.003
ω_{er}	free	31±4
δ	0.062±0.006	0.061±0.006

The quantities directly measurable in the detector are the de-excitation photons N_γ of all the excitons formed and the electrons which escape recombination N_e:

$$N_\gamma = N_{ex} + rN_i \tag{2.17}$$

$$= \left(\alpha F^{-\zeta}(1 - e^{-\beta\varepsilon}) + r\right) N_i \tag{2.18}$$

$$N_e = (1 - r)N_i. \tag{2.19}$$

which leads to a detected S1 and S2 signals given by:

$$S1 = g_1 N_\gamma \tag{2.20}$$
$$S2 = g_2 N_e, \tag{2.21}$$

where the signals S1 and S2 are measured in units of PhotoElectrons (PE), the number of electrons generated, multiplied, and collected by a photo-detector, initially induced by a photon.
The S1 and S2 signals are corrected for geometric effects in the detector and for the finite lifetime of the electrons in LXe. The efficiencies g_1 and g_2 are the gains of the signals S1 and S2. For S1 photons, g_1 is the product of the geometric light collection efficiency (LCE) and the average quantum efficiency of the PMT. For S2 photons, g_2 depends on the efficiency of the electroluminescence photons ϵ, the efficiency with which the electrons are extracted from the liquid to the gas phase, and the average pulse size of a single extracted electron (SE).

Figures 2.4 gives the values obtained from calibrations (see Section 2.2.10) of $g1$ and $g2$ parameters.

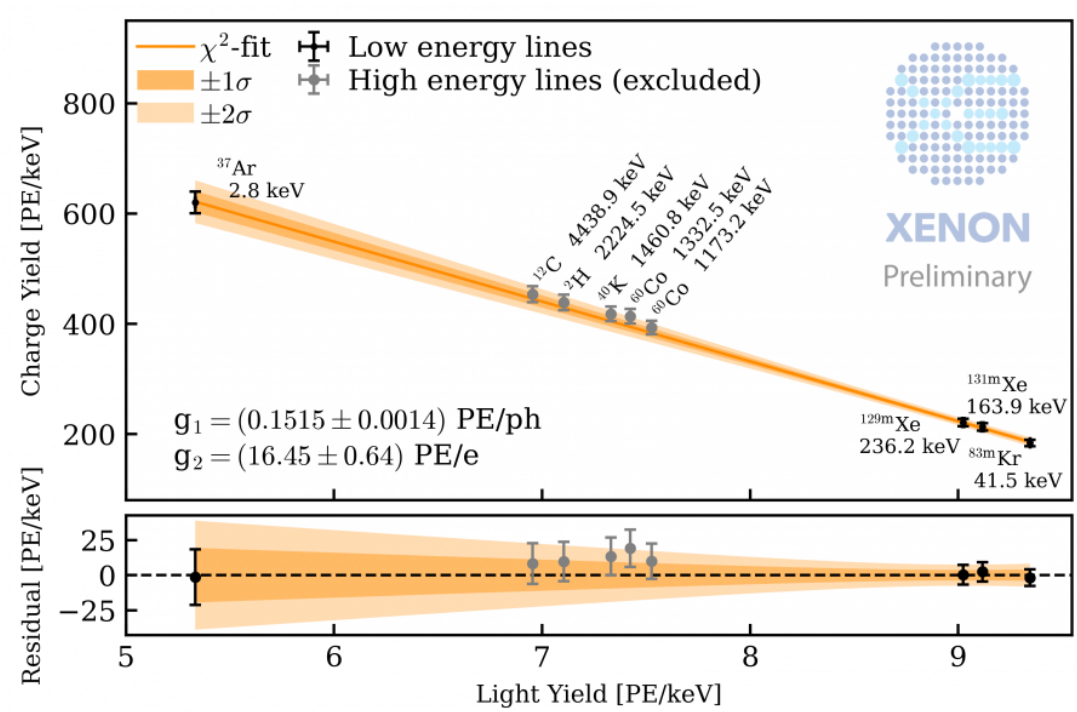

Figure 2.4: Calculation of g_1 and g_2 in XENONnT. This was performed using multiple mono-energetic lines with known energies to extract the best fit for the value of the gains (g_1,g_2) by making a "Doke plot", a plot in charge yield and light yield space. Different energy or different eclectic field are expected to have different charge yield and light yield, but these points will only move along the line as the total quanta number is fixed.

2.2 XENONnT

The XENONnT main detector is a cylindrical TPC, 148 cm long and 137 cm in diameter, placed inside a cryostat filled with 8.3 tons of liquid Xenon distributed in two concentric cylinders, as depicted in Figures 2.5. The sensitive interior volume contains (the TPC itself) 5.9 tons of Xenon and is separated from the exterior volume by a PTFE cage (polytetrafluoroethylene or Teflon). The PTFE cage has surfaces treated with diamond tools to act as a reflector for Xenon UV light. The outer volume acts as an active veto, reducing the number of interactions in the inner volume and allowing multiple scattering events to be identified. This reduces the amount of data collected and improves the ability to reject gamma events as dark matter candidates [100].

A stainless steel *diving bell* is used to maintain a stable liquid-gas interface between the grid electrodes and the anode. An electric field is established between the negatively charged cathode at the bottom of the TPC and the gate electrode at the top; it is used to draw ionization electrons away from the interaction site, pushing them to the liquid-gas interface. A second field is generated between the grid and the positively polarized anode. It makes it possible to extract the electrons from the liquid phase and provide sufficient energy to excite and ionize the gas atoms. See Section 2.2.4 for more details about the electric field configuration.

Like many experiments looking for rare events, one of the leading design goals was to reduce the background event rate to ensure that the detector was not overwhelmed by an unwanted signal. The underground location of 1400 m of rock (3600 water equivalent) below the highest peak of the Gran Sasso mountain chain protects from cosmic radiation (see Figure 2.6). Moreover, the detector is also located inside a water tank to reduce parasitic events further. Careful material analyses were conducted before the detector was assembled to establish a low background noise environment.

In the following sections, the different parts and processes of the XENONnT experiment will be presented starting from the outward (muon and neutron vetoes) towards the innards (TPC, calibrations, and analyses).

2.2.1 The muon veto

Secondary particles produced by cosmic rays can cause contamination for low background experiments, such as XENONnT. For this reason, such experiments must be built where most of these particles cannot penetrate. Only high-energy particles, such as muons or neutrinos, and weakly interacting particles, such as dark matter, can pass through several kilometers of rock. Although muons differ from dark matter in their electrical charge, they can also produce neutrons through spallation, which mimic dark matter signals. Therefore, it is crucial to identify muons and reject their associated signals correctly; This is the main task of the muon veto system.

The muon veto exploits the particularity of muons to induce Cherenkov radi-

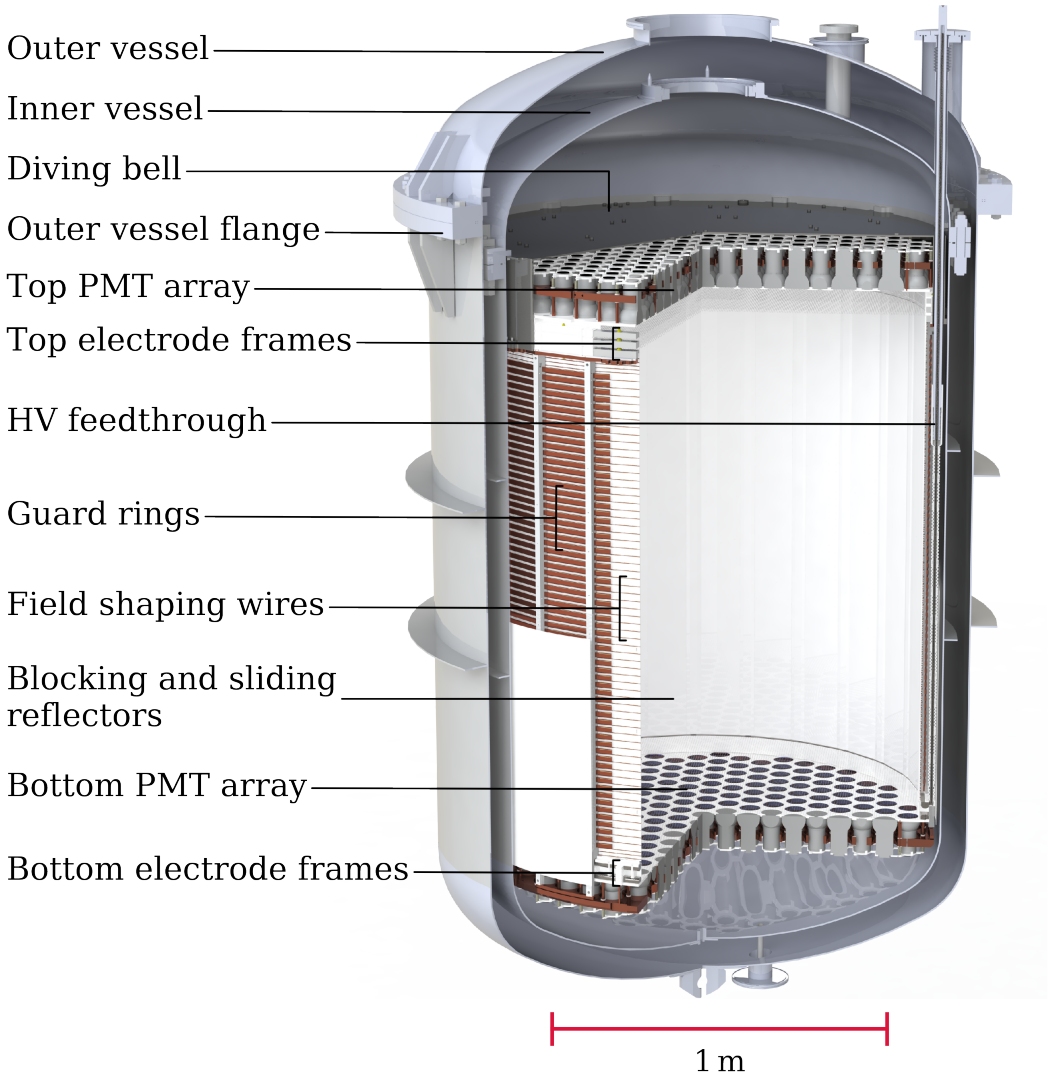

Figure 2.5: Illustration of the XENONnT cryostat and TPC

ation[6]. The Muon Veto consists of a large cylindrical Gadolinium-loaded water tank 10.2 m high and 9.6 m in diameter (see Section 2.2.2 for a discussion on the Gadolinium purpose). Approximately 4 m of water surround the cryostat where lies the TPC, providing an additional passive shield against environmental radioactivity and achieving a factor of 100 in background noise suppression [100]. The water tank is equipped with 84 waterproof Hamamatsu R5912ASSY 8-inch PMTs (see Figure 2.7). Before the PMTs were mounted, they were subjected to high pressure and water testing to simulate water tank conditions. Also, their most important properties (radiant sensitivity, quantum efficiency, etc.) were

[6]Named after the 1958 Nobel Prize in Physics who deciphered its origin [121], Cherenkov light results from the shock wave produced by an electrically charged particle moving through a transparent medium (other than vacuum) at speed greater than that of light in that medium. The light is then emitted inside a cone whose opening depends on the medium index and the particle velocity.

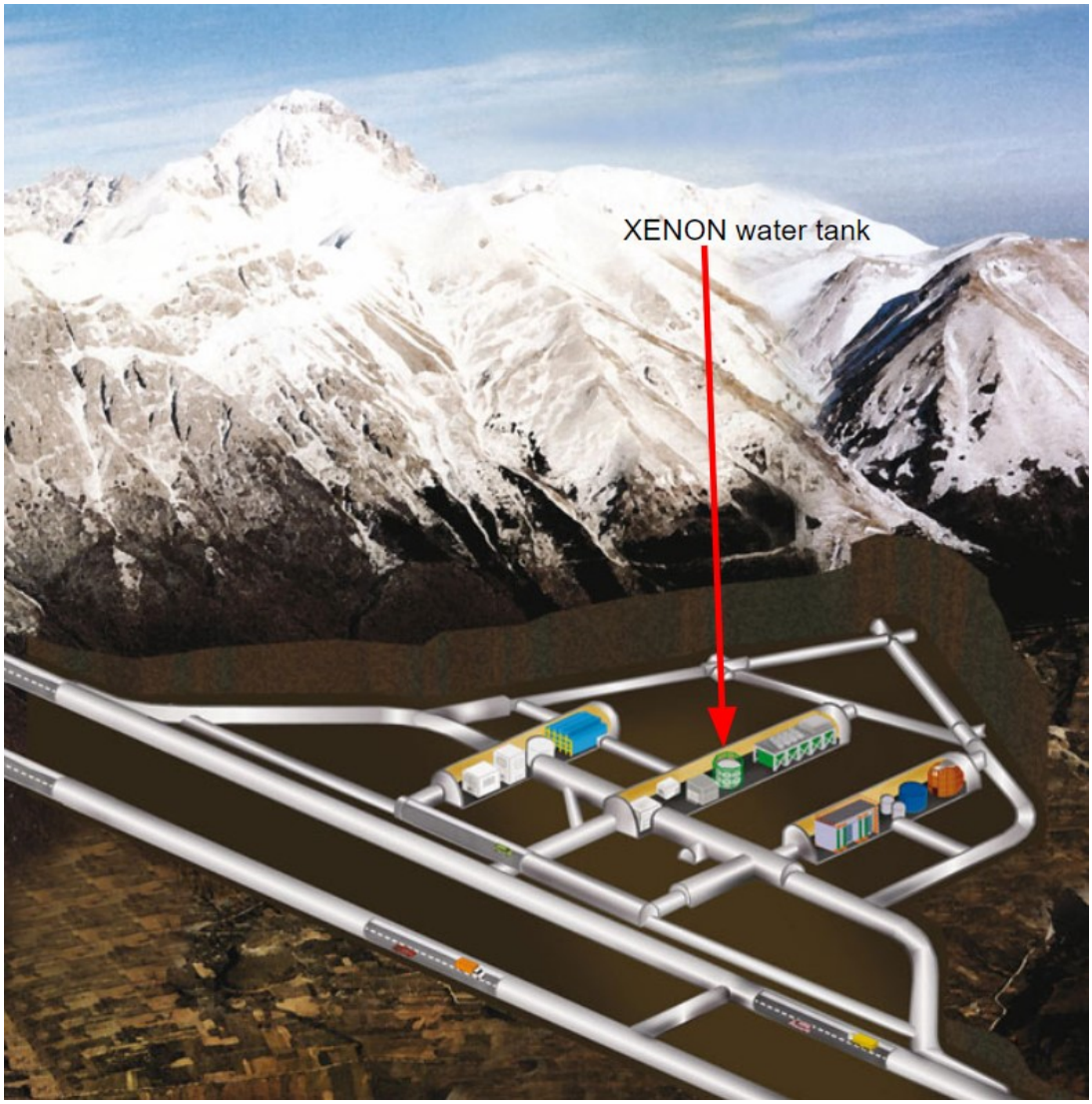

Figure 2.6: The location of the XENON experiment within the LNGS.

measured and classified into different configurations in such a way as to distribute them in the water tank according to these configurations.
The inner part of the water tank is covered with a reflective sheet which, with a reflectivity of 99%, keeps photons inside the reservoir until they reach the PMTs [100].
Thanks (in part) to the muon veto, XENON1T had the lowest background level ever reached in dark matter LXe experiments [99]. This level has been further reduced in XENONnT by improving the purity of the Xenon and adding a neutron veto.

2.2.2 The neutron veto

The XENONnT neutron veto aims to reduce the background of radiogenic neutrons by marking events where the interaction in the TPC coincides with a detected neutron in the neutron vetoes. 120 Hamamatsu R5912-100-10 8-inch

PMTs with high quantum efficiency (approximately 40% at 350 nm) and low radioactivity are placed with reflective panels around the cryostat. The side panels of the neutron veto form an octagonal enclosure of about two meters by three. The PMTs are spread over six equidistant rows. Most of the PMT bodies remain behind the reflective panels to minimize the remaining radioactive background of their materials inside the neutron veto. All reflective surfaces are 1.5 mm thick expanded PTFE (ePTFE), which has light reflectivity greater than 99% for wavelengths above 280 nm [100].

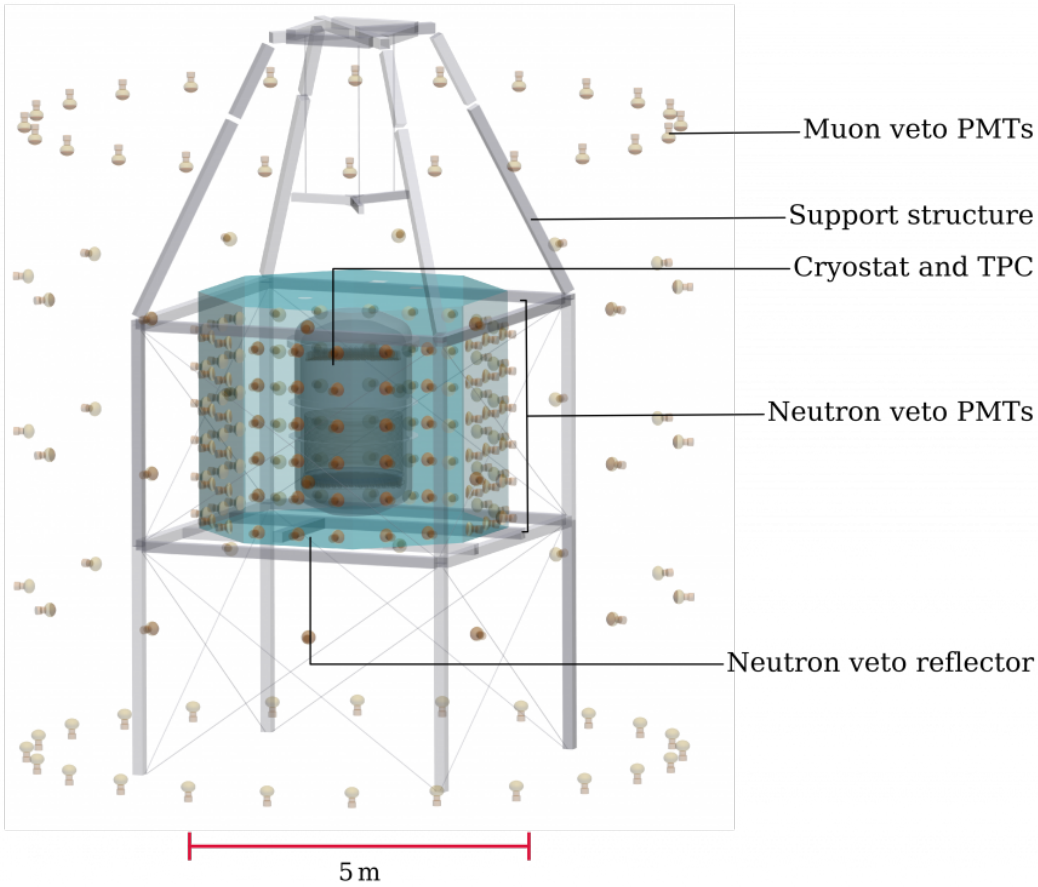

Figure 2.7: Geant4 rendering of the three nested detectors, including muon and neutron veto. The water tank walls, which support the muon veto PMTs, the neutron veto support structure, and other components (e.g. calibration systems) are omitted for clarity. Reflector panels, which optically separate the neutron and muon vetos, are shown as transparent turquoise surfaces.

Neutrons that interact within the volume of the TPC can easily pass through the cryostat and evade further detection in LXe. To increase the probability of neutron detection via neutron capture, the muon veto water tank is loaded with 0.2% of Gadolinium sulfate octahydrate. Therefore, the water around the cryostat moderates neutrons leaving the TPC volume, typically traveling less than 20 cm before being thermalized and captured by the Gadolinium with a probability of 91% (9% for water) [100]. Following neutron capture by Gadolinium, a cascade

of gamma rays with a total energy of about 8 MeV is generated. In the case of capture by water, a single gamma of 2.2 MeV is emitted. The energy deposited by gammas in water, mainly by Compton scattering, is converted into electrons and, ultimately Cherenkov photons. A schematic of this reaction is shown in Figure 2.8.

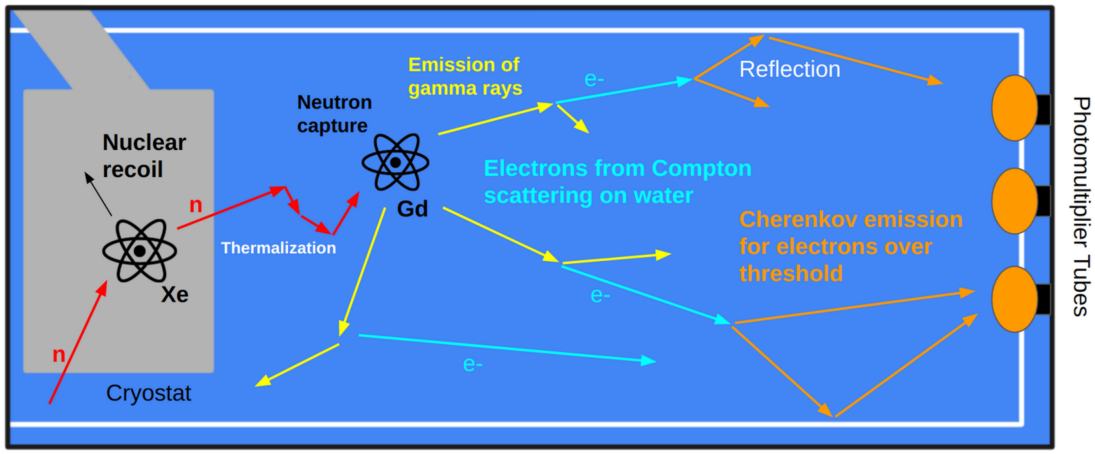

Figure 2.8: Detection principle of radiogenic neutrons captured in XENONnT neutrons veto.

The photons in the neutron veto volume can reflect several times before hitting a photosensor. For this reason, the light collection efficiency is mainly independent of the geometric arrangement of PMTs or their distance from the cryostat but mainly relies on the total photosensitive surface and, therefore, on the number of PMTs. To maximize the LCE, the outer vessel of the cryostat is also lined with ePTFE [100].

2.2.3 Photomultiplier tubes

Photomultiplier tubes are extremely sensitive light detectors that can multiply the current produced by incident light by a factor of millions. This very high gain makes it possible to measure the faintest light sources, down to individual photons.

In XENONnT light detection is based on low-radioactivity Hamamatsu R11410-21 PMTs of 76.2 mm in diameter with a quantum efficiency of 34% [122], mounted in copper blocks. The PMTs have been distributed in the top (253 PMTs) and bottom (241 PMTs) arrays primarily based on their quantum efficiency to ensure that the best-performing PMTs are located in the center of the bottom array, where most of the scintillation light is collected. They are packed as tightly as possible to maximize scintillation light collection efficiency [100].

Before instrumenting the detector with the PMTs, each PMT had to be carefully characterized by measuring its single photoelectron peak, gain, and afterpulse rate (as will be discussed bellow). Some properties like the linearity of the response and photocathode uniformity are expected for most PMTs. In addition, regular calibrations are made using a LED lighting system with four individual

channels. The light shining through the LED is collected by the PMTs, whose output signals are then amplified and digitized with fast analog-to-digital converters.

PMT gains are calibrated once a week by stimulating the emission of photoelectrons using low-intensity light pulses from a blue LED. Figure 2.9 presents the calibration performed on the XENONnT's PMTs, where it is interesting to emphasize the gain stability (fluctuation within +/- 1%).

The operation of a PMT is generally divided into two regimes:

1. Photon counting, where the rate of detected photons is low compared to the time resolution of the detector so that the individual photoelectron pulses do not overlap.
2. Signal integration, for light sources of higher intensities where the individual photoelectron signals cannot be distinguished.

In the second case, to enable waveform discrimination, it is essential to obtain an accurate estimate of the total number of photoelectrons generated and the relative standard deviation of the distribution of single photoelectrons, given the fact that they are the dominant contributors to signal resolution. The response of PMTs is therefore calibrated for the mean of the charge distribution corresponding to a single photoelectron (SPE). Knowledge of the SPE response of the PMT is also necessary to combine the output signals of several different PMTs operating at different gains [123].

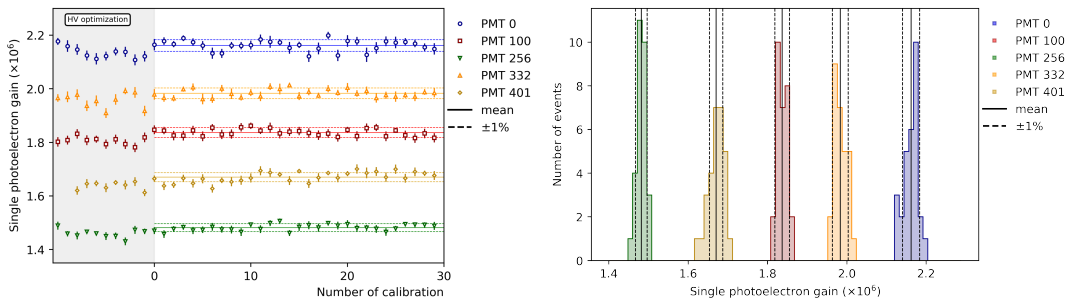

Figure 2.9: (Left) SPE gain of XENONnT as a function of the calibration number. (Right) Single PE gain distribution for 5 random PMTs. The solid line shows the mean, and dashed lines show the +/- 1%.

For a reliable single photoelectron spectrum, the multiple photoelectron events component must be reduced as much as possible. A suitable data with such conditions is LED calibration data with low-intensity illumination. The SPE resolution measurement is shown in Figure 2.10.

PMT afterpulses

Afterpulses are any PMT pulse created inside a PMT and is delayed in time compared to the initial/main pulse that created it. Most commonly, afterpulses are created by ion feedback: residual gases inside the tube vacuum can get ionized by a photoelectron of the initial pulse. Due to the ions' positive charge, they are accelerated backward to the photocathode and, upon impact, cause the

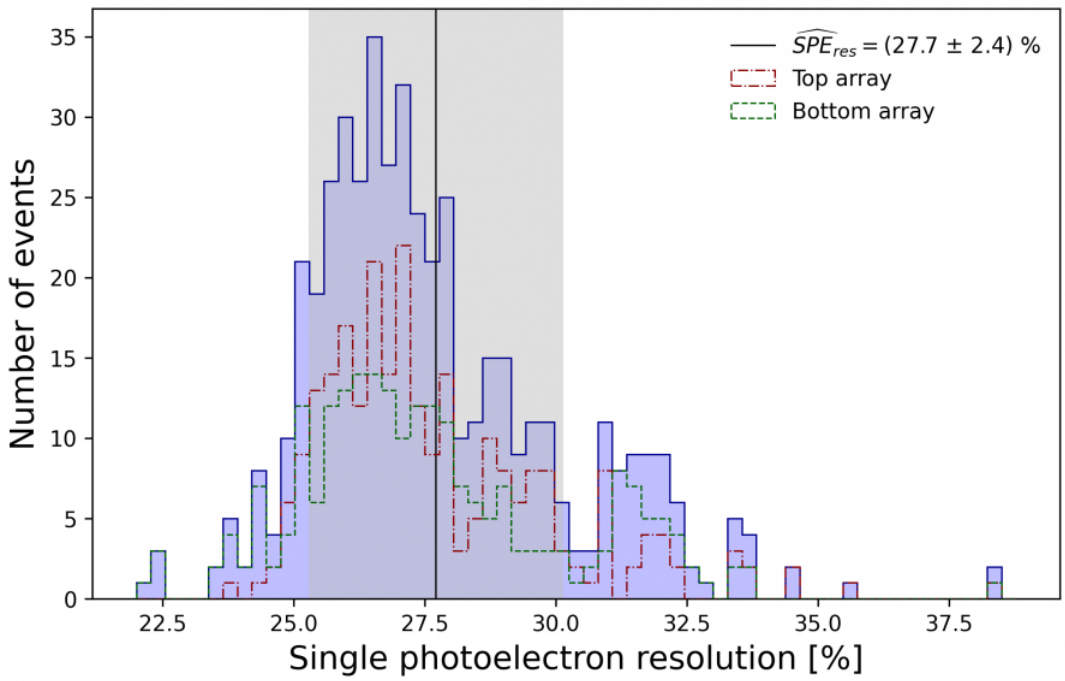

Figure 2.10: SPE resolution defined as σ_{1PE}/μ_{1PE} for the two PMT arrays (top and bottom) + total. The mean and the standard deviation come from the fitting of the SPE spectrum, with very low illumination LED data calibration. The solid black line shows the average SPE resolution.

delayed emission of photoelectrons, forming the afterpulse. Therefore, the delay time of an afterpulse is specific to the mass-to-charge ratio of the ion that created it and depends on the PMT bias voltage. An example of a typical afterpulse delay time spectrum is shown in Figure 2.11, and different contributions are indicated.

2.2.4 Electric field configuration

For large detectors, even a moderate field in the drift region of 100 V/cm results in a significant potential difference between the cathode and the anode. Therefore, a high-voltage source, high-voltage cable, and feedthrough are required to operate these detectors. In these components and certain regions inside the detector, the electric field can be much higher than the drift field in the active region or the amplification field in the gas region. For this reason and to ensure the uniformity of the field inside the active volume of XENONnT, 71 copper field-shaping rings are placed behind the PTFE panels, as illustrated in Figure 2.12. The rings are separated vertically by 15 mm, and the grid-cathode voltage is uniformly graduated via a resistor chain [100].

The drift field is generated using a gate electrode slightly below the liquid-gas interface and a cathode at the bottom of the TPC, as shown in Figure 2.12. The active region is demarcated by these two electrodes, separated by 148.5 cm at operating temperature. The anode is located 8 mm above the gate to create the extraction region kept at a high electric field (around 10 ~ 10 kV/cm) to extract

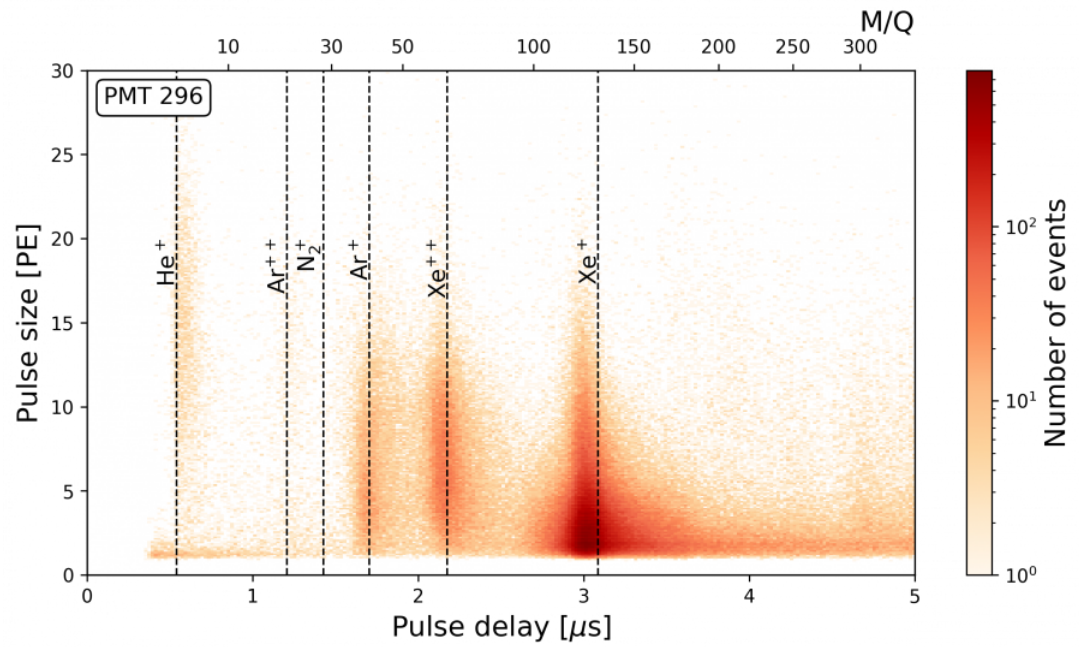

Figure 2.11: Afterpulse spectrum of PMT 296, which has the largest Xenon afterpulse rate of all XENONnT PMTs of about 2.5%. The vertical lines indicate the calculated (theoretical) ion delay time and mass-to-charge ratio.

electrons from the LXe and the Xenon gas to produce the S2 signal. In addition to the anode, gate, and cathode electrodes, the TPC has two screening electrodes positioned directly below (above) the top (bottom) PMT array to protect the PMTs from the field produced by the anode or the cathode. [100].

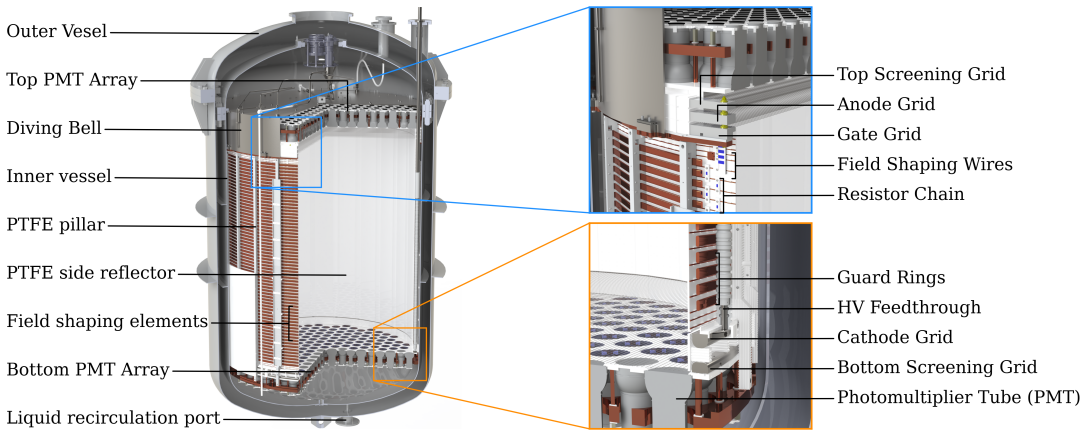

Figure 2.12: Illustration of the TPC, with LXe/GXe piping included. Includes zoom into the top and bottom grid regions.

The electrodes consist of parallel stainless steel wires, 216 μm-thick, except for the cathode (304 μm), stretched onto stainless steel rings. The top electrodes (top screening, anode, gate) have a pitch of 5 mm, while the bottom electrodes (cathode, bottom screening) have a pitch of 7.5 mm. The gate and anode have two and four additional 304 μm-thick wires, respectively, running perpendicu-

larly to all other wires. These perpendicular wires are added to counteract the deformation of the electrode plane under electrostatic forces [100].
Despite the successful testing of the electrodes and their successful performance before the start of data taking, the strength of the drift electric field was limited to 18.3 V/cm during the first scientific run (SR0). This limited value is presumably due to light production from the gate and anode grids. A detailed discussion on the electrodes and the problems they create in XENONnT is presented in Section 3.4.1

In the regions subjected to an electric field, more important emissions are observed that are not correlated with interactions. The exact mechanisms leading to these emissions are not fully known. Nevertheless, the standard hypothesis is that the presence of positive ions and other impurities in the detector would be the primary origin of those emissions. In this context, for XENONnT, particular attention has been paid to the purity of Xenon, so much so that XENONnT is currently the purest LXe dark matter detector in the world [124].

In addition to photoionization, a source suspected of being at the origin of part of the single electron signals is the spontaneous emission of electrons by the electrodes. To reduce this emission, XENONnT has used a passivation technique that consists of treating the electrodes (as well as field shaping ring) with acid solutions, the purpose of which is to microscopically smooth the surface and thus eliminate as much as possible the regions where the potential necessary to extract electrons is low. Figure 2.13 shows the treatment of pieces of the shaping rings with a 1% citric acid bath.

2.2.5 Cryogenics and purification systems

XENONnT uses a system of Pulse Tube Refrigerator cryocoolers to maintain Xenon in the liquid phase in the detector with high-temperature stability. The TPC is placed inside a cryostat, which, coupled with the cooling system, makes it possible to liquefy the Xenon at a temperature of −96 °C.
An emergency storage system (ReStoX) allows one to recover the Xenon in a few hours in case of failure of the cryogenic system.
The cooling power of the pulse tube refrigerator is delivered to the Xenon through a cold finger at the top of the cooling tower. There, the Xe liquefies on the cold finger fins, drips, and is collected by a funnel before flowing into the LXe chamber, located below the cooling tower. An insulation void surrounds the entire system to minimize heat leakage [125].

Maintaining a long electron lifetime is essential for proper detector operation. Therefore, the TPC has strict requirements on the purity of Xenon since electronegative impurities, such as Oxygen, Nitrogen, and water, can absorb scintillation light and trap drift charges, thereby reducing the apparent amplitude of the S1 and S2 signals. Small amounts of these impurities are present in commercial Xenon. Impurities can also be introduced by air leaks or by the outgassing of materials inside the detector. Therefore, it is necessary to constantly clean the Xenon during the detector's operation.
If the electron lifetime is too low, the energy resolution faints. For XENONnT,

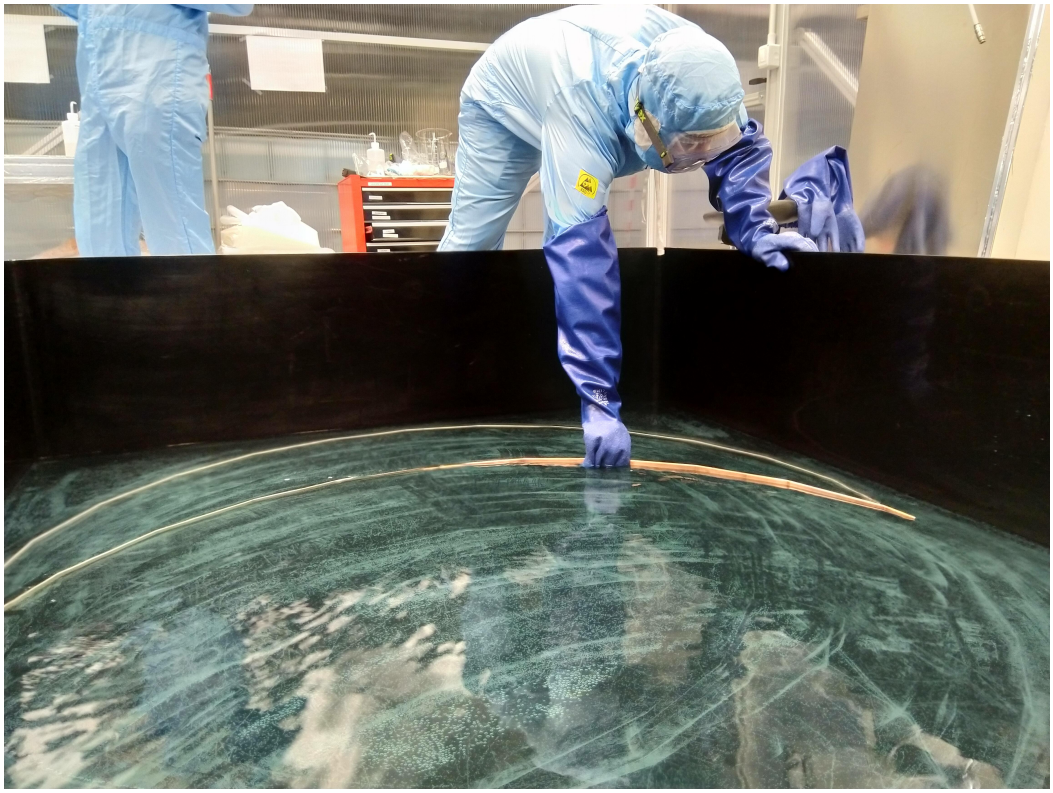

Figure 2.13: Photo showing me treating pieces of shaping rings with a nitric acid bath.

with a drift length of 1.5 m, a liquid purification system was added to the existing gaseous purification system to achieve an even better electron lifetime than XENON1T.
FIGURE 2.14 illustrates the performance of the XENONnT purification system. Thus, the electrons' lifetime has reached a few ms after only about ten days of purification during commissioning. Now, in science data, we have more than 15 ms; this is about 20 times better than XENON1T (~ 0.660 ms) and is the highest ever measured in a LXe detector [124].

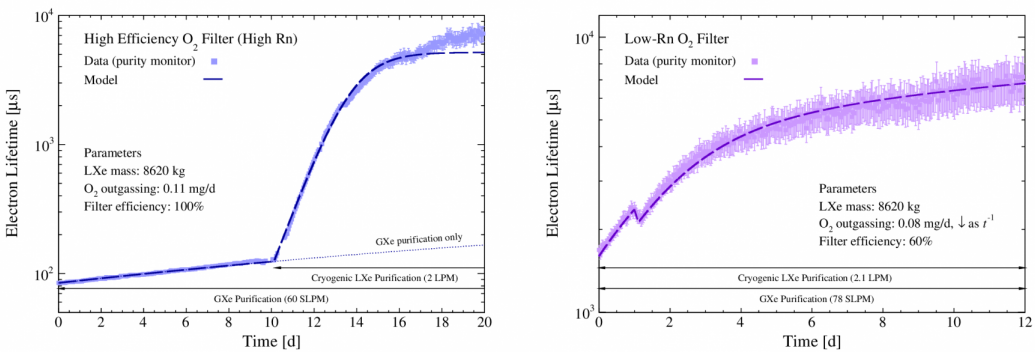

Figure 2.14: (Left) Electron lifetime improvement after the start of cryogenic LXe purification with the high-efficiency O_2 filter. (Right) Electron lifetime improvement after switching to cryogenic LXe purification with the low-Rn O_2 filter.

Xenon circulation occurs in the gas phase, and its purification occurs in the gas and liquid phase. There are two purification channels: one consists of Xenon liquefied in the detector, evaporated at its exit, purified in the gas phase, and recondensed in the detector, and the other consists of LXe constantly circulating through a liquid purification system. Four high-capacity magnetic pumps drive the circulation.

2.2.6 Slow control

The various XENONnT subsystems and their instruments are operated and their status monitored and recorded by a slow-speed control system that is based on General Electric (GE) standard process control hardware and software: Programmable Automation Controllers (PACs) for the hardware and CIMPLICITY SCADA (Supervisory Control And Data Acquisition) for the software [95]. Figure 2.15 presents a diagram illustrating the various subsystems and their interconnections. In the event of an alarm (e.g., parameter out of range, equipment failure, loss of connection, etc.), the persons in charge are notified by e-mail and mobile phone SMS. Nearly 2500 parameters are stored in the GE Proficy Historian database, which offline analysis programs can query via a custom-developed web interface. The Alarm Notification, Slow Monitor Viewer, and Offline Scan Tool have been custom developed by XENON to complement GE's facilities.

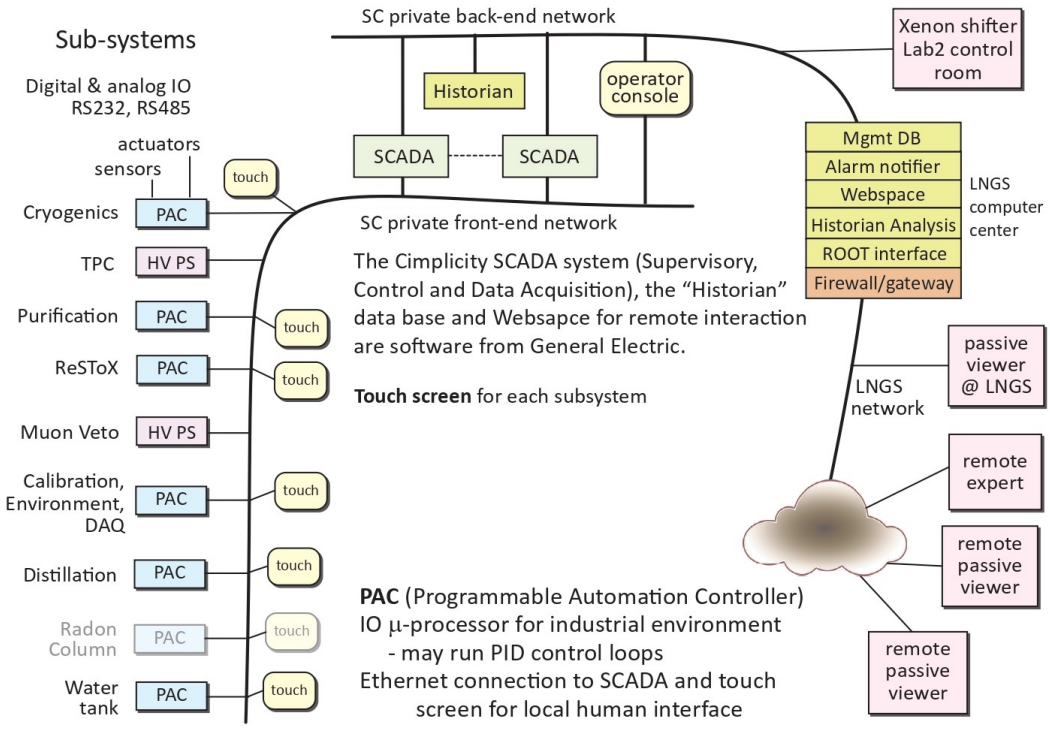

Figure 2.15: Slow Control block diagram.

The actuators and sensors of the cryogenics, LXe purification, LXe storage, Kr distillation, and water purification systems are controlled via individual

PACs connected to a private front-end network. The high voltage power supplies, the acquisition system, and the motor controllers of the calibration system are integrated into the slow control system via standard OPC (Open Platform Communication) servers, the Modbus protocol, or Web services. PAC-level exceptions are communicated to the alarm system using the GE Alarm and Event Express tool. Local operation via touch screens is also possible in case of the unavailability of the SCADA system. However, potentially dangerous operations are further protected by requiring specific conditions to be met before the operation can be performed.

All supervision and data storage elements, such as the database, the alarm system, the slow control viewer, and the underground central control room, are connected to the main private network. Two redundant SCADA servers in active-passive failover mode connect to the PAC and OPC servers on the private front-end network. Two dedicated, redundant fiber links connect the underground detector to the surface laboratory. In the event of a laboratory network failure, the slow control system is directly connected to a backup network outside the LNGS. For safety reasons, the entire slow control system is powered by a dedicated uninterruptible power supply with extended battery life and a backup generator. A firewall protects the system, and only authorized users can perform operations beyond data access, according to their predefined role.

2.2.7 Data acquisition

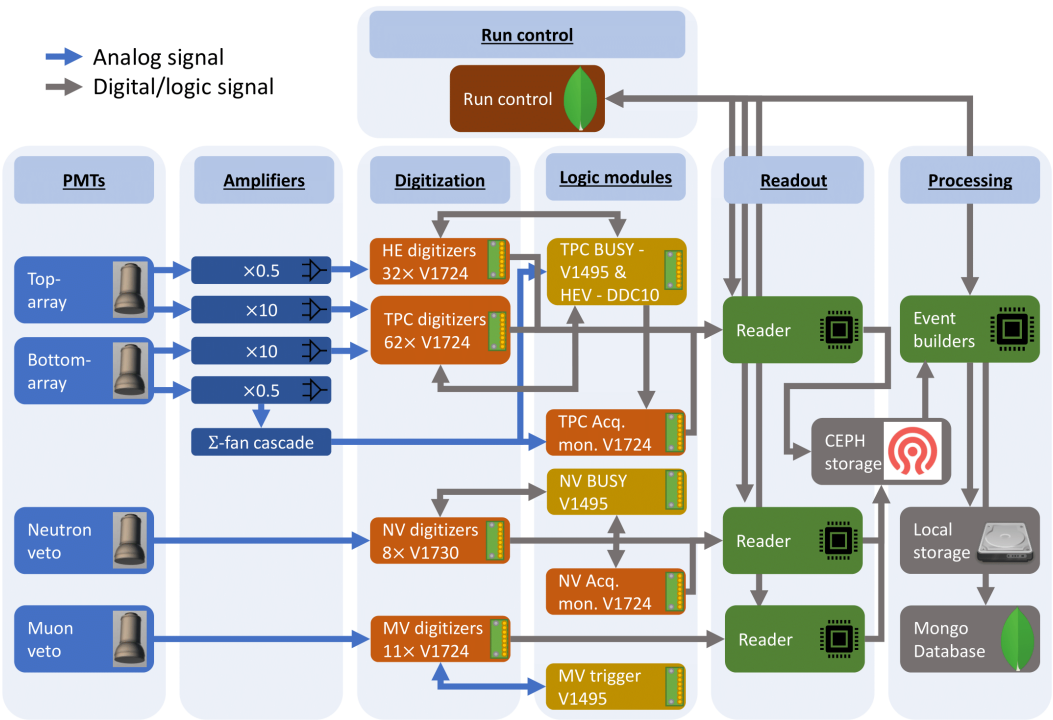

Figure 2.16: XENONnT DAQ diagram.

The Data Acquisition (DAQ) system is responsible for digitizing the signals

from each PMT and identifying and recording each interaction inside the detector. The DAQ is designed around a triggerless readout paradigm. The data is continuously acquired without a global trigger, and the physical interactions are subsequently identified through the software ("Event Building"). Triggerless acquisition allows for the lowest possible energy threshold but requires custom readout logic to provide an independent readout of each detector channel while maintaining full-time synchronization. The system is centered around a MongoDB database, which offers fast data storage, sorting, and retrieval. A software event builder polls this database asynchronously to identify interactions and write them to files. Files are transferred to external sites and processed in a new format for analysis by XENONnT's computer system. During regular operation, the event generator runs a few minutes after the acquisition but can be delayed for hours or days if disturbances further down the pipeline occur [126]. A schematic of the DAQ is shown in Figure 2.16.

2.2.8 Data transfer

XENON data is too large to be stored at a single site, so it must be distributed over a storage grid with multiple locations worldwide (UChicago, NIKHEF, CNAF, CCIN2P3, Weizmann, and many others). Therefore the data coming from the detector are transferred as soon as they are acquired from the DAQ to the grid to ensure a smooth data acquisition by avoiding creating a bottleneck on the DAQ buffer disks of limited size.

Admix (Advanced Data Management in XENON) is the data management and transfer software. Essentially, it uploads the new dataset to the grid and creates the relevant replication rules to move the data where it needs to be. Then, once the data has been transmitted, Admix updates the run database indicating that the data has been successfully transferred. Finally, it cleans the Event Builder disks (located underground on the DAQ system) and the Data Manager disk (located above ground in the LNGS).

2.2.9 Data processing

The reconstruction of events in XENONnT makes it possible, from the detection of the signals S1 and S2, to determine all the information necessary for searching for events corresponding to the desired interaction. For example, reconstructions of position, type of recoil, and deposited energy.

Signal classification

S1 and S2 classification are relatively trivial at high energies, given that S1 and S2 have very distinctive shapes (see Figure 2.17). At low energy, however, S1 and S2 classification becomes more complex owing to the effects of single-electrons, accidental coincidences, afterpulsing, and noise.
On the other hand, signal classification is an essential focus of analysis efforts. The effect of misclassified signals is most prevalent in the set of cuts necessary to remove mis-reconstructed events.

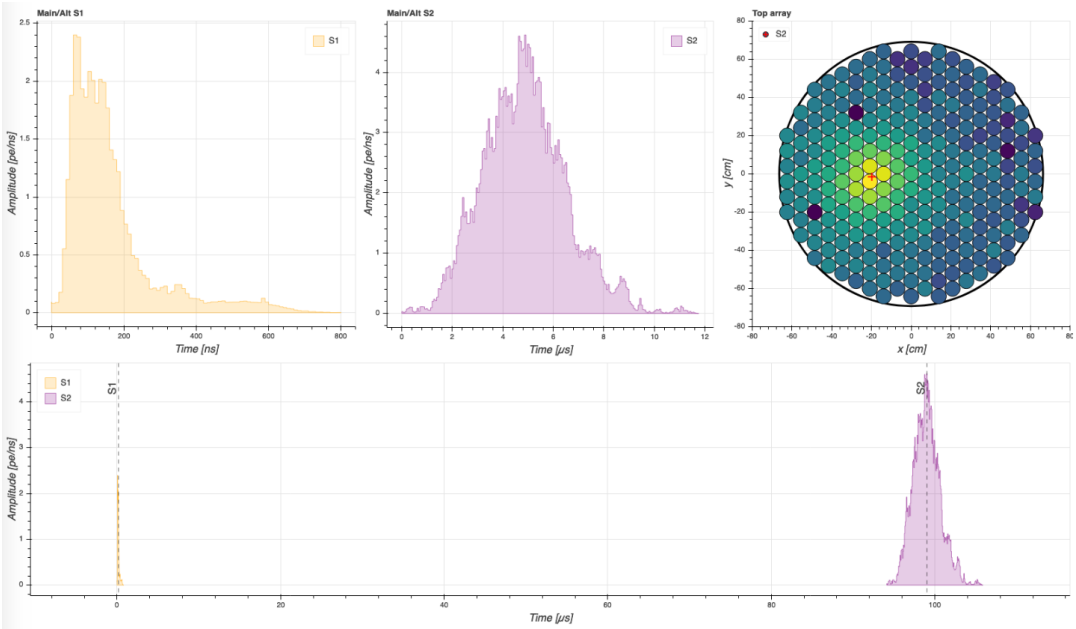

Figure 2.17: S1 and S2 waveform as well as S2 hit pattern of a krypton calibration event.

Recent work in supervised machine learning on XENONnT has shown that a surprisingly simple Bayes network with strong assumptions of independence among features[7], called Naive Bayes Classifier [127], is competitive with state-of-the-art classifiers. These networks are directed acyclic graphs[8] allowing efficient and effective representation of the joint probability distribution over a set of random variables. Each node in the graph represents a random variable, and edges represent direct correlations between the variables. See Figure 2.18 as an example of the structure of the naive Bayes graph.

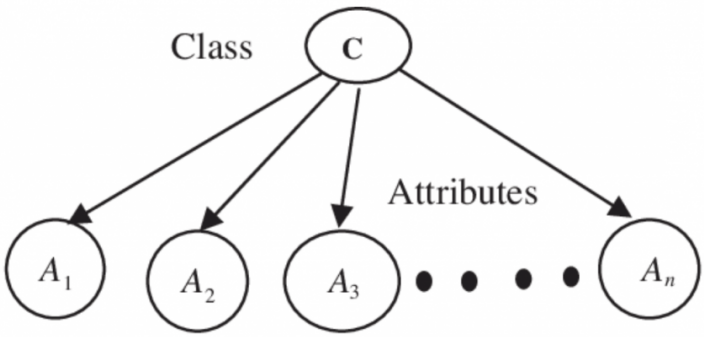

Figure 2.18: A Naive Bayes Bayesian Network Graph.

[7]*Feature* is a term used in machine learning and is a measurable characteristic of the phenomenon under study. It usually chooses numerical features, but structural attributes such as strings and graphs can be used for pattern recognition. Identifying and selecting the independent feature is necessary to develop effective algorithms for pattern recognition, statistical classification, and regression analysis.

[8]An acyclic graph is a graph that does not contain any cycles. It is used to represent a data structure, like a database connecting different information.

One of the most significant advantages of Bayesian methods is that they provide a natural approach for quantifying uncertainty in machine learning; they allow distinguishing between systematic and statistical uncertainty. This is crucial to ensure no biases are introduced by machine-learning methods and, if these are, to account for such given systematic uncertainties.
Figure 2.19 shows the results of the Naive Bayes Classifier to classify the Krypton calibration signals.

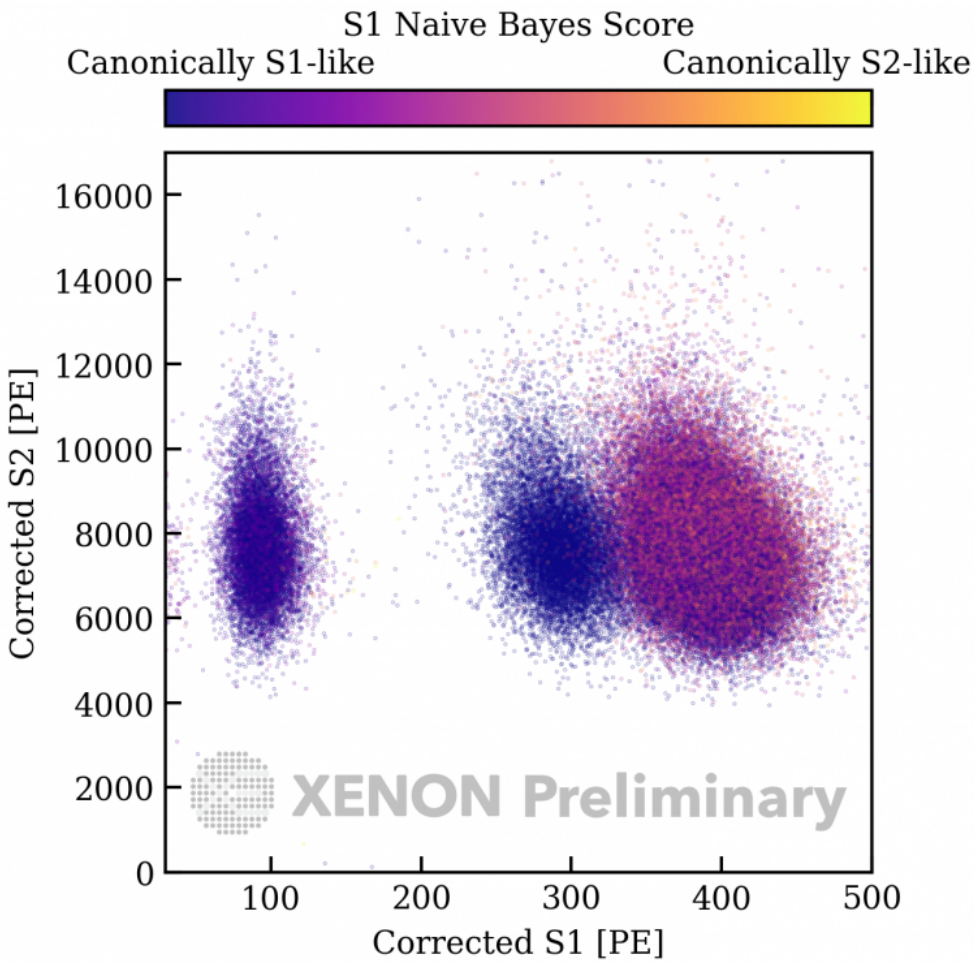

Figure 2.19: A plot of ^{83m}Kr calibration data in corrected S2 area (ionization signal size) vs. corrected S1 area (scintillation signal size). Main S2 area with the color dimension illustrating the S1 of each scatter point's likelihood of being an S2 using the Bayes method. A left-most color scale value indicates that the S1 looks highly canonical or statistically most like the training (simulation) S1. The median color bar values indicate that the S1 looks neither like a canonical S1 or S2, and the rightmost color bar values (where very few points exist) would indicate that the S1 looks most like a canonical S2.

Position reconstruction

XENONnT, like its predecessors, allows a complete determination of the 3D position of interactions. Electrons in liquid Xenon have a uniform drift velocity.

This makes it possible to determine the depth at which the interaction took place by measuring the time difference between the S1 and S2 signals. The position of the event in the XY plane can be determined through algorithms that have as inputs the number of photons observed by each PMT.

Position reconstruction in the XY plane is performed by using the light pattern of the S2 signal on PMTs at the top of the TPC. Given that the electric field allowing the electrons to drift is rectilinear and supposed to be uniform, the XY position of the signal S2 corresponds to the XY position of the interaction.
However, the electric field is never perfectly uniform, especially near the TPC edges. If PTFE panels get charged, this can be critical, as it leads to a volume that is not sensitive to charge signals as the ionization electrons get captured on the panels and cannot be drifted to the liquid/gas surface; this volume is termed as S2-insensitive volume, which is essential for fiducial volume selection and estimation. In order to correct the field distortion effect, the reconstructed positions are corrected to match the uniformity expected for calibration events (^{83m}Kr,^{220}Rn).

There are mainly two algorithms to reconstruct the position. The first is an algorithm based on a statistical test using a likelihood function of the maximum distribution (Top Pattern Fit, TPF). The second is an algorithm based on neural networks (NN).
The TPF method uses a likelihood function that, for a given S2 signal, compares the light distribution measured by each top PMT to that expected from the light-gathering simulations and returns the most likely corresponding XY position.
The NN method uses an artificial neural network trained on simulations with a known position. Once the training is complete, the neural network can determine the position of an interaction faster and with better resolution than the TPF method.

XY position resolution is of the order of a few mm to a few cm, depending on the energy deposited. The resolution at the Z position is of the order of 0.5 mm [128].

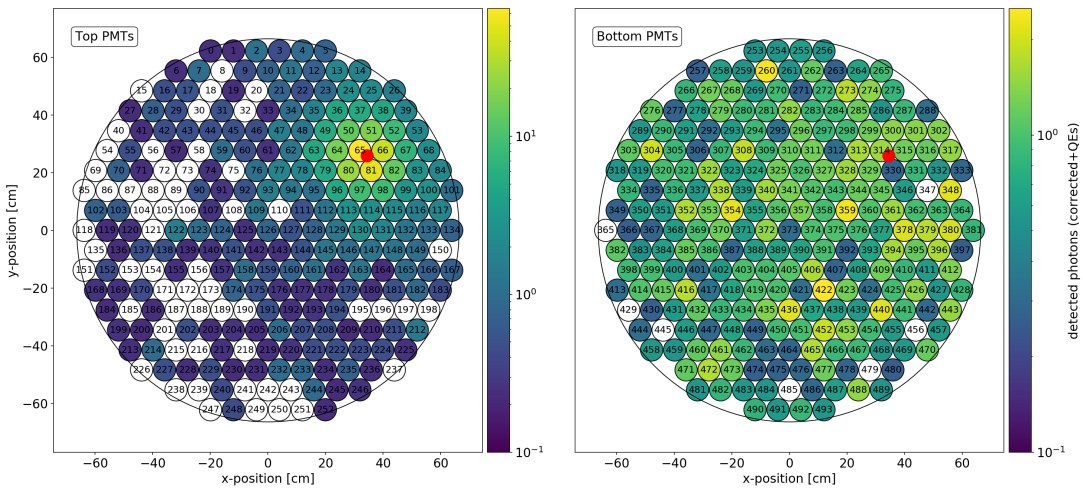

Figure 2.20: Hit pattern and event position reconstruction with a neural network.

Recoil type reconstruction

The ratio of ionization and excitation signals in liquid Xenon distinguishes electronic and nuclear recoils. Thus, the S1 and S2 (or, more precisely, the ratio S2/S1) are different if a nuclear or electronic recoil produces these signals. Nuclear recoils have a higher ionization density than electronic recoils because, beyond a few keV, the stopping power of liquid Xenon is greater for a recoiling nucleus than for an electron, knowing that the density of ionization is defined by the number of ions and electrons per unit length produced by a particle along its trail. A higher ionization density results in more free ions and electrons in a smaller space and, therefore, a greater likelihood of recombinations. Consequently, the S1 signal will be larger while the S2 signal will be smaller (since fewer electrons can escape recombination): the S2/S1 ratio is smaller for nuclear recoils than for electronic recoils.
Ultimately, particles moving through the detector should interact with the electrons of the Xenon atoms, producing electronic recoils, or with the nuclei, producing nuclear recoils. For a given amount of energy deposited by a particle in the detector, the ratio S2/S1 can be used as a discrimination parameter to distinguish between electronic and nuclear recoil events. In this way, the background resulting from electronic recoils can be suppressed by more than 99% while maintaining 50% of nuclear recoil events. [96].
The difference between the S2/S1 ratio bands corresponding to nuclear and electronic recoils is shown in Figure 2.21. These bands are obtained using calibration sources (^{220}Rn for electronic recoils and ^{241}AmBe and a neutron generator for nuclear recoil).

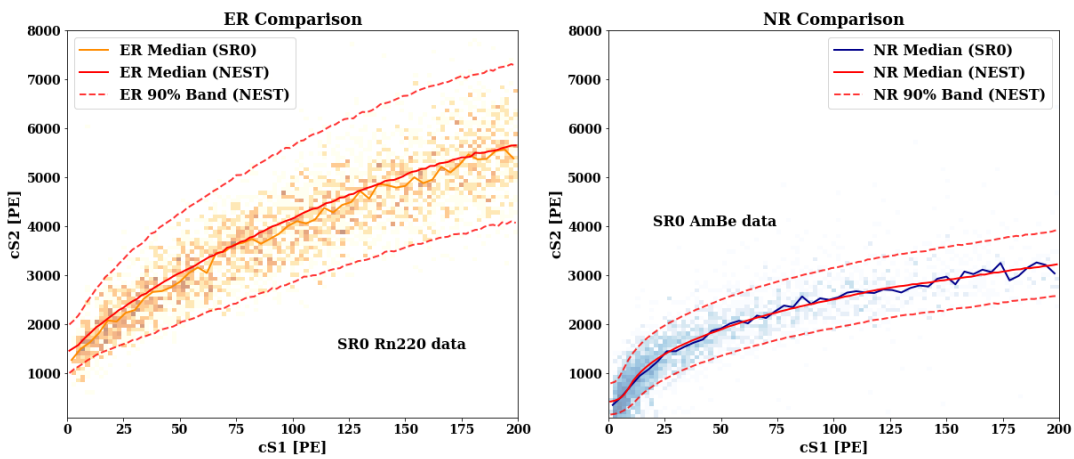

Figure 2.21: ER (left) and NR (right) bands comparisons between XENONnT first science run (SR0) and the NEST model.

Signal corrections

The two observed signals, S1 and S2, are generally proportional to the energy deposited. cS1 and cS2 denote the corrected version of the observed S1 and S2 signals.

In the case of the S1 signal, the probability that a primary scintillation photon reaches a PMT photocathode depends on the interaction position; this position dependency is due to geometric effects (different solid angles covered directly with PMTs, absorption due to different path lengths caused by scattering on the TPC walls and the liquid-gas interface) and to a small extent also due to electric field inhomogeneities. The position dependency is corrected with a data-driven method using monoenergetic ^{83m}Kr calibration data to calculate a correction map. These maps are based on the field distortion corrected coordinates and the uncorrected S1 areas of the 41.6 keV line of ^{83m}Kr.
Same as for S1, various corrections are applied to S2 signals to account for electron and photon losses in the TPC. First, the loss of electrons during the drift from the interaction site to the liquid surface is caused by electronegative impurities present in LXe and quantified by an electron lifetime. As explained previously, the electrons' lifetime is continuously increased under normal detection conditions due to permanent cleaning of the LXe and, therefore, time-dependent. Depending on the XY position, a second correction is applied to correct for varying probabilities of detecting secondary scintillation photons (S2). Finally, near the TPC edges, the signal detection efficiency is reduced mainly due to a lower light collection efficiency at large radii, leading to a systematic reduction in the size of the observed S2 signal. The corrections are defined by requiring a homogeneous S2 response to monoenergetic calibration sources.
Figures 2.22 illustrates the difference in the spectrum of ^{83m}Kr before and after correction.

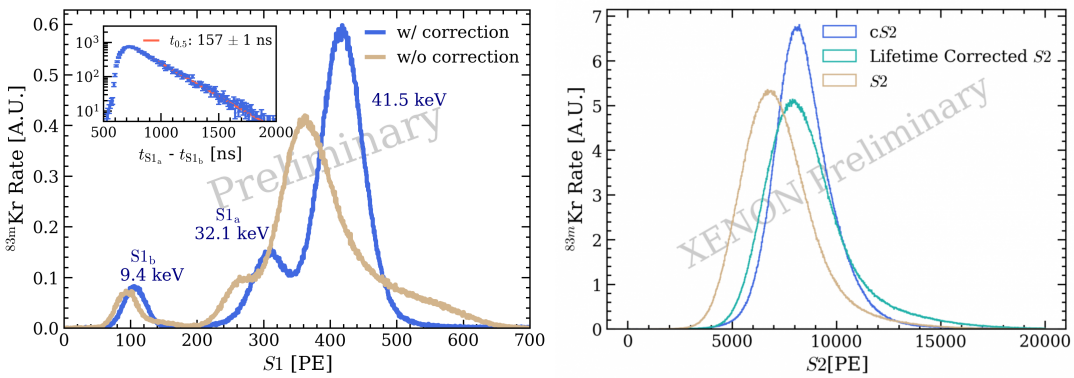

Figure 2.22: (Left) ^{83m}Kr S1 spectra before and after S1 (x,y,z) correction under 18 V/cm drift field. The S1 resolution is much better after correction. Inset plot: The time difference between ^{83m}Kr double scatters. The fitted 157 ± 1 ns half-life is close to the literature value of 156 ns. (Right) Distributions of S2, electron lifetime corrected S2 and cS2 under 18.3 V/cm drifting field.

2.2.10 Calibrations

Characterization of particle interactions in the detector's active region is essential to correctly identify possible dark matter particles. The main objective of XENONnT is the detection of WIMPs above GeV, and these WIMPs should pro-

duce a single NR signal in the active volume. Therefore, it is critical to correctly identify NR interactions in the detector and distinguish them from ER. With this in mind, XENONnT is the subject of several calibration campaigns before and during scientific runs. Spectral and monoenergetic sources, internal and external, are used to measure the ER and NR response of the detector.

External calibration is particularly challenging because of the LXe self-shielding capability, which paradoxically makes it such an attractive dark matter target. The self-shielding of LXe strongly attenuates photons with energies below the MeV scale. Therefore, external γ sources can only be used to calibrate the outermost region of the TPC. Moreover, the higher energy γ-rays tend to produce multiple scatters, with the first scatter mainly concentrated in the outer regions. A very high event rate in the edge region causes saturation effects making fiducial volume calibrations impossible. As a result, the gamma calibrations are carried out thanks to the emissions of remaining radio-impurities in the detector materials (^{60}Co, ^{40}K) and the Xenon isotopes excited after calibration with neutrons (^{129m}Xe, ^{131m}Xe) [126].

Figures 2.23 and 2.24 details the different external calibration subsystems of the XENONnT experiment.

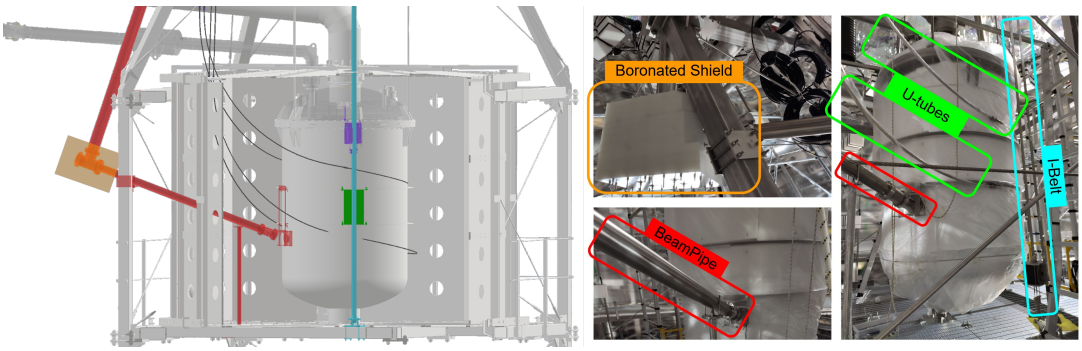

Figure 2.23: (Left) Computer-aided design render of the inner part of the detector with calibration systems highlighted. (Right) Photos with labels of the XENONnT calibration systems.

The *I-belt* allows to move the γ sources (^{228}Th, ^{137}Cs) and the neutron source ^{241}AmBe vertically. In front of the I-belt is an airbox that moves water between the I-belt collimator and the cryostat to allow better low-energy neutrons to reach the Xenon.

The neutron calibration system consists of a *GuidePipe* (6 inches diameter) to lower the neutron generator into place and the *BeamPipe* (4 inches diameter), connected to the TPC. The BeamPipe allows a collimated beam of neutrons from a neutron generator outside the nVeto but inside the water tank orange box in Figures 2.23 left). The connection of these two pipes is surrounded by 20 cm of *borated polyethylene* on all sides to capture the excess neutrons. Without this, the rate of gammas from neutrons captured by the Gd in the water tank will reach saturation levels.
Neutrons enter the TPC/cryostat at an angle of 20 degrees from the XY plane. The beam system is equipped with a new neutron generator that can produce

short pulses of neutrons instead of a constant flux. This makes it possible to distinguish between instantaneous neutron events and gamma events resulting from the capture of neutrons in the water tank. This generator can produce a higher neutron flux, up to 10^7 neutrons/sec.

Finally, One-inch diameter stainless steel *U-tubes* wrap around the cryostat with two Z positions allowing small external sources to be approached to the cryostat.

On the other hand, even if it may seem paradoxical given the fear of contamination, the best way to calibrate the detector is to use radioactive sources introduced directly into the active volume of the detector. To minimize contamination as much as possible, the radioactive sources introduced into the active volume must imperatively be either short-lived isotopes that will decay rapidly or sources that the purification system can efficiently extract. XENONnT uses two internal calibration sources that meet these criteria: a nearly monoenergetic metastable isotope of krypton, ^{83m}Kr, and a radioactive isotope of Radon, ^{220}Rn [126].

Krypton calibration

^{83m}Kr emits two de-excitation gammas, separated in time by 155.1 ns [129], that can be employed in the calibration of XENONnT. ^{83m}Kr diffuses uniformly through the LXe, allowing for efficient calibration of the entire detector. In addition, its two decay lines at 9.41 and 32.15 keV, as well as their pile-up at 41.56 keV, are in the energy range of interest for the direct search for dark matter, and its half-life of only 1.8 hours makes it possible to resume the scientific run after a short delay following the calibration. Figure 2.25 illustrates the decay process leading to the production of the isomeric state[9] ^{83m}Kr.
Since krypton is an inert element, it can not be eliminated by the main purification system. Nevertheless, XENONnT has a dedicated distillation column to remove Krypton from the detector.

To correctly measure the energy of an event in XENONnT, it is necessary to correct for two instrumental effects. First, the dependence on the XY position of the light detected by the PMTs (S1 correction), and second, the finite electron lifetime due to the capture of ionization electrons drifting to the liquid-gas interface by residual impurities in the LXe (S2 correction).
Calibrations with Krypton provide an effective tool to measure and correct both effects.

The S1 measured in the TPC show position dependence due to geometric effects (such as the different solid angles covered directly by the PMTs, absorption due to different path lengths caused by scattering on the walls and on the liquid-gas interface) and, to a lesser extent, due to inhomogeneities of the electric field. Therefore, the same number of initial photons will produce a different S1 signal

[9] An isometric state is a metastable state of the atomic nucleus, in which one or more nucleons occupy higher energy levels than the ground state.

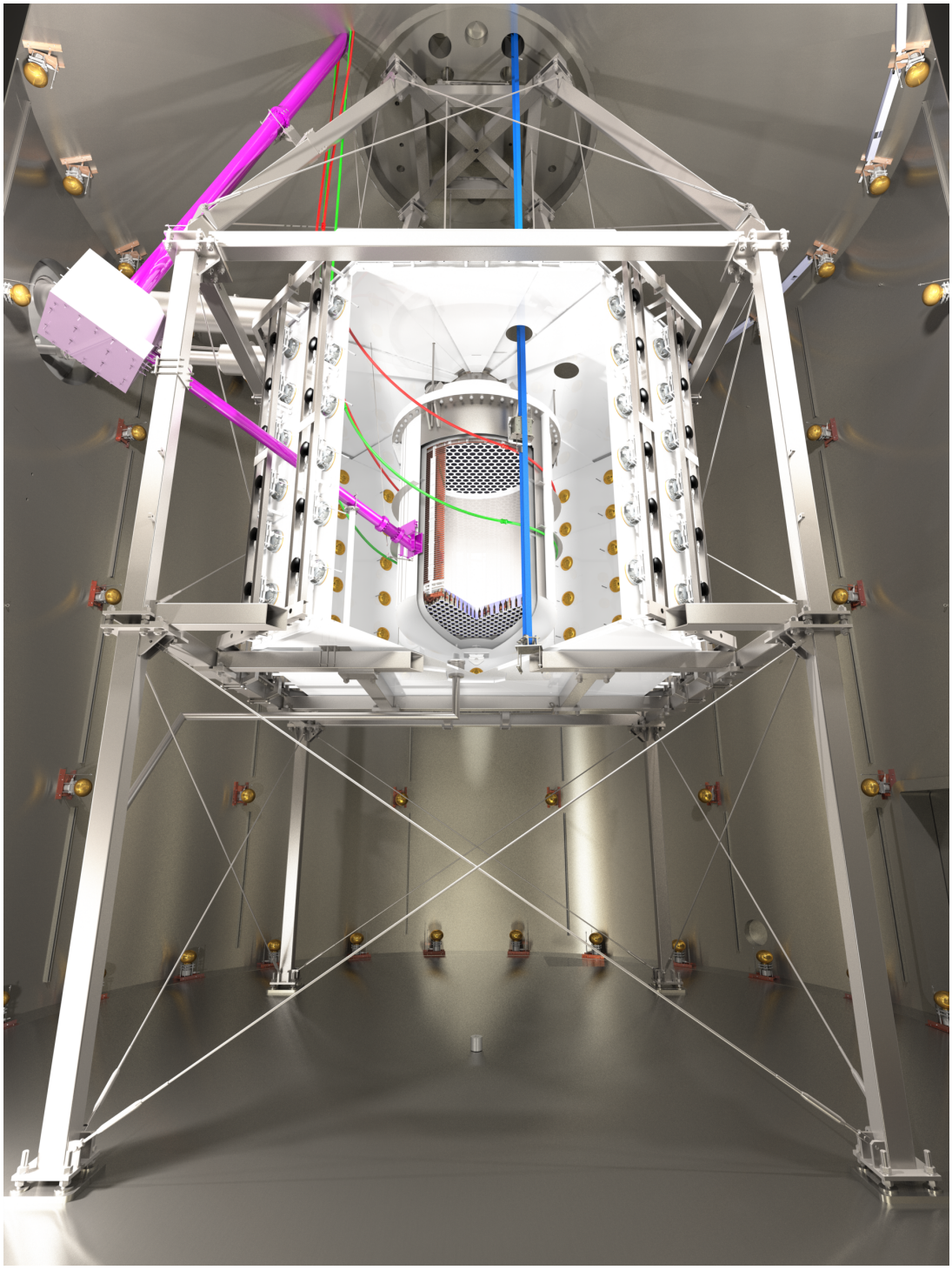

Figure 2.24: Computer-aided design render of the entire detector. The viewpoint is designed to reflect what a viewer would see if they stood outside the water tank, looking up toward the top of the water tank.

intensity at the PMTs.
In order to map the position-related inefficiency, the TPC volume is divided into bins with equal volume, and then Kr events are sorted into the bins. The

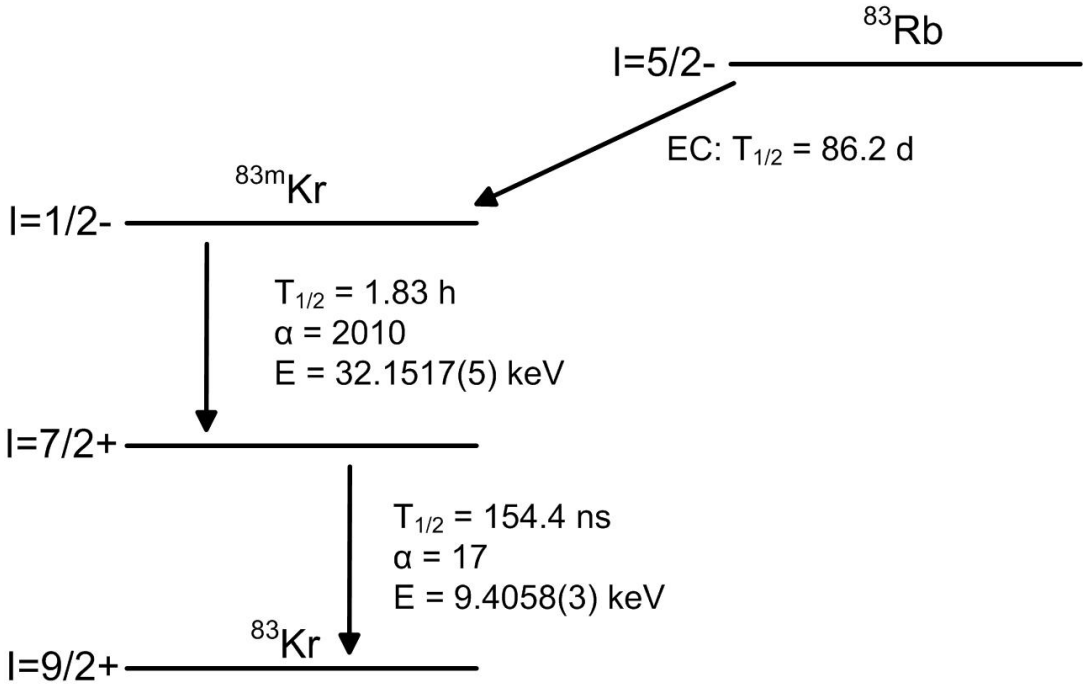

Figure 2.25: The production of the isomeric state ^{83m}Kr by electron capture decay of ^{83}Rb. The isomeric $1/2^-$ state, with its half-life of 1.83 h, is populated in about 78% of all ^{83}Rb decay processes and de-excites by two highly converted γ-transitions. Figure from [130].

corresponding mean S1 value (in PE) is obtained in a loop over each spatial bin with a Gaussian fit. The relative light yield is then calculated by normalizing each bin with the average of all bins. Together with the (x,y,z)-coordinates of the center of gravity for each bin, the relative values are stored as the S1 correction map. This is done for each position algorithm separately. Then these maps are introduced as interpolation to correct the S1 signals (see Figure 2.22).

In the case of S2 signals, Z-position and XY-plane position corrections are applied independently. The Z-dependence results from electron capture on electronegative impurities as they drift and strongly correlate with the purity level of LXe. This correction is a simple unity-normalized exponential adjustment to the surface of the liquid and must be updated regularly to consider the evolution of the free drift time of the electrons. The non-uniformities of the S2 signal in the XY plane are due to variations in the liquid surface and the grid plane's curvature or sag, which changes the extraction efficiency in the XY plane. The corrections are constructed by grouping the ^{83m}Kr data onto a grid and finding average S2 amplitudes for each bin normalized to the center.
Figure 2.26 shows the krypton calibration events in corrected S1 and S2 space (cS1,cS2).

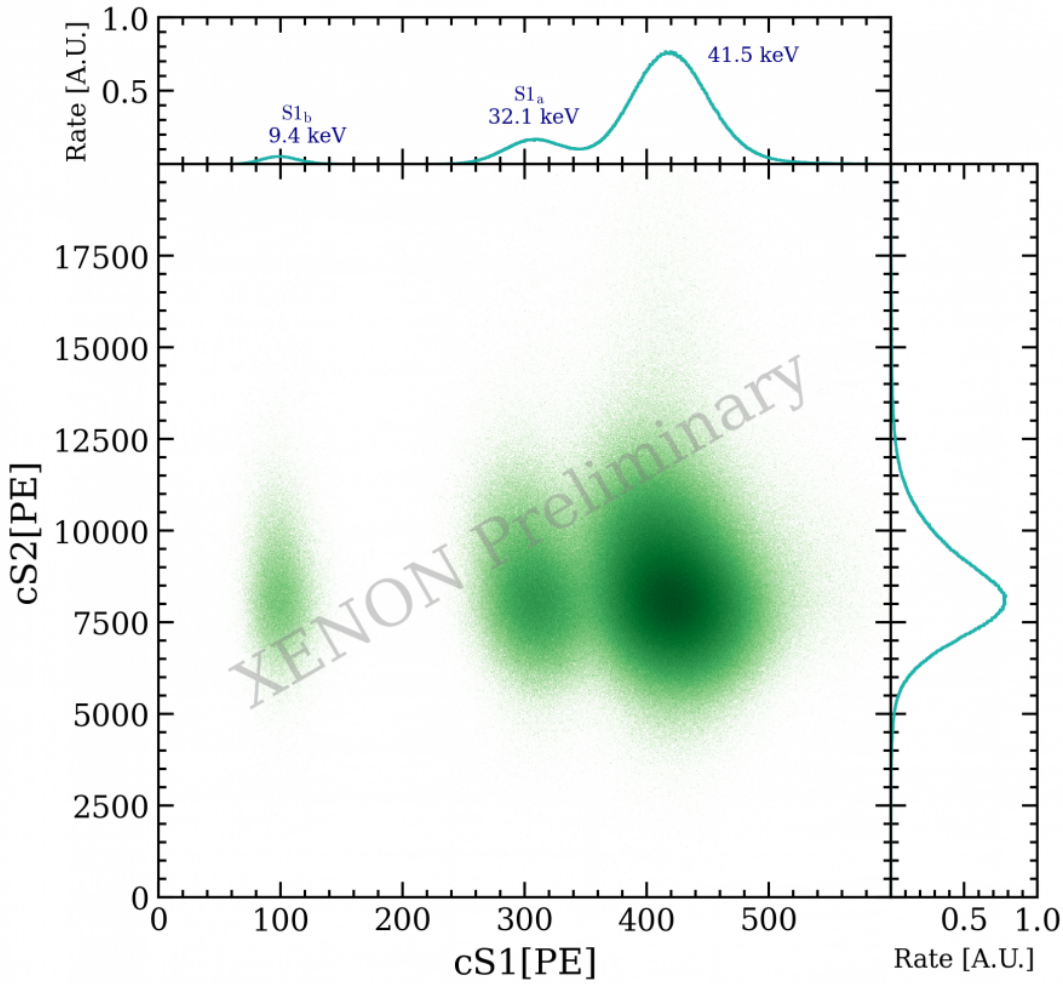

Figure 2.26: cS1 and cS2 distributions of ^{83m}Kr population under 18.3 V/cm drifting field. The plot on the top is the cS1 spectrum, and the one on the right is cS2. Although the two-step decay is visible in cS1 space, due to the large width (~ 4000 ns, strongly dependent on drift time) of ^{83m}Kr cS2 compared with the half-life of the decay (~ 150 ns), most of the cS2 are merged and indistinguishable. While the 32.1 keV and 41.5 keV bulges are true populations, the 9.4 keV bulge shares the same cS2 as the 32.1 keV bulge, as they are from the same double S1 single S2 population.

Radon calibration

^{220}Rn is used to calibrate the electronic recoils at low energy, (2-30) keV. The ^{220}Rn decay chain isotopes provide alpha and beta radiation that improves the tagging efficiency of intrinsic ^{222}Rn event, which is a dominant background source in dark matter experiments (Radon is produced by the decay of Uranium and Radium found naturally in soil and rocks). Given the short decay time of the entire decay chain (see Figure 2.27), any introduced activity disappears within a week, regardless of the volume or rate of purification of a detector. Nevertheless and as in the case of Krypton, XENONnT has a distillation column

specially dedicated to removing traces of Radon from the detector.

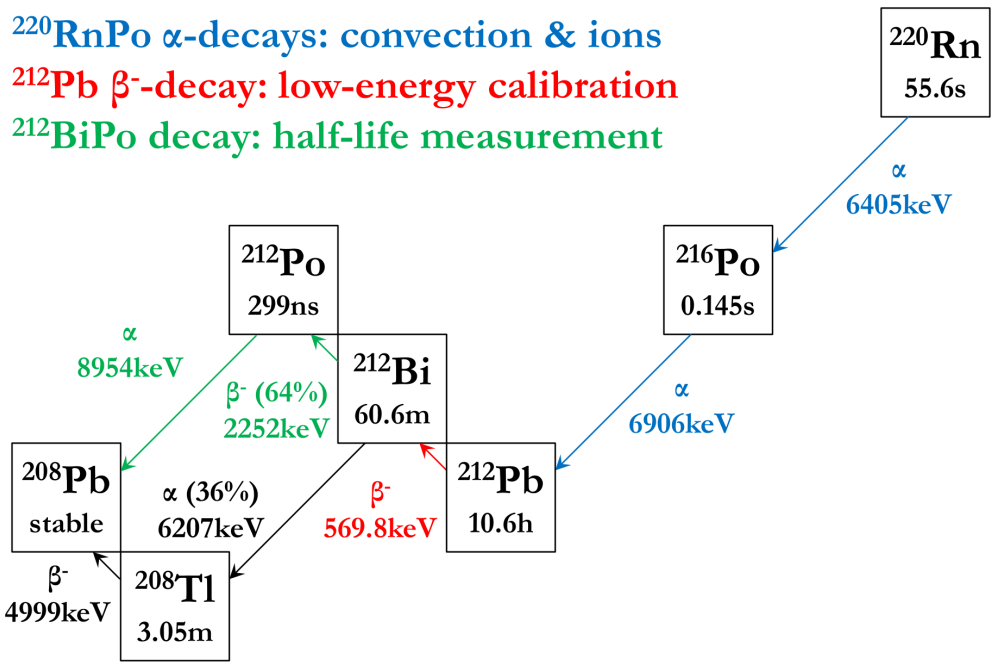

Figure 2.27: The decay chain of ^{220}Rn, following its emanation from a ^{228}Th source. (Figure from [131]).

The decay of ^{212}Pb emits beta particles, which are particularly useful for low-energy calibration. The direct decay of ^{212}Pb to the ground state of ^{212}Bi with a branching ratio of 11.9%, is used for the calibration of electronic recoil occurring in the energy range, (2 – 30) keV [131].
These calibrations then allow making the appropriate cuts to select the electronic recoil band (see Section 2.2.9).

Argon calibration

^{37}Ar decays by electron capture according to the reaction: $^{37}Ar + e^- \longrightarrow ^{37}Cl + \nu_e$, with a half life 35 days. As it decays, ^{37}Ar releases X-rays from the capture of electrons from the K, L, and M shells at 2.822 keV, 0.270 keV, and 0.016 keV with branching ratios of 90%, 9%, and 0.9% [132]. These X-rays are photo absorbed by the Xenon, producing electronic recoil.
On the other hand, after the calibration phase, ^{37}Ar can be efficiently removed by the XENONnT distillation column.

Given the low energy of ^{37}Ar emissions, it is a candidate of choice for measuring the response of Xenon at very low energies. Figure 2.28 shows the charge yield of Xenon at low energy, comparing the XENON1T Bayesian Band fitting Framework (BBF) [117] and NEST models with the experimental data.

^{241}AmBe calibration

For nuclear recoil calibrations, AmBe (mixture of an alpha emitter ^{241}Am + ^{9}Be with an average energy of 4.2 MeV and maximum neutron energy of 11 MeV)

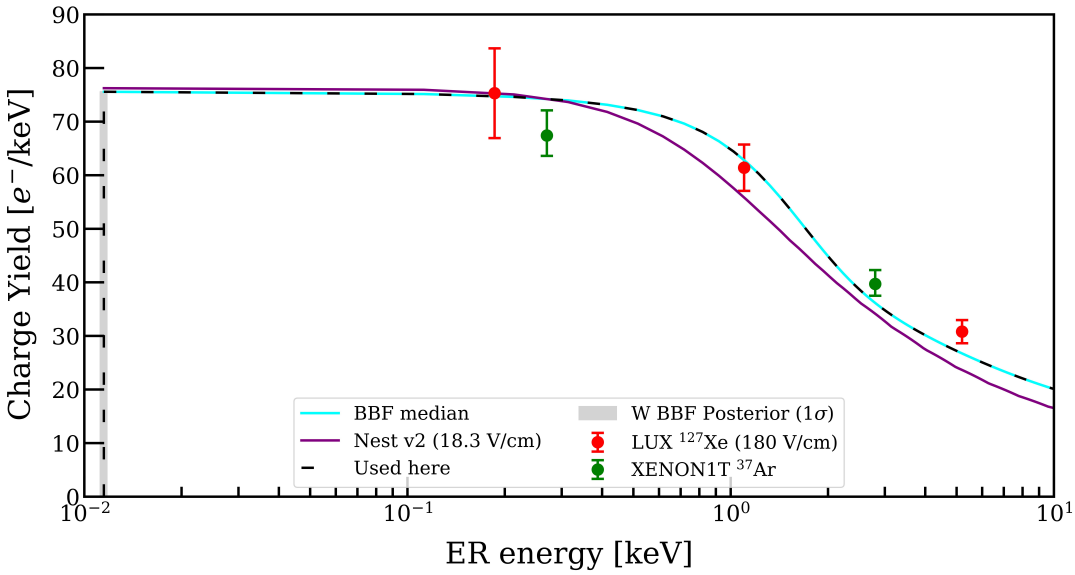

Figure 2.28: The results on the charge yield for the ^{37}Ar L peak and K peak energies (green dots) obtained from XENON1T data are compared with other measurements of the charge yield at different energies. The cyan line is the prediction from BBF, and the violet line is the prediction from NEST. The dotted vertical bar represents the value of 11.5 eV, which is the work function value of the Xenon used.

and D-D (Deuterium-Deuterium) fusion neutron generators are used [95].

An AmBe neutron calibration gives a low-energy neutron source that can be used to calibrate the detector response model for nuclear recoils (NEST, BBF). Additionally, the Xenon isotopes ^{129}Xe and ^{131}Xe can be excited AmBe to decaying states with half-lives of 8.9 and 11.9 days respectively, producing gamma lines and thus allowing to measure g_1 and g_2 (see Section 2.1.3). Figure 2.29 shows an output of an AmBe calibration.

2.3 Simulations and backgrounds

2.3.1 Simulation framework

The XENONnT detector is very complex, so no deterministic model could be possible to describe the entirety of interactions that can occur within. However, with appropriate constraints, Monte Carlo (MC) simulation methods inherited from XENON1T [133] generate the statistical confidence necessary to understand and study the interactions of particles in the detector volumes.
It starts by modeling the detector with the Geant4 toolbox [134]; this model is then used to convert the energy deposited in the TPC into S1 and S2 signals to assess the background and expected signal distributions. This conversion is based on the model of light and charge emission following interaction in LXe, convoluted with detector effects related to collection efficiency and signal reconstruction. These effects have been modeled with NEST, which consists of a

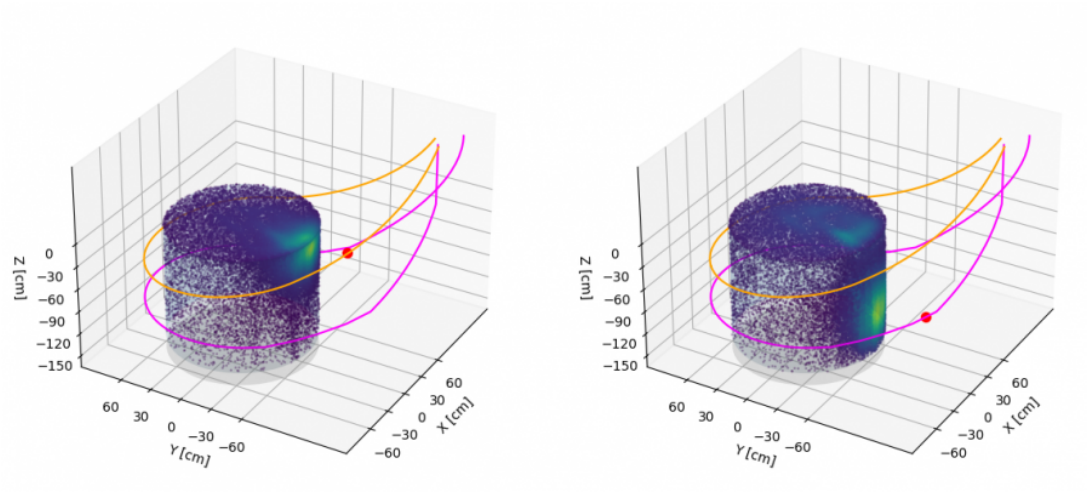

Figure 2.29: 3D plot showing the distribution of events during AmBe calibration and for two separate positions of the source. Also shown are the top and bottom u-tubes. The AmBe source position is indicated in the red dot.

semi-empirical collection of models based on calibration data.
The created simulation data is then processed with the same data processing method as the real data.

2.3.2 Backgrounds

Electronic and nuclear recoil background sources are estimated via MC simulations of the recoil particles in the LXe target. The WIMP signal should be a single NR interaction within the detector volume. Therefore, event selection is limited to single scatters. Although ERs can be effectively distinguished from NRs based on the S2/S1 ratio, statistical leakage of the ER population can still produce events that are indistinguishable from WIMPs. Thus, a detailed understanding of NR and ER background sources is necessary.
The rate of NR backgrounds was estimated for XENONnT in the energy range $(4, 50)$ keV, which corresponds to ERs in the range $(1, 13)$ keV in the S1 signal space [100].

The radioactive isotopes, such as ^{222}Rn and ^{85}Kr, are intrinsic ER background sources uniformly distributed in the active volume and therefore not attenuated by a fiducial volume.
The dominant background noise in XENON1T was caused by beta emissions from ^{214}Pb, a product of the ^{222}Rn decay chain. In XENONnT, the level of ^{222}Rn has been significantly reduced thanks to the meticulous selection of low radon emission materials, detector design, a smaller surface-to-volume ratio, and a dedicated radon distillation column.

The irreducible backgrounds in XENONnT come from interactions induced by neutrinos of solar, atmospheric, or diffuse supernova (DSN) origins. These are spatially uniform due to their very weak interaction [100]. The interaction of neutrinos with electrons contributes to the ER background, while coherent elastic

neutrino-nucleus scattering (CEνNS) contributes to the NR background. Figure 2.30 illustrates the background spectrum of XENONnT, with known contribution' origin given.

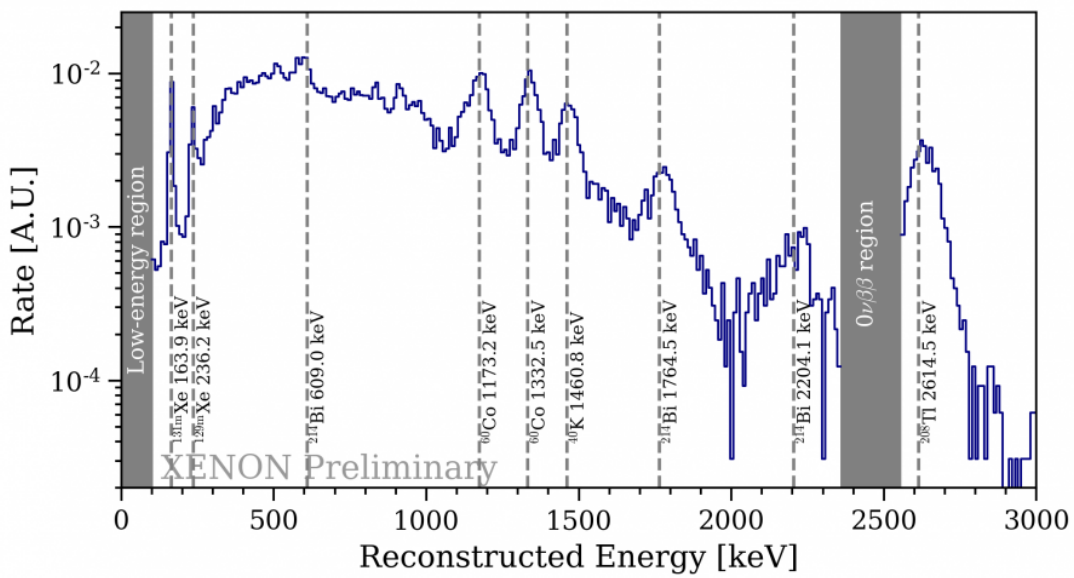

Figure 2.30: XENONnT background energy spectrum using 4.2-day background data. The spectrum presents two blinded regions, as shown in the figure.

The total background rate expected in a fiducial volume of 4 tons is shown in Table 2.3. It is particularly interesting to note that thanks to the different methods for diminishing the ER background, the latter should be lower by a factor of 6 compared to XENON1T [99].

Electronic recoil background

The main origins of the ER background are the detector components that emit γ rays that produce Compton scattering, in addition to β decays and electron captures in the LXe target. Other sources also contribute to the ER background, such as the β decay of ^{85}Kr and ^{214}Pb as well as the electron capture decays of ^{127}Xe and ^{37}Ar.
The contribution of each isotope and each part of the detector is given in Figure 2.31.

Nuclear recoil background

The NR background partly comes from spontaneous fission reactions in detector materials producing radiogenic neutrons. Figure 2.32 shows the contributions of the different materials to the NR background. Nevertheless, the main NR background sources come from radiogenic and cosmogenic neutrons and CEνNS neutrinos.

Cosmogonic neutrons are neutrons produced by cosmic muons interacting in the rock surrounding the detector. These can be tagged efficiently using the

Table 2.3: Estimated background event rates in the 4 t fiducial volume of XENONnT, based on the energy of the recoil event. The energy region of interest in which the event rates are integrated is (1, 13) keV for ERs, and (4, 50) keV for NRs. Assuming an activity concentration of 1 μBq/kg of ^{222}Rn and 0.1 ppt (mol/mol) ^{nat}Kr/Xe. The background contributions from Xe isotopes are determined assuming the 8.9% and 0.095% natural abundances of ^{136}Xe and ^{124}Xe, respectively. (Table from [100]).

Source	Rate [(t.y)$^{-1}$]
ER background	
Detector radioactivity	25 ± 3
^{222}Rn	55 ± 6
^{85}Kr	13 ± 1
^{136}Xe	16 ± 2
^{124}Xe	4 ± 1
Solar neutrinos	34 ± 1
Total	148 ± 7
NR background	
Neutrons	$(4.1 \pm 2.1) \times 10^{-2}$
CEνNS (Solar ν)	$(6.3 \pm 0.3) \times 10^{-3}$
CEνNS (Atm+DSN)	$(5.4 \pm 1.1) \times 10^{-2}$
Total	$(1.0 \pm 0.2) \times 10^{-1}$

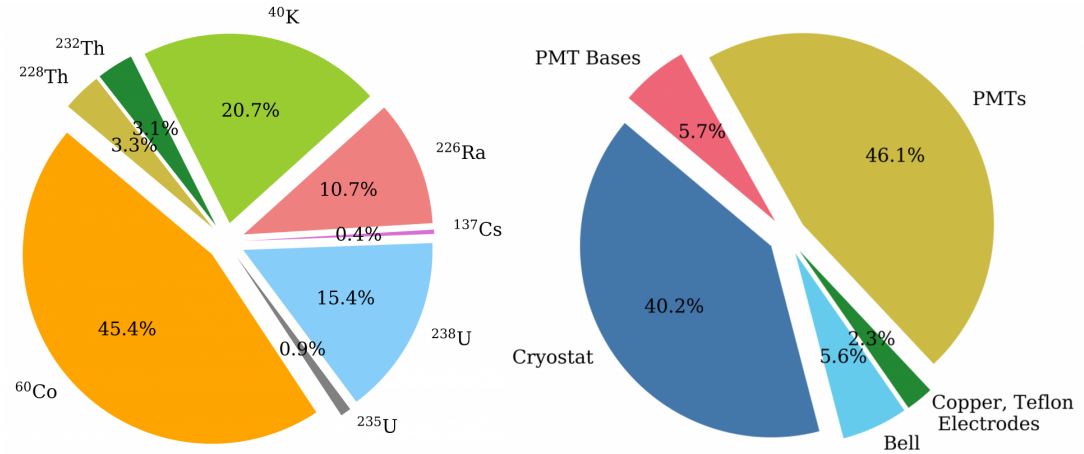

Figure 2.31: (Left) Main ER background source by isotope. (Right) Main ER background source by material component.

muon veto. Furthermore, adding the neutron veto enriched with Gd will further reduce the rate of cosmogenic neutrons to such an extent that this source of background is not included in the estimation of the sensitivity of XENONnT.
CEνNS neutrinos, on the other hand, come from the Sun, the atmosphere, or supernovae, which interact elastically and coherently with the Xenon nucleus. Solar neutrinos from the ^{8}B chain represent the dominant contribution to the total background of the CEνNS.

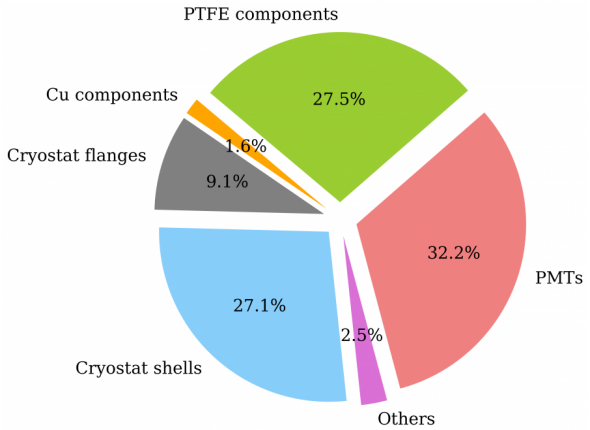

Figure 2.32: Main NR background source by material component.

2.4 Projected XENONnT sensitivity

The profile likelihood method [135] is used to obtain the projection of the sensitivity of XENONnT. This statistical model is largely inherited from that of XENON1T [117]. The signal and background distributions are projected in (cS1, $cS2_b$[10]) space. XENONnT targets a total exposure over its operating period of 20 t.y, obtained by assuming a fiducial mass of 4 tons and a data collection period of five years. However, the latest studies of the calibration data to characterize the background near the TPC edges allowed to extend the fiducial mass to almost 5 tons.

2.4.1 Statistical model

To claim a discovery or place an exclusion limit on dark matter-nucleon cross-section, a frequentist significance test using the profile likelihood ratio statistic should be used, corresponding to the canonical method within the particle physics field.

Maximum likelihood is a general method for estimating the parameters of a statistical model. For example, suppose a series of observations of a random variable y and a potential statistical model for that variable. This model can include the dependence of y on other predictor variables and statistical distribution for the unexplained portion of the variation of y. In general, such a model contains various unknown parameters θ that must be fitted to the observed data. According to the maximum likelihood, the best model parameter estimates are those that maximize the probability of the observed values of the variable. This method can be applied regardless of the model's mathematical form [135].
This likelihood function is defined as:

$$\mathcal{L}\left(\vec{\theta}\right) = \prod_{i=1}^{n} f\left(y_i \,|\, \theta\right). \tag{2.22}$$

[10] $cS2_b$ corresponds to the corrected S2 detected by the bottom PMTs; these are used for energy reconstruction, given their more homogeneous LCE.

The value of θ that maximizes $\mathcal{L}$ is known as the Maximum Likelihood Estimator (MLE) of θ, which will be denoted as, $\hat{\theta}$. If n is a Poisson random variable with mean ν (the case of XENONnT), then it implies that:

$$\begin{aligned} L(\nu;\theta) &= \mathrm{Pois}(n,\nu)\prod_{i=1}^{n} f(y_i\,|\,\theta) \\ &= \frac{\nu^n e^{-\nu}}{n!}\prod_{i=1}^{n} f(y_i\,|\,\theta) \\ &= \frac{e^{-\nu}}{n!}\prod_{i=1}^{n} \nu\, f(y_i\,|\,\theta)\,. \end{aligned} \tag{2.23}$$

This equation is called the *extended likelihood function.* The information encoded in the likelihood is *extended* to correct the expected number of events. This extended likelihood remains in the form of a likelihood, and no different treatment is required to find its MLE estimators.

The goal in the case of XENONnT and the search for dark matter, in general, is to determine, from the knowledge of the waveform of signal and backgrounds, which are assumed to be perfectly known, the number of events of signal n_s and background n_b best able to explain the data. The amplitude of the different components is only known with a certain precision. The numbers of signal and background events expected by the model are, therefore, adjustable parameters and $\hat{n_s}$, $\hat{n_b}$ note the values of n_s and n_b which maximize the likelihood between the model and the data.

The profile likelihood has the advantage of reducing the data to a single variable q_σ defined as:

$$q_\sigma \equiv -2\ln(\lambda(\sigma)), \tag{2.24}$$

where $\lambda(\sigma)$ is the profile likelihood ratio defined as the ratio of the null hypothesis (H_0 or WIMP signal plus background) and the alternative hypothesis (H_1 or background-only):

$$\lambda(\sigma) = \frac{\mathcal{L}(H_0)}{\mathcal{L}(H_1)} = \frac{\mathcal{L}(\sigma,\hat{\hat{\theta}})}{\mathcal{L}(\hat{\sigma},\hat{\theta})}, \tag{2.25}$$

where θ represents the set of nuisance parameters ($\theta \equiv n_b$), $\hat{\sigma}$ and $\hat{\theta}$ are respectively the maximum likelihood estimators associated with the parameter of interest and the nuisance parameters. The notation $\hat{\hat{\theta}}$ refers to the fact that σ is fixed during the maximization of the likelihood function, and is referred as a conditional maximum likelihood estimator.

First, it would be interesting to focus on the methodology for obtaining an exclusion limit from observed data.
Excluding a cross-section σ with a degree of confidence α amounts to saying that if the tested hypothesis σ is true, the probability p that the result of a random XENONnT experiment excludes a cross-section less than σ is given by $p \leq 1-\alpha$. The focus, therefore, consists in knowing the smallest value of cross-section for which this last relation is verified, namely: $p = 1-\alpha$. For each value of σ

tested, we must have the probability distribution $f(q_\sigma \,|\, \sigma)$ of the test q_σ under the hypothesis σ in order to calculate p:

$$p(\sigma) = \int_{q_\sigma^{obs}}^{\infty} f(q_\sigma \,|\, \sigma) dq, \tag{2.26}$$

where q_σ^{obs} is the value of the statistical test q_σ obtained on the observed data for the tested cross-section σ.

In principle, a large Monte Carlo dataset should be generated under the hypothesis σ to derive $f(q_\sigma \,|\, \sigma)$ and this for all the cross-sections tested until obtaining p giving the desired degree of confidence α. In practice, and this is the whole point of this statistical test, the probability distribution $f(q_\sigma \,|\, \sigma)$ follows, according to Wilks' theorem [136], the chi-squared (χ^2) distribution. $f(q_\sigma \,|\, \sigma)$ is therefore independent of σ and perfectly known in advance:

$$f(q_\sigma \,|\, \sigma) = \frac{1}{2}\delta(q_\sigma) + \frac{1}{2}\frac{1}{\sqrt{2\pi q_\sigma}} \exp^{-q_\sigma/2} . \tag{2.27}$$

It is, therefore, possible to find p without generating a Monte Carlo. The cross-section value excluded at 90% confidence is the cross-section value for which $q_\sigma^{obs} = 1.645$.

Second, for the projection, the goal is to know which value of the cross-section is likely to put a limit with 90% confidence in a future experiment if no WIMP had interacted in the detector. The data will be described in this context by an H_0 hypothesis. The canonical method, in this case, is to generate Monte Carlo data under the H_0 hypothesis and, for each value of σ tested, consider the q_σ^{obs} value to be the median of the distribution of the q_σ test under the H_0 hypothesis: $q_\sigma^{obs} = \mathrm{med}(f(q_\sigma \,|\, H_0))$.

In the specific case of XENONnT, the statistical modeling based on the likelihood of the experiment uses an extended unbinned[11] likelihood, $\mathcal{L}$, with probability density functions (PDFs) in $x = (\mathrm{cS1}, \mathrm{cS2_b})$ [100]:

$$\mathcal{L}(\sigma_{\mathrm{DM}}, \theta) = \mathrm{Pois}(N \,|\, \mu_{\mathrm{tot}}(\sigma_{\mathrm{DM}}, \theta)) \cdot \prod_{i=1}^{n} \left[\sum_c \frac{\mu_c(\sigma_{\mathrm{DM}}, \theta)}{\mu_{\mathrm{tot}}(\sigma_{\mathrm{DM}}, \theta)} \cdot f_c(x_i \,|\, \theta) \right] \cdot \mathcal{L}_{\mathrm{anc}}(\theta) \ , \tag{2.28}$$

where $\mu_{\mathrm{tot}}(\sigma, \theta) \equiv \sum_c \mu_c(\sigma, \theta)$ and the ancillary term $\mathcal{L}_{\mathrm{anc}}$ is defined as

$$\mathcal{L}_{\mathrm{anc}}(\theta) \equiv \prod_k \mathrm{Gaus}(\hat{\mu}_k \,|\, \mu_k, \xi_k) \ , \tag{2.29}$$

with k running over the three background components with associated uncertainties, namely neutrons and CEνNS from solar and atmospheric+DSN neutrinos:

$$\begin{aligned} \mathrm{Gaus}(\hat{\mu}_k \,|\, \mu_k, \xi_k) \sim & \mathrm{Gaus}(\hat{\mu}_{\mathrm{Solar}\ \nu} \,|\, \mu_{\mathrm{Solar}\ \nu}, \xi_{\mathrm{Solar}\ \nu}) \cdot \mathrm{Gaus}(\hat{\mu}_{\mathrm{Atm}\ \nu} \,|\, \mu_{\mathrm{Atm}\ \nu}, \xi_{\mathrm{Atm}\ \nu}) \cdot \\ & \mathrm{Gaus}(\hat{\mu}_{\mathrm{n}} \,|\, \mu_{\mathrm{n}}, \xi_{\mathrm{n}}) \\ \mu_{\mathrm{tot}}(\sigma, \theta) \equiv & \sum_c \mu_c(\sigma, \theta). \end{aligned}$$

[11]Unbinned likelihood analysis is the preferred method for analyzing low-background experiments, where the number of events in each time bin is expected to be small.

The likelihood, evaluated for each WIMP mass M_{DM}, is a function of the WIMP cross-section σ_{DM} and the nuisance parameters θ, which parameterize the PDFs f_c and expected values μ_c. Index c runs on background components and WIMP signal. The ancillary measurements' rate uncertainties ξ are considered Gaussian constraints in the term $\mathcal{L}_{\mathrm{anc}}$. The observed events, i, are collected in a vector of length n. The profiled log-likelihood ratio for each WIMP mass considered is:

$$q(\sigma_{\mathrm{DM}}) \equiv -2 \cdot \ln \frac{\mathcal{L}(\sigma_{\mathrm{DM}}, \hat{\hat{\theta}})}{\mathcal{L}(\hat{\sigma}_{\mathrm{DM}}, \hat{\theta})} \tag{2.30}$$

This profile likelihood is used to test both the signal and the null hypothesis, $q(\sigma_{\mathrm{DM}} = 0)$. The likelihood is maximized at $(\hat{\sigma}_{\mathrm{DM}}, \hat{\theta})$, and $\hat{\hat{\theta}}$ are the nuisance parameters that maximize the likelihood for a given σ_{DM}. The distributions of $q(\sigma_{\mathrm{DM}})$ was estimated with $O(10^4)$ toy MC simulations of experimental data, including scientific data and ancillary measurements.

Figure 2.33 (left) shows the expected sensitivity of XENONnT. For the full calculation, see ref. [100].
The figure (left) expresses the median exclusion limit at 90% CL on the SI WIMP-nucleon cross-section. Thus, with an exposure of 20 t y, XENONnT could probe cross sections more than an order of magnitude below the current best limits set by XENON1T [96], reaching the highest sensitivity of $1.4 \times 10^{-48}\,\mathrm{cm}^2$ for a WIMP of $50\,\mathrm{GeV/c}^2$. Projected median discovery levels of XENONnT with significance 3σ (dashed) and 5σ (doted) are shown with sensitivity (solid). The minimum WIMP cross-section at which the experiment has a 50% chance of observing an excess of significance greater than 3σ (5σ) is $2.6 \times 10^{-48}\,\mathrm{cm}^2$ ($5.0 \times 10^{-48}\,\mathrm{cm}^2$), corresponding to a mass of $50\,\mathrm{GeV/c}^2$.
Figure 2.33 (right) gives the sensitivity and discovery power for a WIMP of $50\,\mathrm{GeV/c}^2$ as a function of exposure.

For ER events, the main background source is ^{222}Rn. In order to evaluate the effect of ^{222}Rn on the sensitivity of XENONnT, Figure 2.34 presents the sensitivity of XENONnT at a WIMP of $50\,\mathrm{GeV/c}^2$ for activity concentrations of ^{222}Rn up to 5 μBq/kg. The XENONnT goal of 1 μBq/kg and the 4.5 μBq/kg ^{222}Rn activity concentration achieved with XENON1T [138] are indicated by gray dotted lines. At 4.5 μBq/kg, the sensitivity is ~25% lower than the XENONnT goal of 1 μBq/kg.

Figure 2.35 shows the measurements taken during the SR0 scientific run, confirming that the goal of 1 μBq/kg is a value well within reach of XENONnT.

The goal of 1 μBq/kg has recently been reached and even exceeded, mainly thanks to liquid phase purification.

2.5 Summary

After the considerable efforts made in designing, assembling, and commissioning the XENONnT detector during arduous periods caused by the COVID-19 pandemic, the XENONnT experiment started taking its first science run (SR0)

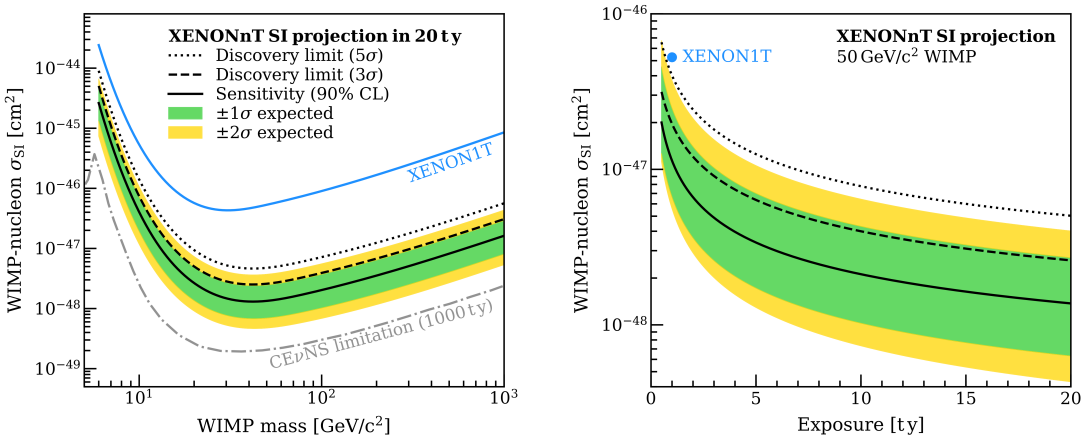

Figure 2.33: The XENONnT sensitivity and discovery power projections in the search for spin-independent WIMP-nucleon couplings. (Left) Median 90% CL exclusion limit (black solid line) for a 20 t.y exposure, with the 1σ (green) and 2σ (yellow) bands. The current strongest exclusion limit obtained with XENON1T [96], is shown in blue. The gray dashed-dotted line represents the discovery limit of an idealized LXe-based experiment with CEνNS as unique background source and a 1000 t.y exposure [137]. The atmospheric neutrino background would significantly slow down the improvement of the discovery potential with increasing exposure below that line. (Right) Sensitivity as a function of exposure, for searching for a 50 GeV/c^2 WIMP in the assumed 4 tons fiducial mass. The dashed (dotted) black lines in both panels indicate the smallest cross-sections at which the experiment would have a 50% chance of observing an excess with significance greater than 3σ (5σ). A two-sided profile construction is used to compute the confidence intervals. (Figure from [100]).

around the middle of 2021 for about six months. The SR0 data is currently being studied, with particular attention given to investigating the excess ER events detected by XENON1T at low energy [99]. The latest publication from XENONnT has just been released and excludes this excess [101]. If XENONnT does not detect any dark matter excess during its lifetime, it can nevertheless place some of the best exclusion limits worldwide on the direct search for dark matter. Exclusion limits are helpful for theoretical modeling, evaluating past dark matter detection claims, and as beneficial information for the next generations of dark matter experiments.
XENONnT has pioneered many new purification and cleaning techniques, which will undoubtedly be used by the next generation experiment, as part of the new XENON-LUX-ZEPLIN-DARWIN (XLZD) consortium [139].

2.6 Summary of my contributions to XENONnT

I joined the LPNHE XENON group on October 1, 2019, as a Ph.D. student, studying the sub-GeV dark matter with XENONnT data as the subject of my thesis. By joining this group, I was honored to be a member of the XENON and

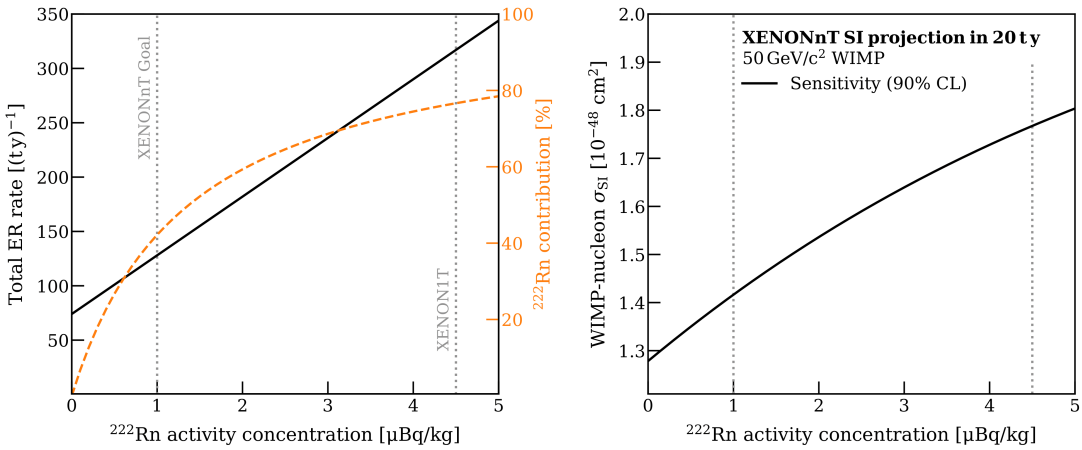

Figure 2.34: (Left) ER background rate in the (3, 100) PE cS1 observable ROI as a function of the ^{222}Rn concentration in LXe. The orange dashed line represents the ^{222}Rn fractional contribution to the total ER background. The dotted grey lines indicate the XENONnT goal of 1 μBq/kg and the 4.5 μBq/kg ^{222}Rn concentration achieved in XENON1T [138]. (Right) Projection of the XENONnT sensitivity to spin-independent couplings of a 50 GeV/c^2 WIMP as a function of the ^{222}Rn concentration in LXe. (Figure from [100]).

DARWIN collaborations.

When I started my thesis, the XENONnT detector was not yet in the construction phase. However, there was hope that the first XENONnT data acquisition would be scheduled for mid-2020. Thus, while waiting for XENONnT data, I joined the computing working group.

I started my steps in the computing working group by taking the responsibility of developing the XENONnT Offline Monitoring tool or XOM. This task consisted of creating a website and web applications that followed key parameters of the detector (such as the electrons lifetime, the light and charge yields, etc.) almost instantaneously via a dedicated web portal.

I was in situ in February 2020 when the construction operations were at their peak. I participated in assembling the detector on the surface and the cryostat underground. I also had the task of treating the copper shaping rings and the electrodes with an acid solution. This treatment aimed to prevent the emission of single electrons by the electrodes. This treatment (and the new purification system) allowed a single electron rate several orders of magnitude lower than that of XENON1T with the constraint that the detector is more extensive and, therefore, this kind of background should be more substantial.

During the year 2020, and at the same time as the first XENONnT data began to be taken, I was responsible for transferring data from the LNGS to the various nodes of the computing grid and accessing the data by analysts.

At the beginning of 2021, the first calibration data started to be taken by XENONnT, and that is when I left the computing working group to focus on analysis. With these calibration data, I made several studies that aimed to know the detector's response at low energy, such as the consistency between the

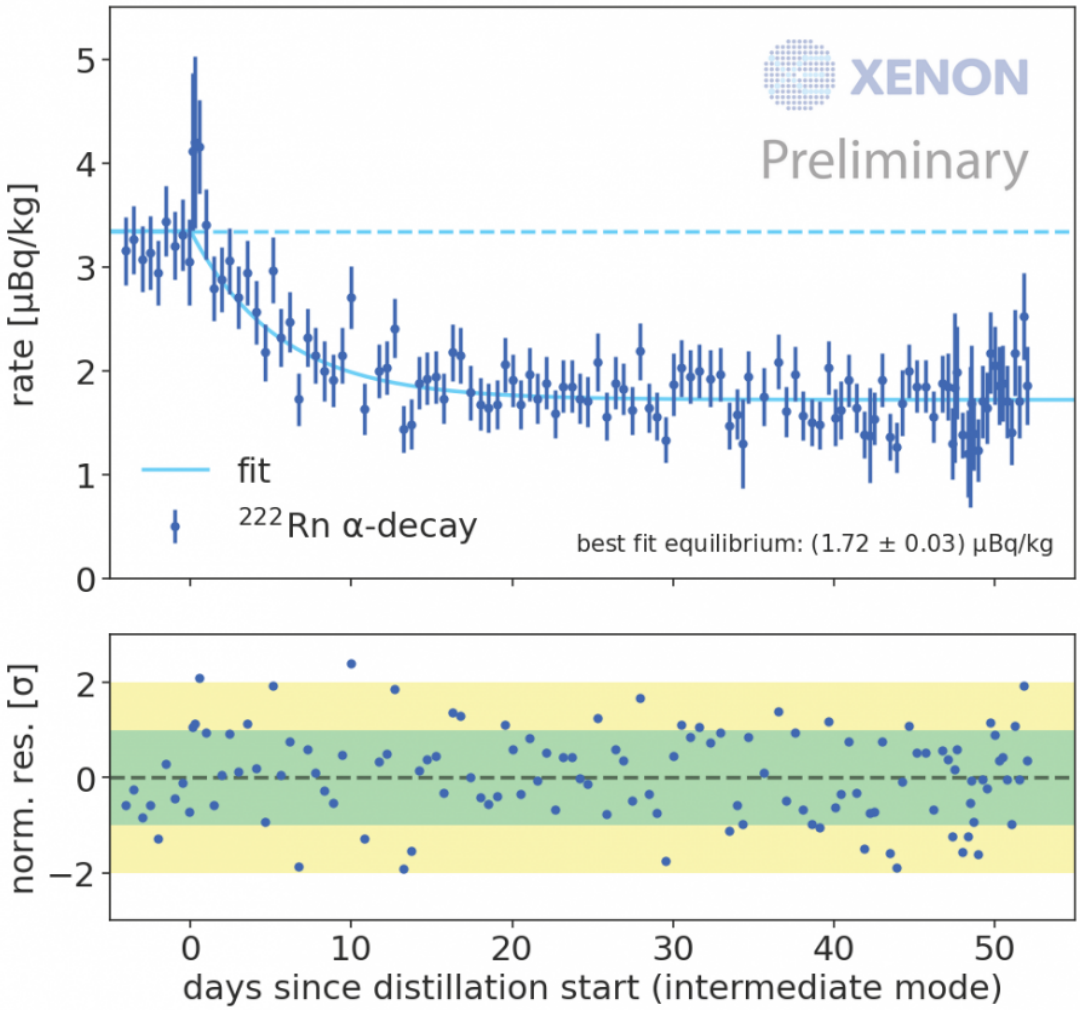

Figure 2.35: Evolution of the radon rate in XENONnT during initial distillation. The distillation is in an intermediate gas-only mode, pending cleaning of the column to be compatible with the high electron lifetime achieved. An additional rate reduction by a factor of ~ 2 is predicted for the final column mode based on previous data from distillation commissioning.

parameters measured by slow control and those obtained by data analysis, the study of small S2, and investigating their origins, verifying data processing..etc. A large part of this work consisted in making machine learning algorithms that aim to classify S1 and S2 signals at low energy.

Towards the end of 2021, my work migrates to the main subject of my thesis, consisting of the study of sub-GeV dark matter with XENONnT data. This work will be the subject of the following chapters.

Chapter 3

Analysis of single electron signals with XENONnT

In an ideal situation, an event in the detector produces only two signals corresponding to S1 and S2 peaks. However, an observation of the waveform of the events recorded by the detector shows the presence of multiple S2 signals of small intensity which follow or even precede the main (or primary) S2 signal. These peaks correspond to the emission of single electrons via various mechanisms, which will be detailed in this chapter. In addition, a phenomenological study of the observation of single electron charge signals by the XENONnT experiment will be presented, followed by a discussion on how this background could be modelized.

3.1 Introduction

Small charge signals have been observed in dark matter dedicated LXe TPCs since their first fully operational generation, such as XENON10 [140] ZEPLIN-II [141] and PANDAX-I [142]. Their observation naturally led to wondering about the mechanisms to which we can attribute the creation of these signals within the TPC. One consensus mechanism is the photoionization of impurities by the light produced in the gas phase by the main S2 [141, 143, 144, 145]. Nevertheless, other mechanisms are also proposed, including the photoelectric effect on the metallic parts of the TPC, the delayed emission of electrons trapped under the surface of the liquid, the capture and the release of drifting electrons by electronegative impurities, the possible existence of long-lived excited states of Xenon, and the Malter effect[1], which results in the emission of electrons from the cathode [146].

Since a low background experiment such as XENONnT must be able to identify and reject all possible sources of background noise, the causes of single electrons must, therefore, be investigated and finally modeled to extend the detector's sensitivity to the entire energy range accessible to it. Moreover, this would allow detectors such as XENONnT, which have proven their potential at

[1]The Malter effect, also known as grid electron emission, is a secondary emission which occurs on a thin insulating layer deposited on a conductive substrate. When the charge build-up rate in the cathode's localized spot is higher than its removal rate, a secondary charge current is created in that spot.

high energy, to be sensitive to signals of leptonic interaction with dark matter, which has been a trendy field in recent years. The study of this type of interaction and its exclusion limit using the first XENONnT data will be the subject of Chapter 4 of this manuscript. Furthermore, in addition to being a background source for the search for leptophilic dark matter, single electrons are also a handy tool for characterizing the detector, which will be discussed in this chapter.

3.2 Phenomenology of single electrons

3.2.1 Single electrons from photoionization

Figure 3.1 illustrates the mechanism recognized as the primary source of single electrons (SE), namely the photoionization of impurities by the S2 light. The photons from S2 signals have the same energy as those from S1 signals ($\lambda \sim 178$ nm). Since Xenon is highly transparent to its scintillation light and as it is produced isotropically, half of the photons emitted as a S2 signal will penetrate the liquid phase.

Following a scattering with an S2 photon, an impurity will release an electron that will drift towards the gaseous phase and thus follow the same path as all ionization electrons released in the liquid phase. If impurities do not absorb it, the electron will lead to a new emission of an S2 signal in the gaseous phase, corresponding to a single electron signal.

Of all the different impurities molecules in LXe, negatively charged impurities, such as O_2^-, are considered the primary photoionization source. This hypothesis is supported by the fact that these negative ions can have relatively low ionization energy (< 1 eV) [145]. In contrast, molecules of neutral impurities such as O_2, N_2, and H_2O generally have ionization energies greater than 10 eV, which seems incompatible with the energy of S1 or S2 photons ($\lambda \sim 178$ nm, which is approximately equivalent to 7 eV).

3.2.2 The waveform properties of single electrons

The first property of the single electron wave function corresponds to the time period when these signals are emitted. As shown in Figure 3.2, SE signals are abundant after a primary S2 signal. If SE signals precede the primary S2, these are probably produced by the S1 photons; hence their marginal number compared to the SEs which follow the primary S2. They can also be produced by the S2 of the preceding event or by a mechanism other than photoionization.

The second important characteristic consists of the spectrum of SEs. The definition of SE assumed by XENON uses the term single electron to name signals of one to a few electrons, corresponding to signals less than ~ 150 PE (up to a pile-up of 4-5 electrons). An example of the SE spectrum is shown in Figure 3.3.

The peak at around 35 PE in Figure 3.3 corresponds to the average light produced by an extracted electron in the gas phase (called the single electron gain or

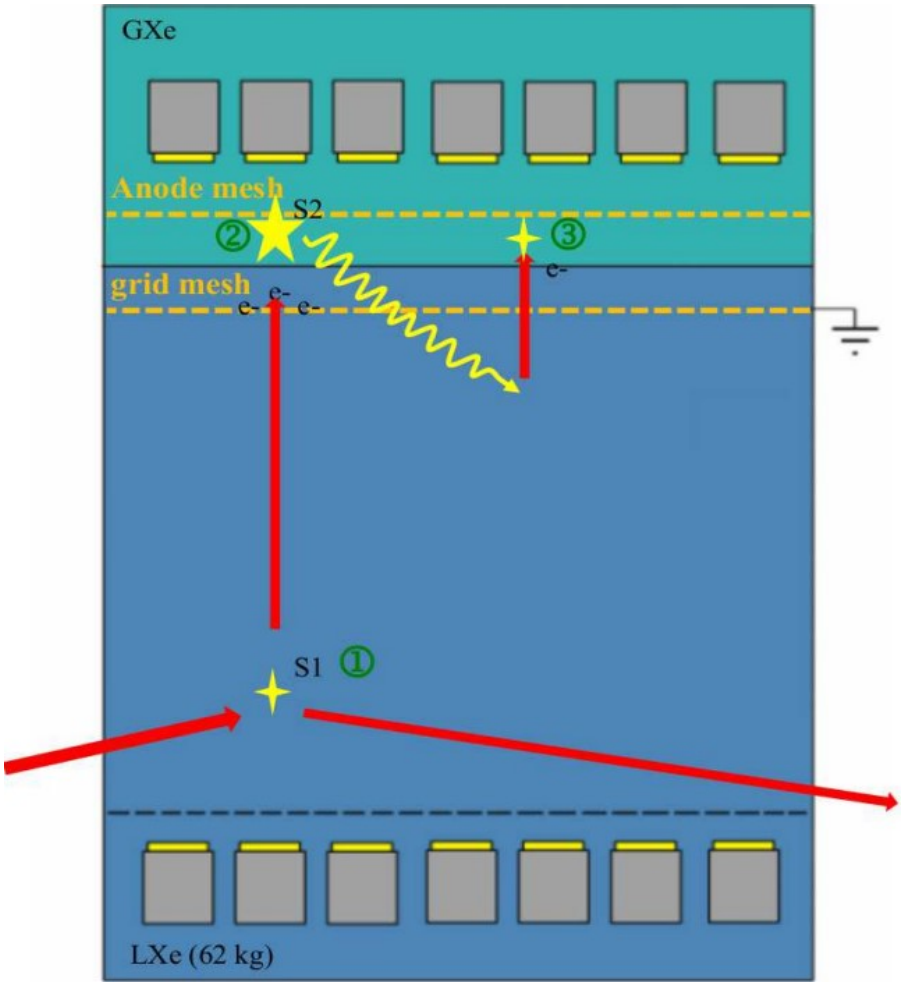

Figure 3.1: A schematic representation of the primary single electron production mechanism. (this illustration is from XENON100, hence the "62 kg").

secondary scintillation gain). The second peak, around 70 PE, corresponds to the temporal coincidence leading to the extraction of two electrons simultaneously towards the gas phase. Nevertheless, this second peak can also be due to the sum of two distinct signals but very close in time (< 300 ns).

In order to characterize the average light emitted by a single electron accelerated in the gas phase, the contribution of each population of electrons must be identified and taken into account. For this purpose, the spectrum must be fitted with the appropriate function. A first approach would be to use a sum of Gaussian distributions representing the distribution of emitted light for each population of single electron signals. However, the spectrum regime is no longer Gaussian at low energy.

To correct the fit of the low energy spectrum (< 20 PE), XENON100 (and partially XENON1T) used a Fermi-Dirac distribution to account for the detection inefficiency of S2 at very low energy. Nevertheless, XENON1T and especially XENONnT has a detection efficiency that reaches 100% around 1-5 PE (see Figure 3.9), making the Fermi-Dirac distribution unneeded. Therefore, a new model is necessary (see Section 3.3).

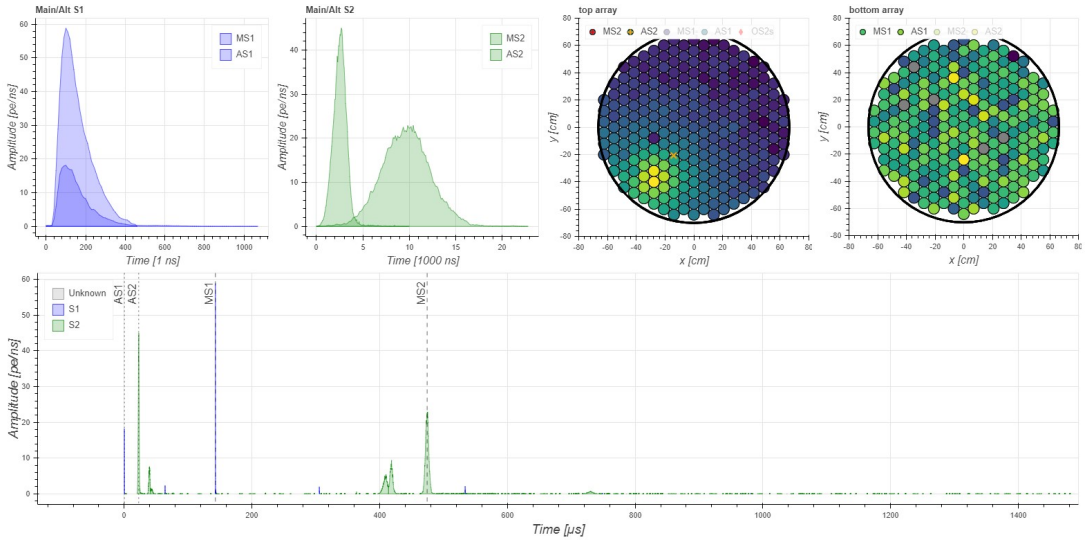

Figure 3.2: Waveform of a ^{83m}Kr calibration event showing the primary S1, S2 as well as the alternate S1, S2 (see Section 2.2.10) in addition to the S2 signal tail, which corresponds to single electrons.)

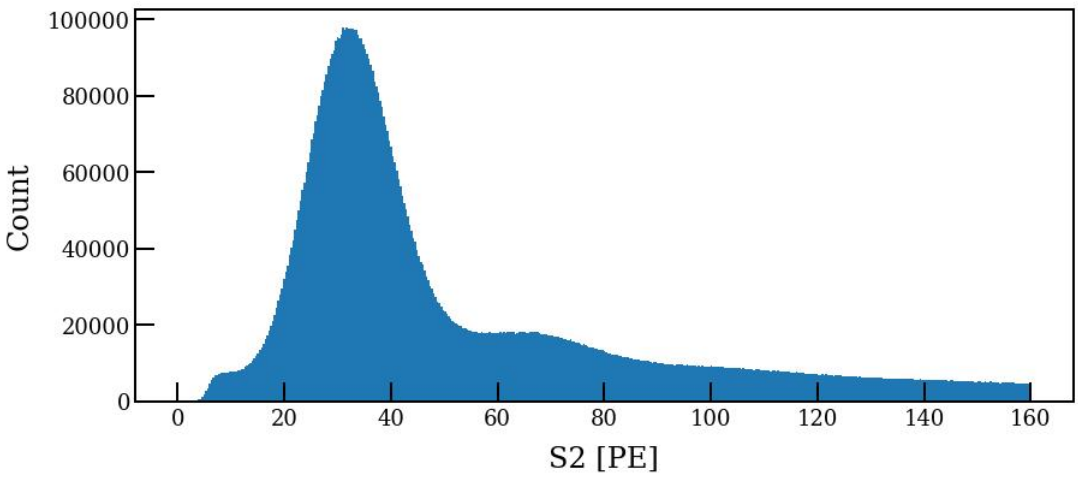

Figure 3.3: Raw spectrum of low energy S2 peaks (single electrons).

3.2.3 Single electrons rate

When large S2 signals are detected, a tail of SE signals follows them temporally; these signals originate from impurities photoionized by S1 photons and by the S2 light in the GXe. This is illustrated in Figure 3.4.

As shown in Figure 3.4, the rate of SE is lower for XENONnT compared to XENON1T. This observation is a solid signal to predict that the XENONnT limit will be better for light dark matter since the rate of SE is the main limiting factor for this study.

The spectrum of primary S2 interactions extends over several orders of magnitude, from five to hundreds of thousands of electrons for the most energetic interactions. An interesting analysis would be to look at the relationship be-

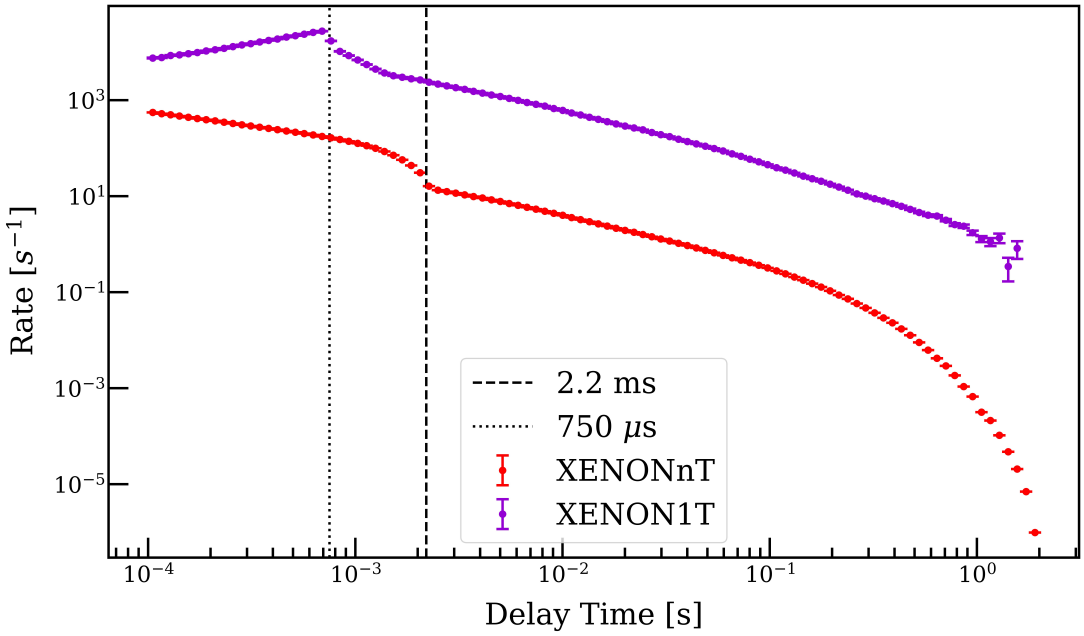

Figure 3.4: The rate of delayed single electron emission as a function of time following an energy deposition in the detector. Also shown the rate observed by XENON1T. The dotted vertical line at 750 µs and 2.2 ms indicates the maximum drift time in XENON1T and XENONnT, respectively. A high rate of delayed SE is observed for several times the maximum drift time. This is due to scintillation light produced from the extraction of photoionization electrons into the GXe region, producing additional photoionization electrons.

tween the number of single electrons observed and the energy of the primary S2 signals.

However, this cannot be done optimally before having the corrected energy spectrum of the S2 for the XENONnT data (which was not yet the case when I carried out this analysis). That said, a preliminary study could be made with the very high energy data of the S2 spectrum, which are the least likely to be significantly modified by a correction, as the fraction of energy lost before detection would be minimal. This study is presented in Figure 3.5, whereas the size of primary S2 increases, the higher the number of delayed electrons is observed, following a relation close to a power law. This power-law dependence does not seem to agree with previous studies [147, 148, 149] that observed a simple proportionality relationship. This may still be caused by the fact that the S2 spectrum is not corrected.

On the other hand, and as illustrated in Figure 3.6, the study of the variation in the rate of single electron signals as a function of the time delay from the preceding primary S2 represents supplementary proof favoring the photoionization hypothesis as the main source of this background.

Figure 3.6 derives the rate of multi-electron signals (up to 4 electrons) as a function of the delay Δt after the previous S2 signal (S2> 150 PE). The method to derive the rate is to fit the low-S2 spectrum with a sum of 5 Gaussians and

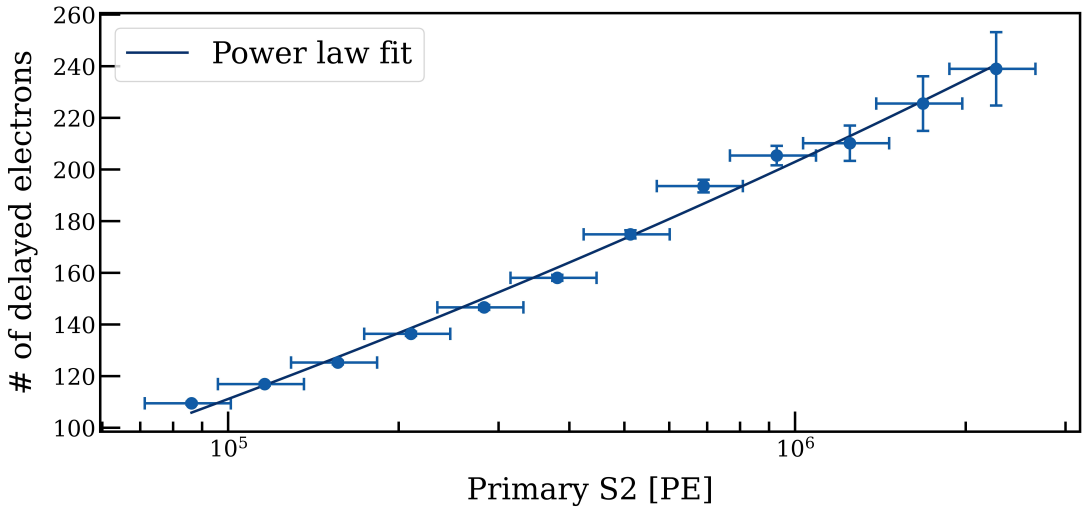

Figure 3.5: The number of delayed electrons observed from 0.1 ms to 1 s after the S2 primary as a function of the size of the S2 primary in photoelectrons. A general trend towards more delayed electrons after larger S2 primaries is observed. This trend seems to follow a power law, as shown by the fit.

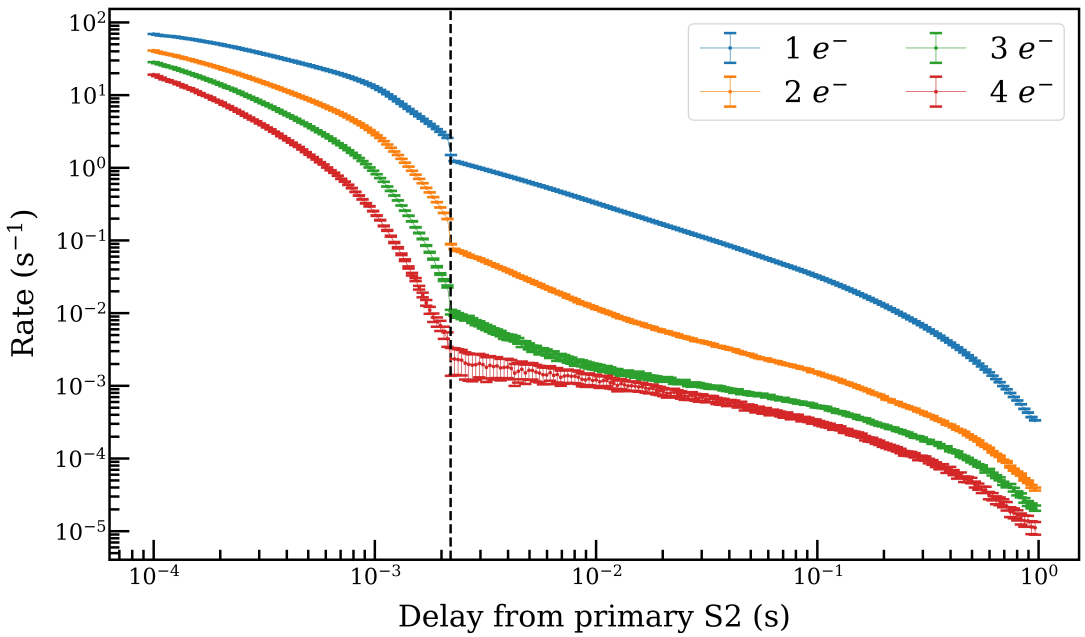

Figure 3.6: Rate of first 4 multi-electron signals as a function of the delay after larger S2s (> 150 PE). The vertical dotted line shows the value of the maximum drift time (2.2 ms).

define the rate as the area under each Gaussian. Afterward, the fit was repeated for 250 values of the delay Δt, in logarithmic space.

An analysis of Figure 3.6 leads to the following observations:

- The statistical uncertainty is negligible everywhere and for any multi-electron population. The only exception appears to be for $N = 4$ in the [2,10] ms range. However, this is simply due to the combination of two

factors: the lack of statistics coming from the drop in the rate and the choice of logarithmic binning.

- After the maximum drift time (2.2 ms), $N = 1$, $N = 2$, and in less extent, $N = 3$ seem to follow a power law, as was the case in previous XENON studies [147, 148, 149]. This could be due to second and third-order photoionizations (photoionization from the light of single electrons creating other single electron signals). This is compatible with the fact that this component is dominant between 2 and 6 ms (due to the dimensions of the TPC). For $N = 4$, this is not evident since the rate is approaching another unknown source of electrons production, for which n-th order photoionizations become subleading.
- Above ~ 10 ms, all distributions $N > 2$ follow similar trends.
- Finally, above 100 ms, even if not evident, there are some slight changes in the slopes, showing maybe the time range after which where single electrons are not correlated anymore to the previous primary S2.

3.3 Modelization of the single electrons spectrum

To establish a reliable model for this single electron signal, one must consider all the underlying physical mechanisms that lead to the SE spectrum. It all starts with a single electron as it accelerates through the gas phase. During its journey through the gas phase, this electron will produce n photons according to a Poisson distribution:

$$\mathbb{P}(n|\lambda) = \frac{\lambda^n}{n!}\mathrm{e}^{-\lambda}, \tag{3.1}$$

with λ the average number of photons produced per electron.

Then the tail of the distribution is probably due to temporal or accidental coincidences of two or more (k) electrons. The scintillation produced by each of them will produce n photons distributed according to the distribution $\mathbb{P}(n \mid k\lambda)$. It will be a distribution with a mean value $k\lambda$ and standard deviation $\sqrt{k}\lambda$. Thus, a first approach to describe the spectrum of Figure 3.3 would be a sum of Poisson distributions representing the S2 distribution of single electrons and their pileups as a sum of Poisson distributions.

However, this model would not be exact because the recorded signal does not correspond directly to the number of photons created by the electrons. What is recorded and what appears in Figure 3.3 corresponds to the number of electrons (photoelectrons) generated by the incident photons on the PMTs. The current multiplication in the PMTs follows a stochastic process that ultimately changes the Poissonian distribution of the signal, making it Gaussian; however, as seen before, the Gaussian model is inadequate.

A more efficient model [148] would be to try to spread the underlying Poisson distribution, which describes the actual physical process of scintillation, with a Gaussian distribution which would explain the spreading around a mean value μ, with a standard deviation σ. For example, for n photons, this would give:

$$f(n|\mu,\sigma) = \int \mathrm{Poisson}(n|\lambda)\mathrm{Normal}(\lambda \mid \mu,\sigma)d\lambda. \tag{3.2}$$

Here, the parameter μ corresponds to the estimation of the secondary scintillation gain since it will be centered around the average value of the number of photons produced. Similarly, σ corresponds to the standard deviation estimate associated with μ as in the Gaussian model. To extend the model to N populations of electrons, it suffices to sum over the Gaussian, such that:

$$f(n|\mu,\sigma) = \sum_{k=1}^{N} \int \text{Poisson}(n \mid \lambda)\text{Normal}(\lambda|k\mu,\ \sqrt{k}\sigma)d\lambda. \tag{3.3}$$

It is now possible to translate this model in terms of the energy, namely the measured S2. This is done by replacing in relation (3.3) the Poisson distribution with the so-called continuous Poisson distribution [148, 150] and writing the model describing the spectrum as:

$$f(x|\mu,\sigma) = \sum_{k=1}^{N} \int \frac{\lambda^x e^{-x}}{\Gamma(x+1)}\text{Normal}(\lambda|k\mu,\ \sqrt{k}\sigma)d\lambda. \tag{3.4}$$

Figure 3.7 presents the fit of the single electron spectrum based on model (3.4). With this fit, it is possible to estimate the secondary scintillation gain with high precision, knowing that this gain is one of the essential parameters of the detector to perform corrections. For example, with the extraction efficiency and the electron lifetime, the single electron gain determines the S2 gain (g_2) necessary to reconstruct deposited energies (see Section 2.1.3).

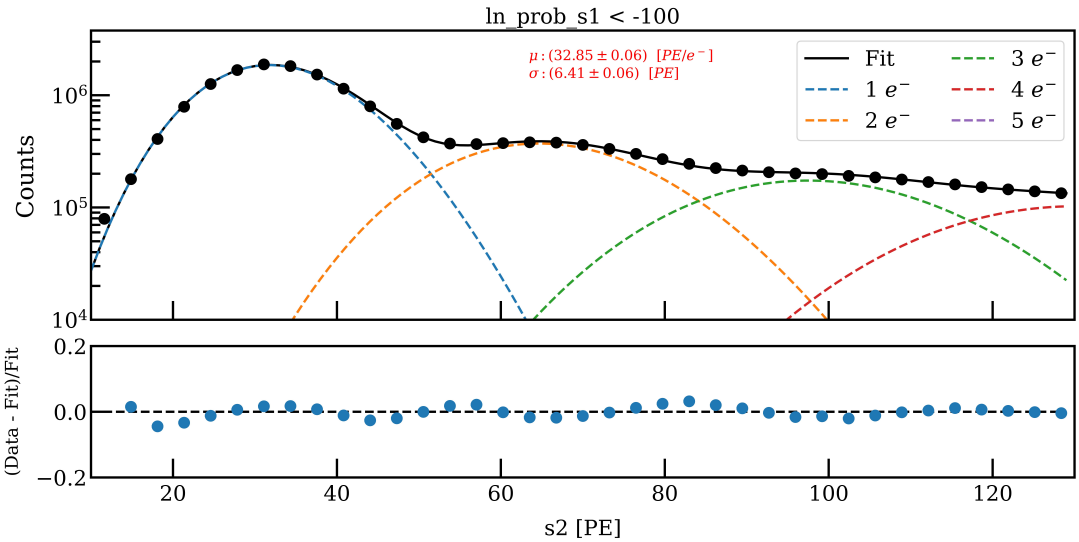

Figure 3.7: The fit plot of the SE spectrum with model (3.4), choosing $N = 5$. In this figure, it is possible to see the value given by the fit for the secondary scintillation gain μ, its standard deviation σ, and the contribution of each electron population to the spectrum. The value `ln_prob_s1` < -100 indicates the probability limit chosen to cut the S1 (see Section 2.2.9).

It should nevertheless be noted that the fit of Figure 3.7 was made for S2 signals between 15 and 130 PE. Values below 15 PE are biased by contamination

of S1s waveform identified as S2. On the other hand, 130 PE is the maximum value for which model (3.4) is defined numerically; this is due to the extremely rapid growth of the gamma function, quickly reaching the maximum values accepted by most computer languages[2].

As indicated in Section 2.2.9, classifying low energy signals (especially for signals < 20 PE) is very challenging. Knowing the parameter `ln_prob_s1`, which gives the probability that a signal is S1 or not, the value for this parameter selected for high energy signals is such that `ln_prob_s1` < -50. This value is not the most suitable for low-energy signals, where distinguishing between signals is even more difficult. In this context, the fit of the SE spectrum can be helpful.

Figure 3.8 shows the fit of the SE spectrum for different values of `ln_prob_s1`. The value of `ln_prob_s1` < -100 appeared to be the best for the SE signals.

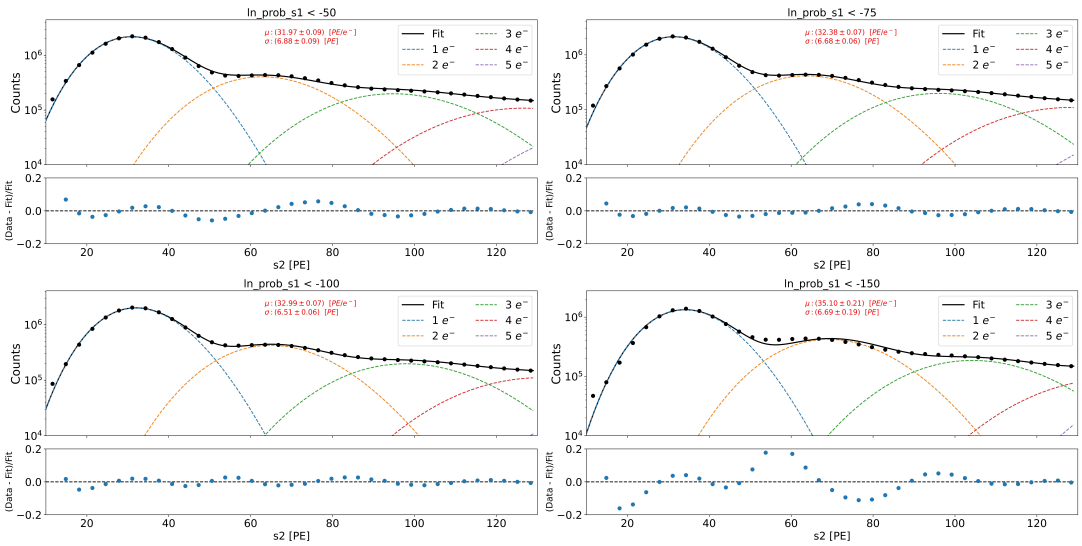

Figure 3.8: Fit of the SE spectrum obtained with different limits on `ln_prob_s1`.

3.3.1 Comparison with a fit with a sum of Gaussians

While the Poisson + Gaussian model has been widely studied and seems well-motivated, it is not overwhelmingly better than a pure Gaussian sum fit. Moreover, given the bias that the low energy classification of signals can have, it is almost always necessary to cut the low part of the spectrum.

As an example, Figure 3.9 illustrates the curve of the two distributions as well as the XENONnT detection efficiency of the S2 signals.

When fitting both models, they had exactly the same parameters. In terms of execution time, the Gaussian fit is faster (0.1 s against 12 s); this is explained by the complexity of the numerical convolutional calculation for the Poisson + Gaussian. This speed means that using a pure Gaussian fit is more judicious for

[2] $\Gamma(131) \approx 10^{220}$!

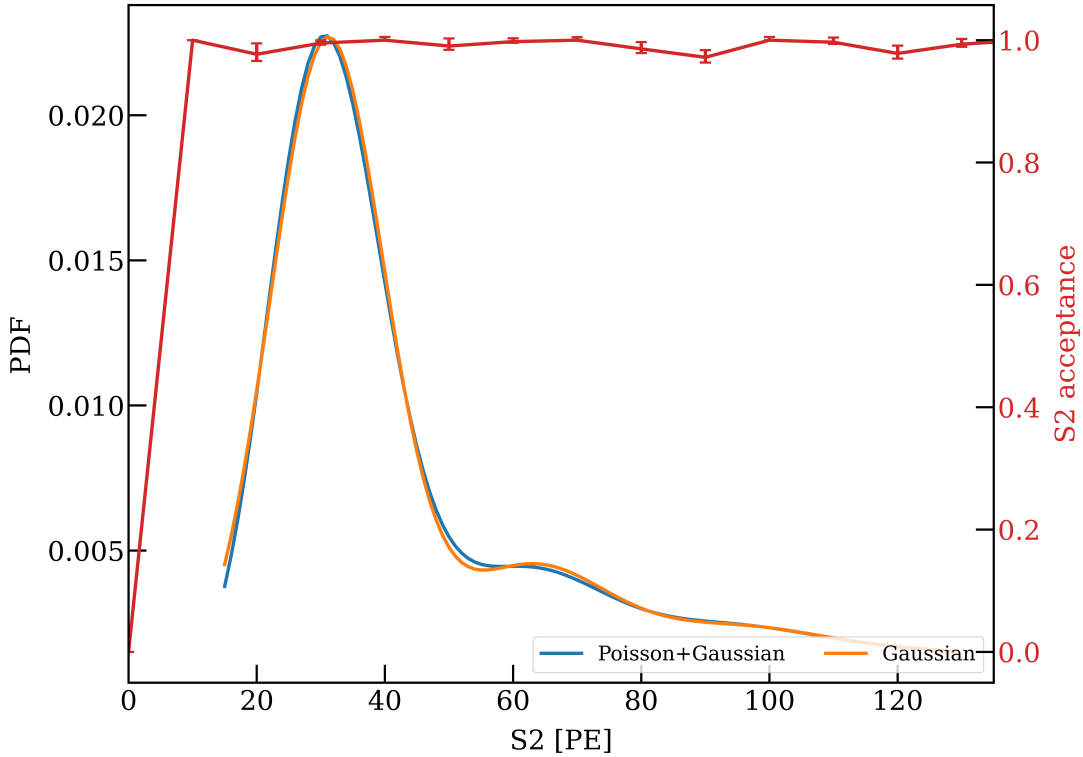

Figure 3.9: Comparison between the distributions given by a fit of 5 Gaussians (orange) and that given by model (3.4) with $N = 5$ (blue). The detection efficiency of S2 is also shown (red).

calculating the gain in a large number of different datasets.
In terms of results, model (3.4) gives a slightly higher gain (31.65 ± 0.10 vs 31.05 ± 0.04 PE/e$^-$) than the pure Gaussian model due to the shift caused by the Poisson distribution component.

Now, we must select a one-electron population and test which of the two models fits this population better. The selection is made according to the following criteria in Table 3.1. Furthermore, the result of the selection in the 50% width (width of the waveform at 50% of its height) as a function of the energy as well as the fits are given in Figure 3.10.

Table 3.1: List of cuts to select the one-electron population of the SE spectrum.

Parameter	Cut
S2 value	$15 < S2 < 130$ PE
50% width	$100 < \text{width} < 500$ ns
Radius	$r < 45$ cm
Proximity of the nearest peak	$\Delta t > 100$ ms

Table 3.2 summarizes the two fits of Figure 3.10 with the parameters of the goodness of fit.
Given this constraining selection, the Gaussian fit seems to give the best fit.

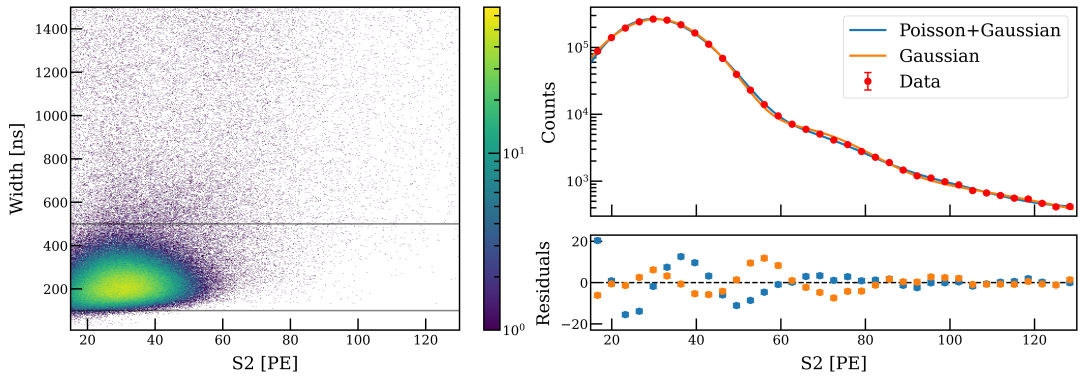

Figure 3.10: (Left) The distribution of selected events in width vs. energy parameter space shows the selected region within the horizontal gray lines. (Right) Comparison between the fit of the two distributions with isolated low-energy S2 events.

Table 3.2: List of parameters and the chi-square extracted from each distribution.

Parameter	Poisson+Gaussian	Gaussian
Gain [PE/e$^-$]	31.05 ± 0.06	30.52 ± 0.04 PE
σ [PE]	7.35 ± 0.07	9.46 ± 0.04
χ^2/NDF	7.81	1.40

3.4 Single electrons as a calibration tool

The single electron background can be used to study the detector response and it is an intrinsic source to calibrate the detector and monitor some of its key features. This is explained by the fact that this background is always present; moreover, it is present in large quantities, even in short data sets and in the data set used for searching dark matter.

3.4.1 The electrodes sagging

For a long time, XENON has observed that the anode and gate electrodes show signs of sagging. This sagging is a combination of three effects: gravitational force, buoyant force, and electrostatic force, the latter being the most significant contributor (see Figures 2.3 and 2.12 for electrode geometry). Wire sagging plays a fundamental role in defining the S2 region and the resulting signal production: a decrease in wire distance from the electrodes leads to a local enhancement of the electric field, meaning an XY dependence of the S2 generated, which should be avoided, even if it is possible to correct it in analysis data.

Thus, to avoid this sagging, and given that the XENONnT detector is wider than its predecessor, it was then decided to add transverse wires to the anode and the grid to stabilize them as much as possible. As a result, the electrodes are made of parallel wires and a few transverse wires, two on the gate, above the parallel wires, and four on the anode, below the parallel wires (see Figure 3.11).

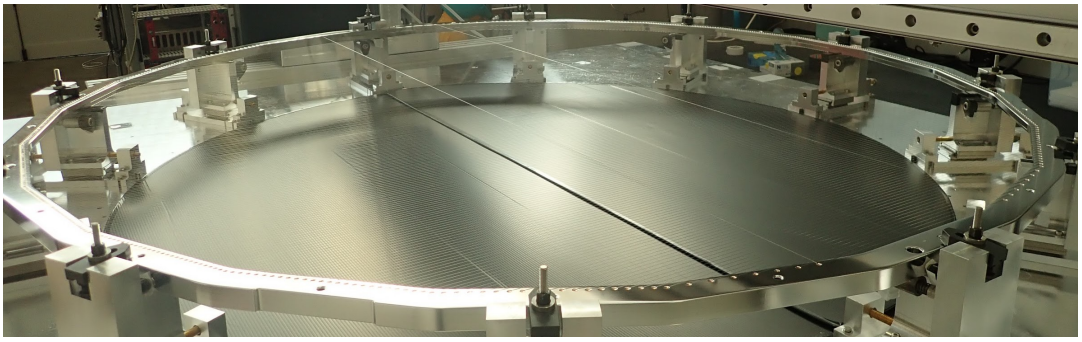

Figure 3.11: Photo of the gate where it is possible to see the two additional transverse wires.

On the other hand, to correct the sagging, it is necessary to estimate it, and in this perspective, the SEs play a crucial role.
This is done first by evaluating the width[3] of SEs signals as a function of XY; a larger width indicates a larger separation between the electrodes.

At first, it is necessary to select the extent of the width of the SEs; this is illustrated in Figure 3.12). Thus, the latter is apparently between 100 and 500 ns.

It is essential that in this study, the dataset contains only single electrons (1 electron signal); otherwise, stacking all the populations will cause the width obtained to be biased, and therefore the argument that the width of these signals must be the same everywhere in the XY plane cannot be true.

After evaluating the typical width of a single electron signal, it is possible to make a map showing the width of SEs (containing a single electron) and see the extent of inhomogeneity due to electrode sagging. This is shown in Figure 3.13. This figure has been obtained by projecting a three-dimensional histogram of each signal's x-y position and width into a two-dimensional histogram of the x-y position where each bin contains the average width of the signals in it.

By observing Figure 3.13, it is clear that the distribution does not follow a radial symmetry, as expected in the case where the extraction field is uniform everywhere, but rather shows a longitudinal asymmetry. The longitudinal inhomogeneity is due to the presence of the transverse wires (see Figure 3.23); without the wires, the inhomogeneity should be exactly central if the detector is perfectly vertical, or otherwise, it should have a slight shift with respect to the detector center (0, 0) in the XY plane.

After having tried several models, the ellipsoidal model ($f(x,y) = ax+by+c+(x^2+y^2-r_{max}^2)/2d$) is the one that gives the best fit. This model would undoubtedly be more suitable if the transverse wires were not present. The result of the fit is presented in Figure 3.14. With the modeling, it would then be possible to see the extent of the sagging in the XY plane and thus take it into account to make the corrections.

It should be noted that despite residual inhomogeneity, the difference in width was greatly improved. This was done through the various configurations (anode

[3]The time range in the waveform containing 50% of the total peak area.

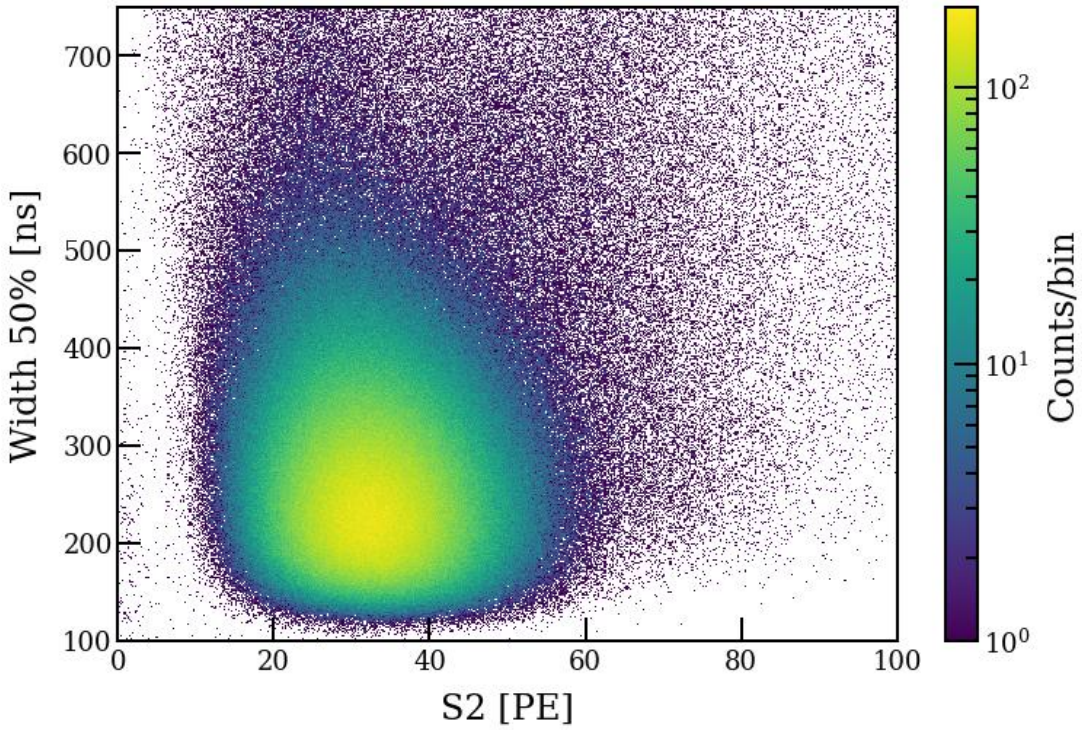

Figure 3.12: Width signal as a function of S2 of single electrons population containing 1 electron. Data extracted from XENONnT SR0 background data set.

voltage, liquid level, etc.) to minimize the sagging effect.

3.4.2 Secondary scintillation gain as a function of the XY position

The secondary scintillation gain map can be obtained in two ways. Either by dividing the XY plane into multiple bins and fitting the SE spectrum for each bin or selecting a window corresponding to the unique electron peak in the SE spectrum and calculating the average area for each bin. In this case, the calculated average value is a less accurate estimate of the secondary scintillation gain. Nevertheless, this method will be used since it is sufficient to show the evolution of gain in the XY plane. Using the second method, the spatial dependence of the secondary scintillation gain is calculated and shown in Figure 3.15.

The secondary scintillation gain as a function of XY is neither homogeneous nor characterized by radial symmetry, as might be expected at first glance from the analysis in the previous section. The only clear and identifiable trace is the transverse wires, which seem to modify the gain quite strongly.
The fact that the gain does not follow the sagging of the electrodes can be explained as follow; even if the electrons quickly acquire the energy necessary to produce secondary signals (since the electric field is locally greater towards the center), on the other hand, they have less distance to do so.
The behavior and the modelization of the secondary scintillation gain will be the subject of the next sections.

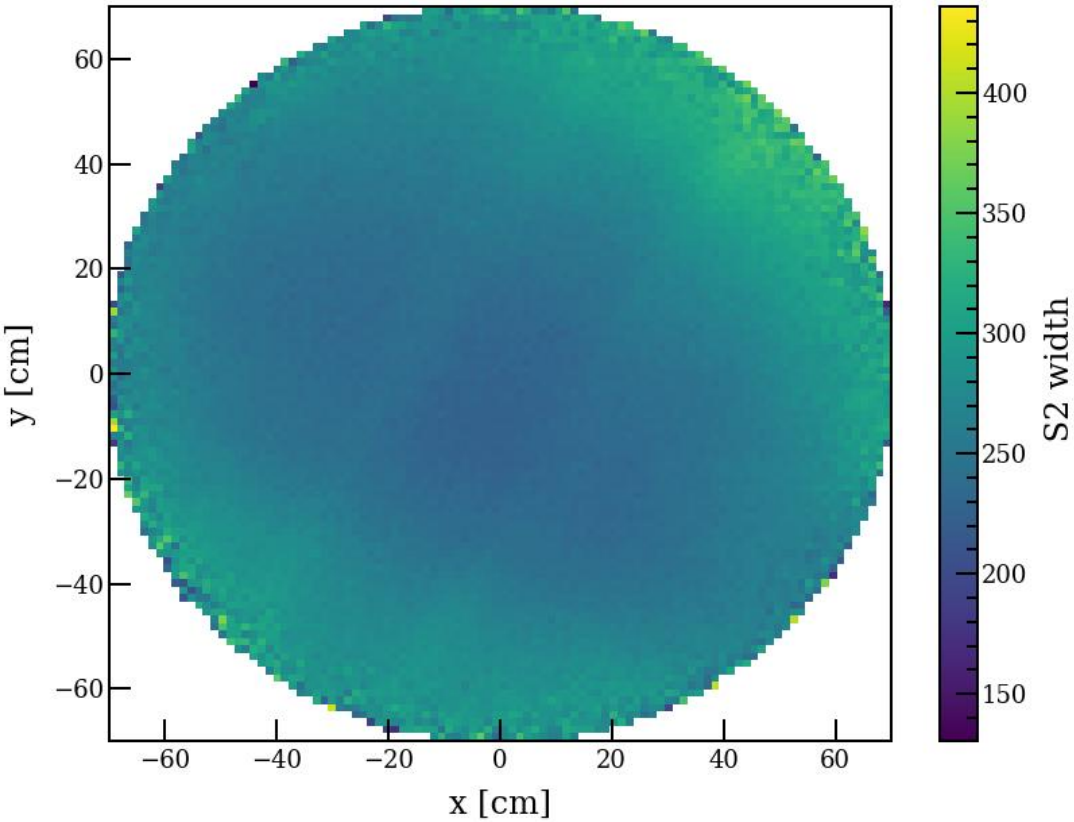

Figure 3.13: The width of single electron signals (1 e^-) as as a function of their reconstructed position.

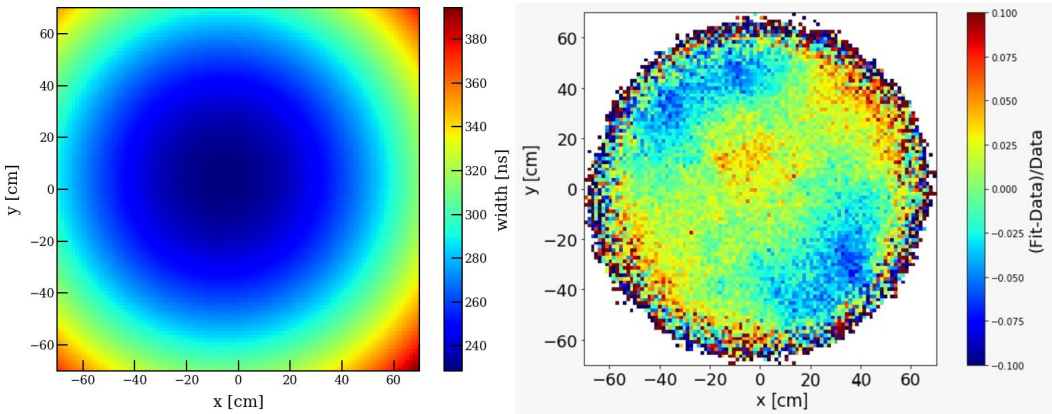

Figure 3.14: (Left) Map obtained with the fit function used. (Right) The difference between the data and the result of the fit function for each bin. The fact that the fit is not centered in (x, y) suggests that the TPC is not perfectly vertical, and this translation of the center is therefore related to gravitational effects.

3.4.3 Time evolution of the secondary scintillation gain

The secondary scintillation gain temporal stability was calculated for the whole first science run (SR0: 5697 runs for an overall duration of more than 137 days). The result is shown in Figure 3.16.

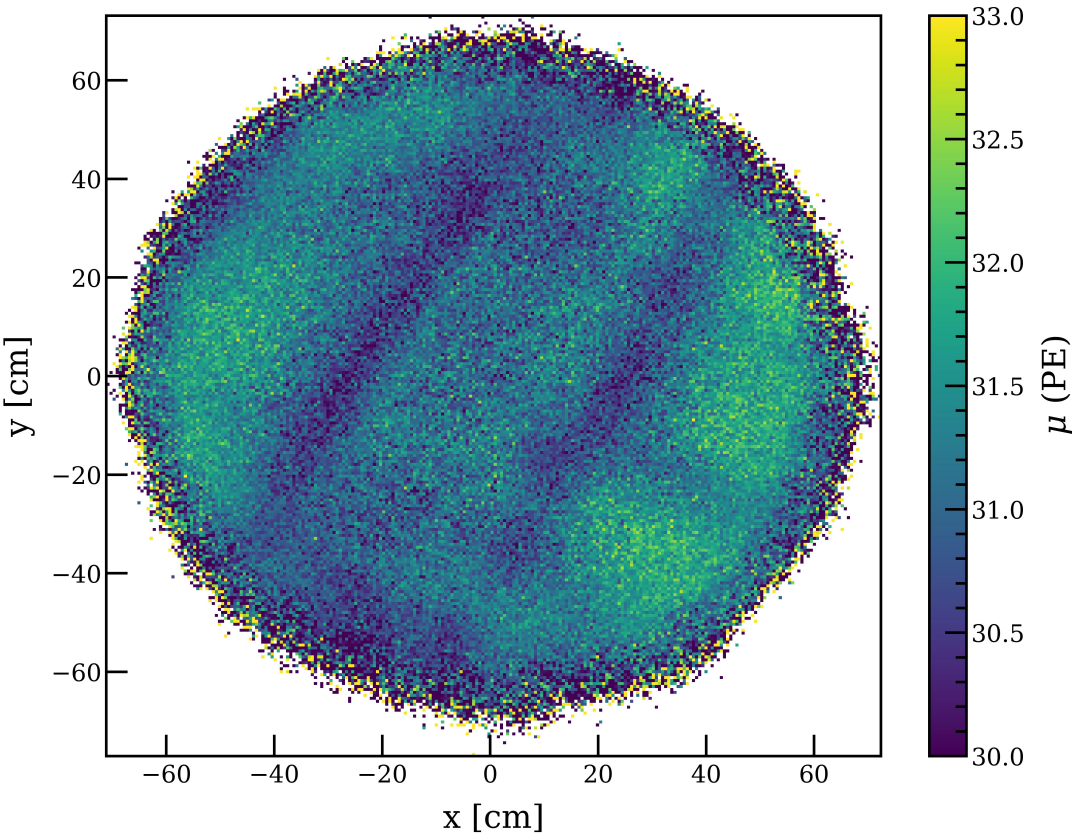

Figure 3.15: Map of the spatial dependence of secondary scintillation gain of single electrons (projected on the XY plane).

The only calibrations done during SR0 are ^{83m}Kr calibrations. The other calibrations were done before and after but not during SR0.
Figure 3.16 shows the existence of no dependence of the value of the gain with the calibration periods. This result was expected because, as explained in Section 3.5, the single electrons are due to background related to the detector response to scintillation light from the main S2 regardless of the source that produces this main S2. On the other hand, the secondary scintillation gain is related exclusively to the physical parameters of the detector, such as anode voltage, GXe pressure, and gas gap width. Therefore, any change should not be related to the calibration source but rather to the temporal stability of these parameters, which is well illustrated by Figure 3.16. The only changes in the gain are related to periods when the detector took data in non-SR0 configuration (corresponding to periods where there are no points in the figure). The gain returns very quickly to its average value afterward. The gain is statistically constant over time, translating to the excellent stability of the detector parameters on which it depends directly.

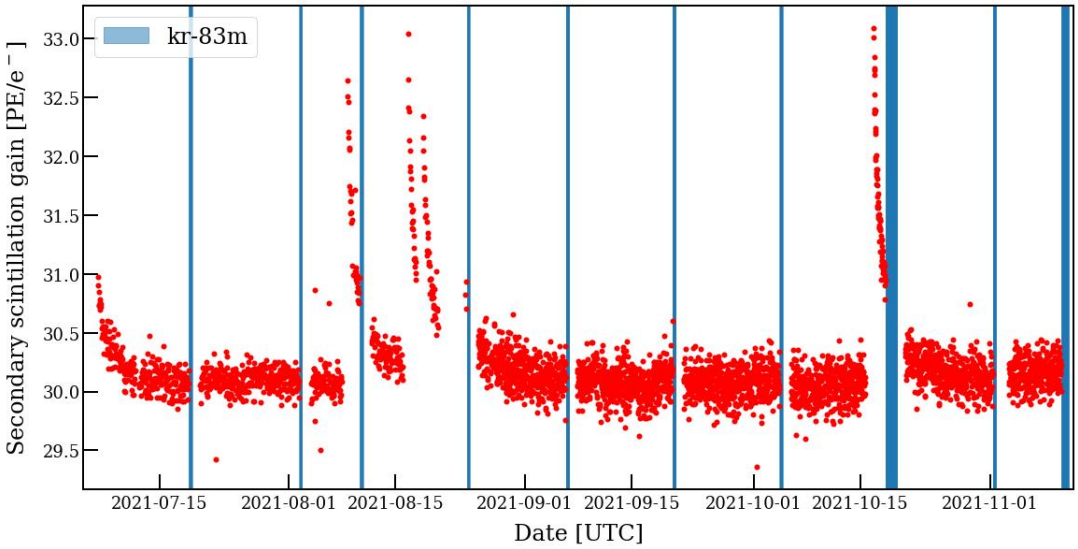

Figure 3.16: The secondary scintillation gain for each run in SR0. In blue are the krypton calibration periods.

3.5 Modelization of the secondary scintillation gain

As introduced in Section 3.3, modeling the single electron spectrum provides a tool to estimate the secondary scintillation gain of the detector as well as the time evolution of its value.

The process leading to the emission of proportional charge signals in the gaseous part is similar to the physics of gas proportional counters, with the difference that here the gas used is Xenon, and the signals are photons and not electrons.

When an electron crosses the gas gap, it meets Xe atoms and excites them by inelastic collisions. Between two inelastic collisions, the electron will undergo several elastic collisions, and as the mass of the electron is negligible compared to that of the atom Xe, the loss of energy due to these collisions is negligible. On the other hand, for the electron to excite Xenon atoms, it must gain a significant amount of kinetic energy. Thus, if the gas pressure increases, the electron will have more intermediate collisions, which will cause a threshold effect on its kinetic energy. Therefore the electron will never be able to reach the energy needed to produce the scintillation of GXe.

In terms of the underlying physical processes, they have been the subject of several studies [151, 152, 153]. The GXe scintillation mechanism in XENONnT is related to the radiative de-excitation of excited Xe_2^* dimers through electroluminescence[4] (see Section 2.1.3 for more details).

However, in general, the emission mechanism depends on the gas pressure; below

[4]Electroluminescence (or secondary scintillation) is the emission of non-thermal light by a material through which an electric current passes. Light is generated either by the collision between molecules of the material and high-energy electrons or by the recombination of electron-hole pairs in semiconductors.

10 mbar, the emission is mainly atomic, with two peaks centered at ~ 130 and ~ 147 nm. For higher pressures, the formation of excited Xe_2^* dimers starts, and the molecular emissions become increasingly important. Dimers de-excitation generates emissions at 147 nm (first continuum) and 172 nm (second continuum). The first and second continua correspond to the VUV radiative decay of the vibrational excimer in the excited and relaxed states, respectively [152].
Above 100 mbar, the second continuum is dominant, and the secondary scintillation shows only a narrow peak at around 172 nm, with an approximately Gaussian width of 10 nm [154]. The energy loss due to the relaxation of the vibrationally excited dimers remains a tiny fraction of the energy the electrons acquire from the electric field. The overall scintillation efficiency reaches values of 80% for reduced electric fields of 4 kV cm^{-1} bar^{-1} [152].

At high pressure (> 400 mbar), it was observed that the secondary scintillation gain was linearly proportional to the pressure [152]. As a result, the secondary scintillation gain (Y) could be parametrized as follows:

$$\frac{Y}{h_g} = aE + bp, \tag{3.5}$$

where h_g is the gas gap width, E is the electric field, and a and b are two key parameters that can be extracted by fitting the model.

On the other hand, to find the secondary scintillation gain for XENONnT, it is necessary to modify the previous equation to incorporate the specificities of the detector. This gives:

$$Y = ah_g \frac{\epsilon_l V_a}{\epsilon_l h_g + d - h_g} + bh_g p, \tag{3.6}$$

where the secondary scintillation gain (Y) depends on three parameters: the potential of the anode (V_a), the height of the gas gap (h_g), and the pressure (p) of the gas. $\epsilon_l = 1.96$ is the permittivity of LXe. d is the distance between the anode and the gate. The values of the parameters are given by the literature ($a = 140$ and $b = -116$) [152].

3.5.1 Comparison between the model and the measured value of the secondary scintillation gain

Now that we have a model of the secondary scintillation gain at our disposal as a function of the detector's parameters, it would be interesting to compare the evolution of the value obtained via the fit of the SE spectrum and the one given by the empirical model to see if they are consistent. This comparison was performed on Krypton calibration data before the start of SR0; at that time, the secondary scintillation gain was higher (about 42 PE/e-, see Figure 3.17). This was before the apparition of the hot spot problem and, therefore, before the reduction of the anode voltage (see Section 3.7.1).

To obtain the value of the secondary scintillation gain via the empirical model (3.6), extracting the values of the potential of the anode, the pressure, and the width of the gas gap is first necessary. These extracted data from the

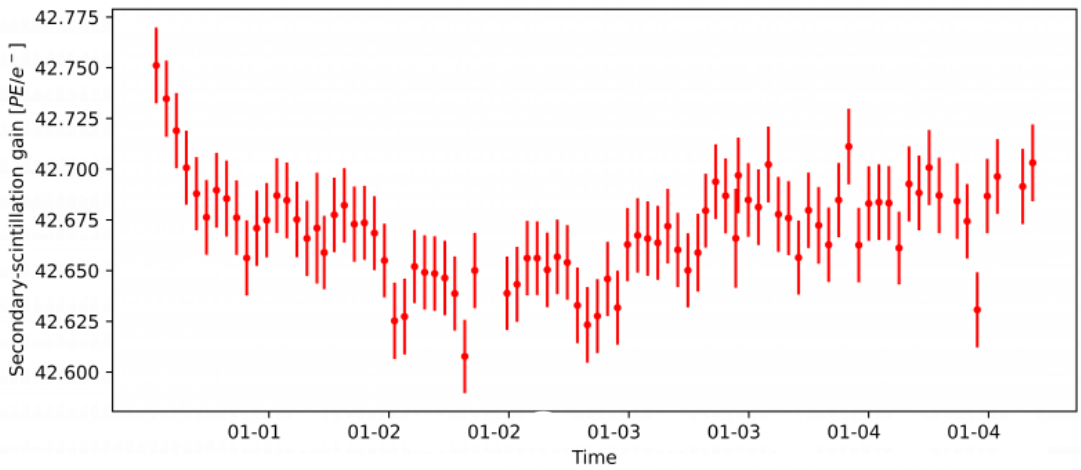

Figure 3.17: Time evolution of the secondary scintillation gain, calculated with the fit of the SE spectrum. Krypton calibration data (pre-SR0, January 2021).

Slow Control database are shown in Figure 3.18. Thus, using the SC data, the evolution of secondary scintillation gain can be obtained via the empirical model (3.6). Figure 3.19 illustrates this evolution.

The first thing to note in Figure 3.19 is that it gives a different value of the secondary scintillation gain than that measured using the SE spectrum. This inconsistency is due to the fact that the empirical model gives the value of the gain in the ideal case. For Y to correspond to what is observed, it must be multiplied by the average light collection efficiency, the quantum efficiencies of the PMTs as well as the charge collection efficiency of the photocathode. These inefficiencies are given by simulations and by the properties of PMTs.
When this study was carried out (January 2021), the following values were used (same values as for SR0); 30% for the average light collection efficiencies, 90% for the average collection efficiency from the photocathode to the first dynode, and 37% for the average quantum efficiency of the PMTs. Therefore Y in Figure 3.19 has been multiplied by $0.30 \times 0.9 \times 0.37 \simeq 0.1$.
This discrepancy leads to another conclusion: if the empirical model is exact and parameters a and b are close to the exact values, then the inefficiencies calculated for XENONnT are lower than the real ones.

However, the goal is not necessarily to see if the two values are consistent with each other but to see the overall evolution. Thus, we realize that the evolution is not coherent; the gain calculated with the spectrum of the SEs is relatively stable, whereas Y increases quickly.

The answer to this inconsistency comes from a problem with one of the short-level meters. XENONnT uses four short-level meters. However, when this analysis was carried out, only two were in operation, the two indeed presented different measurements, but it is difficult to say which one gave the correct measurement. Thus, the increase of Y comes from the gas gap growth, which was due to a fault in the short-level meter, so the one which gave an incorrect measurement could be identified.

It should, however, be noted that the evolution of the other thermodynamic

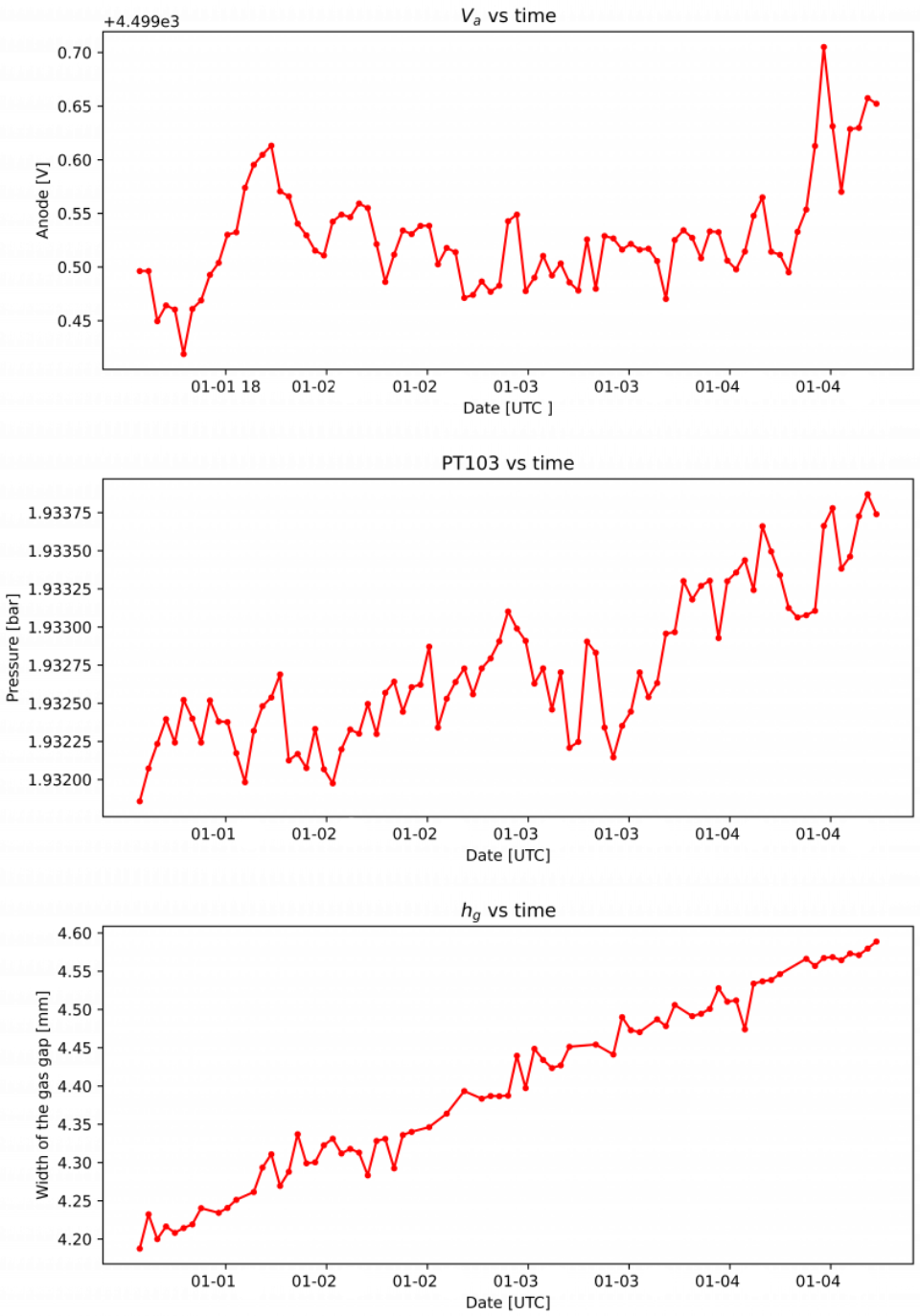

Figure 3.18: The values of the anode potential, the pressure, and the width of the gas gap corresponding to the time at which the selected data were taken (pre-SR0).

parameters of the detector can also identify the faulty short-level meter.

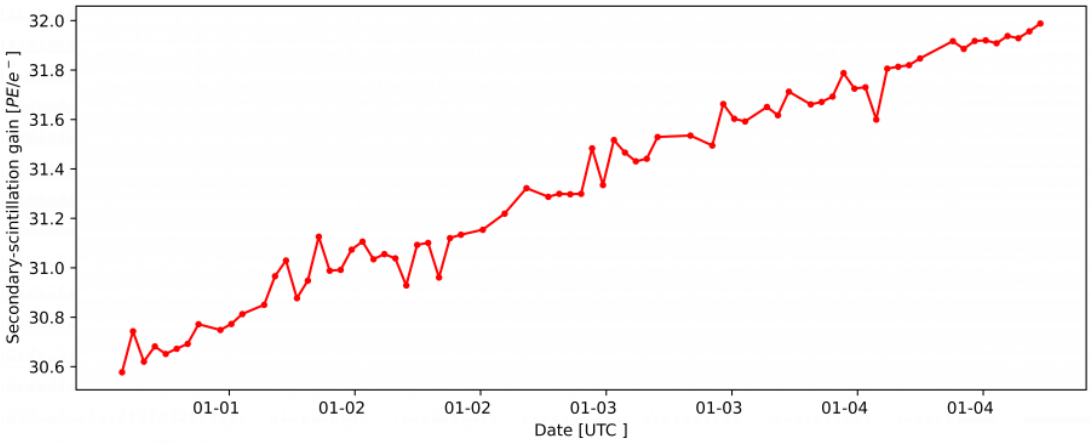

Figure 3.19: Time evolution of the secondary scintillation gain, calculated with the empirical model (3.6).

3.6 Systematic studies of single electrons

Several experiments have been carried out to better understand the single electron signal [155], to use it for calibration purposes, or to measure the properties of Xenon [156]. However, none had a complete and ultimate quantification of these new mechanisms as an objective.

The XENON (with XENON10, XENON100, XENON1T, and XENONnT experiments), ZEPLIN and LUX collaborations provide the current state of the art in this domain. LUX has published a study [145] of these electron backgrounds under different experimental conditions, trying to identify possible mechanisms that may contribute to electron emission. The same is done by XENON as well [149]. Using previous data, a study [157] showed quantitative agreement between an electron emission model and the data, suggesting some ways to eliminate single electrons.

Despite all these efforts, it is clear that the large TPCs searching for dark matter can neither disentangle different sources of this background nor quantify the effectiveness of specific elimination techniques, their configuration not being ideal for carrying out systematic studies. The only possible way is to build a dedicated configuration as proposed by the XeLab project.
Figure 3.20 gives the sketches of the detector.

The research planned by this project aims to exploit at LPNHE a small-scale replica of XENONnT, consisting of LXe TPC of a few kilograms which will be used to study the main supposed sources of single electron emissions systematically.

Two distinct mechanisms will generate single electrons:

1. photoionization using dedicated laser sources producing VUV light of the same wavelength as that produced by Xenon scintillation,
2. spontaneous emission of electrons from high voltage metallic components as in a diode.

First, the goal would be the identification of sources. This phase will be done using the production mechanisms suggested in the literature and by modifying

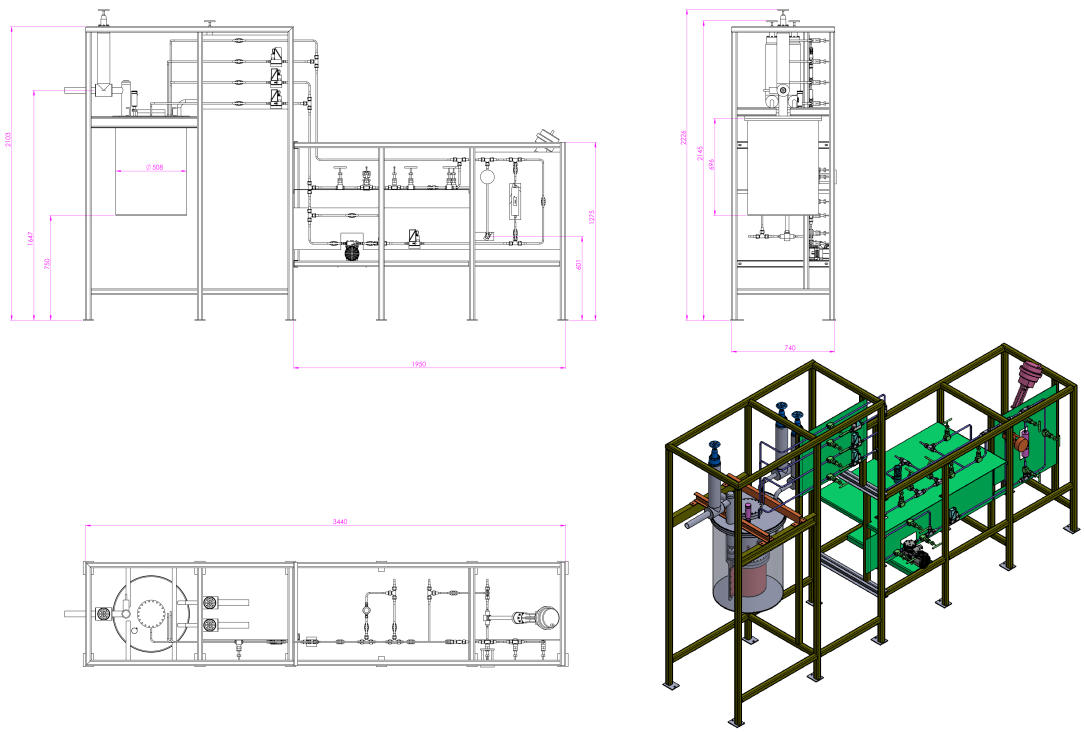

Figure 3.20: Plans for the future XeLab detector.

experimental conditions (change in impurity levels, drift field, intensities of the liquid-gas extraction field, and detector tilt) in order to identify each source and its order of magnitude. The expected results of this step are to identify the spatiotemporal behavior of each source tested and produce solid models to describe them to be used later for the analysis of current and future dark matter detectors. As an input for the likelihood inference process (such as presented in Section 2.4.1), a robust background model of the single electron signal will allow dark matter detectors to be more sensitive to light dark matter particles in a parameter space so far unexplored.

Second, a study will be conducted to reach these sources. It is not sufficient to characterize a background signal, but the knowledge acquired on the production of electrons should be used to reduce, or even eliminate, some of the sources of electrons, with the final goal of reducing the total background noise for the search for light dark matter particles. Some sources are innocuous, such as photoionization on impurities, where the critical action is already known and consists of maintaining the Xenon at very high purity levels. However, the main challenge is eliminating all mechanisms involving the presence of high-voltage electrodes in a TPC. They are believed to be the main source of electron production apart from photoionization.

If the studies are ultimately successful, these results should significantly impact the physics reach of XENONnT, and future generation experiments like DARWIN [139] (using 50 tons of Xenon) and, more broadly, in the field of low-mass dark matter research.

The opening of a new detection channel in XENONnT, and more generally in

LXe TPCs, increases the chances of detecting dark matter and, in case it is not detected, of exploring deeper into the parameter space available and to further constrain its properties.

3.7 Data selection and cuts

As already explained, the exact origin of the background noise of the SEs is currently unknown. Even if some contributors, such as impurities, spontaneous emissions by the electrodes, or delayed emissions due to the potential well between the liquid and gas phases, are recognized as contributors with great certainty. However, this is not enough because the part of each source's contribution is unknown, nor the exact mechanism by which this contribution takes place, nor if there are other origins that are so far unknown. All this means that the SEs background, which is dominant in the sub-GeV region, is an important complexity factor for this type of analysis. This forces us to make more restrictive cuts to search for subsets of signals where it is reasonably expected that this background is smaller.

During the first phase of the XENONnT detector, about 200 days of data were taken. However, these 200 days include testing and calibration periods and periods when the detector exhibited non-standard behavior (see Figure 3.21). To select the set of events to make the analysis subject of this manuscript, it is then necessary to eliminate all the periods that are not dedicated to the search for dark matter. By doing this, a live-time of about 33 days is obtained.

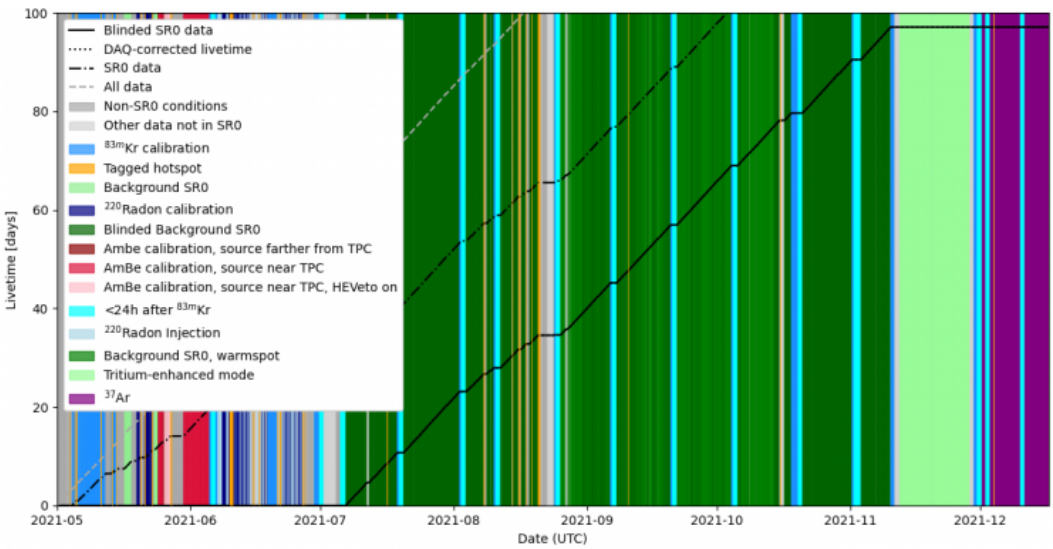

Figure 3.21: Summary of the different data taking and calibration periods during the XENONnT SR0 run. The "dark matter" data are in dark green ("Blinded Background SR0").

It is worth noting that this live-time is a minimal and very conservative choice. Since the XENONnT data acquisition is triggerless, the Sub-GeV search has 16 times longer live-time than for XENON1T, so a conservative choice is

allowed. That said, adding other datasets that can potentially be relatively homogeneous with the primary data would also be possible. This data includes, for example, the data taken to study the low energy excess observed by XENON1T. These data are supposed to have a higher tritium level. However, the studies [101] on these data show that they are comparable to the rest of the data and do not show any remarkable features.

First of all, in order to investigate the data quality of the dataset used, Figure 3.22 shows the single electron gain and the standard deviation for all the runs in the background data (the one used for searching dark matter). Moreover, it can be concluded that the gain is very stable; therefore, the detector parameters are highly stable during SR0 background data. This is further illustrated by the fact that there are 40 points outside the two-standard deviation interval in a total of 1191 runs. Although the dispersion of the SE gain is mainly negligible, only the runs inside the yellow band will be retained.

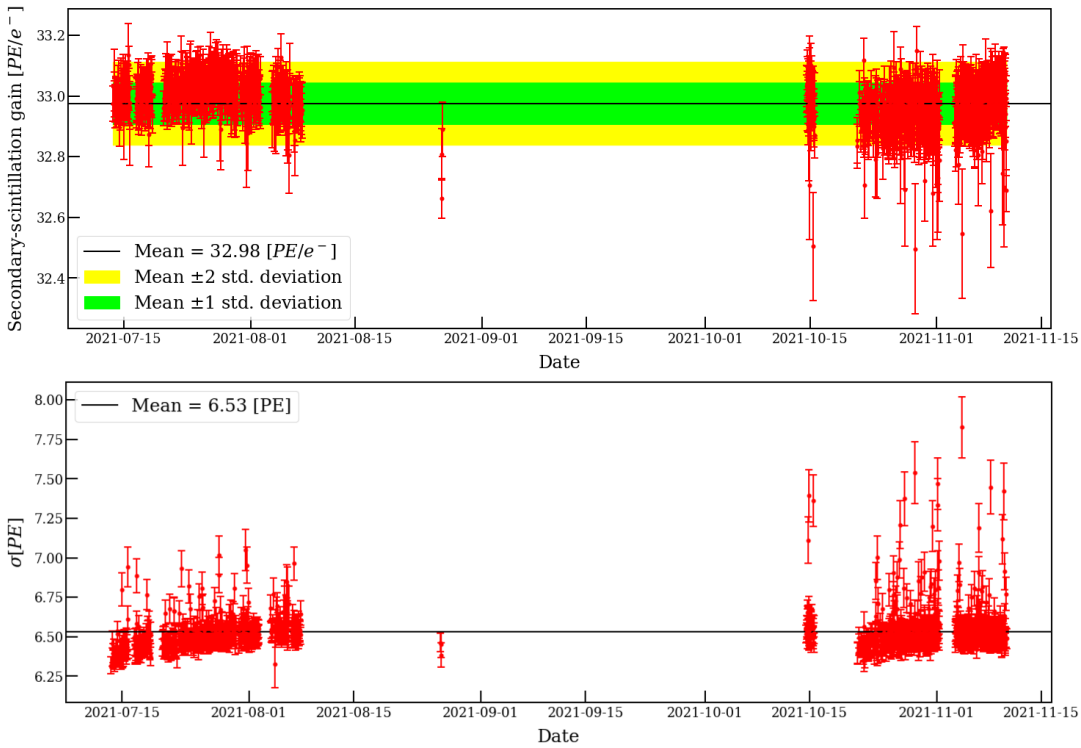

Figure 3.22: (Top) Secondary scintillation gain for each run present in the SR0 background dataset calculated with pure Gaussian model, the horizontal black line indicates the average value and the bands indicate the region of one and two standard deviations, respectively, in green and yellow. (Bottom) The standard deviation of the first Gaussian of the single electron spectrum calculated for the same dataset as the gain. The large gap between August and October corresponds to dark matter data with some irregularities, such as the presence of a hot spot or if the anode was powered up less than three days before; therefore, this can affect the SE gain or during DAQ firmware tests, etc.

Another observation that could be made from Figure 3.22 is that the smaller the gain, the larger the standard deviation; this is due to an artifact of the fitting

algorithm that tends to have an inverse proportionality relationship between the mean of the Gaussian and its σ. This was demonstrated in [148].

3.7.1 The transverse wires problem

Although the idea of adding wires was well motivated, this nevertheless had undesirable effects and constituted a significant source of limitation for XENONnT during SR0.
Firstly the presence of a hot spot[5] on one of the wires, which is activated at high voltage, has limited the extraction electric field leading to a lower extraction efficiency. Moreover, via mechanisms that are still not well defined, it seems that there is an over-density of SE signals correlated with the position of the wires, which are visible in the Figure 3.23.

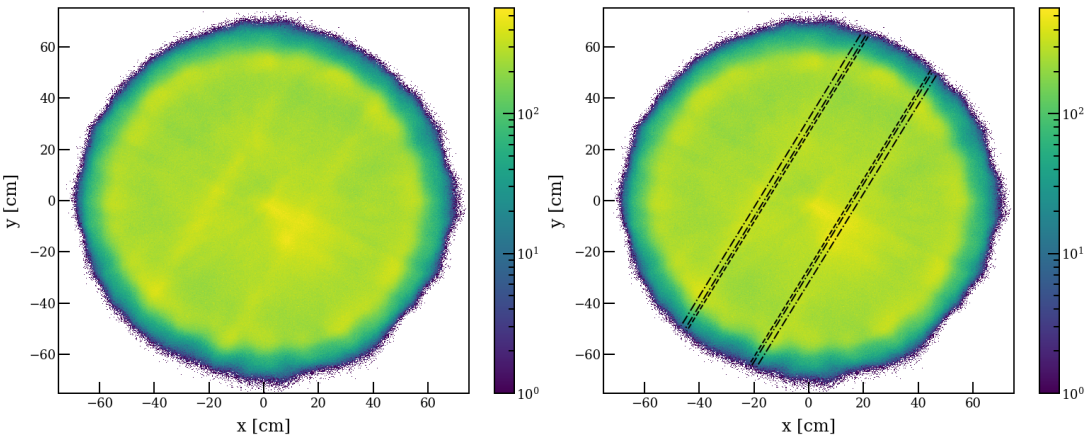

Figure 3.23: Map of SE emissions as a function of XY (using multilayer perceptron algorithm for position reconstruction). For clarity, the figure on the left is left intact. The figure on the right shows the location of the 2 transverse wires of the gate ('–') and the 4 of the anode ('-.').

In addition to the overdensity correlated to the position of the wires, in the center of Figure 3.23, another overdensity is also present. This is probably related to artifacts of the reconstruction algorithm. To validate this hypothesis, Figure 3.24 gives the same results as Figure 3.23 but with a different position reconstruction algorithm, where we see that the location of the overdensity has changed, but that linked to the wires has remained in the same place.
In the rest of the study, it is the multilayer perceptron algorithm that will be used. This is the default position reconstruction method and the most extensively tested.

Given that the position of the transverse wires is linked to background emissions in the SE region (region of interest for the search for sub-GeV dark matter), these must be cut.

[5]A hot spot is a region of the XY plane that generates measurable S2-like signals, which are uncorrelated to interactions in the target volume. In most cases, these emissions are linked to impurities stuck to one of the electrodes and, therefore, locally enhance the grid electron emission.

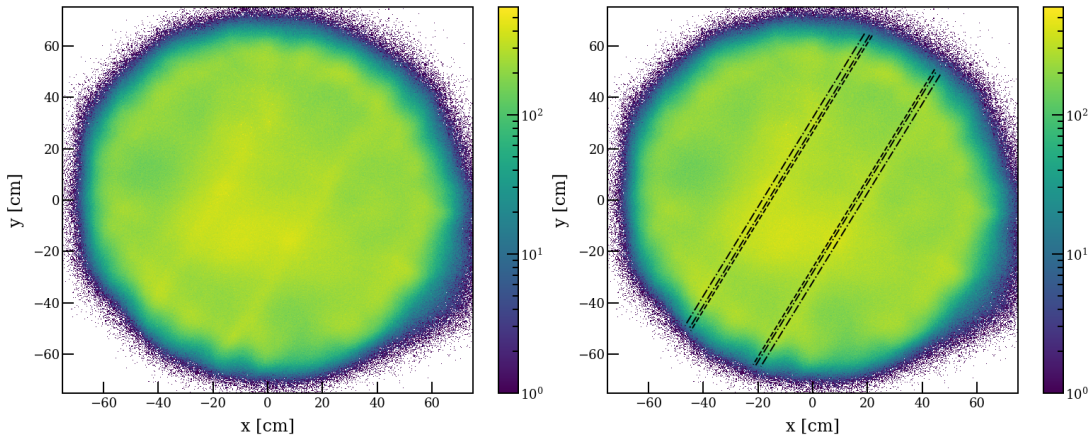

Figure 3.24: Map of SE emissions as a function of XY (using convolutional neural network algorithm for position reconstruction). For clarity, the figure on the left is left intact. The figure on the right shows the location of the 2 transverse wires of the gate ('–') and the 4 of the anode ('-.').

The cut chosen is once again very conservative, consisting of cutting all signals with a spatial distance in the XY plane of less than 4.45 cm (±4.45 cm). This value was taken because, on the one hand, the visible extent of the overdensity corresponding to the wires does not exceed 4 cm, and on the other hand, the electric field between the gate and the anode is very uniform, and the dispersion of extracted electrons therein is negligible.
However, this cut will reduce the exposure by decreasing the fiducial mass, but it is necessary to avoid contamination. The result of this cut is shown in Figure 3.25.

3.7.2 Fiducial volume

In addition to the previous cut, which was made to protect against contamination from transverse wires, another spatial cut is also necessary; this one aims to eliminate the outer regions known to have high background noise. Since there is no S1 for low energy interaction, the depth cannot be accurately determined, therefore, a cut on the radius is the only one possible.
That said, the width of the signals gives an estimate of the depth at which they emanate; however, this exact relationship is difficult to uncover. This has been the subject of a study based on machine learning methods that I have done but will not be used here for lack of maturity.

Figure 3.26 shows the distribution of the SE signals as a function of R^2, it exhibits four peaks (R^2 ~(100,500,3000,4000)). The first one corresponds to the central overdensity already discussed above. The drop corresponds to the combination of the two transverse wires cuts. The third and the fourth peaks correspond to the emission linked to edge effects as well as to the inefficiency inherent to the detection of S2 signals that occur in the detector edges (this inefficiency has been discussed in Section 2.2.9).

As shown in Figure 3.26, the detector edges background emissions can be

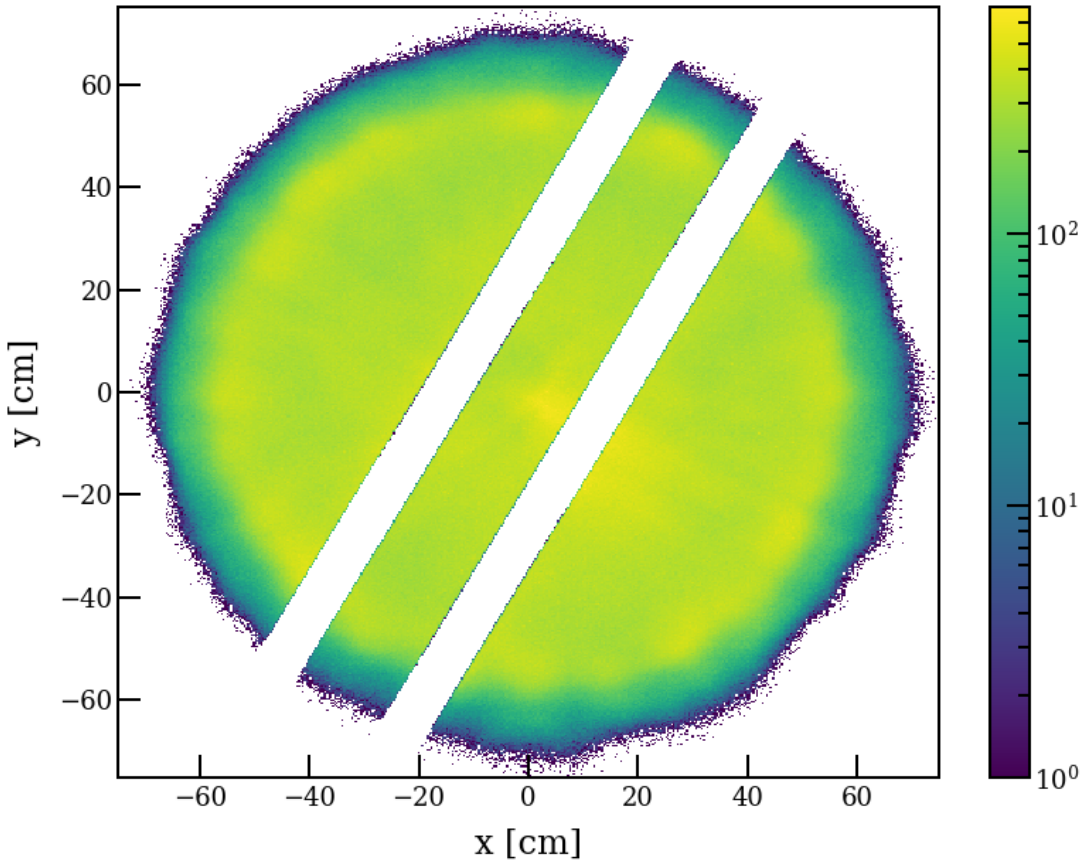

Figure 3.25: Map of SE emissions as a function of XY, showing the near transverse wires cut.

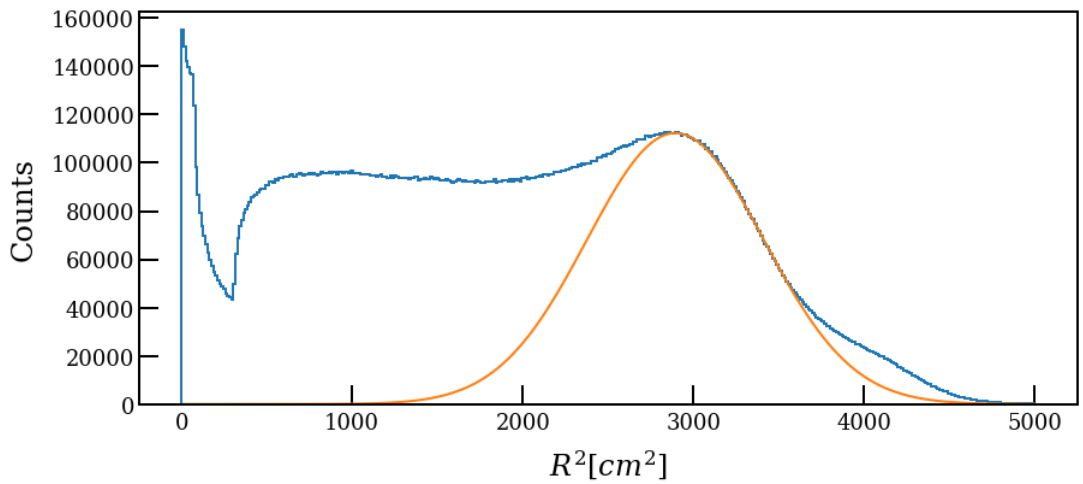

Figure 3.26: Distribution of SE as a function of the square of the radius. Also shown in orange is the Gaussian fit of the distribution region that is expected to be originating from edge emissions.

fitted with a Gaussian. R^2 = 2000 cm^2 roughly equals the radius where the contribution of external emissions begins to modify the signal distribution. Con-

sequently, it is this limit that will be chosen; it corresponds to a radius of less than 45 cm.

Another choice would be to make a full cut, which would cut all the background (i.e., a cut for $R^2 > 1000$ cm^2). In order to judge the relevance of a cut at $R^2 = 2000$ cm^2 or $R^2 = 1000$ cm^2, it is necessary to estimate the sensitivity for each value, i.e., the signal event rate compared to the background rate. The method to evaluate the sensitivity consists in considering the signals as background, and the sensitivity is obtained by the ratio between the XY area and the square root of the number of events. This is presented in Figure 3.27.

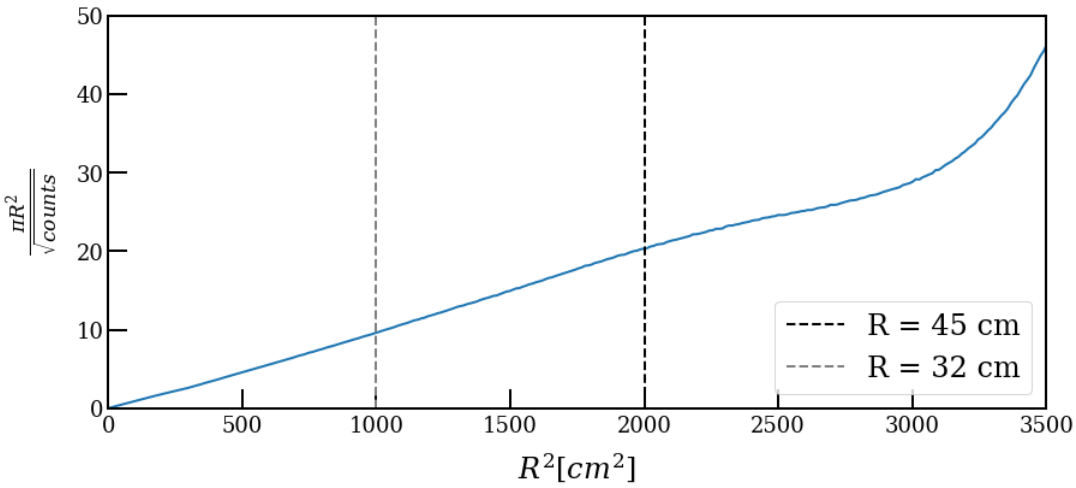

Figure 3.27: The sensitivity (as explained above) as a function of R^2.

Figure 3.27 is consistent with Figure 3.26 and shows that the cut at $R^2 = 2000$ cm^2 is better than that at $R^2 = 1000$ cm^2, in another word the sensitivity is greater given a cut at $R^2 = 2000$ cm^2. Moreover, it also seems that the edge emissions are minor and do not decrease the sensitivity, and therefore no cut is necessary. However, the cut at 45 cm will be kept for the present analysis, given the known fact that the reconstructed events position can be biased in the edge.

This cut affects the fiducial volume of the detector hence the exposure. The fiducial volume is initially given by $\pi \times 0.68^2 \times 1.47 \simeq 2.14$ m^3. To this, it is required to remove the volume lost after the cut on the wires, $2(0.089 \times 0.64) \times 1.47 \simeq 0.17$ m^3, and that from the radius cut, $\pi \times (0.68^2 - 0.45^2) \times 1.47 \simeq 1.2$ m^3. Therefore, the fiducial volume is, $2.14 - 0.17 - 1.2 = 0.77$ m^3.

Finally, we obtain the fiducial mass by applying a cross-multiplication rule, $m_f = 2.12$ t. In order to have the exposure, this fiducial mass cannot be multiplied directly by the live-time of the data set, as is the case for a usual analysis. The reason for this comes from the fact that the live-time is calculated by investigating the best Δt between the SE and the primary that maximizes the sensitivity.

3.7.3 Single electron selection

For the single electron analysis, the number of single electrons observed as a function of time after an S2 primary is counted. However, to correctly identify

the number of delayed electrons observed, one must know the efficiency of single electron selection. In this context, it is necessary to fit the single electron spectrum and extract each Gaussian area (corresponding to each population of single electrons).

Figure 3.28 (left) shows a 2D histogram of the the signal width at 50% as a function of S2 for low energy S2. There is a clear population of single electrons in the lower left corner and 2 electrons towards the upper right. To fit the S2 spectrum, Figure 3.28 (left) was projected down to the x-axis, as shown in Figure 3.28 (right).

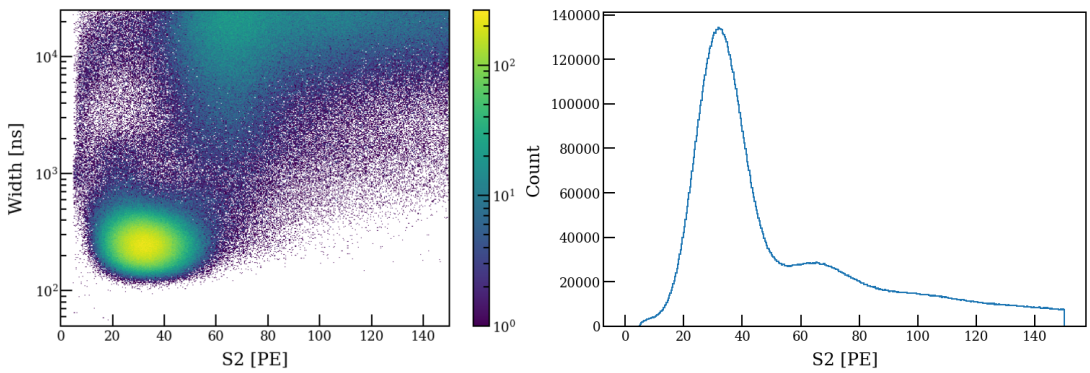

Figure 3.28: S2 signal temporal width at 50% area of the peak (left) and number of event (right) as function of the S2 energy.

The fit used to model the few electron populations is a sum of Gaussians. This method was compared to the one with a Poissonian convoluted with a Gaussian in Section 3.3.1. The fit is made with 5 Gaussians such that:

$$f(x) = \sum_{i=1}^{5} A_i e^{-\frac{(x-i\mu)}{2(\sqrt{i}\sigma_1)^2}} \tag{3.7}$$

Using Equation (3.7), the mean, standard deviation, and amplitude for the single electron population can be estimated. The amplitude for all other electrons was a free parameter, whereas $\mu_n = n \times \mu_1$ and $\sigma_n = \sqrt{n} \times \sigma_1$.

The goal is to determine the boundaries of the single electron cut. If we select a significant part (high efficiency) of the Gaussian SE, we will obtain a lower purity because of the contamination of the 2nd Gaussian. A compromise would be to choose the SE population within $\pm 2\sigma$ of the mean. From this, it becomes possible to determine the purity of single electron selection from double electrons and what percentage of the SE population is excluded from the $\pm 2\sigma$ cuts.

"Purity" is defined by the level of confidence that we only have single electrons in the selection. From the fit, the purity is the integral of the fit function (red) in the selected region (blue area) divided by the data (black) in the selected area.

Efficiency is the total amount of single electrons in the selected cut of $n \times \sigma$. And from the fit, the efficiency is the fit in the selected region (blue area) divided by

the total Gaussian fit (red).
Finally the corrected electron number = raw electron number × (purity/efficiency).

Table 3.3 gives the purities and efficiencies extracted from FIGURE 3.29 for selecting the three electron populations.

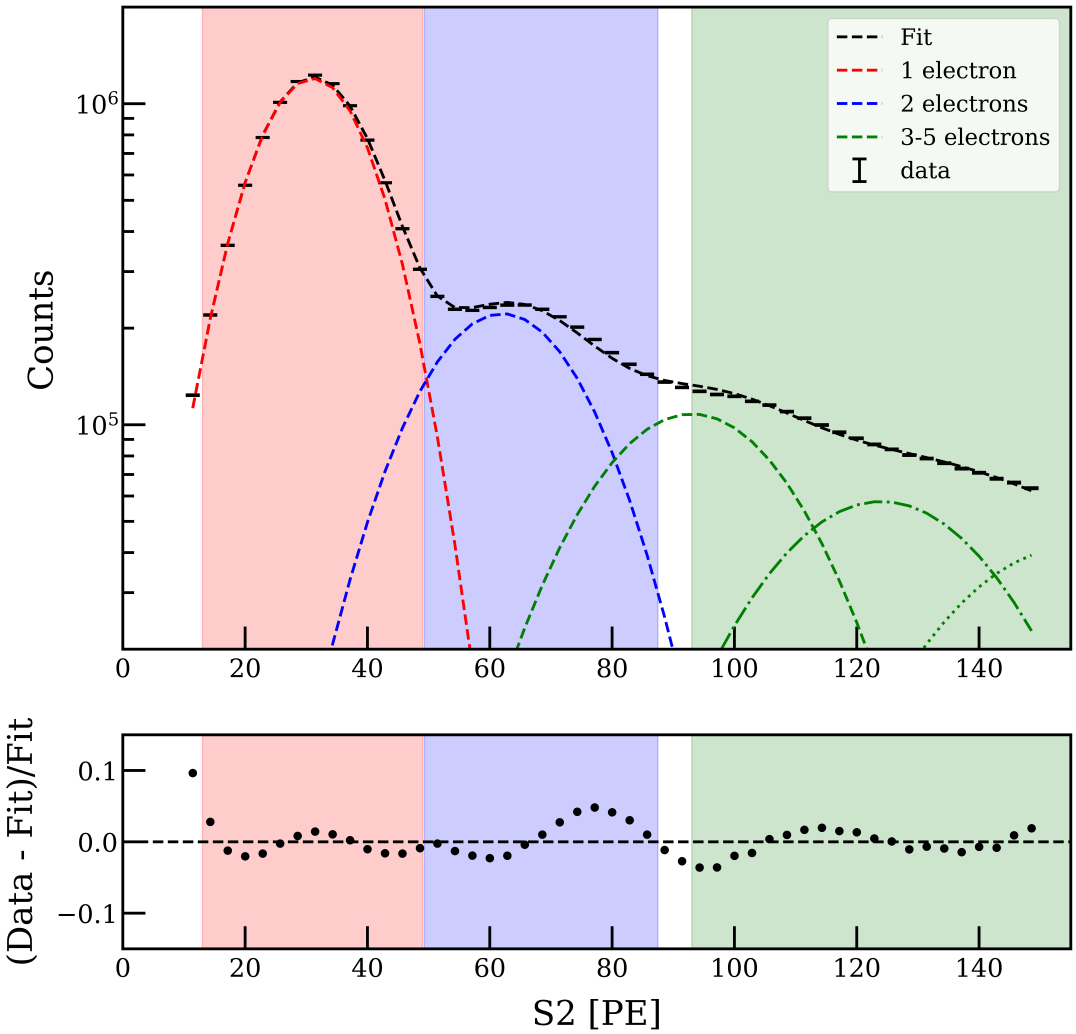

Figure 3.29: Fit the SE spectrum using Equation 3.7. The red, blue, and green bands respectively indicate the limits for the selection of populations with one electron, two electrons, and 3 to 5 electrons.

3.7.4 Area fraction top cut

As the events studied are S2 signals produced by a single or a few electrons, we can then use the area fraction top value (AFT, fraction of the signal energy measured by the top PMTs) of these peaks to clean the data. This cleaning aims to select the events that have occurred in the drift region. The background event sample is shown in FIGURE 3.30 in the AFT parameter space with respect to energy. The solid red lines indicate the SR0 cut on the "AFT vs S2" space (S2AFT); thus, signals with an AFT above the cutoff should be occurring in the

Table 3.3: Extracted mean, purity, and efficiency for each electron population.

Parameter	1 e^-	2 e^-	3-5 e^-
Section	$\mu_1 \pm 2\sigma$	[μ_2 - 1σ , μ_2 + 2σ]	[$^-\mu_3$, $^-\mu_5$]
Mean [PE]	31.03 ± 0.04	62.05 ± 0.08	(93.08) ... (155.13)
Purity	96.83 %	76.32 %	99.41 %
Efficiency	97.06 %	81.20 %	69.43 %
Raw e^- number	10^7		
Corrected e^- nbr.	9.98×10^6		

gas, and signals with an AFT below the cutoff should correspond to signals occurring below the cathode.

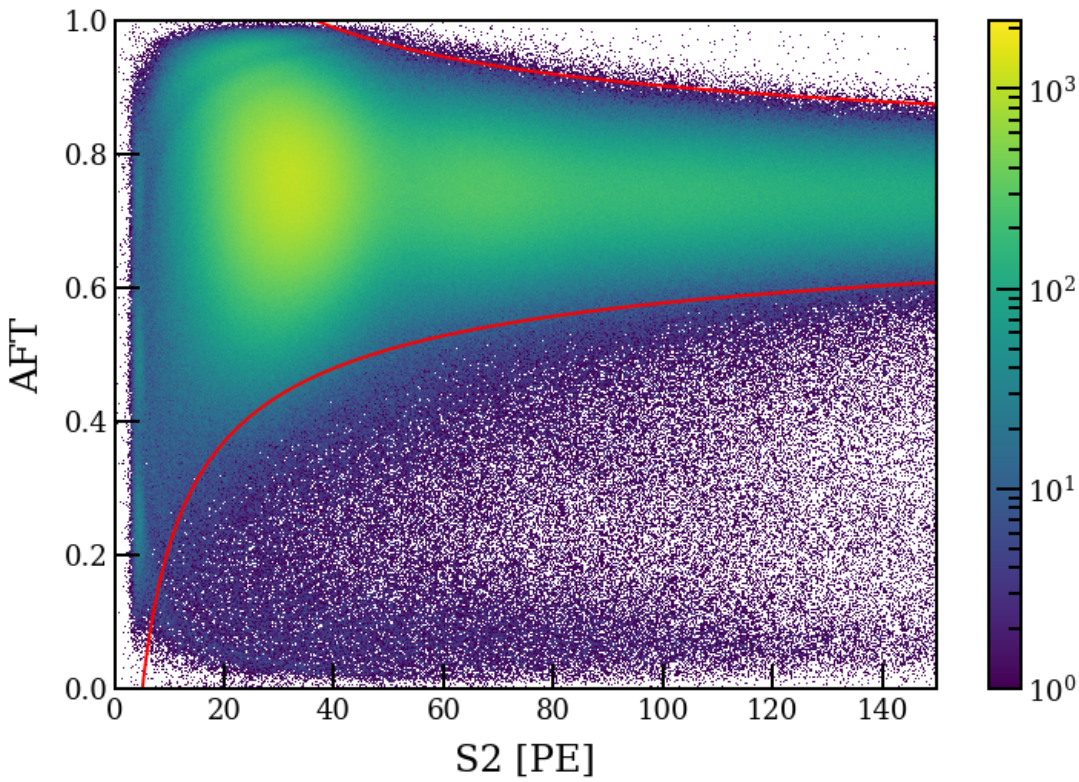

Figure 3.30: AFT distribution of single electrons. The red lines delimit the selection of the retained events; those between the two fits.

The S2AFT cut is defined with upper and lower bound fitted with the empirical formula $q = a + b/\sqrt{s2}$, where q is the quantiles of S2AFT in each S2 bin. Finally, the standard deviation is the arithmetic square root of the Poisson distribution expectation.

The fit values are given below:

$$\mathrm{AFT} < 0.7513 + \frac{1.5053}{\sqrt{\mathrm{S2}}} \tag{3.8}$$

$$\mathrm{AFT} > 0.7449 - \frac{1.6804}{\sqrt{\mathrm{S2}}} \tag{3.9}$$

To quantify the acceptance of the SR0 S2AFT cut on single electron signals, events with AFT = 1 or 0 are removed; this is since considering that the average number of photons produced by an S2 is about 32, it is unlikely that a true S2 produced by an SE has an AFT=1 (or AFT=0). The cut is then applied to the remaining data, and the estimation of the cut acceptance in the SE region is shown in Figure 3.31.

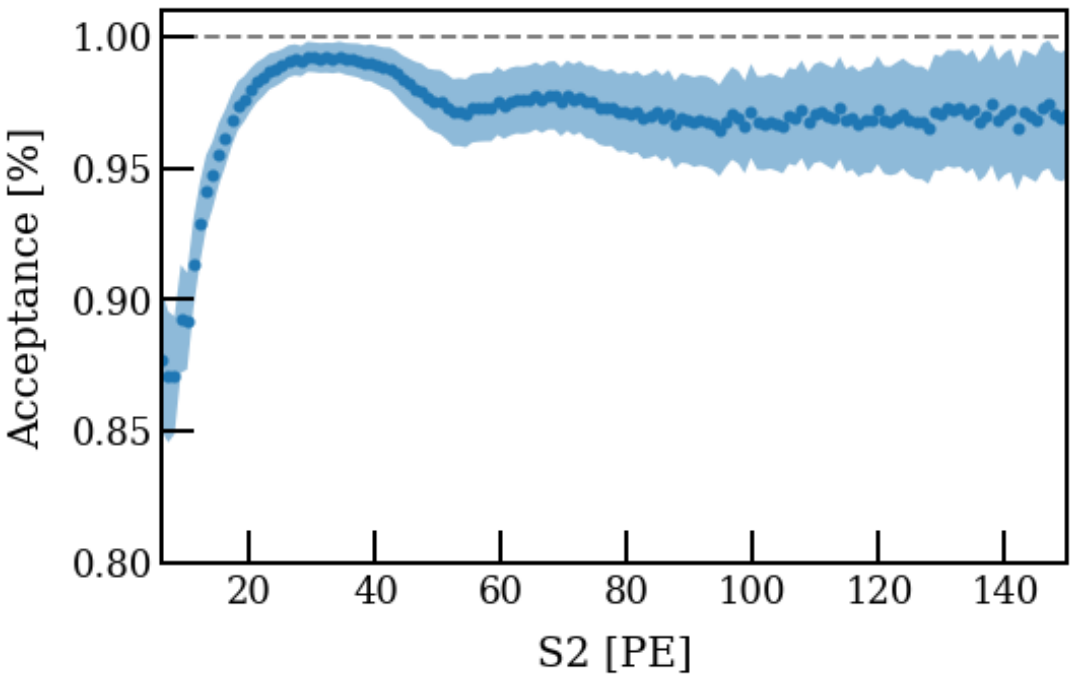

Figure 3.31: Acceptance of S2AFT cut on single electrons.

As expected by looking at Figure 3.30, below 40 PE, on the population of single electrons, the cut acceptance is very high, on the order of 98%. Above 70 PE, however, the acceptance starts to decrease, mainly due to the sample lacking sufficient statistics and the occurrence of outliers below the AFT band. The discrepancy between the acceptances below 40 PE and above 70 PE should be treated as an uncertainty in the signal's shape since it is impossible to conclude whether these outliers are indeed outliers or residual contamination from misidentified S1.
Finally, this acceptance loss will be accounted for in the following SE spectrum by correcting the signal shape on a bin-by-bin scheme using the derived acceptance from Figure 3.31.

3.7.5 Classification and selection of primary S2 signals

The study of the distribution of the primary S2 in the data makes it possible to classify them into five main classes, which will be used to disentangle the origin of the SEs. These five classes correspond to five categories of primary interactions, namely events that occur in the LXe phase (subdivided into Compton scatterings and alphas), events that occur in the GXe phase, events that are probably due to a pile-up of photoionization electrons, and the events where the S2 appears to be a misclassified S1.

Classification of primary S2 signals

Two quality parameters of S2 signals are examined to classify the main S2 signals, namely S2AFT, and S2Width[6]. All parameters related to events that require the presence of an S1 are excluded because the data linking S1 with S2 are still blinded for SR0; only the signals are available. For this reason, the S2PatternLikelihood[7] and the traditional drift time-dependent S2 width cut are not applied.

Figure 3.32 shows the S2 primary events from a sample of background data evenly distributed in SR0 with no cut applied yet. As a reminder, primary S2 is defined as any peak classified by the classification algorithm as S2 with an energy greater than 150 PE. Cut values are shown on the AFT. The AFT cut is only defined up to 10^4 PE, so an extrapolation is drawn beyond this level as a dotted line. For the S2Width cut, the figures' values are the proposed values, which are entirely graphical. The cut should typically depend on the drift time. However, this parameter is not accessible in blinded data.

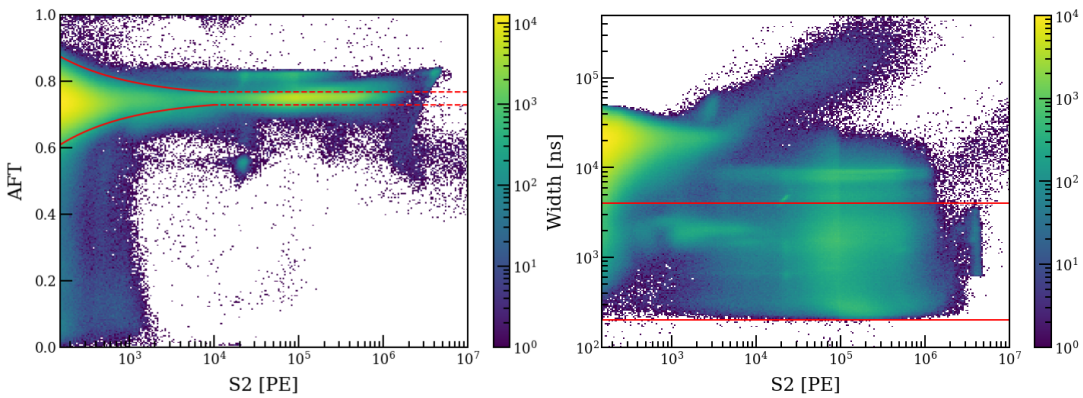

Figure 3.32: Distribution of primary S2 signals as a function of the AFT and the width at 50%. Also, shown in red is the cut in each parameter.

From the two plots in Figure 3.32, it is possible to identify some populations. From the AFT graph, a population of S1-like primaries is identifiable by its AFT well below the base limit of the S2AFT cut. Above the upper limit of the S2AFT

[6]See Section 3.7.3

[7]S2 pattern likelihood evaluates the similarity between data and expectation with S2 pattern intensity distribution on the top PMT array.

cut, we have the population of gaseous events. On the other hand, from the S2Width plots, we observe a sample of extended (in time) S2 events.

Note that there is no need to refine these cuts or quantify their acceptance as a function of the energy since excluding primary S2 in the final data selection simply acts as a live-time effect, which will be taken into account.

The five primary classes identified in the sample events are:

1) S1-Like

These are the events whose AFT values are less than 0.6. No width cut is made since the remaining populations are relatively clean in this parameter space, as shown in Figure 3.33.

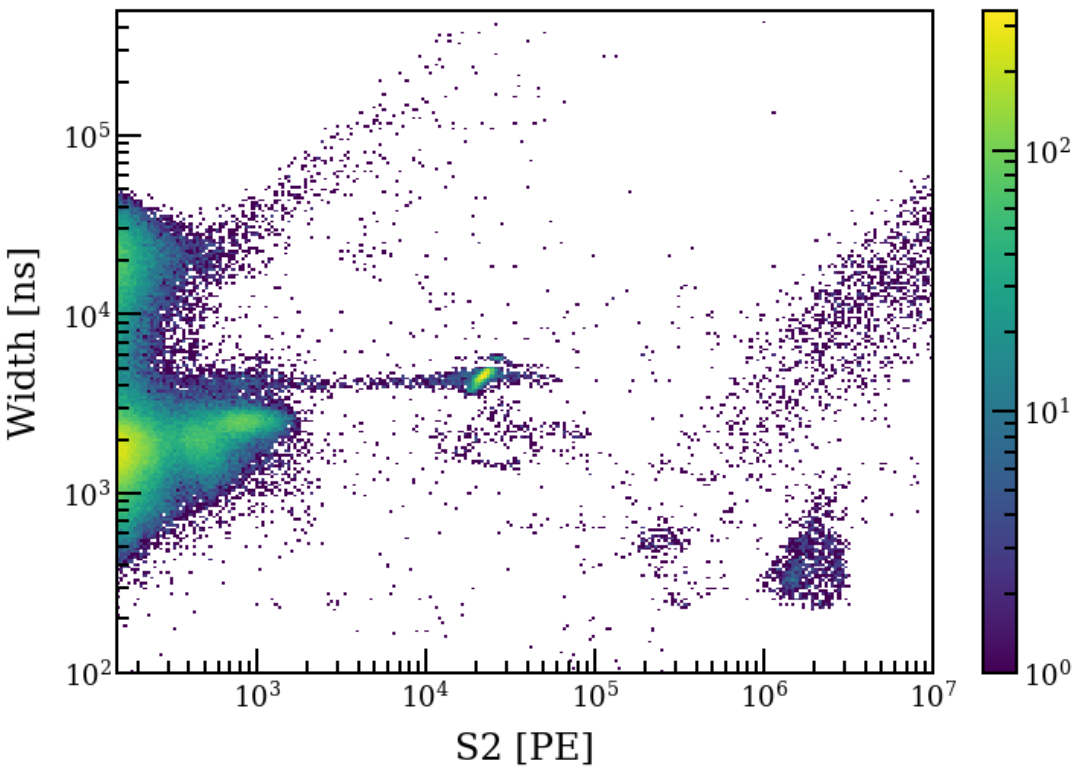

Figure 3.33: Width at 50% distribution of S1-like events

2) Gas events

These events correspond to signals whose AFT values are greater than the upper limit of the S2AFT cut. Additionally, these events must have energies below 10^4 PE to avoid leakage from the AFT band at higher energies, as shown in Figure 3.34, where the blue dotted line indicates this upper threshold.

3) Track events

These events consist of signals exhibiting very wide distributions in time, most likely due to stacking many individual S2 signals over time. Therefore, the proposed cut requires that these events have S2Widths wider than 4000 ns. The distribution of those events is shown in Figure 3.35.

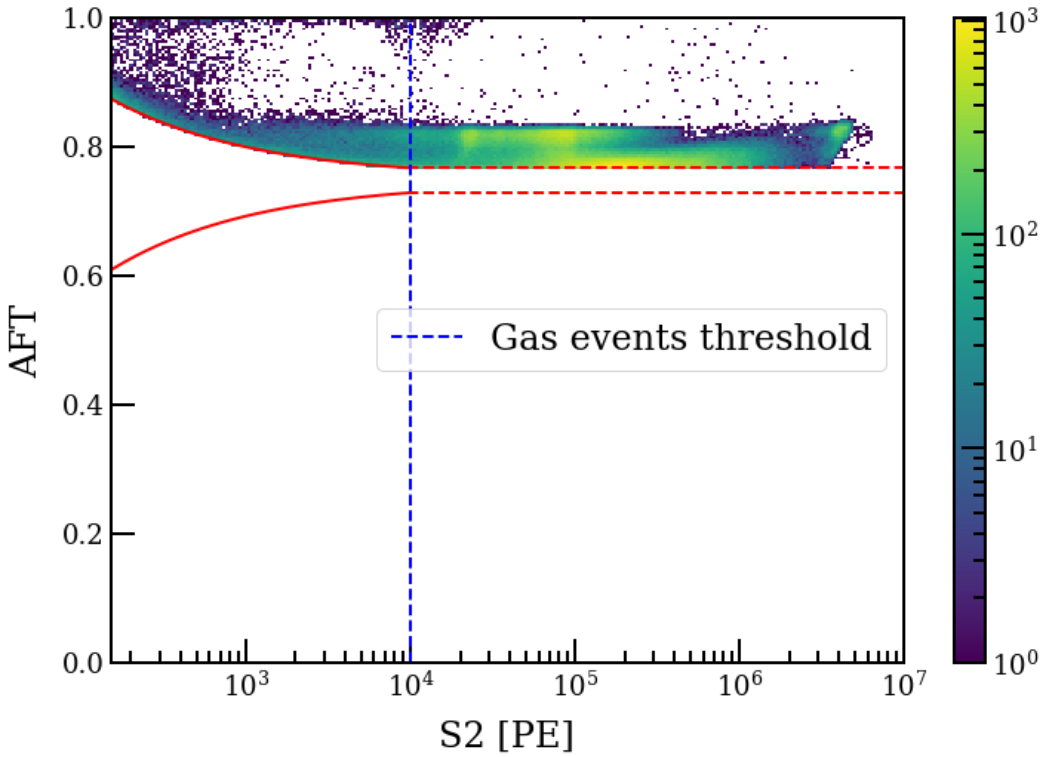

Figure 3.34: AFT value as a function of S2. The blue dashed line indicates the threshold of the gas event.

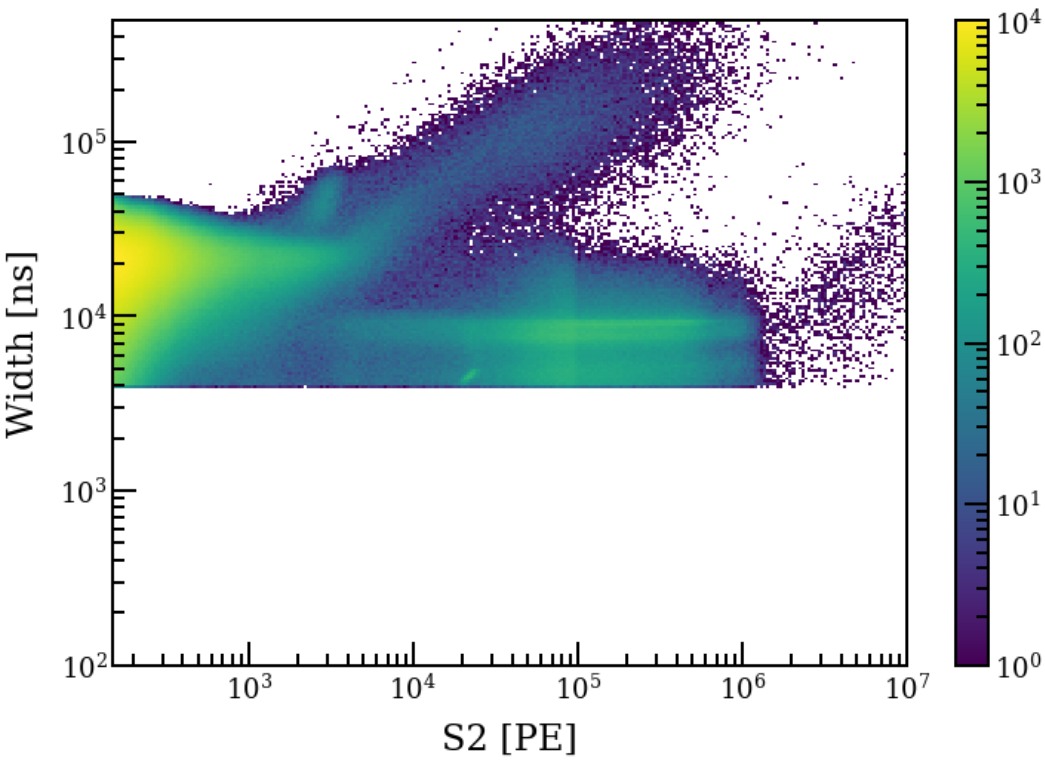

Figure 3.35: Width at 50% distribution of track events.

4) Liquid events

These events are defined as S2 events originating from interactions inside the LXe. In terms of parameter space, these events must be inside the S2AFT selection and have widths between 200 and 4000 ns, as shown in Figure 3.32 (right).

5) Alpha events

The last category corresponds to events generated by alpha particles, and these signals are a subset of liquid events. In order to select alpha events, a plot of S2 as a function of S1 is plotted, where the connection between S1 and S2 is made so that they are close in time with a maximum time difference corresponding to the total drift time. In addition, any event with multiple S1s is eliminated. Then in the space S1vsS2, a rectangle is selected where inside, S1 is between 35,000 PE and 60,000 PE, and S2 is between 14,000 PE and 30,000 PE. This selection is shown in Figure 3.36.
The alpha peak region is selected such that it includes all alpha peaks between and including ^{222}Rn and ^{216}Po since they are the primary known source of alpha background in XENONnT.

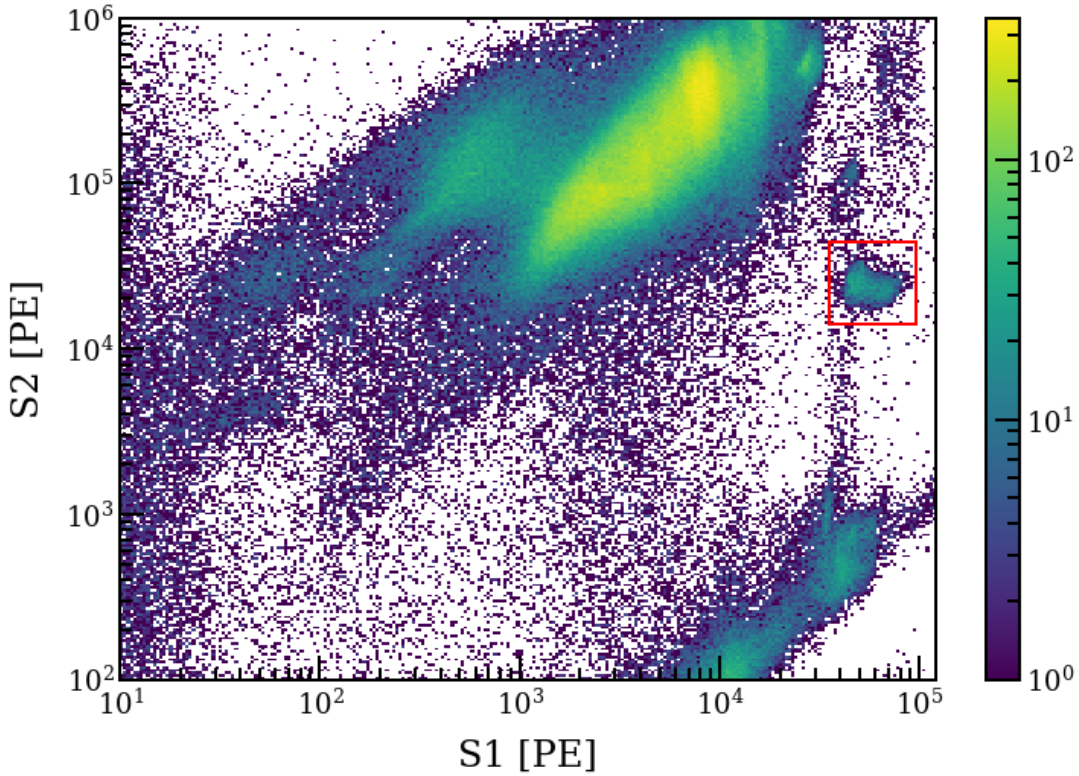

Figure 3.36: Cut box selection of alpha events.

Investigation of multiple interaction sites

Now let us look at populations 4 and 5; Since some of the hypotheses tested on the origin of single electrons directly link their production to interactions in

LXe, it would be necessary to consider possible events with multiple interactions. One way to observe the effect of multiple interactions is to plot the number of primary S2s against the most energetic signal energy in a constructed event (with S1 and multiple S2s). This plot is shown in Figure 3.37.

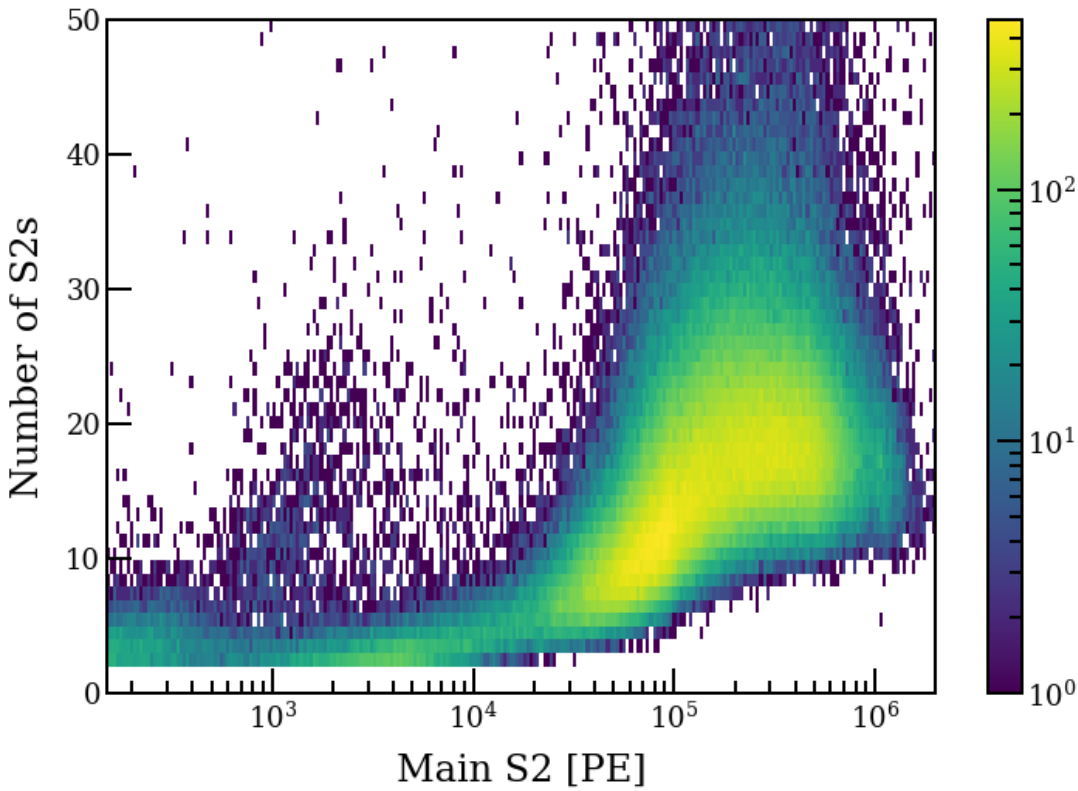

Figure 3.37: Distribution of the number of S2 signals in an event as a function of the energy of the main S2.

As seen in Figure 3.37, many events contain multiple interactions. Consequently, cutting all events with more than 2 (or even 3) primary S2 reduces the selection to a few percent of the liquid. Even if the primary S2 events are not in themselves the main object of this study, they are automatically excluded from the final selection. Nevertheless, these provide much information on the correlation or not of the low energy events and thus allow to exclude the correlated events from the selection for the search for dark matter.
Without necessarily wanting to cut the events with multiple interactions, it would nevertheless be possible to characterize them. This characterization consists in examining the distribution of these secondary S2 peaks in the two-parameter spaces already used to categorize the primary S2 signals. Figure 3.38 shows the S2Width values of the 2nd, 3th, 8th, and 16th largest (in energy) S2 peaks.

Figure 3.38 illustrates the phenomenon we expected to observe, namely that we go from events that closely resemble the distribution of the primary S2 in the parameter space S2Width for the second and third largest peaks to distributions dominated by "track" type events. This transition is explained by the fact that for larger S2, many more photo-ionization electrons are produced (as demonstrated

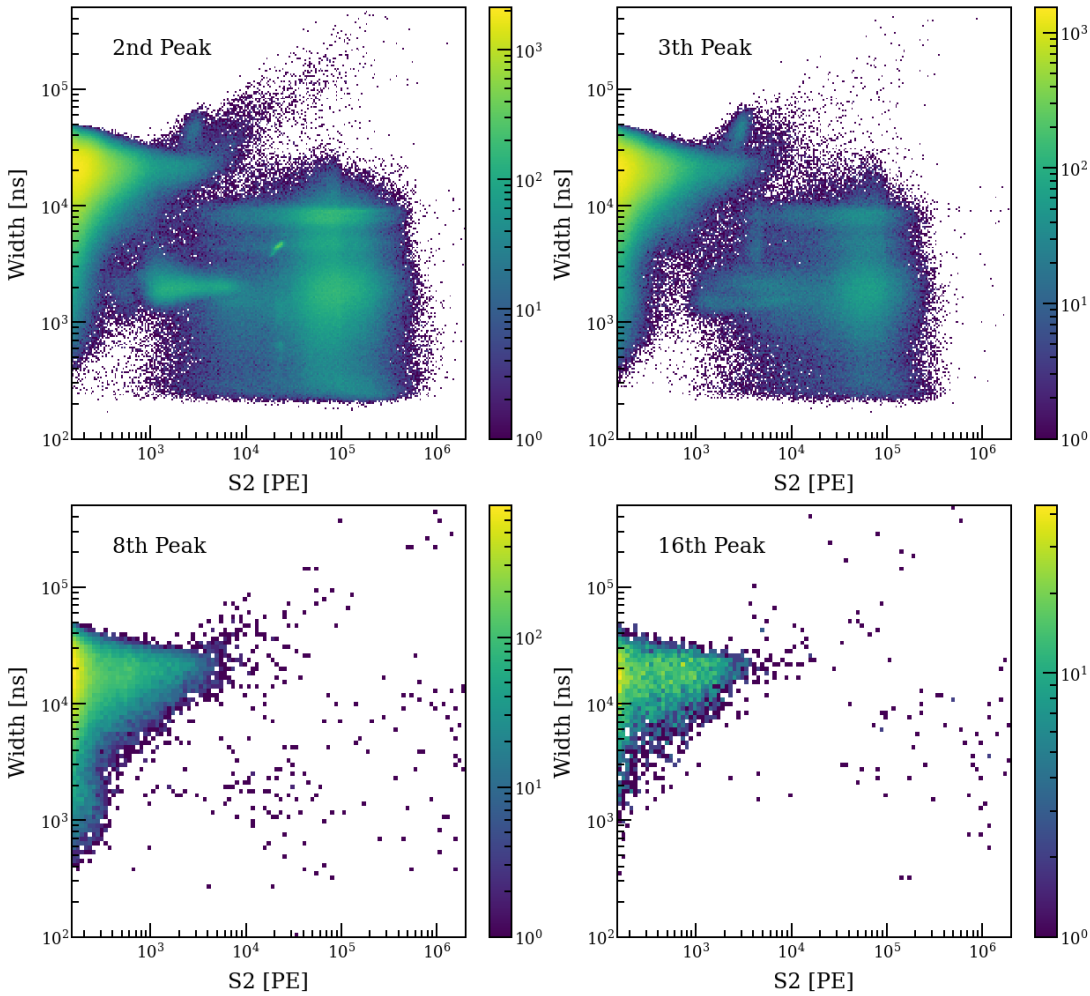

Figure 3.38: Distribution of the signal width at 50% for specific secondary S2 peaks.

in Section 3.2.3). Thus, as the rate becomes large enough, these photo-ionization electrons accumulate and are detected as large S2 with a large width.

In order to eliminate these S2s, resulting from photo-ionization electrons pile up, the cut to events occurring in the liquid is applied. Figure 3.39 gives the updated version of Figure 3.37 after applying the liquid event cut.

Figure 3.39 shows that the liquid events cut does not eliminate all the secondary S2 peaks (especially at very high energy). Thus an additional cut will be applied and consists in keeping only the four largest secondary peaks and then inspecting each correlation of SE at each of these peaks. The number of peaks with more than four secondary peaks represents about 1% of the selection shown in Figure 3.39.

3.7.6 Primary live-time cut

The primary event live-time is the time difference between one primary S2 and the following primary S2. This time difference gives the time window to search

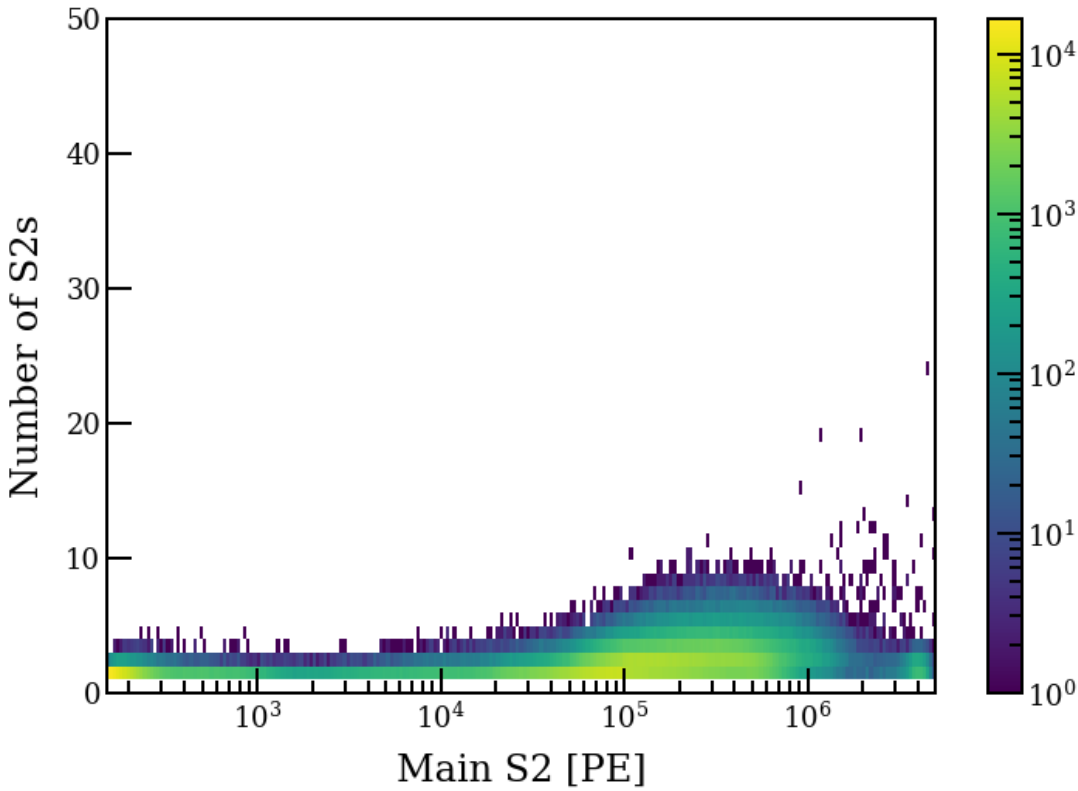

Figure 3.39: Distribution of the number of S2 signals surviving the liquid event cut in an event as a function of the energy of the main S2.

for SE (or light dark matter) events. Summing all these time windows in the total event selection gives the time exposure of the study.

The primary live-time cut aims to find the maximum time difference between two primary signals. Suppose the interval is calculated between two primary signals without an upper limit. In that case, this may lead to overestimating the exposure because it may include times between the triggering of two runs, for example. Thus, Figure 3.40 shows that there are primary S2 signals with a live-time of about 2.8 s, so the question is, is this event regular or is this lifetime too large?

To answer this question, we assume that the number of primary S2s follows a Poisson distribution:

$$P(x) = \frac{e^{-\mu}\mu^x}{x!}$$

Then the mean of the Poissonian should be equal to the product of the frequency f and the time interval t such that $\mu = ft$. Thus, the lifetime of an event is, therefore, the time interval T during which zero events are observed after an event, which results in:

$$P(T > t) = P(x = 0|\mu = ft) = e^{-ft}.$$

Finally, the probability density function can be calculated by normalizing the integral from 0 to infinity:

$$\mathrm{PDF}(t) = ae^{-ft} \tag{3.10}$$

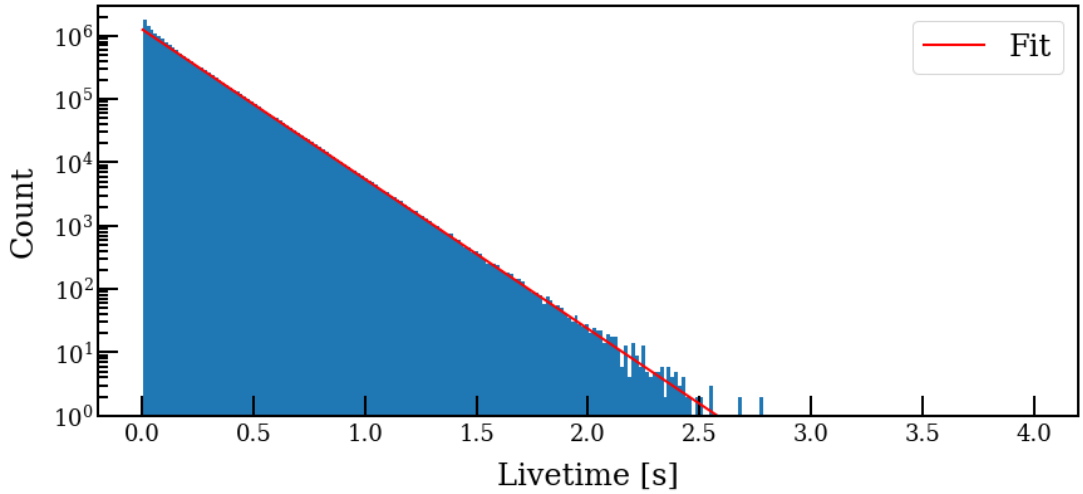

Figure 3.40: Primary S2 live-time distribution. In red the fit of the distribution with a power law.

By fitting the time windows distribution (Figure 3.40) with Equation (3.10), we obtain a frequency $f = 5.44$ Hz. Therefore, the probability $p(t > 2.8)$ for it to occur at $t = 2.8$ s is $p(t > 2.8) = P(x = 0|\mu = 5.44 * 2.8) = e^{-15.232} \simeq 2.4 \times 10^{-7}$, which is an occurrence that is expected in a selection of 1.64×10^7 events.

In conclusion, no cuts on the primary S2 live-time are necessary.

3.7.7 Cut on overlapping S2s

The study of single electron signals and their cut-off to look for possible dark matter signals is mainly based on examining low energy signals (below 150 PE), which follow a primary S2 (defined as any S2 greater than 150 PE).
Given that the rate of SE after a primary S2 seems to continue well after the maximum drift time (see Figure 3.6), even considering possible second-order photoionization signals, this observation leads us to think about other causes, such as what happens if two primary S2s are close in time. Indeed if two primary signals are close in time, it is expected that the single electron trains could overlap, which would skew the correlations so that we cannot be sure which primary S2 produced a SE signal.
This problem can be solved by applying a cut on a given primary S2 according to the size and time of the S2 which precedes it; this would suppress the events (and their corresponding electron trains) which could overlap.

Figure 3.41 illustrates an example of the data layout after eliminating the signals identified as S1. Thus, after a primary S2, all the signals SE following the latter are counted until arriving at the next primary S2.

The number of SEs and the time between the two primary S2s is used to calculate the single electron rate. However, as illustrated in Figure 3.41 (bottom), we must be careful which single electrons are associated with which primary S2 because just using the time proximity method does not necessarily give the correct result for the rate.

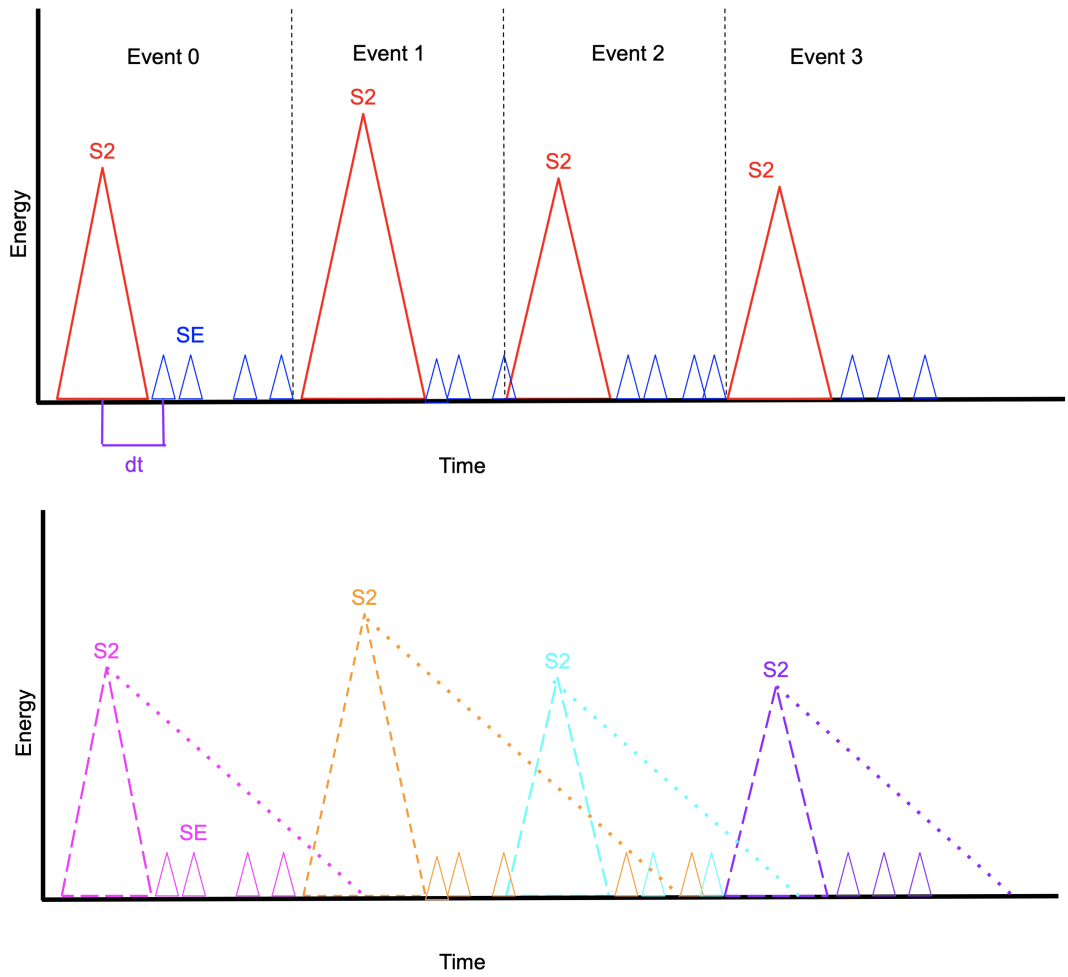

Figure 3.41: Diagram illustrating the overlap between the SE trains following primary S2 signals.

Calculation of overlap cut

The rate of single electrons following a primary S2 is expected to follow an exponential, based on the fact that these emissions should be Poissonian. However, during the study made with XENON1T, it turned out that this was not the case and that the rate follows a power law with a power of −0.7 or −1.1, depending on whether the rate studied corresponded to SE correlated or not with the position of the primary S2 [149]. This can be explained by the fact that the SE rate does not include only one signal type (in this case, it should follow a Poissonian) but include some pileup of multiple signals.

Assuming that the rate follows a power law, this leads that the latter can be modeled as follows:

$$\text{Rate} = C\ S2_i\ (\frac{\Delta t_i^j}{\tau})^{-\gamma}, \tag{3.11}$$

where, C is a constant. $S2_i$ is the size of the S2 in PE. Δt_i^j is the time between $S2_i$ and the single electron in consideration SE_j. τ is the time constant. Finally, γ is the power of the power law.

To estimate the single electron overlap of $S2_i$ at j and the contribution of $S2_{i-1}$ at j, one must calculate the ratio of the two rates:

$$\text{Ratio} = \frac{C\ S2_i\ (\frac{\Delta t_i^j}{\tau})^{-\gamma}}{C\ S2_{i-1}\ (\frac{\Delta t_{i-1}^j}{\tau})^{-\gamma}} \tag{3.12}$$

$$= \frac{S2_i}{S2_{i-1}}\ (\frac{\Delta t_i^j}{\Delta t_{i-1}^j})^{-\gamma} \tag{3.13}$$

$$= \frac{S2_i}{S2_{i-1}}\ (\frac{t^j - t_i}{t^j - t_{i-1}})^{-\gamma}, \tag{3.14}$$

From the previous section, the rate of primary S2 signals is of the order of 5 Hz. Therefore, the previous equation can be simplified as follows:

$$\frac{S2_i}{S2_{i-1}}\ (\frac{t^j - t_i}{t^j - t_{i-1}})^{-\gamma}\ >> 1 \tag{3.15}$$

$$\implies S2_i\ (\frac{t^j - t_i}{t^j - t_{i-1}})^{-\gamma} >> S2_{i-1}. \tag{3.16}$$

According to the threshold taken by the study made by XENON1T, we will require to avoid contamination that $S2_{i-1} \leq 10\%\ S2_i\ (\frac{t^j - t_i}{t^j - t_{i-1}})^{-\gamma}$. Finally, to take into account all the previous primary S2s, which can also contaminate the study time window, it is then necessary to generalize the threshold:

$$\sum_{k \neq i} S2_k\ \sum_j (\frac{t^j - t_k}{t^j - t_i})^{-\gamma} \leq 0.1\ S2_i. \tag{3.17}$$

It would be interesting to note that the dependence on the time constant, τ, has disappeared. Only the dependence on γ remains, determined by the rate fitting.

Calculation of the power law parameter γ

Figure 3.42 shows the fit of the single electron rate (without cutting on the correlation in position). This fit gives a $\gamma = -0.9$, which is compatible with the values of γ found via the study of XENON1T data [149].

3.7.8 Position correlation cut

We already saw that the SEs were temporally correlated with the previous primary S2 signals. The goal will now be to investigate the spatial correlation between the position of delayed single electron signals, i.e., single electrons that occur more than 1 ms after an interaction in the detector, and the position of the previous primary.

For this study, the data selected consists of 100 runs (~50h) taken randomly from the data set selected in Section 3.7. In addition, the SE events must pass the SE selection (see Section 3.7.3), the primary S2 of the set must pass the liquid event selection (see Section 3.7.5), and the overlap cut (see Section 3.7.7).

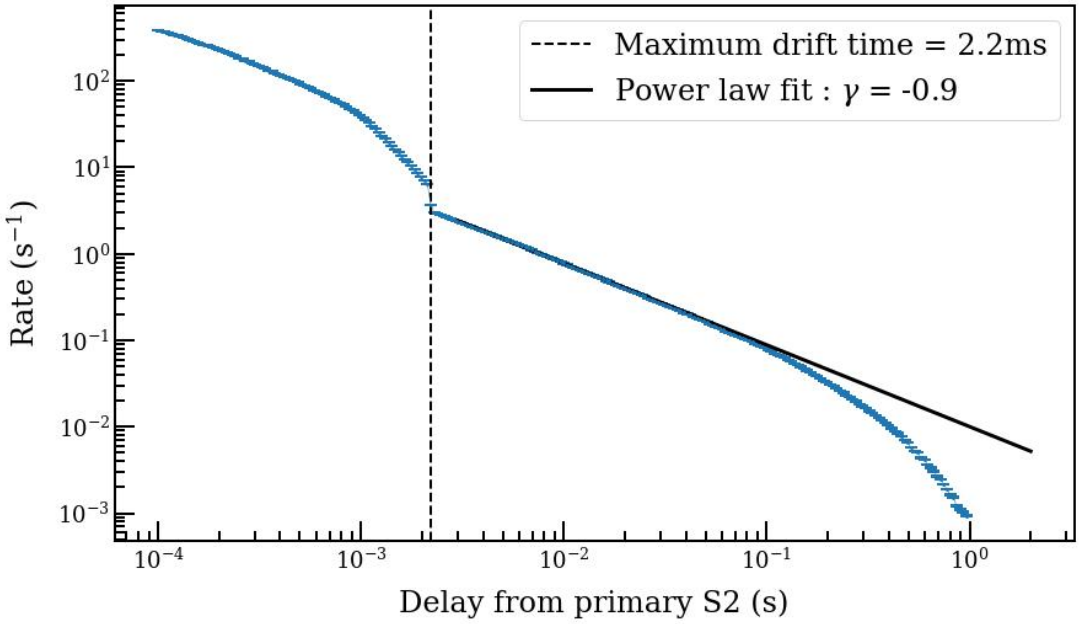

Figure 3.42: SE rate following an S2 primary. The dotted vertical line marks the maximum drift time. In black, the curve fit of rate after the maximum drift time.

After applying the abovementioned cuts to the entire detector, Figure 3.43 illustrates the distance distribution between the primary interaction that preceded an SE signal and the SE itself.
It should be noted that only the primary signal must be inside the fiduciary volume; the SE can always come from anywhere in the detector.

As expected, Figure 3.43 shows that the rate of SE near the place of interaction of a primary signal is much higher than in the rest of the detector, thus giving new proof that these signals are indeed causally linked to the primaries that precede them. Moreover, the effect of the wire leads to the distribution not having a quite radial symmetry.

The goal now consists of quantifying the correlated electrons spatial extent in order to cut them from the final selection. To do this, finding a model that describes the distribution of Δx vs. ΔY is necessary. This distribution is expected to be the sum of two distributions, an uncorrelated event distribution and a spatially correlated event distribution.

For the uncorrelated distribution, the choice of a flat or uniform distribution as the model would not be correct since this choice does not consider non-uniformities in the distribution of primary S2 and single electrons in the data. A second choice, the one chosen, which seems more judicious, consists of randomly sampling a number N_{prim} of primary S2 interactions and, separately, N_{se} of SE from the data. For each sampled primary S2 interaction, the Δx and the Δy are calculated relative to the total sample of SE[8].Finally, the background model is normalized for the number of interactions in the dataset to allow consistency when comparing the scale factor between different datasets. This is shown in

[8]For FV slices, random primary events are selected from the FV. SE sample selection is still not spatially constrained.

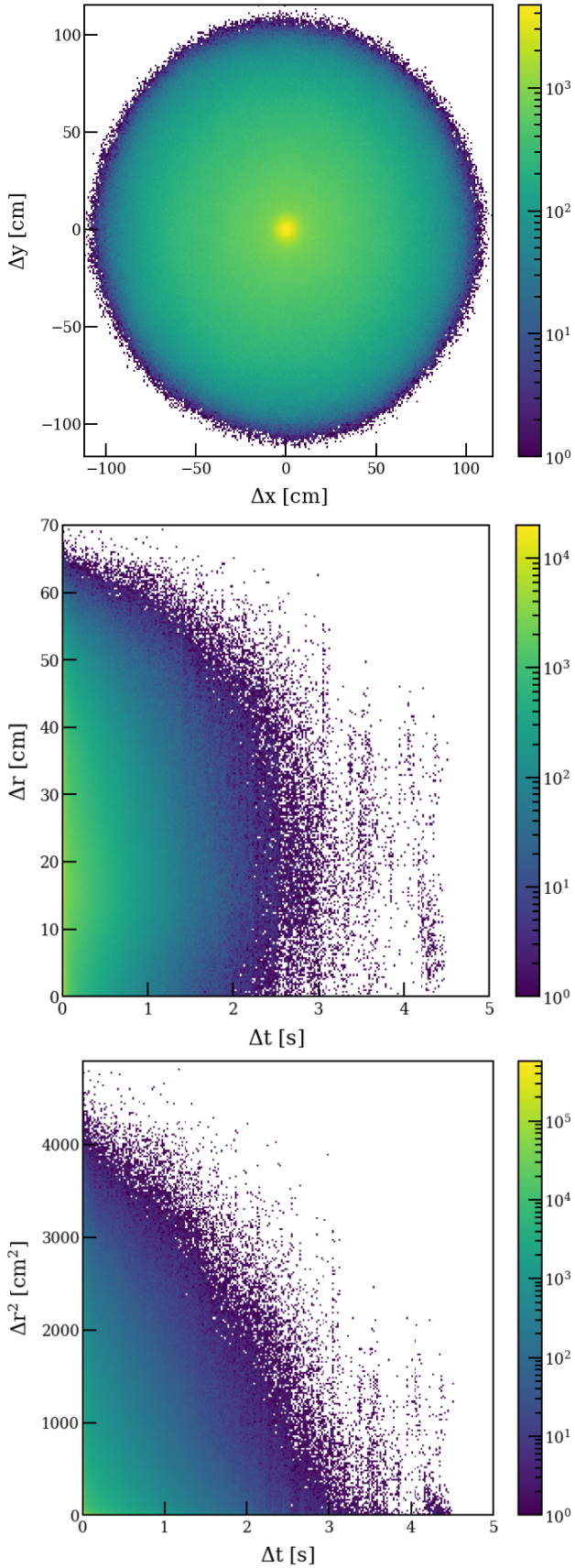

Figure 3.43: Position correlation of SE signals to the preceding primary

the lower panel of Figure 3.44 in the orange dotted line; this plot represents the distribution if no correlation exists.

On the other hand, a Gaussian distribution cannot describe the correlated distribution due to the S2-size-dependent position reconstruction of both the primary S2 and the delayed electron broadening the distribution's tails. Thus, to represent these effects, a choice was made to use a Cauchy-Lorentz distribution represented by the green dotted line in Figure 3.44. The width of the Cauchy-Lorentz distribution, defined as half-width at half-height, is consistent with the XENONnT position reconstruction uncertainty for single electrons.

Finally, since the region of enhanced emissions is small relative to the total area of the detector in the XY plane, the total electron emission rate can be comparable to the rest of the detector. Therefore, using the combined model shown in the cyan line of Figure 3.44, it is possible to define a region of positionally correlated electrons to have occurred at < 5 cm from the S2 primary, where the boundary is chosen so that $> 99\%$ of the electrons delayed in the chosen radius are attributable to the Cauchy-Lorentz distribution, as shown in the lower panel of the Figure 3.44 by the vertical red lines.

All the selections made in this chapter will be used in the next chapter to set limits on various models of dark matter at low energy.

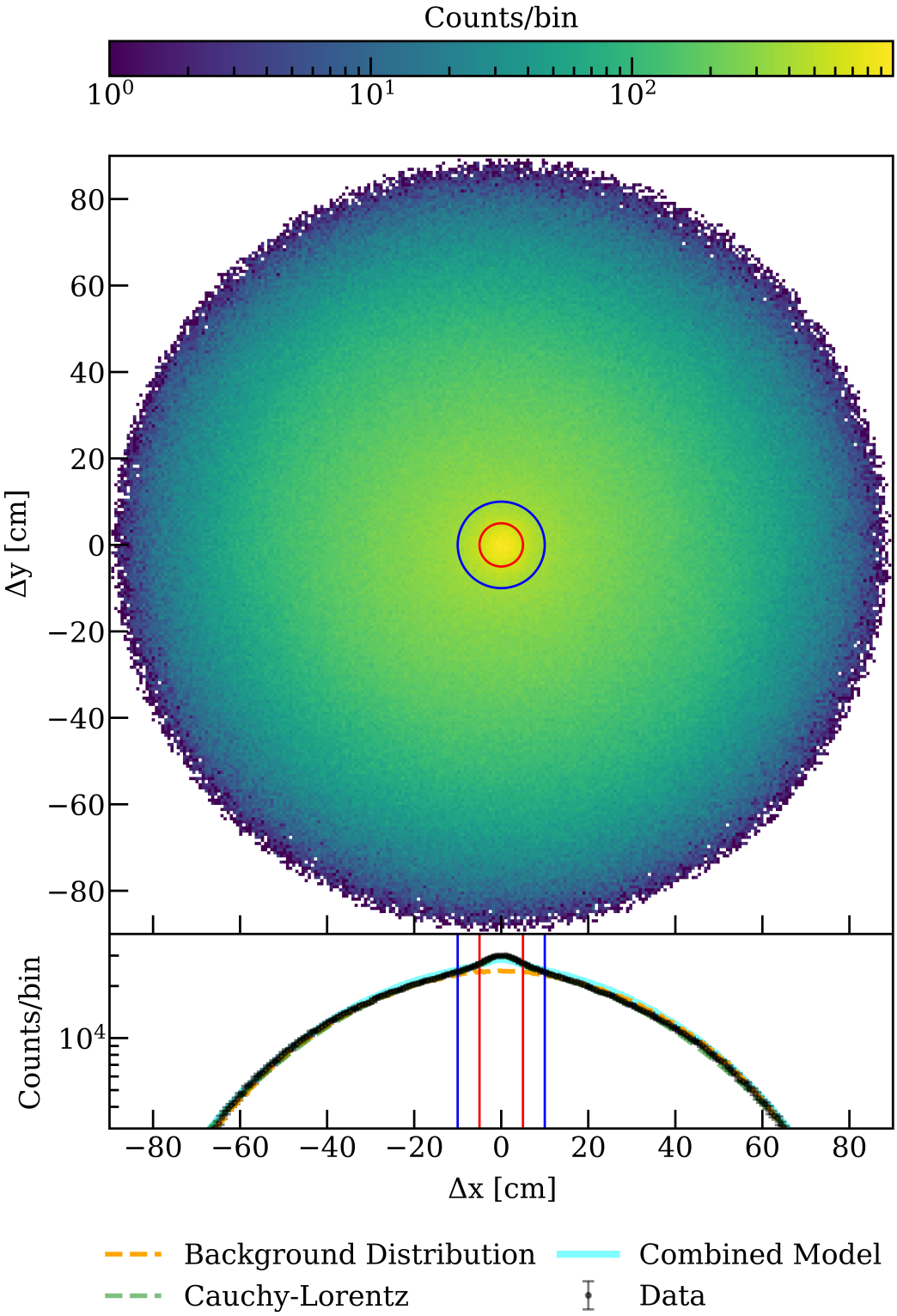

Figure 3.44: (Top) The difference in x-y between SE and the previous primary S2. (Bottom) Comparison between the observed and expected difference on the x-axis. The orange line shows the expected difference if no position correlation exists. The dashed green line represents the best fit of a Cauchy-Lorentz distribution to the correlated population. The combined model is shown in cyan. The red (blue) lines indicate the position correlated (uncorrelated < 5 cm) selection.

Chapter 4

Search for sub-GeV dark matter using SR0 XENONnT electronic recoils data

This last chapter deals with the theoretical study of dark matter-electron interactions, using the characterization of the intensity of single electron backgrounds and the study of the correlation in time and position of these emissions with high-energy events presented in the previous chapter. It was possible to remove correlated single electrons backgrounds, and the remaining dataset is used to set 90% confidence upper limits for dark matter-electron scattering. This limit (not shown in this manuscript see Section 4.9) is obtained through the search for dark matter interacting with electrons in the XENONnT detector and producing a small number of electrons (1-5 electrons). This analysis provides lower mass sensitivity than the S2-only analysis of nuclear recoils. This chapter first presents the calculations of cross-section and interaction rates. Secondly, limits on dark matter scenarios are presented, including leptophilic dark matter, dark photons, and dark solar photons.

4.1 Introduction

The XENON experiment, via its XENON1T detector, holds the sensitivity record for dark matter with a mass greater than 0.1 GeV/c^2 (except for the $2-3$ GeV/c^2 region, see Figure 4.1). Despite substantial improvements in sensitivity generation after generation, it remains challenging for noble liquid experiments to be competitive in dark matter mass regions below 1 GeV/c^2. This lack of sensitivity is due to the intrinsic scintillation properties of nuclear recoils preventing experiments using noble materials from reaching sub-GeV masses for analyses based on the S1 and S2 signals. Lower thresholds can nevertheless be achieved in S2-only studies [97], which remove the requirement for the scintillation signal (S1) since charge yield is higher at low energy. In the few electron energy range, the background noise of single electrons, being not modeled to date, prevents any possibility of detection claims and imposes highly restrictive cuts to reduce it as much as possible.

Nevertheless, steady progress in narrowing the dark matter parameter space has made lighter particles more attractive as possible candidates. On the other hand, XENONnT being highly pure, represent a compelling opportunity to investigate the low-mass dark matter through a noble liquid detector.

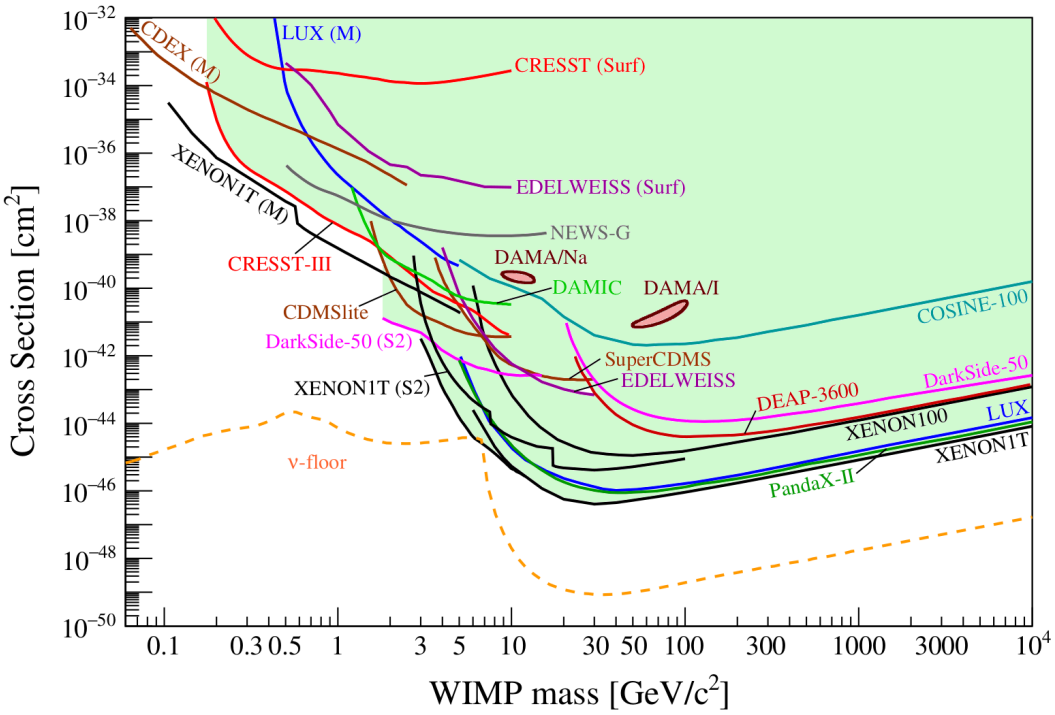

Figure 4.1: Current status of searches for spin-independent elastic WIMP-nucleus scattering assuming the standard parameters for an isothermal WIMP halo: $\rho_0 = 0.3$ GeV$/cm^3$, $v_0 = 220$ km/s, $v_{esc} = 544$ km/s. Results labeled "M" were obtained assuming the Migdal effect [158]. Results labeled "Surf" are from experiments not operated underground. The ν-floor shown here for a Ge target is a discovery limit defined as the cross section σ_d at which a given experiment has a 90% probability of detecting a WIMP with a scattering cross section $\sigma > \sigma_d$ at ≥ 3 sigmas. It is computed using the assumptions and the methodology described in [159, 160]. However, it has been extended to a very low dark matter mass range by assuming an unrealistic 1 meV threshold below 0.8 GeV$/c^2$. (Figure from [53]).

Recently, there has been increased interest in methods for detecting low-mass dark matter in direct detection experiments [53]. In this context, the main difficulty that must be overcome lies in the fact that for low-mass dark matter, the recoil energy deposited in the detector is low compared to the threshold values necessary for detection. This problem is exacerbated when the dominant interaction is with nucleons. Nevertheless, some promising detection strategies involve new analytical methods in addition to new detection technologies. One of these methods, which has been the subject of several studies in recent years, is based on the Migdal effect [161, 158]. Analyzes have focused primarily on elastic nuclear scattering. However, inelastic dark matter scattering is a characteristic

of many classes of dark matter models [162, 163].

Assuming that a dark matter particle diffuses on a nucleus, the Migdal effect predicts that electrons can be released due to this interaction. This type of interaction eliminates the problem related to the energy threshold, and these Migdal electrons can then provide the main channel to detect sub-GeV dark matter directly.

The Migdal effect should be distinguished from ionization and excitation in scintillation processes. It can occur even in single atom scatters, whereas scintillation arises due to atoms' interaction in detectors. It should also be noted that the Migdal effect can ionize/excite electrons in inner orbitals, which is not expected in scintillation processes.

Despite the enormous advantage provided by the introduction of the Migdal effect in studies, the fact remains that Migdal interactions are based on interactions with nucleons; as a result, the sensitivity decreases exponentially for dark matter particles with a mass lower than 0.1 GeV/c^2V, considering canonical assumptions [97, 163]. Hence, the search for lighter dark matter must be done via interactions with electrons. This type of dark matter is generally called leptophilic dark matter; this designation includes dark matter which only interacts with electrons (truly leptophilic) but also dark matter, which interacts with nucleons, but whose interaction with nucleons is too weak to be detected.

Candidate particles for leptophilic dark matter arise from classes of theories beyond the classical WIMP paradigm, postulating light dark matter with mass in the MeV region. In these scenarios, the dark matter resides in a so-called hidden sector (see Section 1.5.4), which would provide a new gauge group independent of the Standard Model.

Most early hidden sector models predicted the existence of a more or less complete mirror of the Standard Model. These mirror models included copies of SM particles, which could even form large compact structures in the Universe [164, 165, 166]. In the same way as for MACHOs, microlensing experiments refute the existence of these large structures [9]. However, the idea that dark matter could be in a hidden sector remained.

Hidden sector dark matter models have evolved since then. Updated theories postulate that dark matter only interacts with the Standard Model through its coupling to the Higgs [167]. However, the discovery of the Higgs restricted the production cross-sections and hence the coupling across the Higgs. Nowadays, the main model predicts that the interaction between dark matter and electrons would be mediated by a gauge boson of a hidden sector Abelian group, which couples with charged SM particles via kinetic mixing[1] with the photon [168].

The Abelian discrete symmetries are generally imposed to control the allowed couplings in theories beyond the Standard Model. For example, according to the general laws of quantum physics, the existence of new particles affects the interactions between the particles of the Standard Model. In particular, it affects the stability of the proton. A new Abelian symmetry, called R-parity (also known as matter parity) [169], was therefore postulated to protect the proton by making

[1] *Kinetic mixing* is a phenomenon in which a new gauge boson (the 'dark photon') can change back and forth into a regular photon.

it stable. This symmetry has another notable consequence: it makes stable the lightest supersymmetric particle, naturally making it a potential candidate for dark matter [74].

The exploration of the hidden sector is motivated by several reasons. First, it is an alternative to the famous WIMP model, which is increasingly challenged by the significant sensitivity limits reached in recent years. These experimental results lead to consider that dark matter is either lighter or interacts much more weakly than the WIMP model predicts (or both). On the other hand, the hidden sector models could be the harbinger of a new area of physics at scales that would be experimentally inaccessible, known as the *high-precision/low-energy frontier*.

Another view favoring the hidden sector, which is more prosaic, boils down to a question of stability. In general, heavier particles decay into lighter particles. So lighter particles, being more stable, are much more likely candidates for dark matter.

4.2 Direct detection rates

There are various sub-GeV candidates from hidden sector models. This section will be devoted to the scattering of dark matter with an electron, in which a fermion or a dark matter candidate scalar boson scatters on a bound electron in a Xenon atom. The calculations are largely inspired by [170].

Below a certain mass of dark matter, the energy of nuclear recoils will be below the detection threshold, i.e., below the recoil energy needed to generate the ionization and scintillation signal, which could be detected as an S1-S2 couple in the case of XENONnT. Although the S1-S2 signal cannot be detected for some small energies deposited through NR ($q^2/2m_{nucleus}$), the total energy of dark matter particles ($\frac{1}{2}m_\chi v_\chi^2$) might be greater than the binding energy of an electron in the outer shell or the energy difference between some atomic levels. Therefore, if dark matter particles had interactions with electrons, it would be possible to have signals from inelastic atomic processes leading to ionization or excitation of the Xe atom.

The following calculation aims to estimate the difference in energy between signals emitted by the interaction of dark matter particles with a nucleon and an electron.

The energy released by nuclear recoil is

$$E_{\rm NR} = \frac{q^2}{2m_N} \leq \frac{2\mu_{\chi N}^2 v^2}{m_N} \simeq 1 \text{ eV} \times \left(\frac{m_\chi}{100 \text{ MeV}}\right)^2 \left(\frac{10 \text{ GeV}}{m_N}\right), \tag{4.1}$$

where m_N is the mass of the nucleus, $q \sim m_\chi v$ is the momentum transferred, and $v \simeq 10^{-3}c \approx 300$ km/s is the dark matter velocity. For $m_\chi = 30$ GeV, $E_{\rm NR} \sim 1$ MeV. However, for lighter dark matter, for example $m_\chi = 100$ MeV, the recoil energy decreases to $E_{\rm NR} \sim 10$ eV, which is well below the detection thresholds of XENON detectors, i.e $\mathcal{O}(1)$ keV$_{\rm nr}$). This can be explained by the fact that the

energy from the recoil nucleus is not efficiently transferred to the electrons and, therefore, not enough to ionize or excite even a single electron. As a result, dark matter particles with masses below approximately 100 MeV escape detection, regardless of their cross-section.

The energy transferred to the electron, ΔE_e, can be obtained from the momentum lost by the dark matter particle, $\vec{q}$, via the conservation of energy:

$$\Delta E_e = -\Delta E_\chi - \Delta E_N = -\frac{|m_\chi \vec{v} - \vec{q}|^2}{2m_\chi} + \frac{1}{2} m_\chi v^2 - \frac{q^2}{2m_N} = \vec{q} \cdot \vec{v} - \frac{q^2}{2\mu_{\chi N}} \,. \tag{4.2}$$

where the term $\frac{q^2}{2\mu_{\chi N}}$ takes into account that the atom will recoil as a whole, thus, replacing $\mu_{\chi N}$ with m_χ, maximizes (4.2) with respect to $\vec{q}$ and gives the maximum energy transferred to the electron.

$$E_e \equiv \Delta E_e = -\Delta E_\chi \leq \frac{1}{2} \mu_{\chi N} v^2 \simeq \frac{1}{2} \text{ eV} \times \left(\frac{m_\chi}{\text{MeV}} \right) . \tag{4.3}$$

From Equation (4.3), it follows that for a dark matter particle of $\mathcal{O}(50 \text{ MeV})$, E_e can be greater than the binding energy of the outer shell of the Xe atomic states. Under those circumstances, the ionized electron will be detected as a single electron signal if it survives the drift and is extracted to the gaseous phase. Moreover, suppose the electron, during its extraction, is provided with an energy higher than the W value (see Figure 4.2). In that case, it will produce an additional number of ionization electrons in the LXe. If they survive the drift and are extracted to the GXe, they will produce a signal similar to a temporal pile-up of single electrons.

Ultimately, the calculation of the events rate is significantly more complex than the corresponding calculation of the nuclear recoil rates. This is due to the fact that the electrons are bound in a multi-electron system. Therefore, a non-relativistic quantum mechanical perspective drives the whole dynamics of the system and operates at two key points.

First, the electron is in the atomic orbital, i.e., a state of the atomic Hamiltonian. Therefore, rough calculations that do not consider the existence of other electrons and their effect on the electron in question may not yield accurate results. Nevertheless, once correctly calculated, the quantum effects can be fully encoded in an atomic form factor. This form factor function is different for each specific target material but is independent of the dark matter model [170].

Second, after the collision with the dark matter particle, the ionization electron will be in an unbound state of this multi-fermion system. However, its final state is deformed by an effective nuclear charge.
Figure 4.3 illustrates the excitation of an electron to a higher energy level or an unbound state.

4.2.1 Excitation rates

Following the model-independent approach of [170], it is possible to subsequently parameterize the elastic scattering cross-section.

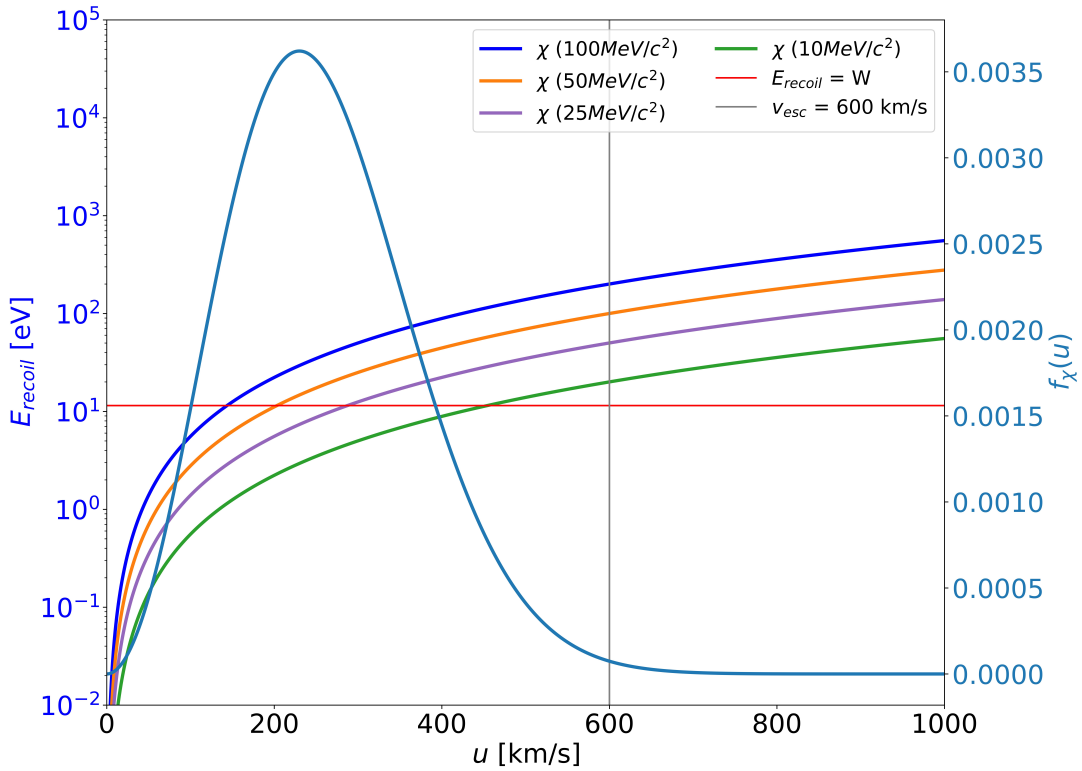

Figure 4.2: The maximum electronic recoil energy as a function of dark matter velocity. The cyan curve gives the velocity distribution of the standard halo model.

Suppose a dark matter particle scatters with an electron in a stationary bound state (as is the case for electrons orbiting an atomic nucleus). In this case, the DM can excite the electron from an initial energy level 1 to an excited energy level 2 by transferring an energy $\Delta E_{1\to 2}$ and momentum $\vec{q}$. The cross-section of this process can be derived in a standard method using non-relativistic quantum mechanics. Nevertheless, to facilitate the connection with the underlying particle physics, it would be preferable to derive it from the usual cross-section formula in field theory. The electron is treated as being bound to a static background potential, which is to say that the supposed atoms are infinitely heavy and can absorb momentum without recoiling. This approximation can be justified by the fact that the momentum transfers in question are generally of the order of keV, which results in an $< 1\%$ error.

The cross section for free $2 \to 2$ ($n_i = n_f = 2$) scattering is given by

$$\sigma v_{\text{free}} = \frac{1}{4E'_\chi E'_e} \int \frac{d^3q}{(2\pi)^3} \frac{d^3k'}{(2\pi)^3} \frac{1}{4E_\chi E_e} (2\pi)^4 \delta(E_i - E_f) \delta^3(\vec{k} + \vec{q} - \vec{k}') \overline{|\mathcal{M}_{\text{free}}(\vec{q})|^2}\,, \quad (4.4)$$

where $\mathcal{M}_{\text{free}}$ is the field-theory matrix element, and $\overline{|\mathcal{M}|^2}$ represents its absolute square averaged over initial spins and summed over final spins.

If the electron were unbound, the non-relativistic scattering amplitude would be given by

$$\langle \chi_{\vec{p}-\vec{q}}, e_{\vec{k}'} | H_{\text{int}} | \chi_{\vec{p}}, e_{\vec{k}} \rangle = C\, \mathcal{M}_{\text{free}}(\vec{q}) \times (2\pi)^3 \delta^3(\vec{k} - \vec{q} - \vec{k}')\,, \quad (4.5)$$

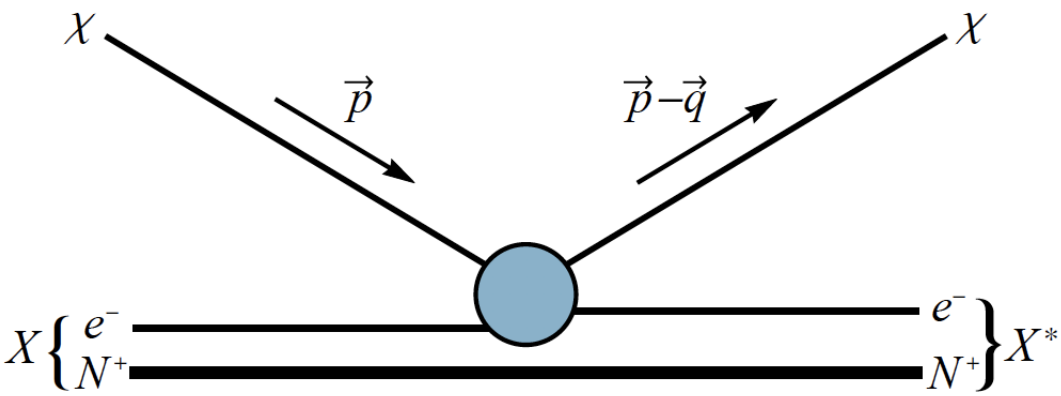

Figure 4.3: The scattering of a dark matter particle with a bound electron. The DM transfers momentum $\vec{q}$ to the Xe atom, exciting it from the ground state X to an excited state X^*, which can be either a higher-energy bound state or an ionized state. (Figure taken from [170])

where $|\chi_{\vec{p}}, e_{\vec{k}}\rangle$ is the plane wave state for a dark matter particle of momentum $\vec{p}$ and a momentum electron $\vec{k}$, H_{int} is the interaction Hamiltonian and C is a coefficient of no real importance. However, as the electron is bound, the non-relativistic scattering amplitude is given by

$$\begin{aligned}\langle \chi_{\vec{p}-\vec{q}}, e_2|H_{\text{int}}|\chi_{\vec{p}}, e_1\rangle &= \left[\int \frac{\sqrt{V}d^3k'}{(2\pi)^3}\widetilde{\psi}_2^*(\vec{k}')\langle \chi_{\vec{p}'}, e_{\vec{k}'}|\right]H_{\text{int}}\left[\int \frac{\sqrt{V}d^3k}{(2\pi)^3}\widetilde{\psi}_1(\vec{k})|\chi_{\vec{p}}, e_{\vec{k}}\rangle\right] \\ &= C\,\mathcal{M}_{\text{free}}(\vec{q}) \times \int \frac{Vd^3k}{(2\pi)^3}\widetilde{\psi}_2^*(\vec{k}+\vec{q})\widetilde{\psi}_1(\vec{k})\,, \end{aligned} \tag{4.6}$$

where $\widetilde{\psi}_1$, $\widetilde{\psi}_2$ are the momentum-space wave functions (normalized to unity) of the initial and final electron levels. The normalization of the plane waves for the states of free and bound electrons gives: $\langle e_{\vec{k}}|e_{\vec{k}}\rangle = \langle e_1|e_1\rangle = (2\pi)^3\delta^3(\vec{0}) \equiv V$, where V is the volume of space (which will vanish at the end).

Finally, the cross-section formula of free $2 \to 2$ scatterings is used to find the cross section of the excitation process. However, two substitutions are needed: one for the modified scattering amplitude and the other for the difference in the phase of the final state. By squaring Equations (4.5), (4.6), it can be seen that the bound state scattering amplitude can be taken into account by performing the replacement

$$V(2\pi)^3\delta^3(\vec{k}-\vec{q}-\vec{k}')|\mathcal{M}_{\text{free}}|^2 \longrightarrow |\mathcal{M}_{\text{free}}|^2 \times V^2|f_{1\to 2}(\vec{q})|^2\,, \tag{4.7}$$

where $f_{1\to 2}(\vec{q})$ is the *atomic form factor*.

$$f_{1\to 2}(\vec{q}) = \int \frac{d^3k}{(2\pi)^3}\widetilde{\psi}_2^*(\vec{k}+\vec{q})\widetilde{\psi}_1(\vec{k})\,. \tag{4.8}$$

Since there is only one final state of the electron that is considered, then the phase space integral of the final state can be eliminated:

$$\text{free-electron phase space} = V\int \frac{d^3k'}{(2\pi)^3} \longrightarrow 1\,. \tag{4.9}$$

The combination of Equations (4.4), (4.7), (4.9), allows to obtain the formula of the cross-section of a dark matter particle to excite an electron from level 1 to level 2:

$$\sigma v_{1\to 2} = \frac{1}{4E'_\chi E'_e}\int \frac{d^3q}{(2\pi)^3}\frac{1}{4E_\chi E_e}2\pi\delta(E_i - E_f)\overline{|\mathcal{M}_{\text{free}}(\vec{q})|^2} \times |f_{1\to 2}(\vec{q})|^2 . \tag{4.10}$$

And since it is the non-relativistic regime that is considered, then the energies are given by

$$E_i = m_\chi + m_e + \frac{1}{2}m_\chi v^2 + E_{e,1} \tag{4.11}$$

$$E_f = m_\chi + m_e + \frac{|m_\chi \vec{v} - \vec{q}|^2}{2m_\chi} + E_{e,2} . \tag{4.12}$$

According to [170], the a reference cross section $\overline{\sigma}_e$ parametrizing the DM-electron coupling is given by

$$\overline{|\mathcal{M}_{\text{free}}(\vec{q})|^2} \equiv \overline{|\mathcal{M}_{\text{free}}(\alpha m_e)|^2} \times |F_{\text{DM}}(q)|^2 \tag{4.13}$$

$$\overline{\sigma}_e \equiv \frac{\mu_{\chi e}^2 \overline{|\mathcal{M}_{\text{free}}(\alpha m_e)|^2}}{16\pi m_\chi^2 m_e^2} , \tag{4.14}$$

where $F_{DM}(q)$ is the *dark matter form factor*, which parameterizes the full momentum dependence of $\mathcal{M}$. The precise functional form of $F_{DM}(q)$ depends on the specific interaction.

Considering Equation (4.14), the cross-section simplifies to

$$\sigma v_{1\to 2} = \frac{\overline{\sigma}_e}{\mu_{\chi e}^2}\int \frac{d^3q}{4\pi}\,\delta\Big(\Delta E_{1\to 2} + \frac{q^2}{2m_\chi} - qv\cos\theta_{qv}\Big) \times |F_{\text{DM}}(q)|^2 |f_{1\to 2}(\vec{q})|^2 . \tag{4.15}$$

Depending on the dark matter form factor, there are three cases of interest regarding the phenomenology of the relict abundance of light dark matter:

- $F_{DM}(q) = 1$, where the scattering can be approached as a point interaction, resulting, for example, from an exchange of heavy vector mediators.
- $F_{DM}(q) = \frac{\alpha m_e}{q}$, corresponding to an electric dipole moment coupling.
- $F_{DM}(q) = (\frac{\alpha m_e}{q})^2$, where the interaction is via the exchange of an ultralight vector mediator.

4.2.2 Ionization form factor

Following the formula presented in [52] for $\frac{d\langle\sigma^i_{ion}v\rangle}{d\ln E_R}$, it can be shown that the velocity-averaged cross section for the ionization of an atomic electron, can be written as:

$$\frac{d\langle\sigma^i_{ion}v\rangle}{d\ln E_R} = \frac{\overline{\sigma}_e}{8\mu_{\chi e}^2}\int q\,dq\big|f^i_{ion}(k',q)\big|^2\big|F_{\text{DM}}(q)\big|^2\eta(v_{\min}) \tag{4.16}$$

where $\eta(u)$ is the mean-inverse velocity and v_{min} is the minimum velocity required for a dark matter particle of mass m_χ in order to ionize an electron from its initial

bound state.
$\eta(v_{\min})$ is defined as,

$$\eta(v_{\min}) = \int \frac{d^3v}{v}\, g_\chi(v)\, \Theta(v - v_{\min})\,, \tag{4.17}$$

and $v_{\min}$ is a function of q and the energy transfer and is given by

$$v_{\min}(q, \Delta E_{1\to 2}) = \frac{\Delta E_{1\to 2}}{q} + \frac{q}{2m_\chi}\,. \tag{4.18}$$

The fact that the electron is in an atomic bound state is described by the ionization form factor $\left|f^i_{ion}(k', q)\right|$. The wavefunctions of the electron must be determined both in its bound and free states in order to calculate the form factor. Also, for the amplitude of this transition, it is assumed that the atomic potential is spherical and with filled shells. Thus, $|\langle \text{unbound}|e^{iqx}|\text{bound}\rangle|^2$ will constitute a coherent sum over all possible bound states. This allows to define the dimensionless *ionization form factor*, for the transition from a bound state $\psi_i(\vec{x})$ to an unbound state $\psi_{k'l'm'}$, given from the relation:

$$\left|f_{\text{ion}}(k', q)\right|^2 = \frac{2k'^3}{(2\pi)^3} \sum_{\substack{\text{occupied}\\ \text{states}}} \sum_{l'm'} \left| \int d^3x\, \widetilde{\psi}^*_{k'l'm'}(\vec{x})\psi_i(\vec{x})e^{i\vec{q}\cdot\vec{x}}\right|^2. \tag{4.19}$$

The first sum is over all degenerate initial states that are occupied by the atomic electrons. Here $\psi_i(\vec{x})$ is the wavefunction of the bound state i, and $\psi_{k'l'm'}$ is the final state of the ionized electron, which is an unbound eigenstate of the atomic Hamiltonian. The energy of the ionization electron is $E_R = k'^2/2m_e$, and the energy spectrum is a continuum of states $\psi_{k'l'm'}$ described by the quantum numbers l' and m'. Asymptotically, the free electron can be approximated by a plane wave for a large enough radius of separation from the ion.

The main difficulty in calculating event rates is reflected in Equation (4.19). It must be estimated in such a way as to best take into account the dynamics governing the initial and final states of the electrons.
Since unbounded wave functions are complex to compute, it would be useful to approximate the outgoing electron as a free-plane wave. In this case, assuming plane wave final states for the scattered electron, so that $k' = \sqrt{2m_e E_{\text{er}}}$, the ionization form factor for spherically symmetric shells with quantum numbers $(n\,\ell)$ reduces to

$$|f^{n\ell}_{\text{ion}}(k', q)|^2 = \frac{(2\ell+1)k'^2}{4\pi^3 q} \int dk\, k|\chi_{n\ell}(k)|^2\ , \tag{4.20}$$

where $\chi_{n\ell}$ is the radial part of the bound-state wave function and the integral spans the allowed values of k between $|k' \pm q|$, normalized to $\int k^2 dk|\chi_{nl}(k)|^2 = (2\pi)^3$. $\chi_{n\ell}$ can be evaluated analytically considering the so-called Roothaan-Hartree-Fock (RHF) method [171], which consists of expanding the radial atomic orbitals

R_{nl} as a superposition of Slater-type orbitals [2]:

$$R_{nl} = \sum_k C_{nlk} \frac{(2Z_{lk})^{n_{lk}+1/2}}{a_0^{3/2}\sqrt{2n_{lk}!}} \left(\frac{r}{a_0}\right)^{n_{lk}-1} \exp\left(-\frac{Z_{lk}r}{a_0}\right), \tag{4.21}$$

with n_{lk} the principal quantum number, Z_{lk} the orbital exponent for the kth Slater-type orbitals, and l the azimuthal quantum number. The orbital expansion coefficients C_{nlk} are given by the solution of Roothaan-Hartree-Fock equations in [172].

In the simple scenario, we consider that the outgoing electron with momentum p' to be correctly described by a plane wave function. However, the effect of nuclear attraction must also be taken into account. To do this, we use the assumption that the state of the electron is described by the continuous state solution of the Schrödinger equation for a hydrogen-like atom, with an effective charge Z_{eff}:

$$\begin{aligned}\tilde{R}_{p'l} =&(2\pi)^{3/2}(2p'r)^l \frac{\sqrt{\frac{2}{\pi}}\left|\Gamma(l+1-\frac{iZ_{eff}}{p'a_0})\right| \exp(\pi Z_{eff}/2p'a_0)}{(2l+1)!} \\ &\times e^{-ip'r}{}_1\mathrm{F}_1\left(l+1+\frac{iZ_{\text{eff}}}{p'a_0}; 2l+2; 2ip'r\right),\end{aligned} \tag{4.22}$$

where ${}_1\mathrm{F}_1$ is the confluent hypergeometric function. As a result,

$$\begin{aligned}\chi_{nl}(p) = &\sum_k C_{nlk} 2^{-l+n_{lk}} \left(\frac{2\pi a_0}{Z_{lk}}\right)^{3/2} \left(\frac{ipa_0}{Z_{lk}}\right)^l \frac{(1+n_{lk}+l)!}{\sqrt{2n_{lk}!}} \\ &\times {}_2\mathrm{F}_1\left[\frac{1}{2}(2+l+n_{lk}); \frac{1}{2}(3+l+n_{lk}); \frac{3}{2}+l; -\left(\frac{pa_0}{Z_{lk}}\right)^2\right],\end{aligned} \tag{4.23}$$

where ${}_2\mathrm{F}_1$ is the hypergeometric function.

Equation (4.19) is calculated for the simple case where the outgoing electron wave function could be described by the asymptotic behavior of Equation (4.22) for $r \to \infty$, i.e. a plane wave. In this case, it is possible to correct for ignorance of the nucleus effect by multiplying the rate with the Fermi-factor. This factor comes from the asymptotic ratio behavior of Equation (4.22) near the nucleus and its asymptotic behavior at infinity. The fermi factor obtained is:

$$F(p', Z_{\text{eff}}) = \left|\frac{\tilde{R}_{p'l}(r=0)}{\tilde{R}_{p'l}(r=\infty)}\right|^2 = \frac{2\pi Z_{\text{eff}}}{p'a_0} \frac{1}{1-\exp(-\frac{2\pi Z_{\text{eff}}}{p'a_0})} \tag{4.24}$$

[2]The hydrogen-like atomic orbitals are the solutions of the Schrödinger equation applied to a monoelectronic system. The study of a system comprising several electrons leads to the introduction of an electron-electron repulsive Coulomb potential in writing the complete Hamiltonian, which entails considerable complications for its resolution. In order to make this resolution easier, Slater's method consists in "transforming" a polyelectronic atom into a hydrogenic atom; this is done via the definition of new analytical forms for the radial parts, which depend only on n and thus become independent of the number quantum l: $R(r) = Nr^{n-1}e^{-\zeta r}$ where N is a normalization constant and the parameter ζ is a constant related to the nucleus effective charge (Z_{eff}), often taken as being equal to Z_{eff}/n.

That being said, studies like [173] points out that an approach based on approximating an outgoing electron as a plane wave is only valid for large momentum transfers. In such a case, Equation (4.22) will be closer to its asymptotic form. However, for small q, the correction provided by Equation (4.24) is inadequate for large atoms like Xe because their outer atomic orbitals are far from the asymptotic limit $r \to 0$. Therefore, it is necessary to use the full hydrogen-like wave function of the continuous spectrum of Equation (4.22).

According to the method presented in [173], the bound state R_{nl} is treated as if it came from a Coulomb potential $V_{\text{eff}} = Z^{nl}_{\text{eff}}/r$, with effective charges Z^{nl}_{eff}. Z^{nl}_{eff} is then obtained by matching this hydrogen-like energy spectrum with the bound state Roothaan-Hartree-Fock spectrum of [172], thus:

$$-(13.6\ \text{eV}) \times \frac{(Z^{nl}_{\text{eff}})^2}{n^2} = E_{\text{RHF}}, \tag{4.25}$$

Finally, this Z^{nl}_{eff} can be used in Equation (4.22) to evaluate a more accurate form factor. In order to perform this, it would be more sensible to start by expanding the factor $e^{i\mathbf{qr}}$ in Equation (4.20) in a linear combination of spherical harmonics, using the expansion of plane wave, then evaluate Equation (4.20) as a function of the unbound state $\tilde{R}_{p'l'}(r)$ by summing over l':

$$\begin{aligned} |f^{nl}_{ion}(p',q)|^2 =& \frac{4p'^3}{(2\pi)^3} \sum_{l'} \sum_{L=|l'-l|}^{l'+l} (2l+1)(2l'+1)(2L+1) \begin{pmatrix} l & l' & L \\ 0 & 0 & 0 \end{pmatrix}^2 \\ & \times \left| \int dr r^2 \tilde{R}_{p'l'}(r) R_{nl}(r) j_L(qr) \right|^2, \end{aligned} \tag{4.26}$$

where the integral over the spherical harmonics is rewritten in terms of the Wigner 3j-symbols.

Ultimately, the ionization form factor used here was given to our Collaboration by Rouven Essig, the auteur of the main articles discussing the detection of sub-GeV dark matter. This ionization form factor is calculated by the Hartree-Fock method in which the potential $V_{eff} = Z^{nl}_{eff}/r$ is determined, as explained above.

Figure 4.4 gives the plots of $|f^{nl}_{ion}(p',q)|^2$ as a function of recoil energy and q, for the atomic orbitals (4s, 4p, 4d, 5s, 5p) of the Xe atom.

From Figure 4.4, it should be noted that the form factors provided do not cover the entire allowed region for higher masses. However, much of the uncovered region should be massively removed (because it is far from the white line). For $E_R \gtrapprox 200$ eV however, some relevant data, especially for internal shells, is missing. It will be, therefore, assumed that the form factors are zero there, which should lead to conservative rates.

4.2.3 Events rate

Now that all the necessary factors are at our disposal, it is possible to proceed to the calculation of the expected event rates for the ionization of a Xe atom by

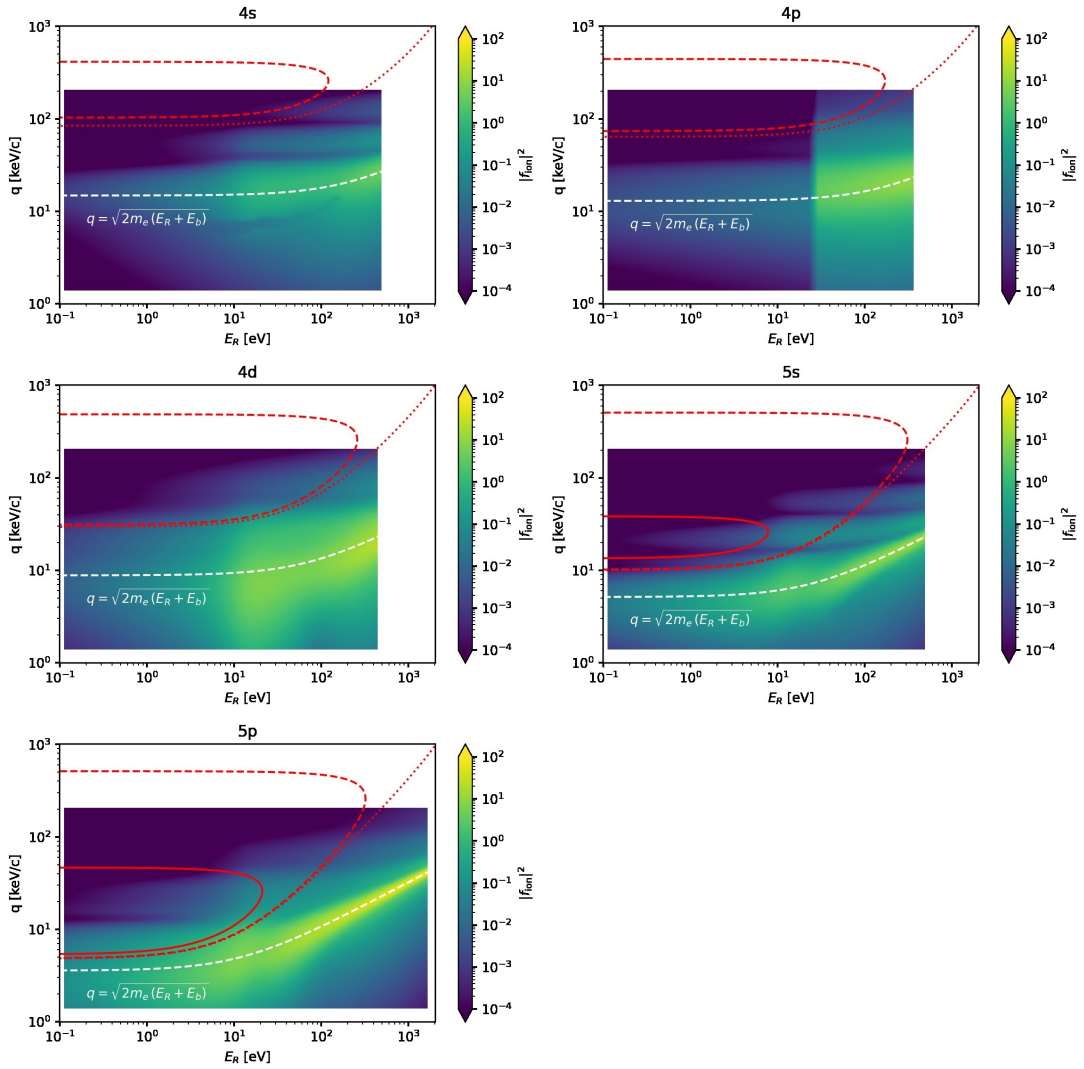

Figure 4.4: Distribution of the ionization form factor calculated from Equation (4.26), considering the Hartree-Fock calculation of the unbound states. The dashed white line shows $q = \sqrt{2m_e(E_b + E_R)}$, with E_b the binding energy and E_R the recoil energy. This region is approximately where the form factor is strongest. Red contours show the kinematically allowed region (that is, where the minimum required DM velocity is less than the maximum DM velocity under the standard halo model) for: $m_\chi = 10$ MeV$/c^2$ (solid), $m_\chi = 100$ MeV$/c^2$ (dashed) and $m_\chi = 1000$ MeV$/c^2$ (dotted).

collision with a dark matter particle in lepton interaction. The differential event rate is proportional to the thermally averaged differential cross section for each atomic orbital:

$$\frac{dR}{d\ln E_R} = N_T \frac{\rho_\chi}{m_\chi} \sum_{n,l} \frac{d\langle \sigma_{ion}^{nl} u\rangle}{d\ln E_R}, \tag{4.27}$$

where N_T is the number of target nuclei per unit mass and ρ_χ is the local density of χ. p Considering only the shells $n = 5$ and $n = 4$. The relation (4.26) can be made more explicit concerning the order of magnitude of the rate, assuming à

cross-section of 10^{-40} cm^2 the reference rate obtained is:

$$\frac{6.2}{A}\frac{\text{events}}{\text{kg-day}}\left(\frac{\rho_\chi}{0.4\frac{\text{GeV}}{\text{cm}^3}}\right)\left(\frac{\overline{\sigma}_e}{10^{-40}\text{cm}^2}\right)\left(\frac{10\text{MeV}}{m_\chi}\right)\frac{d\langle\sigma_{ion}v\rangle/d\ln E_R}{10^{-3}\overline{\sigma}_e}, \tag{4.28}$$

where A is the mass number of the target material.

Figure 4.5 presents the event rates as a function of the recoil energy for a particle of dark matter with a mass of 1 GeV and a cross-section of $\overline{\sigma}_e = 4.10^{-44}$ cm^2. The $F_{DM} = 1$ was used, corresponding to interaction via an exchange of heavy vector mediators. Figure 4.5 also shows the individual contributions to the rate of each of the atomic orbitals considered, where it is possible to see the validity of choice to consider only the higher nuclear orbitals.

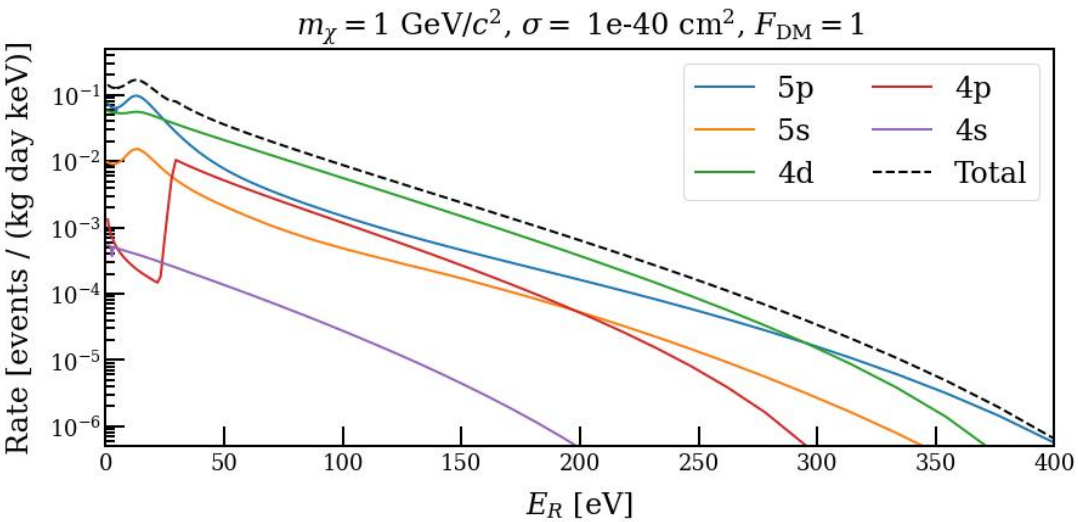

Figure 4.5: Event rate as a function of recoil energy, calculated from Equation (4.28). Also presented the individual contributions to the total rate of each atomic orbital of the outer and adjacent shells.

In Figure 4.6 are plotted the same values represented by Figure 4.5 but for an ultra-light mediator of the interaction (with $F_{DM} = 1/q^2$). In Figure 4.6, we observe a minor contribution from the lower orbitals due to the suppression of momentum transfer from the dark matter form factor.

4.3 Detector response

This section describes the detector's response for the SE-level (S2-only analysis) regarding the conversion of deposited energy into an observable signal. As the signals of interest consist of up to 5 extracted electrons, it is evident that this is below the lowest energy for which the ER charge yield for LXe has been measured, i.e., 186 eV [174]. However, concerning LXe, relevant results have been published using an extrapolation of the LXe response to ER following only the theoretical understanding of the ionization process [175, 97].

As for the physics models, initial assumptions indicate that the primary interaction will generate at least one or more recoiling electrons. The response

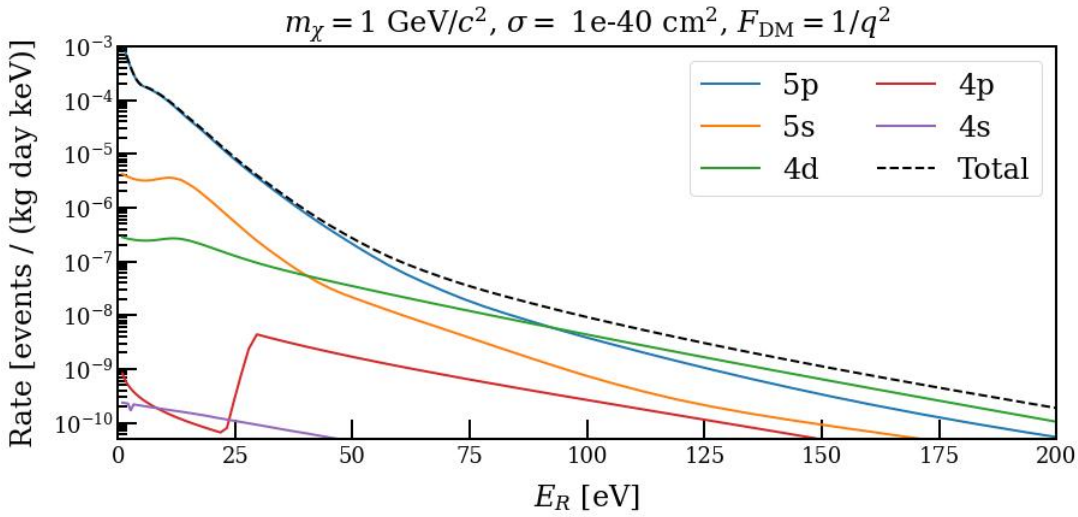

Figure 4.6: Event rates for $F_{DM} = 1/q^2$. Also presented the individual contributions to the total rate of each atomic orbital of the outer and adjacent shells.

of LXe to the recoiling electrons is based on the extrapolation of the Q_y (LXe charge yield) for ERs; this is then convoluted to the signal in order to have an estimation of the number of electrons observed and finally put it as an expected signal in the statistical framework.

4.3.1 Ionization electrons

The differential events rates dR/dE resulting from ab initio calculations for the various physical models predict a certain number of initial electrons generated from each interaction. If they survived the drift and extracted to the GXe, these ionization electrons themselves could produce a signal in the S2 region of SE or of their pileups. However, if their energy E_R is larger than $W = 11.5$ eV, then in principle, following the theoretical understanding of the ionization process of an electron recoiling in the LXe, this should create a certain number of secondary electrons. It is possible to assume that this model could describe the charge yield mechanism based on the plateau of the ER charge yield, namely in the constant value of $1/W \sim 75$ quanta/keV produced (see Figure 2.28).

Following the BBF model and the calculation presented in Section 2.1.3, it is possible to write the charge yield in the given form:

$$Q_y = \frac{1}{W}\frac{1-\langle r\rangle}{1+\langle N_{ex}/N_i\rangle}, \tag{4.29}$$

as usual, $\langle N_{ex}/N_i\rangle$ is the exciton-to-ion ratio related to the excitation and ionization cross-section of the electrons on Xe atoms, assumed to be constant. Here it is given the value of the BBF posterior: 0.15. Based on Equation (4.29), the probability of a quanta to become an electron can be given from the expression $p_{qe} = \frac{1-\langle r\rangle}{1+\langle N_{ex}/N_i\rangle}$. For example, for $\langle N_{ex}/N_i\rangle = 0.15$, this probability amounts to $p = 0.77$, for an ER of 11.5 eV.

A deposit of energy E by a specific physical interaction, described by the differential rate dR/dE, will produce a quanta floor(EQ_y). A binomial process, therefore, describes the number of ionization electrons produced with a success probability (probability of having an electron) p_{qe}. Thus, the rate of production of k electrons will be:

$$R_k = \int dE \frac{dR}{dE} \text{Binom}\Big(k|N = \text{floor}(EQ_y), p_{qe} = \frac{1 - \langle r \rangle}{1 + \langle N_{ex}/N_i \rangle}\Big). \tag{4.30}$$

4.3.2 Detected electrons

The observed electrons counts cannot be compared to the rate (4.30) because the drift effects of these electrons are not taken into account, i.e., the probability that electronegative impurities absorb them along their way (*electron lifetime*). Also, the *extraction efficiency* is not yet included.

In order to account for the various inefficiencies, suppose that starting from N_e electrons generated at a depth of z, the number of electrons that survive drift and the extraction can be modeled by:

$$N_{ext} \sim \text{Binom}(N_e, \epsilon_{ext} \exp(-z/(\tau_e \cdot v_d))) \tag{4.31}$$

where ϵ_{ext} is the extraction efficiency, τ_e the electron lifetime and v_d the electron drift velocity.

In the following, a discussion will be presented on how the effects of these two inefficiencies have been taken into account.

Electron lifetime

First, it is known that the number of electrons observed depends on the depth at which the interaction took place; these phenomena result from a parameter named electrons lifetime, which is a function of time. Given that the supposed main contributor to the loss of electrons is the absorption by electronegative impurities, it is expected that over time and with the cleaning of Xenon, these impurities will decrease, and conjointly the electrons' lifetime increases.

A canonical approach used by XENON consists in using a conservative approach based on the assumption that, since these electrons can come from any depth, it would then be possible to use an average value for a uniform distribution of electrons in the range $0\ \mu\text{s} \leq t_{\text{drift}} \leq 2200\ \mu\text{s}$ and an average electron lifetime. However, suppose the time distribution of the electrons' lifetime is strongly non-uniform. In that case, another method is used (for example, recently by [149]) and consists of dividing the exposure period into ten-time slices. The final rate will be a weighted sum over these slices corrected for each lifetime. Figure 4.7 shows the histogram corresponding to the electron lifetimes of the datasets used.

From Figure 4.7, we see that the lifetime of the electrons is relatively uniform over the dataset used. Therefore it is the first method that will be used, corresponding to correcting the rate by a global electrons lifetime of 15000 μs.

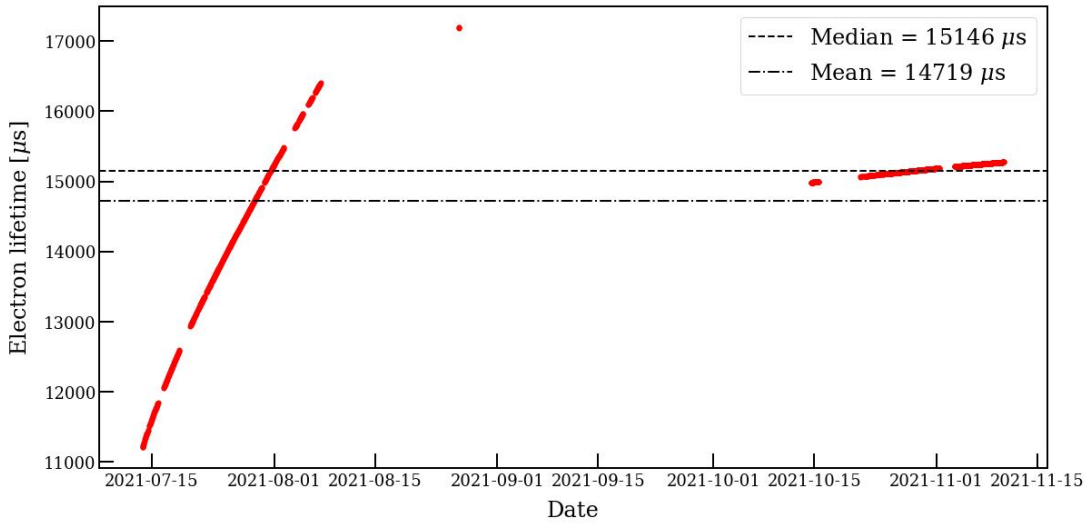

Figure 4.7: Electron lifetime evolution for the background datasets used in the analysis.

In Figure 4.8, the fact that the rate is higher for a lower lifetime electron at low energy can be explained by assuming that the Xenon is dirtier, then the signal which should have been $2e^-$ becomes $1e^-$ because of a higher probability of being caught up by the impurities, which results in a migration from the $2e^-$ peak to the $1e^-$ peak.

Extraction efficiency

Second, the extraction efficiency depends on the extraction electric field, which becomes a function of the position (x, y) due to the sagging of the anode. However, assuming this dependency is low (as in XENON1T), we consider taking only a single value for the extraction efficiency.
The extraction efficiency is defined as:

$$\epsilon_{ext} = \frac{g2}{g_{\mathrm{SE}}}, \tag{4.32}$$

where $g2$ is the ionization gain and g_{SE} is the single-electron gain.
The default extraction efficiency in SR0 is 16.45/32.36 = 50%.

We can now write the rate of n detected electrons R_n as

$$\begin{aligned} R_n = \tau_e \int dE \frac{dR}{dE} \mathrm{Binom}\Big(k|N = \mathrm{floor}(EQ_y), \\ p_{qe} = \frac{1 - \langle r \rangle}{1 + \langle N_{ex}/N_i \rangle}\Big) \mathrm{Binom}(n|k, \epsilon_{ext} \exp(-z/(\tau_{e,i} \cdot v_d))), \end{aligned} \tag{4.33}$$

where τ_e is the contribution of the electron lifetime.

From Figure 4.9 shows the number of electrons coming from each atomic orbital and contributing to the observed rates.

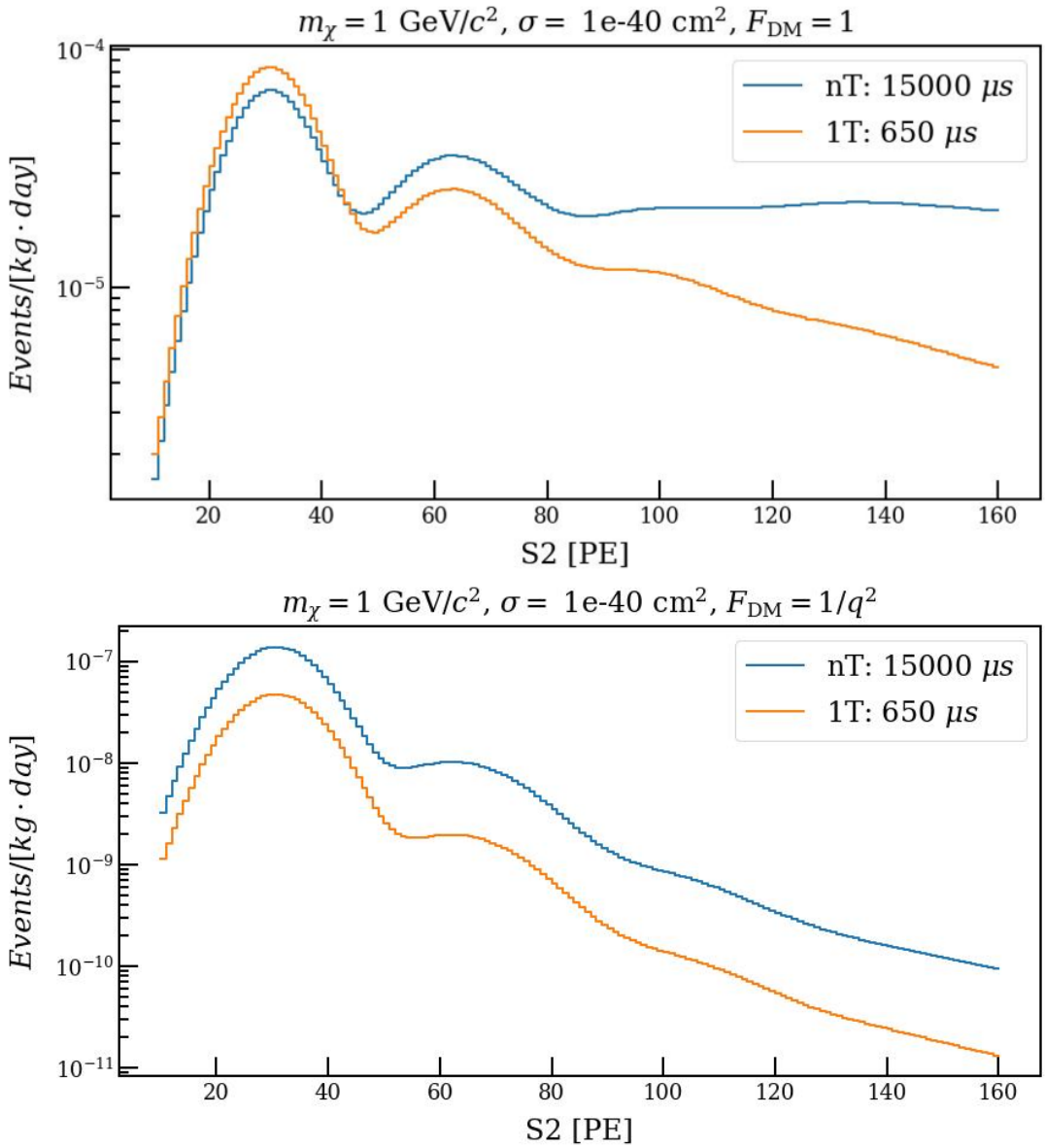

Figure 4.8: Comparison between the expected event rate as a function of electron lifetime. The values chosen correspond to the values of XENON1T and the value taken here for XENONnT. The rate was calculated for $F_{DM} = 1$ (top) and $F_{DM} = 1/q^2$ (bottom).

4.3.3 Generation of the S2 signal

Depending on the boundary setting approach, we could further bend the PMT part of the detector response into the equation rate (4.33) to report our knowledge of S2 signal generation based on secondary scintillation light produced by detected electrons, its amplification by PMTs, digitization and peak finding, and software classification. Each extracted electron will emit G photons, where G is the secondary scintillation gain, approximately 32 PE, during SR0. The spread of gas gain is $\Delta G \approx 7$ PE. Following the recent XENON analysis paper [117], the secondary scintillation light produced by the extracted N_{ext} electrons can be

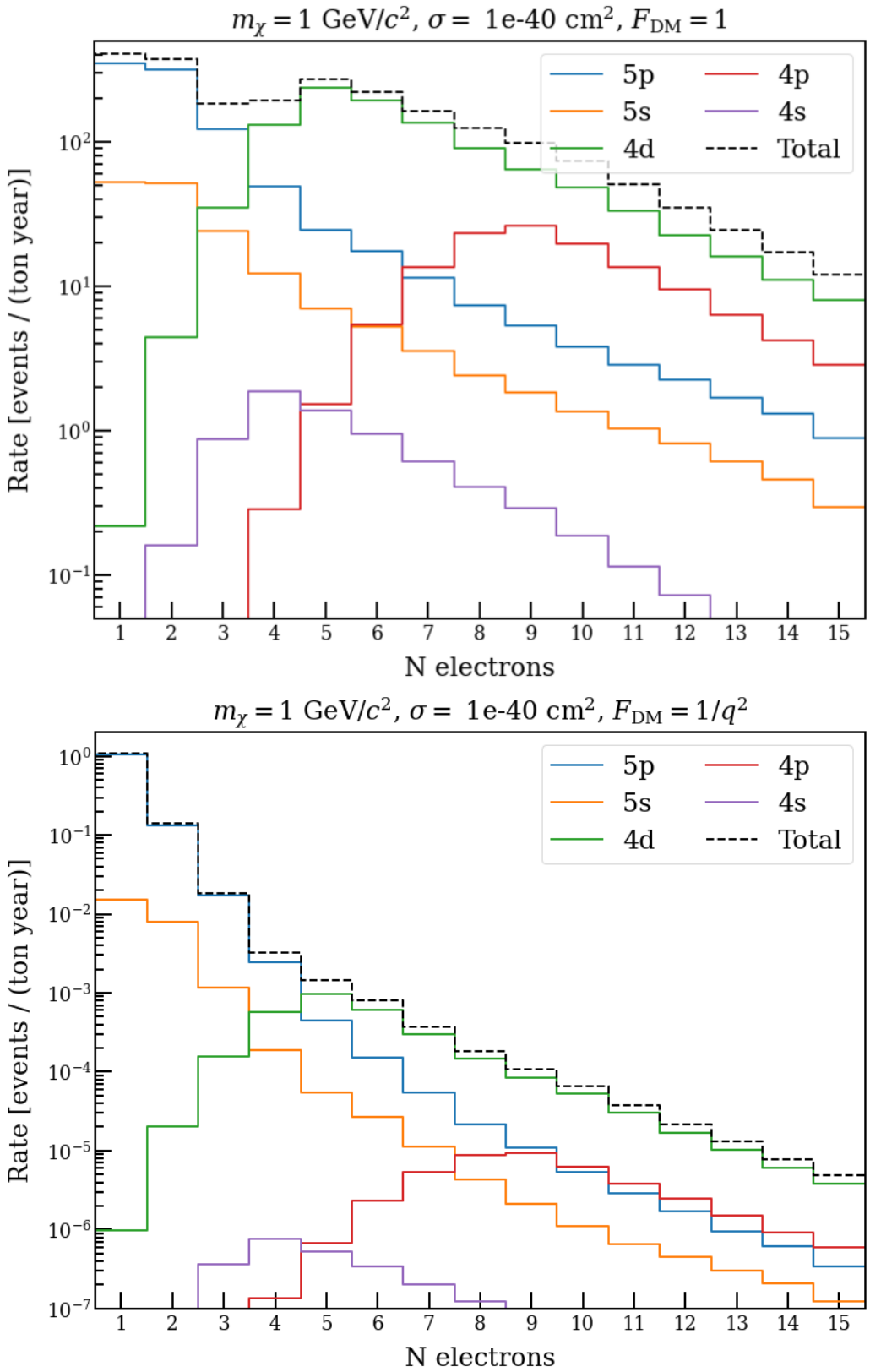

Figure 4.9: Rate of observed electrons coming from each atomic orbital. The rate was calculated for $F_{DM} = 1$ (top) and $F_{DM} = 1/q^2$ (bottom).

modeled by:

$$N_{prop} \sim \text{Normal}(N_{ext}G,\ \sqrt{N_{ext}}\Delta G). \tag{4.34}$$

Here, the so-called reconstruction bias and the propagation of this bias must also be taken into account. This is defined as the ratio $B = (A_{rec} - A_{true})/A_{true}$, where A_{rec} is the number of reconstructed PEs, and A_{true} is the number expected number of PEs detected for a given peak. Two major causes for this bias are gate photoionization and post-pulse signals in the PMTs, which can be merged by the peak detection algorithm with an S2 peak or cause it to split. This bias and its propagation can be estimated from simulations. However, this calculation is still in progress for XENONnT at the time of the present analysis; therefore, the estimated values for XENON1T will be used. Also, in the analysis paper, the relationship between S2 and N_{prop} is modeled as:

$$S2/N_{prop} - 1 \sim \text{Normal}(\delta_{S2}, \Delta\delta_{S2}), \tag{4.35}$$

where δ_{S2} is the bias and $\Delta\delta_{S2}$ its spread.

As a result, the S2 reconstruction will be included in Equation (4.33) via a Gaussian Normal$(S2|\mu,\sigma)$ with mean $\mu = nG(1+\delta_{S2})$ and $\sigma = \sqrt{n\Delta G^2 + (\mu\Delta\delta_{S2})^2}$:

$$R(S2, z) = \sum_n R_n \text{Normal}(S2|\mu,\sigma) \tag{4.36}$$

Finally, its projections on S2 and z give:

$$\begin{aligned} R(S2) &= \int dz \sum_n R_n \text{Normal}(S2|\mu,\sigma), \\ R(z) &= \int dS2 \sum_n R_n \text{Normal}(S2|\mu,\sigma). \end{aligned} \tag{4.37}$$

4.3.4 Systematic uncertainties

All parameters encountered while investigating the detector response will be sources of systematic errors and therefore should be taken into account in the limit setting. The following table 4.1 presents the list of these parameters and how the respective systematic uncertainty is considered.

4.4 Backgrounds for sub-GeV DM search in XENONnT

In an S2 analysis only, in the region of interest of a few detected electrons $(1, 2 \ldots, 5)$, the prominent background noise is dominated by SE trains. These could be produced by a variety of mechanisms that have been proposed. Among them are effects such as delayed emission of electrons initially captured by impurities, electrons trapped in the liquid-gas interface, and their subsequent delayed extraction, etc. Since it does not exist a background model for these emissions

Table 4.1: Systematic uncertainties related to the detector response

Parameter	Median value	Uncertainty considered
W-value	11.5 eV	[-0.3, 0.2] eV
$\langle N_{ex}/N_i \rangle$	0.15	[-0.06, 0.04]
q_0	1.13 keV	[-0.32, 0.24] keV
q_1	0.47 keV	[-0.15, 0.18] keV
γ_{er}	0.124	0.003
ω_{er}	31 keV	4 keV
δ_{er}	0.24	0.06
Electron lifetime τ_e	15000 μs	1σ
Extraction efficiency	0.5	1σ
Single electrons gain g_{SE}	32.36 PE/e^{-1}	0.077 PE/e^{-1}
Δg_{SE} (spread of g_{SE})	7.35	0.0034
Reconstruction bias δ_{S2}	f(S2), from X1T sim	1σ variation
$\Delta\delta_{S2}$ (spread of δ_{S2})	f(S2), from X1T sim	1σ variation

to date, there is no possibility of background subtraction. It then becomes impossible to claim an excess of events on the merits. However, the background noise in the studied energy range has smaller components like CEνNS and the standard background of ERs, which can extend to the domain of SEs, mainly due to ^{214}Pb and ^{85}Kr and materials.

4.4.1 Coherent neutrino-nucleus scattering

The minimum energy of a neutrino to cause an energy recoil E_R of a particle of mass m is

$$E_\nu^{min} = \frac{1}{2}(E_R + \sqrt{E_R^2 + 2E_R m}), \tag{4.38}$$

with a differential events rate given by

$$\frac{dR}{dE_R} = \int_{E_\nu^{min}}^{\infty} dE_\nu \frac{d\Phi_\nu}{dE_\nu}\frac{d\sigma}{dE_R}, \tag{4.39}$$

where $d\Phi_\nu/dE_\nu$ is the neutrino flux and $d\sigma/dE_R$ is the differential scattering cross-section.

Regarding neutrino-electron interactions, if the rate is calculated considering free electrons, then the recoil energies are well above our region of interest, inside which the rate of this process is consequently sub-dominant [176]. Moreover, considering the electrons are bound in the Xe atom, this rate receives an even more significant suppression [177].

Now consider a neutrino flux that could be the source of interactions with the nucleus; these can be produced by this specific spectral region of neutrino fluxes on Earth where the ^{8}B contribution dominates, from the following beta decay process:

$$^8\mathrm{B} \rightarrow ^8\mathrm{Be} + \mathrm{e}^- + \nu_e, \tag{4.40}$$

with a flux of 5.69×10^6 cm^{-2}s^{-1} according to the solar model BS05(OP) [178]. The differential cross section for nuclear recoil with energy E_R, is given from [160] by:

$$\frac{d\sigma}{dE_R} = \frac{G_F^2}{4\pi} Q_W^2 m_N (1 - \frac{m_N E_R}{2E_\nu^2}) \cdot F^2(E_R), \tag{4.41}$$

with G_F the Fermi constant, $F(E_R)$ the Helm form factor and Q_w the weak nuclear hypercharge. for N neutrons, Z protons, and a weak mixing angle θ_w, the weak nuclear hypercharge is given by:

$$Q_w = N - Z(1 - 4\sin^2\theta_w). \tag{4.42}$$

4.4.2 Residual ER background

The residual ER background in the single electron region is mainly due to the low energy tail of the decay ^{214}Pb $\xrightarrow{\beta}$ ^{214}Bi but also ^{85}Kr and materials. The background rate of ^{214}Pb is a constant background in energy and time consisting of several contributions/sources. Main contribution is the direct beta-decay of ^{214}Pb to the ^{214}Bi groundstate with a branching ratio of 12.7(9)% [179]. An approximate activity concentration of ^{214}Pb can be inferred from the detector's alpha-decay rates of radon daughters from the ^{222}Rn chain. ^{222}Rn is created within the detector materials and continuously emanates into the LXe volume, where it is homogeneously distributed. The decay of ^{222}Rn, ^{218}Po and ^{214}BiPo[3] can give lower and upper bounds for the ^{214}Pb decay rate.

The background due to Kr-85 was regularly monitored, during SR0, by measurements of the concentration of ^{nat}Kr/Xe with a rare gas mass spectrometry. The material background is flat below 200 keV and is generated by Compton scattering gamma rays, reaching the internal volume [133]. The highest contribution comes from the ^{60}Co contamination of the SS cryostat. However, in the fiduciary volume, this background should be subdominant.

Considering the values of XENON1T for all the ER backgrounds [99], we obtain a total rate of 1.42×10^{-4} events/(kg · day · keV).

4.4.3 Comparison between background sources

Figure 4.10 shows a comparison between the CEνNS event rate and the low ER background, with the signal expected from a matter particle of mass m_χ = 100 MeV, diffusing with a bound electron of the Xe atom, with a cross-section $\sigma_e = 10^{-36}$ cm^2. The dark matter rate obtained here corresponds to the order of magnitude of the signals excluded, considering the limits achieved at low energy [149].

As shown in Figure 4.10, the background event rate is six orders of magnitude lower in the SE region. Therefore, it does not seem necessary to do a background subtraction for this study (background unrelated to SE).

[3] β-α coincidences of ^{214}Bi β decay and subsequent ^{214}Po α decay.

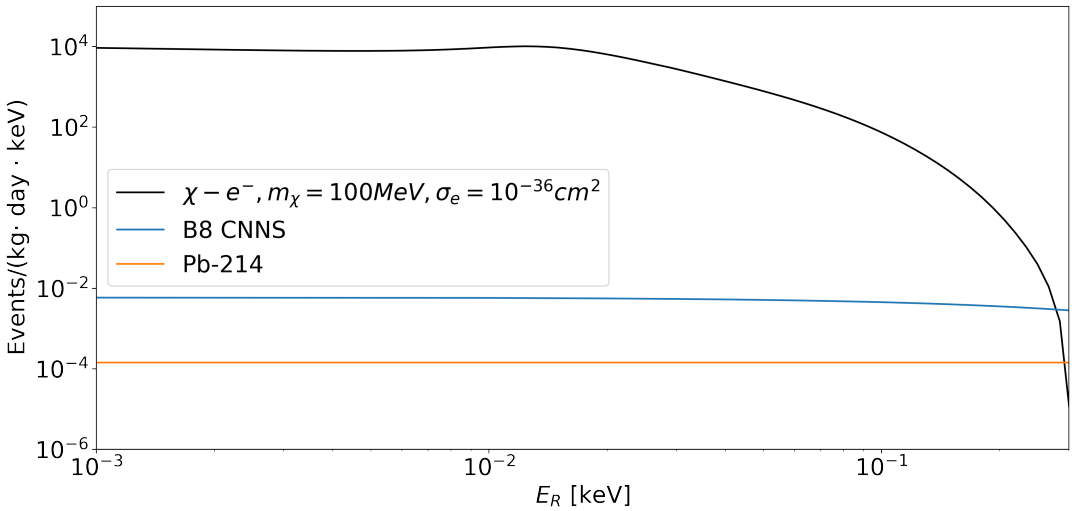

Figure 4.10: Electron-DM interaction event rates compared to CEνNS and flat ER background in the SE region.

4.5 Search for bosonic dark matter

In addition to fermionic dark matter candidates, low-energy research also allows limits to be placed on bosonic dark matter. Candidates for light dark matter arise from the same theoretical model of the hidden sector, where the dark photon appears as a mediator of the dark sector's interaction with SM. However, nothing prevents dark matter from being partly or entirely made up of pseudo-scalar or vector bosons, such as ALPs or dark photons. In this case, dark matter could be directly detected since it could be absorbed by the atoms of the detector target, depositing their rest mass energy and producing ionization signals.

By following the same procedure for the DM-e interaction, it is possible to derive the detector's response at the expected rate and compare it to the events counted in our SE to extract an interaction limit.

4.5.1 Dark photon

The dark photon A' is a vector boson resulting from the hidden sector's broken gauge group $U(1)_D$. This is an essential property because the mediator particles of electromagnetism and dark electromagnetism can mix. However, electromagnetism is perfectly known, and the data agree with the theoretical predictions. Therefore, the mixing of usual and dark photons is very weak. In this context, dark photons could constitute all the dark matter for sufficiently small kinetic mixing and $m_{A'}$ since the lifetime of the dark photon can be longer than the age of the Universe. However, even if this mixture is tiny, it is enough to allow the production of dark photons from (visible) particles of the Standard Model.
The relevant part of the Lagrangian is:

$$\mathcal{L} = -\frac{1}{4}F'^{\mu\nu}F'_{\mu\nu} - \frac{\kappa}{2}F^{\mu\nu}F'_{\mu\nu} + \frac{1}{2}m_{A'}A'^{\mu}A'_{\mu}. \tag{4.43}$$

Regarding its detection, the dark photon could be absorbed as a non-relativistic massive particle, with a coupling $e\epsilon$ to electrons. The expected signal is monoenergetic with $E = m_{A'}$ and is a function of the Xe atom's photoelectric absorption cross-section σ_{PE}. The absorption cross-section of A' is given by

$$\sigma_{A'}(E_{A'} = m_{A'}) \simeq \epsilon^2 \sigma_{PE}(E = m_{A'}), \tag{4.44}$$

with an absorption rate for a Xe target of:

$$\text{Rate} \simeq \frac{4.7 \times 10^{23}}{A} \epsilon^2 \left(\frac{keV}{m_{A'}}\right)\left(\frac{\sigma_{PE}(E = m_{A'})}{\text{barn}}\right) \quad \text{kg}^{-1}\text{d}^{-1}. \tag{4.45}$$

Figure 4.11 illustrates the expected event rate calculated with Equation (4.45).

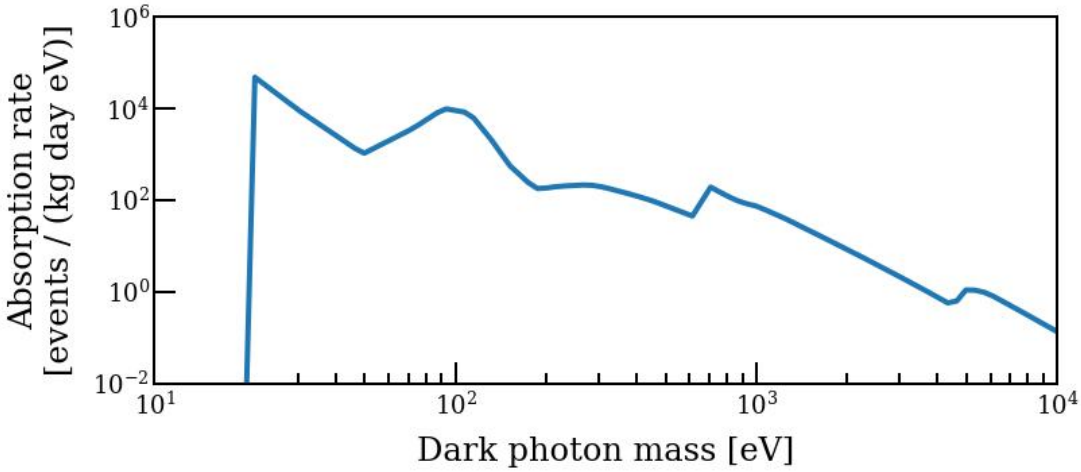

Figure 4.11: Dark photon differential events rate.

4.5.2 Axion-like particles

The axion was initially proposed as a solution to the strong CP problem and is a pseudo-scalar particle that can couple to the SM axial current $\partial^\mu a J^A_\mu / f_a$, with f_a a constant describing the scale at which the Peccei-Quinn symmetry is broken (see Section 1.5.3). In this model of the axion, the mass m_a and the constant f_a are linked through:

$$m_a = 5.7\,\mu\text{eV}\left(\frac{10^{12}\,GeV}{f_a}\right). \tag{4.46}$$

In addition to the original axion, other well-motivated models postulate axion-like particles. The ALPs are abundant in many BSM models, they can have couplings with gluons, photons, and fermions.
The minimal Lagrangian of these models can be written as follow:

$$\mathcal{L} = \frac{1}{2}\partial_\mu a \partial^\mu a - \frac{1}{2} m_a^2 a^2 + i g_{are} a \bar{e} \gamma_5 e, \tag{4.47}$$

where the dependence in g_{aee} can be absorbed in f_a as $g_{aee} = 2m_e/f_a$.

ALPs could achieve the correct relic density in a wide mass range via the misalignment mechanism (Peccei–Quinn theory) or by thermal or non-thermal production.

In direct detection, ALPs are constrained regardless of the production mechanism. The interaction of ALP with electrons is responsible for the "axioelectric" effect, in which the axion is absorbed by a bound Xe atom electron resulting in a monoenergetic energy signal $E = m_a$.

For a Xe target, the absorption rate is given by [180]:

$$\text{Rate}_{\text{ALPs}} = \frac{1.9 \times 10^{19}}{A} g_{ae}^2 \left(\frac{m_a}{keV}\right)\left(\frac{\sigma_{PE}(E = m_a)}{b}\right) \quad \text{kg}^{-1}\text{d}^{-1} \tag{4.48}$$

for a local DM energy density of $\rho_{DM} = 0.4\text{GeV/cm}^3$.

4.5.3 In-medium correction

The non-relativistic dark photon carries a negligible momentum which is only a fraction $O(10^{-3})$ of its rest energy ω because $|\mathbf{q}| = m_V u_{DM}$ and $u_{DM} \approx 10^{-3}c$. This property is in contradiction with the SM photon for which $|\mathbf{q}| = \omega$. Nevertheless, the absorption of a dark photon by an atom is similar to that of an ordinary photon since their wavelengths are longer than the typical dimension of the atom. Thus the wave function or the dark photon, which is $exp(-i\mathbf{qr})$, can be taken equal to one [85]. The interaction between a dark photon and an electron, in the non-relativistic approximation of the Hamiltonian, can be written as $\mathbf{p}\epsilon$ where ϵ is the dark photon polarization vector. That is, the dipole term is dominant over the higher multipole terms, and thus the dark photon and SM absorption processes are characterized by similar transition matrix elements.

The absorption rate given above for both cases can be translated to the formula:

$$\text{Rate per atom} = \frac{\rho_{DM}}{m_V c^2}\kappa^2 \sigma_\gamma(\omega = m_V)c. \tag{4.49}$$

This formula is only accurate if the so-called in-medium effects can be ignored. However, for energies close to the threshold energy of the first ionization of the Xe atom (12.1 eV), it is necessary to consider the modification of the kinetic mixture $V - \gamma$ due to the effects of dispersion in the dielectric medium of LXe. In this case, the correct matrix element for the absorption process is given by

$$M = -\frac{e\kappa m_V^2}{m_V^2 - \Pi_{T,L}(q)}\langle p_f|J_{em}^\mu(0)|P_i\rangle \epsilon_\mu^{T,L}(q), \tag{4.50}$$

where p_f and p_i are the final and initial momentum of the electron, $\epsilon_\mu^{T,L}$ is the polarization vector of the dark photon for the two polarization modes, and $\Pi_{T,L}$ are the polarization functions related to the optical properties of the material. For example, for isotropic and non-magnetic material, we have:

$$\Pi_L = (\omega^2 - \mathbf{q}^2)(1 - n_{ref}^2), \quad \Pi_T = \omega^2(1 - n_{ref}^2), \tag{4.51}$$

with n_{ref}, the complex refractive index of the medium. When $|\mathbf{q}| \ll \omega$ as is the case here, assuming that the dark photon and the ALPs play the role of

cold dark matter, then the polarization functions of the two modes are equal $Pi_L = \Pi_T \approx \Pi$.

Ultimately, the absorption rate per dark matter particle for a detector is given by [181]:

$$\Gamma_{T,L} = -\kappa^2 \times \frac{m_V^4}{|m_V^2 - \Pi_{T,L}|^2} \mathrm{Im}(\Pi_{T,L}). \tag{4.52}$$

This is finally added to Equation (4.49) for $m_V^2 \gg \Pi$, to then deduce the absorption rate per dark matter particle [182]:

$$\Gamma \approx \kappa^2 \omega \mathrm{Im}(n_{ref}^2) = \kappa^2 \sigma_\gamma \frac{N_{at}}{V}, \tag{4.53}$$

where $\frac{N_{at}}{V}$ is the number density of atoms in the detector's target.

To calculate the rate from Equation (4.52) one should use the refractive index of the Xe for different photon energies can be found in [183].
There then remains the problem resulting from the difficulty of experimentally determining the real part of the refractive index related to the refraction of photons of energies close to the threshold. As a result, the latter is not available for energies below 30 eV. In this case, the only solution is to use the Kramers-Kroning relations between the real and imaginary parts of the refractive index to calculate $\mathrm{Re}(n_{refr})$ from $\mathrm{Im}(n_{ref})$.

The complex refractive index is defined as $n_{refr} = n(\omega) + i\kappa(\omega) = (1-\delta) - i\beta$ with $n(\omega)$ the real refractive index and $\kappa(\omega)$ the attenuation coefficient. The parameters β and δ are tabulated for a Xenon density of $0.5887 \times 10^{-2} gr/cm^3$. Thus, for energies close to the threshold of 12.1 eV where the $n(\omega)$ is not available, the Kramers-Kroning relation is then used [184], it gives:

$$n(\epsilon) = 1 + \frac{2}{\pi} \mathcal{P} \int_0^\infty \frac{\epsilon' \kappa(\epsilon')}{\epsilon'^2 - \epsilon^2} d\epsilon', \tag{4.54}$$

where $\mathcal{P}$ represents the Cauchy principal value of the integral.

Figure 4.12 shows the real and imaginary parts of the refractive index of Xenon corresponding to the analysis made for XENON10. Also, Figure 4.13 is compared the rate of absorption calculated from Equation (4.52) to the rate calculated from Equation (4.45), where it can be seen that the two are approximately equal for energies far from the energy threshold of the first ionization of the Xenon atom.

4.6 Limits setting on the neutrino magnetic moment

Obtaining an extremely low background noise in underground detectors in search of dark matter allows an extension of research topics towards neutrino physics. Moreover, in [185], it was predicted that the parallel trajectories of the underground detectors in search of dark matter and those studying solar neutrinos would inevitably cross when the dark matter detectors reached the size of a ton.

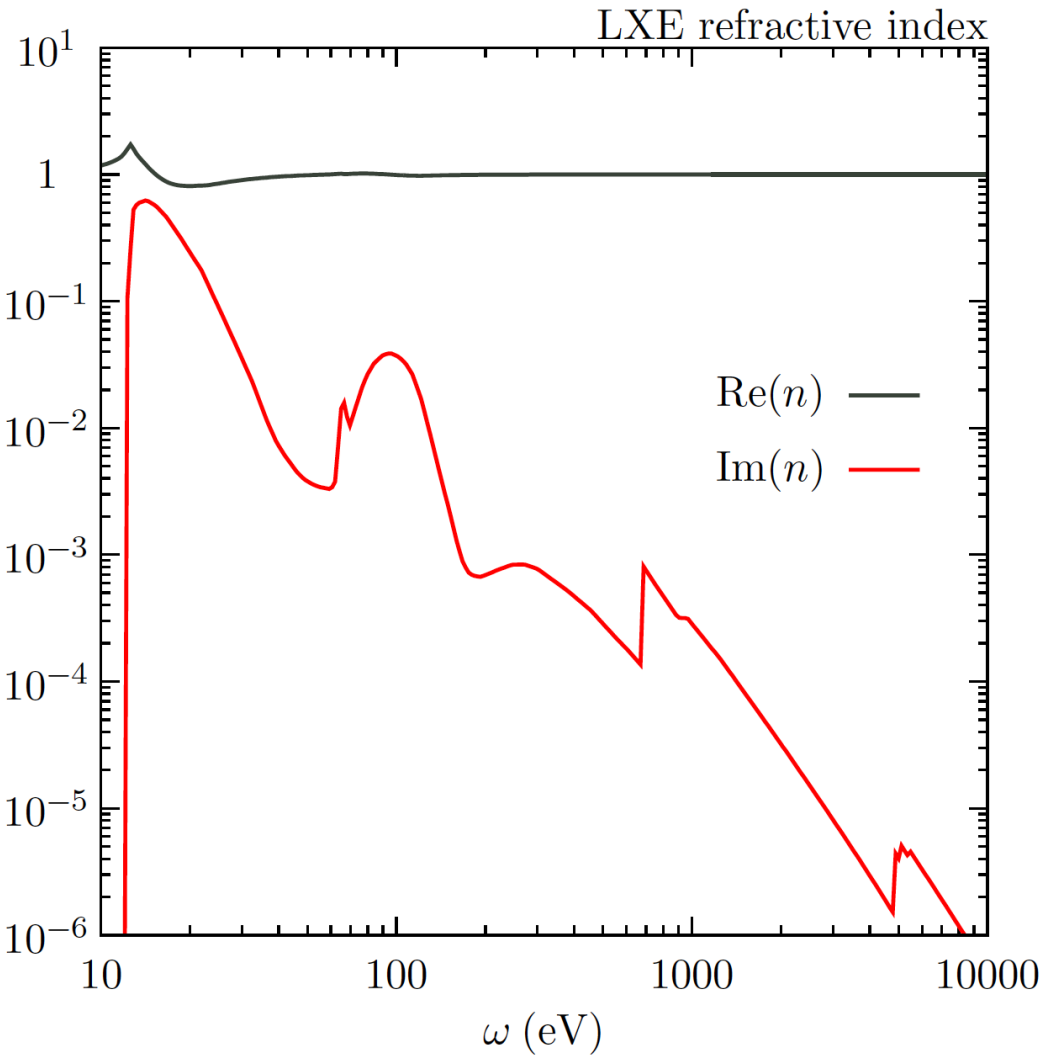

Figure 4.12: Refraction index plot of the XENON10 analysis. (Figure from [100]).

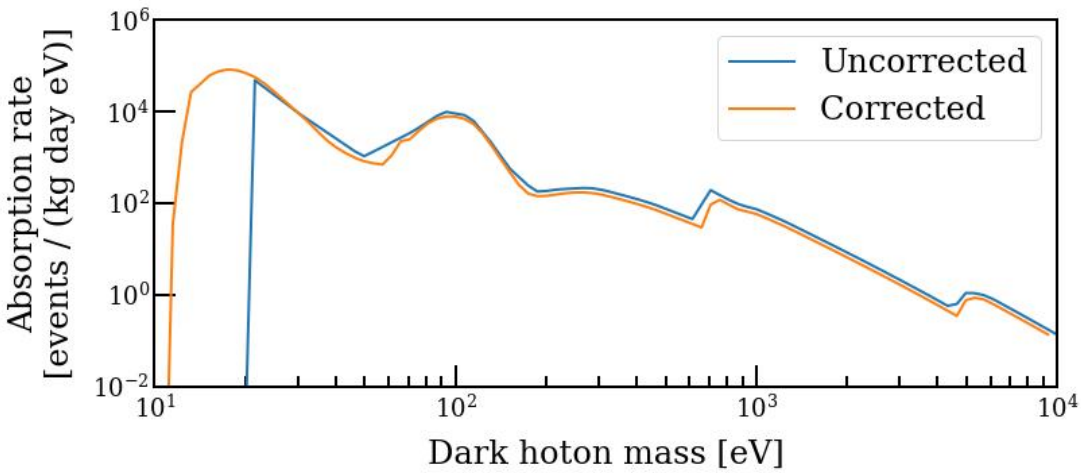

Figure 4.13: In-medium correction effect on the dark photons absorption rate.

Furthermore, it is well known that the irreducible background of neutrinos is a limit for direct detection detectors, which can only be overcome with the study of the annual modulation of the background or a possible recourse to directional detection techniques.
That said, thanks to the extremely low ER background of XENONnT, it is possible to study the potential electromagnetic properties of neutrinos. For example, one interpretation that was emitted to explain the excess of events over the expected XENON1T background is increased solar neutrino-electron scattering due to magnetic moment interaction. Since this interaction has a predicted cross-section that falls proportionally to E_r^{-1} [160], finding a magnetic moment constraint at the lowest possible energy is preferable. There, of course, still prevails the problem of the resulting unmodeled backgrounds, namely single electrons. However, this does not preclude examining what limit can be set for μ_ν in this lowest possible energy range for which the detector is sensitive.

4.6.1 Solar neutrinos ν-e scattering

As XENON detectors increase in sensitivity, solar neutrinos start to contribute as a non-negligible ER background, even though they are subdominant. This fact reflects the exceptional sensitivity achieved since the rate of such interactions is predicted to be very low in the standard model. The differential SM cross-section for $\nu - e^-$ scattering, via the exchange of weak W and Z vector bosons, is given by:

$$\frac{d\sigma(E_\nu, E_r)}{dE_r} = \frac{G_f^2 m_e}{2\pi}\left[(g_u + g_a)^2 + (g_u - g_a)^2\left(1 - \frac{E_r}{E_\nu}\right)^2 + (g_a^2 - g_u^2)\frac{m_e E_r}{E_\nu^2}\right], \quad (4.55)$$

where $g_u = 2\sin^2\theta_w - \frac{1}{2}$ and $g_a = 1/2$ with θ_w the weak mixing angle. E_r is the recoil energy and E_ν the neutrino energy. We must also consider the survival probability of μ_e due to the neutrinos oscillations from the solar core to the detector. For neutrino energies below 1 MeV, this probability is about 0.55 [186]. Then the events differential rate of $\nu - e^-$ scattering is given by:

$$\frac{dR}{dE_r} = \int_{E_\nu^{min}}^{\infty} dE_\nu \frac{d\Phi_\nu}{dE_\nu}\frac{d\sigma}{dE_r}, \quad (4.56)$$

where $d\Phi_\nu/dE_\nu$ is the neutrino flux (see Figure 4.14). Also E_ν^{min} is the minimum neutrino energy for the recoil with energy E_r of a particle with mass m and is given by the relation:

$$E_\nu^{min} = \frac{1}{2}(E_r + \sqrt{E_r^2 + 2E_r m}). \quad (4.57)$$

4.6.2 Neutrino magnetic moment

With regard to the possible electromagnetic properties of the neutrino, the possibility of the existence of its magnetic moment is most studied. The magnetic moment should be a measurable quantity representing the spin or angular

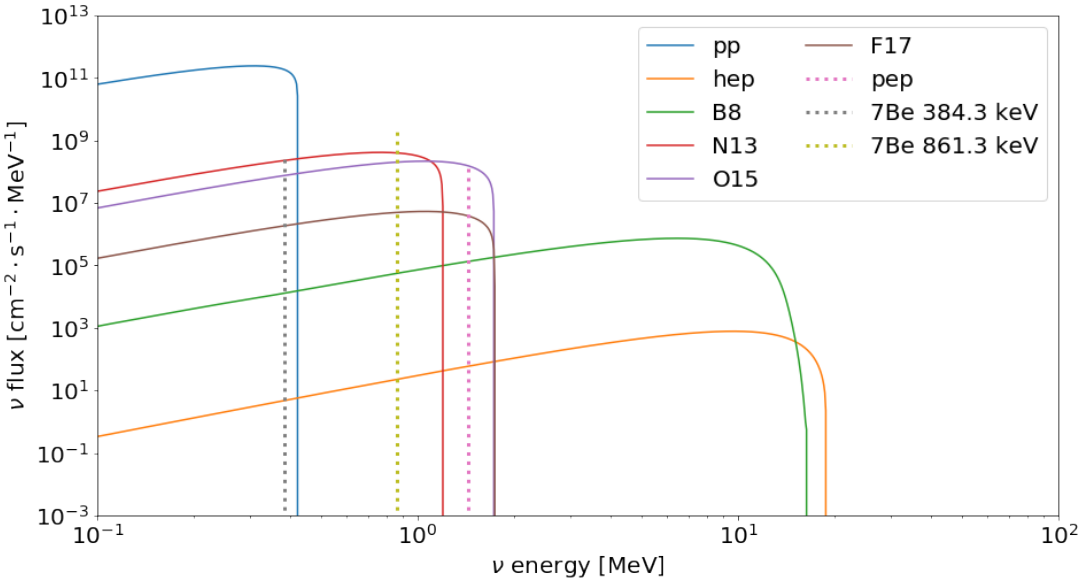

Figure 4.14: Solar neutrino spectrum

momentum of the particle. Another view of the matter presents the magnetic moment as a measurable quantity representing one of the electromagnetic components of the particle interaction. In the neutrino case, the magnetic moment would allow an electromagnetic interaction with the electrons.

In general, we can have two kinds of magnetic moment, the "Dirac" magnetic moment, which is responsible for the transition $\nu_L \to \nu_R$, and the transition magnetic moment $\nu_{eL} \to \nu^c_{\mu R}$. If we add a right neutrino to the standard model, then through a one-loop electroweak diagrams (Figure 4.15 left), a non-zero neutrino mass implies a non-zero Dirac magnetic moment, proportional to its mass and given by :

$$\mu_\nu = \frac{3eG_F m_\nu}{8\sqrt{2}\pi^2} = 3\times 10^{-19}\left(\frac{m_\nu}{1\text{ev}}\right)\nu_B, \tag{4.58}$$

with, $\nu_B = e/2m_e$ the Bohr magneton.

Following the electroweak symmetry breaking and assuming that the neutrino is a Dirac Fermion, the electromagnetic dipole moment can be described by the following effective Lagrangian [187]:

$$\mathcal{L} = \mu_\nu^{ij}(\bar{\nu}_i\sigma_{\mu\nu}\nu_j F^{\mu\nu}) + h.c, \tag{4.59}$$

with $F^{\mu\nu}$ the field strength for electromagnetism and μ_ν^{ij} a complex parameter describing the neutrino's electric and magnetic moments.

The value of the neutrino moment given by Equation (4.58) is extremely small and is beyond the reach of current detectors. Hence, observing a magnetic moment much larger than this value would imply the existence of physics beyond the SM. This is since there are extensions of the SM predicting a magnetic neutrino moment through other contributions in the vertex function of the neutrino in Figure 4.15 (right), with a value that could be orders of magnitude larger than

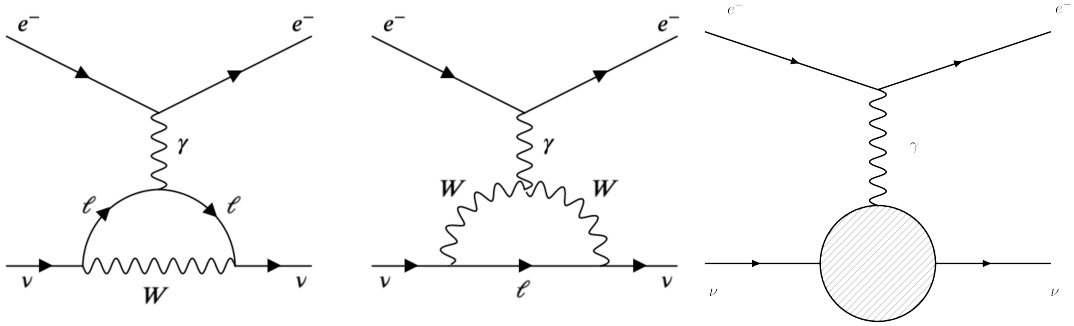

Figure 4.15: (Left) Electroweak one-loop contributions to the magnetic neutrino moment. (Right) General vertex function to the elastic neutrino scattering off an electron.

that of the SM and could be within range of the sensitivity of current detectors [188].
Thus, following this hypothesis, neutrino-electron scattering should be enhanced by the magnetic moment of the neutrino through a cross-section of the form [160]:

$$\frac{d\sigma(E_\nu, E_r)}{dE_r} = \mu_\nu^2 \frac{\pi\alpha^2}{m_e^2}\left(\frac{1}{E_r} - \frac{1}{E_\nu}\right), \tag{4.60}$$

with α the fine-structure constant.
Figure 4.16 illustrates the expected event rate calculated with Equation (4.60).

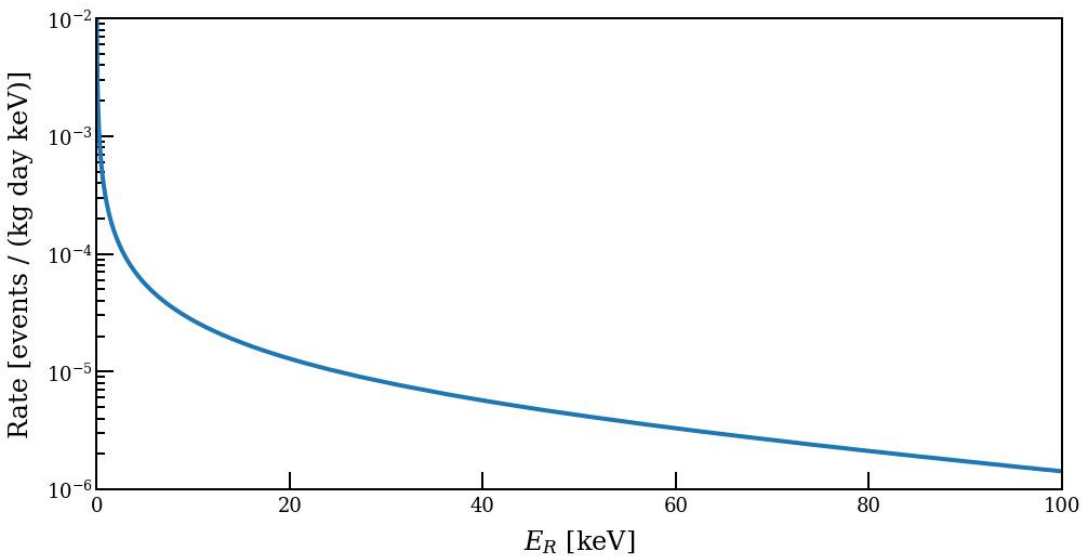

Figure 4.16: Differential events rate of the scattering through a magnetic neutrino moment.

4.6.3 Limit setting procedure

To set a conservative limit on μ_ν, we will take a limit based on the Poisson upper limit of the number of observed events. Thus, the probability of observ-

ing n events, given an unknown signal of mean s, is given from the Poisson distribution by:

$$P(n|s) = \frac{s^n}{n!}e^{-s}. \tag{4.61}$$

And the upper limit for the unknown signal, s_{up}, at a C.L. α, is given from:

$$s_{up} = \frac{1}{2}F^{-1}_{\chi^2}(1-\alpha, 2(n+1)). \tag{4.62}$$

The limit obtained for this value of μ_ν for which the number of expected events does not exceed the s_{up} of observed events at 90% C.L will be soon given by the collaboration in a dedicated paper.

4.7 Limits on dark photons from solar emission

This section aims to set limits to the coupling of dark photons coming from the sun. Although these limits are not intended to be as low as the limits derived from relic-density dark matter, they are more conservative because studies of relic-density dark photons are based on the assumption that all relic-density dark matter is composed of dark photons. This assumption is not used in the case of solar dark photons because the production rates from known processes in the sun can be directly calculated.

In this context, several studies have calculated the flux of hypothetical dark photons coming from stellar interiors; these calculations assume that these particles only interact with ordinary matter by kinetic mixing through the longitudinal and transverse modes of plasmon oscillations [189]. For the longitudinal oscillation of the plasmons, the dispersion relation is equal to the frequency of the plasma, ensuring the existence of a region inside the stars where the kinetic mixing between photons and dark photons reaches a maximum, leading to a resonance [190].

Here the final objective is to set limits to the coupling constant of the dark photon κ as a mass function by calculating the production rates from the resonant production mode. Thus, single-electron-only S2 analyzes are applied to define a 90% upper confidence limit on the Dark Photon coupling in the mass range corresponding to the SE signals.

4.7.1 Dark photons production in the Sun

Although many hypotheses exist about the production of dark photons in the sun, only the resonant mechanism is considered here. This choice comes from the fact that the resonance mechanism is the dominant production mechanism in the energy range corresponding to the frequency energy range of the sun's plasma; therefore, it is possible to neglect the contributions of the subdominant processes, such as Bremsstrahlung and Thomson diffusion [190].

In order to effectively model the resonant solar production, it is first necessary to find a reliable solar model which contains the parameters of interest, namely the temperature, the frequency of the plasma, and the rates of variation of the

frequency of the plasma according to the solar radius. Thus, the most robust solar model currently is the BS05(OP) (or Standard Solar Model) [178], and with this model, it is possible to derive the parameters mentioned above thanks to the solar electron densities.

Because of the refraction, the dispersive properties of photons change inside the media. If the medium is locally isotropic, the propagation of transversely polarized photons can be understood as carriers of an effective mass [190]. The latter depends on the plasma frequency, which in turn is mainly determined by the density of free electrons:

$$\omega_p^2 \approx 4\pi\alpha n_e/m_e, \tag{4.63}$$

with, ω_p the plasma frequency, α the fine-structure constant, n_e the free electron number density and m_e the electron mass.

By extracting the electron densities of the BS05(OP) model as a function of the solar radius, it becomes possible to estimate $d\omega_p^2/dr$ and ω_p using a linear interpolation of the data. This way, we can find the solar radius at which the resonant production will occur and get the other quantities at that radius.

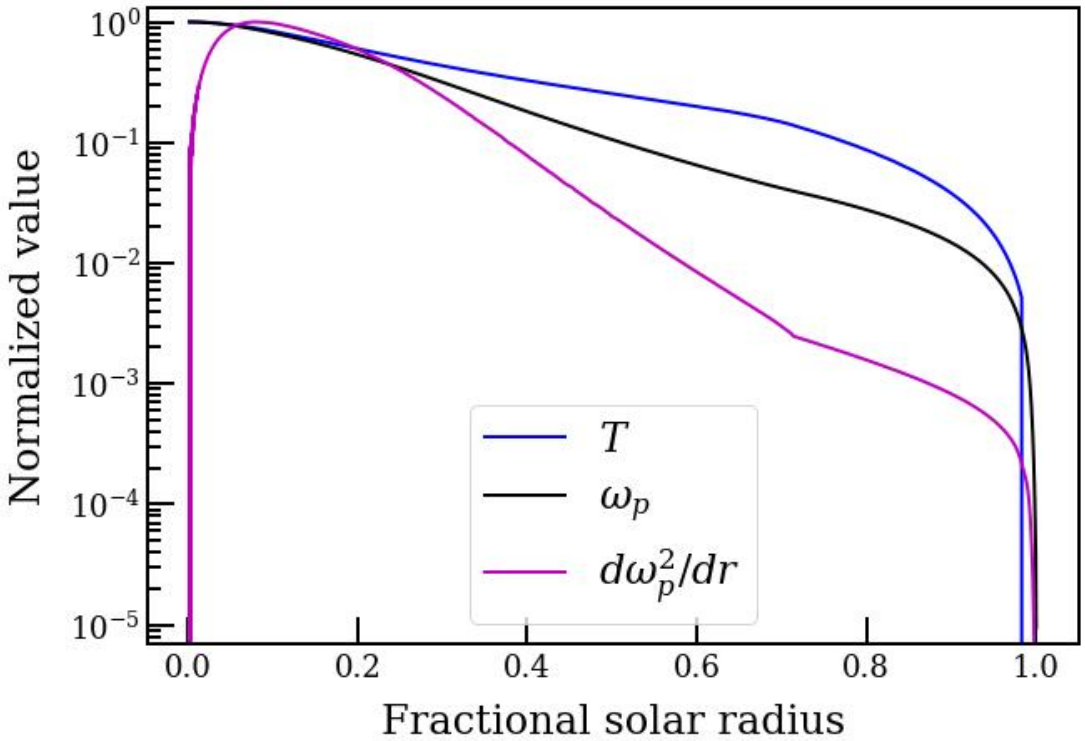

Figure 4.17: Derived parameters from the solar model.

Following the previous calculation, the goal is to find the luminosity and the flux on Earth of dark photons polarized longitudinally and transversely produced by the resonance of given energies and masses. To do this, the resonance conditions are used: $\omega_p = \omega$ for the longitudinal polarization, and $\omega_p = m_{DP}$ for the transverse polarization. Applying these resonance conditions allows finding

the radial shell of the sun, r_{res}, at which resonant production will occur. The production rate is given by [182]:

$$\frac{d\Phi_{T,L}}{d\omega} = \frac{1}{4\pi R_{\oplus}^2} \frac{2r_{res}^2}{e^{w/T|_{r_{res}}} - 1} \frac{\sqrt{w^2 - m_{DP}^2}}{\sqrt{\frac{d\omega_p^2}{dr}|_{r_{res}}}} \times \begin{cases} \kappa^2 m_V^2 \omega^2 & \text{longitudinal,} \\ \kappa^2 m_V^4 & \text{transverse,} \end{cases} \tag{4.64}$$

with $R_{\oplus}$ the Earth radius and κ the dark photon kinetic mixing parameter. FIGURE 4.18 gives the flux intercepted by the Earth from resonant solar production of dark photons, derived from Equation (4.64).

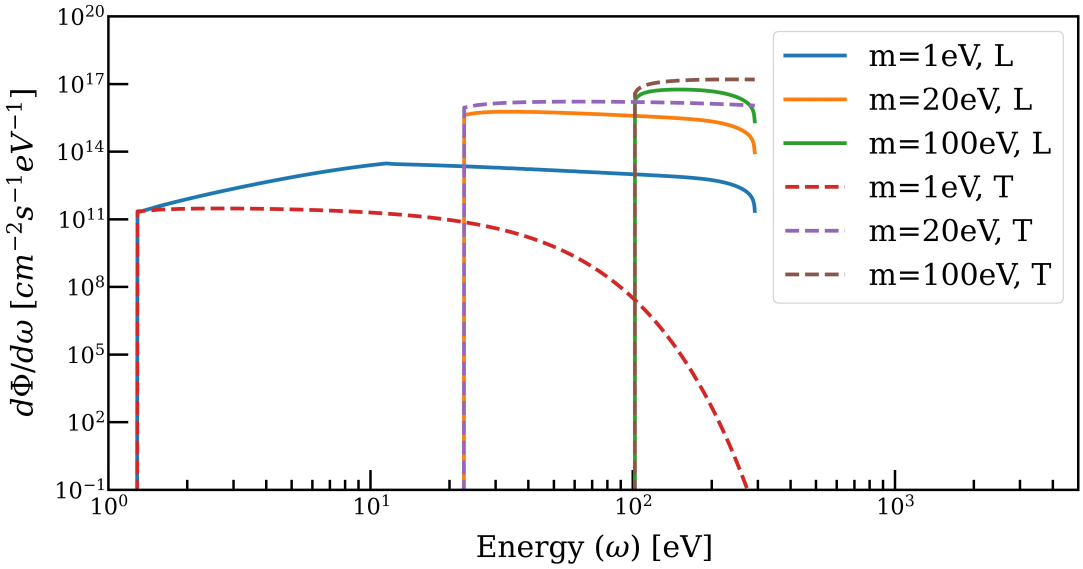

Figure 4.18: Dark photon flux at earth from resonant solar production.

4.8 Dark photon absorption in LXe

After determining the flux of dark photons as a function of mass and energy, it is necessary to determine the absorption rate of these dark photons. As the energies in question are relatively low, it makes more sense to use effects in the middle.

In this case, the liquid Xenon is considered a continuous fluid. The absorption rate is calculated for the medium as a whole rather than the sum of the interactions between the dark photon and the individual atoms.

To determine the rate of absorption, we estimated the values at different masses and energies for the polarization functions in LXe:

$$\Pi_T = \omega^2(1 - n_{ref}^2), \Pi_L = m_{DP}^2(1 - n_{ref}^2). \tag{4.65}$$

From there, it is possible to deduce the effective mixing parameter:

$$\kappa_{T,L}^2 = \frac{\kappa^2 m_{DP}^4}{(m_{DP}^2 - Re\Pi_{T,L})^2 + (Im\Pi_{T,L})^2}, \tag{4.66}$$

and then the absorption rate per dark photon:

$$\Gamma_{abs;T,L} = -\frac{\kappa^2_{T,L} Im\Pi_{T,L}}{\omega}. \tag{4.67}$$

The next step is to combine the previously derived flux rates (Equation (4.64)) with the absorption rates (Equation (4.67)) to obtain the total dark photons absorbed in liquid Xenon. This is done assuming that when a dark photon is absorbed, all of its energy is deposed into the medium. The total rate obtained is given by [180]:

$$\begin{aligned} R_{exp}(\kappa, m) = \int_m^{\omega_{max}} \frac{\omega}{\sqrt{\omega^2 - m^2}} \Bigg[& \frac{d\Phi_T}{d\omega}(\kappa, m, w)\Gamma_T(\kappa, m, w) \\ & + \frac{d\Phi_L}{d\omega}(\kappa, m, w)\Gamma_L(\kappa, m, w) \Bigg] d\omega. \end{aligned} \tag{4.68}$$

Thus, the differential form of Equation (4.68) is used to find the rate at a given energy with an energy spacing $d\omega$ equal to 1 eV. Then, the detector's response to an energy deposit is calculated at each energy.

4.9 Conclusion

We presented in this chapter the state of the art of the search for dark matter in the sub-GeV range that could be extracted by the set of data collected so far by XENONnT, whose data taking is still ongoing. Given the rigorous blinding policy adopted by the XENON Collaboration and that the data taking is not finished yet, it is impossible to publicly show any result on the exclusion limits, not even preliminary. However, we presented a complete list of all dark matter models that such analysis can scoop. For each of them, we presented the theoretical background, the way how the data rate should be interpreted, and the procedure to derive a limit.

This chapter also shows that the very low S2-only signal provided by the XENONnT detector can scope an extremely rich set of dark matter models, namely in the sub-GeV range. This is not the mainstream analysis for which XENONnT has been conceived, however, we showed how XENONnT could be competitive also in this analysis stream.

Chapter 5

Conclusion

This thesis has developed several study topics related to dark matter interacting with electrons through various analyzes of data acquired during the first scientific run of the XENONnT experiment. Understanding the detector's response to small charge signals helps to characterize the detector using single electrons, which also offers essential information about various phenomenologies. Finally, a search was undertaken for MeV mass scale dark matter using the detector's sensitivity to few-electron signals.

This thesis also presented a detailed study of the low-S2 spectrum, corresponding to the extraction of a few electrons and their proportional scintillation in the gas phase. The abundant single electrons derived from the photoionization of impurities in the liquid phase were used to build a model that could describe the spectrum of single electrons and their temporal stacks. With this model of the low-S2 spectrum, it was possible to measure the amount of light produced by an electron extracted from the liquid-gas interface. It also allows for the characterization of many parameters of the detector, such as the secondary scintillation efficiency. Furthermore, allowing for the study of the anode sagging due to gravity and the electrostatic force exerted on it. This study compared the secondary scintillation gain with the S2 gain of the monoenergetic calibration source. The data were compared to a theoretical model of the extraction process referring to microphysical methods. One of them concerns the trapping of electrons in the potential formed just below the phase boundary and their ability to be extracted later. Understanding this delayed emission mechanism is essential to the search for light matter, constituting a fundamental background.

The detector's sensitivity to S2 light produced by single electrons finds its utility in searching for dark matter particles with masses on the MeV scale, scattering with Xe atomic electrons, which is an emerging possibility in the framework of sectoral theories. This thesis has therefore been the occasion to present in detail the theoretical calculation of the event rate, taking into account a many-body quantum mechanical treatment of the initial and final states of the electron. Based on the theoretical and experimental understanding of electron recoil charge efficiency, the theoretical signal was convoluted with the detector response allowing the expected rates of a few electrons (1-5) to be calculated. These are compared to the observed rates of single electrons from the

low-S2 spectrum. This research's primary background is due to the plethora of mechanisms producing single electrons inside the detector. As this background increases with detector size, the most robust exclusion limits with a noble liquid target to date, for dark matter masses below 20 MeV, are still given by the XENON10 detector. Therefore, it is necessary to use the knowledge acquired on the phenomenology of single electrons to find a region of the total exposure which presents, as much as possible, a reduced rate of single electrons. By developing adequate cuts, it was possible to eliminate a significant part of the background noise due to single electron trains.

Moreover, with the development of a machine learning algorithm to classify low-energy S1 and S2, it was possible to improve further the sensitivity for the search for light dark matter. Finally, despite the extended single electron background resulting from the detector size, it is shown that it is possible to set a competitive exclusion limit for dark matter masses below 30 MeV precisely because of its better understanding and the extraordinary purity of the XENONnT detector. The actual limit is not shown since data taking is still going on, data are still blinded, and the presented cuts are still under improvement.

The era of Skipper silicon charge-coupled device (CCD) detectors like DAMIC or SENSEI is approaching. They are expected to dominate the search for a DM-electron interaction due to the very low bandgap energy, low leakage current, and the possibility of identification and rejection of the background based on excellent spatial resolution. However, this dominance is limited in the mass region below 10 MeV, as they quickly lose their sensitivity for higher masses. The present work shows that in the domain above 10 MeV, the large two-phase liquid Xenon detectors mainly developed for the search for dark matter WIMP can still probe the parametric space of the theory and have not reached the limit of their scientific potential. In addition, it is necessary to make dedicated efforts with small two-phase liquid Xenon TPC prototypes, carefully study the single electron background, and find ways to reduce it or develop a complete background model. Such an effort is now starting at LPNHE, the laboratory in which this thesis was carried out, aiming in the coming years to further strengthen the scientific potential of large Xenon detectors in the search for dark matter particles at the sub-GeV scale.

Bibliography

[1] Lord William Thomson Kelvin. *Baltimore lectures on molecular dynamics and the wave theory of light*. CUP Archive, 1904.

[2] Rudolf Clausius. "XVI. On a mechanical theorem applicable to heat". In: *The London, Edinburgh, and Dublin Philosophical Magazine and Journal of Science* 40.265 (1870), pp. 122–127.

[3] Gabriella De Lucia et al. "The formation history of elliptical galaxies". In: *Monthly Notices of the Royal Astronomical Society* 366.2 (2006), pp. 499–509.

[4] M Fukugita, CJ Hogan, and PJE Peebles. "The cosmic baryon budget". In: *The Astrophysical Journal* 503.2 (1998), p. 518.

[5] Henri Poincaré. "La voie lactée et la théorie des gaz". In: *Bulletin de la société astronomique de France* 20 (1906), pp. 153–165.

[6] Fritz Zwicky. "On the Masses of Nebulae and of Clusters of Nebulae". In: *The Astrophysical Journal* 86 (1937), p. 217.

[7] Horace W Babcock. "The rotation of the Andromeda Nebula". In: *Lick Observatory Bulletin* 19 (1939), pp. 41–51.

[8] JG De Swart, Gianfranco Bertone, and Jeroen van Dongen. "How dark matter came to matter". In: *Nature Astronomy* 1.3 (2017), pp. 1–9.

[9] Kim Griest and P Murdin. "Wimps and machos". In: *Encyclopedia of Astronomy & Astrophysics, IOP Publishing Ltd* (2006).

[10] Wikimedia Commons. *Rotation curve of spiral galaxy Messier 33 (Triangulum)*. 2018. URL: `https://commons.wikimedia.org/wiki/File:Rotation_curve_of_spiral_galaxy_Messier_33_(Triangulum).png`.

[11] Vera C Rubin and W Kent Ford Jr. "Rotation of the Andromeda nebula from a spectroscopic survey of emission regions". In: *The Astrophysical Journal* 159 (1970), p. 379.

[12] Albert Bosma. "The distribution and kinematics of neutral hydrogen in spiral galaxies of various morphological types". PhD thesis. Rijksuniversiteit te Groningen., 1978.

[13] Scott Dodelson and Fabian Schmidt. *Modern cosmology*. Academic Press, 2020.

[14] George R Blumenthal et al. "Formation of galaxies and large-scale structure with cold dark matter". In: *Nature* 311.5986 (1984), pp. 517–525.

[15] Michele Cappellari et al. "The ATLAS3D project–XV. Benchmark for early-type galaxies scaling relations from 260 dynamical models: mass-to-light ratio, dark matter, Fundamental Plane and Mass Plane". In: *Monthly Notices of the Royal Astronomical Society* 432.3 (2013), pp. 1709–1741.

[16] Julien Lesgourgues and Sergio Pastor. "Neutrino mass from Cosmology". In: *Advances in High Energy Physics* 2012 (2012).

[17] Particle Data Group et al. "Review of particle physics". In: *Progress of Theoretical and Experimental Physics* 2020.8 (2020), p. 083C01.

[18] G. Gamow and S.M. Ulam. *My World Line; an Informal Autobiography*. Viking Press, 1970, p. 44. ISBN: 9780670503766.

[19] Adam G Riess et al. "Observational evidence from supernovae for an accelerating universe and a cosmological constant". In: *The Astronomical Journal* 116.3 (1998), p. 1009.

[20] Nabila Aghanim et al. "Planck 2018 results-VI. Cosmological parameters". In: *Astronomy & Astrophysics* 641 (2020), A6.

[21] Urbain Le Verrier. "Lettre de M. Le Verrier à M. Faye sur la théorie de Mercure et sur le mouvement du périhélie de cette planète". In: *Comptes rendus hebdomadaires des séances de l'Académie des sciences* 49 (1859), pp. 379–383.

[22] Mordehai Milgrom. "A modification of the Newtonian dynamics as a possible alternative to the hidden mass hypothesis". In: *The Astrophysical Journal* 270 (1983), pp. 365–370.

[23] Ernesto López Fune. "Dark matter and galaxy rotation curves". PhD thesis. Scuola Internazionale Superiore di Studi Avanzati., 2017.

[24] KG Begeman, AH Broeils, and RH Sanders. "Extended rotation curves of spiral galaxies: Dark haloes and modified dynamics". In: *Monthly Notices of the Royal Astronomical Society* 249.3 (1991), pp. 523–537.

[25] Benoit Famaey et al. "Insight into the baryon-gravity relation in galaxies". In: *Physical Review D* 75.6 (2007), p. 063002.

[26] Norsiah Hashim et al. "Rotation curve with MOND and dark matter halo profile for ESO138-G014". In: *arXiv preprint arXiv:1407.0379* (2014).

[27] Douglas Clowe et al. "A direct empirical proof of the existence of dark matter". In: *The Astrophysical Journal* 648.2 (2006), p. L109.

[28] Maxim Markevitch et al. "Direct constraints on the dark matter self-interaction cross section from the merging galaxy cluster 1e 0657–56". In: *The Astrophysical Journal* 606.2 (2004), p. 819.

[29] David Harvey et al. "The nongravitational interactions of dark matter in colliding galaxy clusters". In: *Science* 347.6229 (2015), pp. 1462–1465.

[30] RH Sanders. "Neutrinos as cluster dark matter". In: *Monthly Notices of the Royal Astronomical Society* 380.1 (2007), pp. 331–338.

[31] J Bonn et al. "Results from the Mainz neutrino mass experiment". In: *Progress in Particle and Nuclear Physics* 48.1 (2002), pp. 133–139.

[32] Etienne Pointecouteau and Joseph Silk. "New constraints on modified Newtonian dynamics from galaxy clusters". In: *Monthly Notices of the Royal Astronomical Society* 364.2 (2005), pp. 654–658.

[33] Garry W Angus et al. "On the proof of dark matter, the law of gravity, and the mass of neutrinos". In: *The Astrophysical Journal* 654.1 (2006), p. L13.

[34] Garry W Angus, Benoit Famaey, and David A Buote. "X-ray group and cluster mass profiles in MOND: unexplained mass on the group scale". In: *Monthly Notices of the Royal Astronomical Society* 387.4 (2008), pp. 1470–1480.

[35] Garry W Angus. "Is an 11 eV sterile neutrino consistent with clusters, the cosmic microwave background and modified Newtonian dynamics?" In: *Monthly Notices of the Royal Astronomical Society* 394.1 (2009), pp. 527–532.

[36] Garry W Angus et al. "Cosmological simulations in MOND: the cluster scale halo mass function with light sterile neutrinos". In: *Monthly Notices of the Royal Astronomical Society* 436.1 (2013), pp. 202–211.

[37] Bernard Carr. "Baryonic dark matter". In: *Annual Review of Astronomy and Astrophysics* 32.1 (1994), pp. 531–590.

[38] Katherine Freese, Brian Fields, and David Graff. "Death of stellar baryonic dark matter". In: *Sources and Detection of Dark Matter and Dark Energy in the Universe*. Springer, 2001, pp. 159–167.

[39] John S Mulchaey et al. "Diffuse X-ray emission from the NGC 2300 group of galaxies-Implications for dark matter and galaxy evolution in small groups". In: *The Astrophysical Journal* 404 (1993), pp. L9–L12.

[40] David A Buote and Claude R Canizares. "X-ray constraints on the intrinsic shapes and baryon fractions of five abell clusters". In: *arXiv preprint astro-ph/9504049* (1995).

[41] John N Bahcall et al. "M dwarfs, microlensing, and the mass budget of the galaxy". In: *arXiv preprint astro-ph/9406019* (1994).

[42] DJ Fixsen. "The temperature of the cosmic microwave background". In: *The Astrophysical Journal* 707.2 (2009), p. 916.

[43] European Space Agency. *Planck CMB*. 2013. URL: `https://www.esa.int/ESA_Multimedia/Images/2013/03/Planck_CMB`.

[44] S. Weinberg. *Cosmology*. OUP Oxford, 2008. ISBN: 9780191523601. URL: `https://books.google.fr/books?id=2wlREAAAQBAJ`.

[45] Wayne Hu and Scott Dodelson. "Cosmic microwave background anisotropies". In: *Annual Review of Astronomy and Astrophysics* 40.1 (2002), pp. 171–216.

[46] PS Bhupal Dev, Anupam Mazumdar, and Saleh Qutub. "Constraining non-thermal and thermal properties of dark matter". In: *Frontiers in Physics* 2 (2014), p. 26.

[47] Steen Hannestad et al. "Neutrino and axion hot dark matter bounds after WMAP-7". In: *Journal of Cosmology and Astroparticle Physics* 2010.08 (2010), p. 001.

[48] Leanne D Duffy and Karl Van Bibber. "Axions as dark matter particles". In: *New Journal of Physics* 11.10 (2009), p. 105008.

[49] Jonathan L Feng. "Dark matter candidates from particle physics and methods of detection". In: *Annual Review of Astronomy and Astrophysics* 48 (2010), pp. 495–545.

[50] Leszek Roszkowski, Enrico Maria Sessolo, and Sebastian Trojanowski. "WIMP dark matter candidates and searches—current status and future prospects". In: *Reports on Progress in Physics* 81.6 (2018), p. 066201.

[51] Gary Steigman, Basudeb Dasgupta, and John F Beacom. "Precise relic WIMP abundance and its impact on searches for dark matter annihilation". In: *Physical Review D* 86.2 (2012), p. 023506.

[52] Rouven Essig, Jeremy Mardon, and Tomer Volansky. "Direct detection of sub-GeV dark matter". In: *Physical Review D* 85.7 (2012), p. 076007.

[53] Julien Billard et al. "Direct detection of dark matter–APPEC committee report". In: *Reports on Progress in Physics* (2022).

[54] Marco Cirelli et al. "PPPC 4 DM ID: a poor particle physicist cookbook for dark matter indirect detection". In: *Journal of Cosmology and Astroparticle Physics* 2011.03 (2011), p. 051.

[55] Stefan Funk. "Indirect detection of dark matter with γ rays". In: *Proceedings of the National Academy of Sciences* 112.40 (2015), pp. 12264–12271.

[56] Christopher M Karwin et al. "Fermi-LAT Observations of γ-Ray Emission toward the Outer Halo of M31". In: *The Astrophysical Journal* 880.2 (2019), p. 95.

[57] Christopher M Karwin et al. "Dark matter interpretation of the Fermi-LAT observations toward the outer halo of M31". In: *Physical Review D* 103.2 (2021), p. 023027.

[58] Kohei Hayashi et al. "Dark matter distribution in the Galactic dwarf spheroidal galaxies". In: *Journal of Physics: Conference Series*. Vol. 1468. 1. IOP Publishing. 2020, p. 012011.

[59] MAGIC collaboration et al. "Limits to dark matter annihilation cross-section from a combined analysis of MAGIC and Fermi-LAT observations of dwarf satellite galaxies". In: *Journal of Cosmology and Astroparticle Physics* 2016.02 (2016), p. 039.

[60] R Abbasi et al. "Search for GeV-scale dark matter annihilation in the Sun with IceCube DeepCore". In: *Physical Review D* 105.6 (2022), p. 062004.

[61] Zeren Simon Wang and Kechen Wang. "Long-lived light neutralinos at future Z factories". In: *Physical Review D* 101.11 (2020), p. 115018.

[62] Stefano Giagu. "WIMP dark matter searches with the ATLAS detector at the LHC". In: *Frontiers in Physics* 7 (2019), p. 75.

[63] JD Lewin and PF Smith. "Review of mathematics, numerical factors, and corrections for dark matter experiments based on elastic nuclear recoil". In: *Astroparticle Physics* 6.1 (1996), pp. 87–112.

[64] Katherine Freese, Mariangela Lisanti, and Christopher Savage. "Colloquium: Annual modulation of dark matter". In: *Reviews of Modern Physics* 85.4 (2013), p. 1561.

[65] Richard W Schnee. "Introduction to dark matter experiments". In: *Physics of the Large and the Small: TASI 2009*. World Scientific, 2011, pp. 775–829.

[66] Justin I Read. "The local dark matter density". In: *Journal of Physics G: Nuclear and Particle Physics* 41.6 (2014), p. 063101.

[67] Georges Aad et al. "Observation of a new particle in the search for the Standard Model Higgs boson with the ATLAS detector at the LHC". In: *Physics Letters B* 716.1 (2012), pp. 1–29.

[68] Serguei Chatrchyan et al. "Observation of a new boson at a mass of 125 GeV with the CMS experiment at the LHC". In: *Physics Letters B* 716.1 (2012), pp. 30–61.

[69] Hironari Miyazawa. "Baryon number changing currents". In: *Progress of Theoretical Physics* 36.6 (1966), pp. 1266–1276.

[70] Hironari Miyazawa. "Spinor currents and symmetries of baryons and mesons". In: *Physical Review* 170.5 (1968), p. 1586.

[71] Savas Dimopoulos and Howard Georgi. "Softly broken supersymmetry and SU (5)". In: *Nuclear Physics B* 193.1 (1981), pp. 150–162.

[72] Mark W Goodman and Edward Witten. "Detectability of certain dark-matter candidates". In: *Physical Review D* 31.12 (1985), p. 3059.

[73] Mariangela Lisanti. "Lectures on dark matter physics". In: *New Frontiers in Fields and Strings: TASI 2015 Proceedings of the 2015 Theoretical Advanced Study Institute in Elementary Particle Physics*. World Scientific, 2017, pp. 399–446.

[74] Gerard Jungman, Marc Kamionkowski, and Kim Griest. "Supersymmetric dark matter". In: *Physics Reports* 267.5-6 (1996), pp. 195–373.

[75] Richard H Helm. "Inelastic and elastic scattering of 187-Mev electrons from selected even-even nuclei". In: *Physical Review* 104.5 (1956), p. 1466.

[76] Jihn E Kim and Gianpaolo Carosi. "Axions and the strong C P problem". In: *Reviews of Modern Physics* 82.1 (2010), p. 557.

[77] Roberto D Peccei and Helen R Quinn. "CP conservation in the presence of pseudoparticles". In: *Physical Review Letters* 38.25 (1977), p. 1440.

[78] Jeffrey Goldstone. "Field theories with «Superconductor» solutions". In: *Il Nuovo Cimento (1955-1965)* 19.1 (1961), pp. 154–164.

[79] Hans-Thomas Janka et al. "Nucleon spin fluctuations and the supernova emission of neutrinos and axions". In: *Physical Review Letters* 76.15 (1996), p. 2621.

[80] Keith A Olive et al. "Review of particle physics". In: *Chinese physics C* 38.9 (2014), p. 090001.

[81] Mikhail A Shifman, AI Vainshtein, and Valentin I Zakharov. "Can confinement ensure natural CP invariance of strong interactions?" In: *Nuclear Physics B* 166.3 (1980), pp. 493–506.

[82] Michael Dine, Willy Fischler, and Mark Srednicki. "A simple solution to the strong CP problem with a harmless axion". In: *Physics letters B* 104.3 (1981), pp. 199–202.

[83] AR Zhitnitskij. "On possible suppression of the axion-hadron interactions". In: *Yadernaya Fizika* 31.2 (1980), pp. 497–504.

[84] Martin Bauer et al. "The low-energy effective theory of axions and ALPs". In: *Journal of High Energy Physics* 2021.4 (2021), pp. 1–46.

[85] A Derevianko et al. "Axio-electric effect". In: *Physical Review D* 82.6 (2010), p. 065006.

[86] E Aprile et al. "First axion results from the XENON100 experiment". In: *Physical Review D* 90.6 (2014), p. 062009.

[87] AH Abdelhameed et al. "New limits on the resonant absorption of solar axions obtained with a 169Tm-containing cryogenic detector". In: *The European Physical Journal C* 80.5 (2020), pp. 1–7.

[88] Christina Gao et al. "Reexamining the solar axion explanation for the XENON1T excess". In: *Physical Review Letters* 125.13 (2020), p. 131806.

[89] Lotty Ackerman et al. "Dark matter and dark radiation". In: *Physical Review D* 79.2 (2009), p. 023519.

[90] Letizia Diamante. "New Portal to Unveil the Dark Sector of the Universe". In: *Institute for Basic Science (IBS)* 3 (2017).

[91] Alessandra Filippi and Marzio De Napoli. "Searching in the dark: the hunt for the dark photon". In: *Reviews in Physics* 5 (2020), p. 100042.

[92] E Aprile et al. "Design and performance of the XENON10 dark matter experiment". In: *Astroparticle Physics* 34.9 (2011), pp. 679–698.

[93] J Angle et al. "First results from the XENON10 dark matter experiment at the Gran Sasso National Laboratory". In: *Physical Review Letters* 100.2 (2008), p. 021303.

[94] Elena Aprile et al. "The XENON100 dark matter experiment". In: *Astroparticle Physics* 35.9 (2012), pp. 573–590.

[95] Elena Aprile et al. "The XENON1T dark matter experiment". In: *The European Physical Journal C* 77.12 (2017), pp. 1–23.

[96] E Aprile et al. "Dark Matter Search Results from a One Tonne.Year Exposure of XENON1T". In: *arXiv preprint arXiv:1805.12562* (2018).

[97] Elena Aprile et al. "Light dark matter search with ionization signals in XENON1T". In: *Physical Review Letters* 123.25 (2019), p. 251801.

[98] Elena Aprile et al. "Search for light dark matter interactions enhanced by the Migdal effect or Bremsstrahlung in XENON1T". In: *Physical review letters* 123.24 (2019), p. 241803.

[99] Elena Aprile et al. "Excess electronic recoil events in XENON1T". In: *Physical Review D* 102.7 (2020), p. 072004.

[100] E Aprile et al. "Projected WIMP sensitivity of the XENONnT dark matter experiment". In: *Journal of Cosmology and Astroparticle Physics* 2020.11 (2020), p. 031.

[101] E Aprile et al. "Search for New Physics in Electronic Recoil Data from XENONnT". In: *arXiv e-prints* (2022), arXiv–2207.

[102] JJ Choi et al. "Exploring coherent elastic neutrino-nucleus scattering using reactor electron antineutrinos in the NEON experiment". In: *arXiv preprint arXiv:2204.06318* (2022).

[103] Laura Baudis. "WIMP dark matter direct-detection searches in noble gases". In: *Physics of the Dark Universe* 4 (2014), pp. 50–59.

[104] Gloria B Lubkin. "Dubna cyclotrons paired to accelerate xenon". In: *Physics Today* 25.1 (1972), p. 19.

[105] Richard A Muller et al. "Liquid-filled proportional counter". In: *Physical Review Letters* 27.8 (1971), p. 532.

[106] William M White. *Encyclopedia of Geochemistry: A Comprehensive Reference Source on the Chemistry of the Earth*. Springer International Publishing, 2020.

[107] AS Barabash. "Average (recommended) half-life values for two-neutrino double-beta decay". In: *Czechoslovak journal of physics* 52.4 (2002), pp. 567–573.

[108] Meng Wang et al. "The AME 2020 atomic mass evaluation (II). Tables, graphs and references". In: *Chinese Physics C* 45.3 (2021), p. 030003.

[109] DR Nygren. *The time-projection chamber: A new 4. pi. detector for charged particles: A new 4. pi. detector for charged particles*. Tech. rep. Stanford Linear Accelerator Center, Menlo Park, CA (USA); Lawrence Berkeley ..., 1974.

[110] Carlo Rubbia. *The liquid-argon time projection chamber: a new concept for neutrino detectors*. Tech. rep. 1977.

[111] Marlo Martin. "Exciton Self-Trapping in Rare-Gas Crystals". In: *The Journal of Chemical Physics* 54.8 (1971), pp. 3289–3299.

[112] Jeremy Mock et al. "Modeling pulse characteristics in Xenon with NEST". In: *Journal of Instrumentation* 9.04 (2014), T04002.

[113] E Aprile et al. "XENON100 dark matter results from a combination of 477 live days". In: *Physical Review D* 94.12 (2016), p. 122001.

[114] Laura Baudis, Patricia Sanchez-Lucas, and Kevin Thieme. "A measurement of the mean electronic excitation energy of liquid xenon". In: *The European Physical Journal C* 81.12 (2021), pp. 1–12.

[115] G Anton et al. "Measurement of the scintillation and ionization response of liquid xenon at MeV energies in the EXO-200 experiment". In: *Physical Review C* 101.6 (2020), p. 065501.

[116] Tan Takahashi et al. "Average energy expended per ion pair in liquid xenon". In: *Physical Review A* 12.5 (1975), p. 1771.

[117] XENON Collaboration et al. "XENON1T dark matter data analysis: Signal and background models and statistical inference". In: *Physical Review D* 99.11 (2019), p. 112009.

[118] J Thomas and DA Imel. "Recombination of electron-ion pairs in liquid argon and liquid xenon". In: *Physical Review A* 36.2 (1987), p. 614.

[119] DS Akerib et al. "Tritium calibration of the LUX dark matter experiment". In: *Physical Review D* 93.7 (2016), p. 072009.

[120] Matthew Szydagis. "NEST, or, the Noble Element Simulation Technique". In: (2013).

[121] Pavel A Cherenkov. "Visible light from clear liquids under the action of gamma radiation". In: *Comptes Rendus (Doklady) de l'Aeademie des Sciences de l'URSS* 2.8 (1934), pp. 451–454.

[122] Vasile C Antochi et al. "Improved quality tests of R11410-21 photomultiplier tubes for the XENONnT experiment". In: *Journal of Instrumentation* 16.08 (2021), P08033.

[123] R Saldanha et al. "Model independent approach to the single photoelectron calibration of photomultiplier tubes". In: *Nuclear Instruments and Methods in Physics Research Section A: Accelerators, Spectrometers, Detectors and Associated Equipment* 863 (2017), pp. 35–46.

[124] G Plante et al. "Liquid-phase purification for multi-tonne xenon detectors". In: *arXiv preprint arXiv:2205.07336* (2022).

[125] L Scotto Lavina. "The challenges of the direct dark matter search with liquid xenon". PhD thesis. Sorbonne University, 2018.

[126] E Aprile et al. "The XENON1T data acquisition system". In: *Journal of Instrumentation* 14.07 (2019), P07016.

[127] Nir Friedman, Dan Geiger, and Moises Goldszmidt. "Bayesian network classifiers". In: *Machine learning* 29.2 (1997), pp. 131–163.

[128] E Aprile et al. "Energy resolution and linearity of XENON1T in the MeV energy range". In: *The European Physical Journal C* 80.8 (2020), pp. 1–9.

[129] EA McCutchan. "Nuclear data sheets for A= 83". In: *Nuclear Data Sheets* 125 (2015), pp. 201–394.

[130] S Rosendahl et al. "A novel 83mKr tracer method for characterizing xenon gas and cryogenic distillation systems". In: *Journal of Instrumentation* 9.10 (2014), P10010.

[131] Elena Aprile et al. "Results from a calibration of XENON100 using a source of dissolved radon-220". In: *Physical review D* 95.7 (2017), p. 072008.

[132] VI Barsanov et al. "A technology and facility for extraction, purification, and collection of 37Ar from calcium oxide". In: *Instruments and Experimental Techniques* 49.4 (2006), pp. 454–460.

[133] E Aprile et al. "Physics reach of the XENON1T dark matter experiment." In: *Journal of Cosmology and Astroparticle Physics* 2016.04 (2016), p. 027.

[134] Sea Agostinelli et al. "GEANT4—a simulation toolkit". In: *Nuclear instruments and methods in physics research section A: Accelerators, Spectrometers, Detectors and Associated Equipment* 506.3 (2003), pp. 250–303.

[135] Glen Cowan et al. "Asymptotic formulae for likelihood-based tests of new physics". In: *The European Physical Journal C* 71.2 (2011), pp. 1–19.

[136] Samuel S Wilks. "The large-sample distribution of the likelihood ratio for testing composite hypotheses". In: *The annals of mathematical statistics* 9.1 (1938), pp. 60–62.

[137] F Ruppin et al. "Complementarity of dark matter detectors in light of the neutrino background". In: *Physical Review D* 90.8 (2014), p. 083510.

[138] J Aalbers et al. "222 Rn emanation measurements for the XENON1T experiment". In: *The European Physical Journal C-Particles and Fields* 81.4 (2021).

[139] J Aalbers et al. "DARWIN: towards the ultimate dark matter detector". In: *Journal of Cosmology and Astroparticle Physics* 2016.11 (2016), p. 017.

[140] J Angle et al. "Search for light dark matter in XENON10 data". In: *Physical Review Letters* 107.5 (2011), p. 051301.

[141] B Edwards et al. "Measurement of single electron emission in two-phase xenon". In: *Astroparticle Physics* 30.2 (2008), pp. 54–57.

[142] Xiang Xiao et al. "Low-mass dark matter search results from full exposure of the PandaX-I experiment". In: *Physical Review D* 92.5 (2015), p. 052004.

[143] E Santos et al. "Single electron emission in two-phase xenon with application to the detection of coherent neutrino-nucleus scattering". In: *Journal of High Energy Physics* 2011.12 (2011), pp. 1–20.

[144] E Aprile et al. "Observation and applications of single-electron charge signals in the XENON100 experiment". In: *Journal of Physics G: Nuclear and Particle Physics* 41.3 (2014), p. 035201.

[145] DS Akerib et al. "Investigation of background electron emission in the LUX detector". In: *Physical Review D* 102.9 (2020), p. 092004.

[146] Louis Malter. "Thin film field emission". In: *Physical Review* 50.1 (1936), p. 48.

[147] Maxime Le Calloch. "Study of the single electron charge signals in the XENON100 direct Dark Matter search experiment". PhD thesis. Université de Nantes, 2014.

[148] Jean-Philippe Zopounidis. "Search for leptonically interacting dark matter with the XENON1T electronic recoil data". PhD thesis. Sorbonne université, 2020.

[149] Elena Aprile et al. "Emission of Single and Few Electrons in XENON1T and Limits on Light Dark Matter". In: *arXiv preprint arXiv:2112.12116* (2021).

[150] Andrii Ilienko. "Continuous counterparts of Poisson and binomial distributions and their properties". In: *arXiv preprint arXiv:1303.5990* (2013).

[151] Masayo Suzuki and Shinzou Kubota. "Mechanism of proportional scintillation in argon, krypton and xenon". In: *Nuclear Instruments and Methods* 164.1 (1979), pp. 197–199.

[152] CMB Monteiro et al. "Secondary scintillation yield in pure xenon". In: *Journal of Instrumentation* 2.05 (2007), P05001.

[153] David Nygren. "High-pressure xenon gas electroluminescent TPC for 0-ν β β-decay search". In: *Nuclear Instruments and Methods in Physics Research Section A: Accelerators, Spectrometers, Detectors and Associated Equipment* 603.3 (2009), pp. 337–348.

[154] M Salete SCP Leite and LEITE MSSCP. "Radioluminescence of rare gases". In: (1980).

[155] D Yu Akimov et al. "Measurement of single-electron noise in a liquid-xenon emission detector". In: *Instruments and Experimental Techniques* 55.4 (2012), pp. 423–428.

[156] Jingke Xu et al. "Electron extraction efficiency study for dual-phase xenon dark matter experiments". In: *Physical Review D* 99.10 (2019), p. 103024.

[157] Peter Sorensen. "Electron train backgrounds in liquid xenon dark matter search detectors are indeed due to thermalization and trapping". In: *arXiv preprint arXiv:1702.04805* (2017).

[158] Masahiro Ibe et al. "Migdal effect in dark matter direct detection experiments". In: *Journal of High Energy Physics* 2018.3 (2018), pp. 1–36.

[159] J Billard, F Mayet, and D Santos. "Assessing the discovery potential of directional detection of dark matter". In: *Physical Review D* 85.3 (2012), p. 035006.

[160] J Billard, E Figueroa-Feliciano, and L Strigari. "Implication of neutrino backgrounds on the reach of next generation dark matter direct detection experiments". In: *Physical Review D* 89.2 (2014), p. 023524.

[161] A Migdal. "Ionizatsiya atomov pri yadernykh reaktsiyakh". In: *Sov. Phys. JETP* 9 (1939), p. 1163.

[162] David Smith and Neal Weiner. "Inelastic dark matter". In: *Physical Review D* 64.4 (2001), p. 043502.

[163] Nicole F Bell et al. "Low-mass inelastic dark matter direct detection via the Migdal effect". In: *Physical Review D* 104.7 (2021), p. 076013.

[164] Tsung-Dao Lee and Chen-Ning Yang. "Question of parity conservation in weak interactions". In: *Physical Review* 104.1 (1956), p. 254.

[165] I Yu Kobzarev, LB Okun, and I Ya Pomeranchuk. "POSSIBILITY OF OBSERVING MIRROR PARTICLES". In: *Yadern. Fiz.* 3 (1966).

[166] Zurab Berezhiani. "Mirror world and its cosmological consequences". In: *International Journal of Modern Physics A* 19.23 (2004), pp. 3775–3806.

[167] Brian Patt and Frank Wilczek. "Higgs-field portal into hidden sectors". In: *arXiv preprint hep-ph/0605188* (2006).

[168] Bob Holdom. "Two U (1)'s and epsilon charge shifts". In: *Phys. Lett., B* 166.2 (1986), pp. 196–198.

[169] Glennys R Farrar and Pierre Fayet. "Phenomenology of the production, decay, and detection of new hadronic states associated with supersymmetry". In: *Physics Letters B* 76.5 (1978), pp. 575–579.

[170] Rouven Essig et al. "Direct detection of sub-GeV dark matter with semiconductor targets". In: *Journal of High Energy Physics* 2016.5 (2016), pp. 1–54.

[171] Clemens Carel Johannes Roothaan. "New developments in molecular orbital theory". In: *Reviews of modern physics* 23.2 (1951), p. 69.

[172] Carlos F Bunge, Jose A Barrientos, and A Vivier Bunge. "Roothaan-Hartree-Fock ground-state atomic wave functions: Slater-type orbital expansions and expectation values for Z= 2-54". In: *Atomic data and nuclear data tables* 53.1 (1993), pp. 113–162.

[173] P Agnes et al. "Constraints on sub-GeV dark-matter–electron scattering from the DarkSide-50 experiment". In: *Physical review letters* 121.11 (2018), p. 111303.

[174] DS Akerib et al. "Ultralow energy calibration of LUX detector using Xe 127 electron capture". In: *Physical Review D* 96.11 (2017), p. 112011.

[175] Rouven Essig et al. "First direct detection limits on sub-GeV dark matter from XENON10". In: *Physical review letters* 109.2 (2012), p. 021301.

[176] Rouven Essig, Mukul Sholapurkar, and Tien-Tien Yu. "Solar neutrinos as a signal and background in direct-detection experiments searching for sub-GeV dark matter with electron recoils". In: *Physical Review D* 97.9 (2018), p. 095029.

[177] Jiunn-Wei Chen et al. "Low-energy electronic recoil in xenon detectors by solar neutrinos". In: *Physics Letters B* 774 (2017), pp. 656–661.

[178] John N Bahcall, Aldo M Serenelli, and Sarbani Basu. "New solar opacities, abundances, helioseismology, and neutrino fluxes". In: *The Astrophysical Journal* 621.1 (2005), p. L85.

[179] Shaofei Zhu and EA McCutchan. "Nuclear Data Sheets for A= 214". In: *Nuclear Data Sheets* 175 (2021), pp. 1–149.

[180] Itay M Bloch et al. "Searching for dark absorption with direct detection experiments". In: *Journal of High Energy Physics* 2017.6 (2017), pp. 1–21.

[181] Haipeng An, Maxim Pospelov, and Josef Pradler. "Dark matter detectors as dark photon helioscopes". In: *Physical review letters* 111.4 (2013), p. 041302.

[182] Haipeng An et al. "Direct detection constraints on dark photon dark matter". In: *Physics Letters B* 747 (2015), pp. 331–338.

[183] Burton L Henke, Eric M Gullikson, and John C Davis. "X-ray interactions: photoabsorption, scattering, transmission, and reflection at E= 50-30,000 eV, Z= 1-92". In: *Atomic data and nuclear data tables* 54.2 (1993), pp. 181–342.

[184] Tianqi Sai et al. "Designing refractive index fluids using the Kramers–Kronig relations". In: *Faraday Discussions* 223 (2020), pp. 136–144.

[185] Anirban Majumdar, DK Papoulias, and Rahul Srivastava. "Dark matter detectors as a novel probe for light new physics". In: *Physical Review D* 106.1 (2022), p. 013001.

[186] Il'idio Lopes and Sylvaine Turck-Chieze. "Solar neutrino physics oscillations: Sensitivity to the electronic density in the Sun's core". In: *The Astrophysical Journal* 765.1 (2013), p. 14.

[187] André De Gouvêa and James Jenkins. "What can we learn from neutrino electron scattering?" In: *Physical Review D* 74.3 (2006), p. 033004.

[188] P Vogel and J Engel. "Neutrino electromagnetic form factors". In: *Physical Review D* 39.11 (1989), p. 3378.

[189] Javier Redondo. "Helioscope bounds on hidden sector photons". In: *Journal of Cosmology and Astroparticle Physics* 2008.07 (2008), p. 008.

[190] Javier Redondo and Georg Raffelt. "Solar constraints on hidden photons re-visited". In: *Journal of Cosmology and Astroparticle Physics* 2013.08 (2013), p. 034.